Carrier induced ferromagnetism in (Cd,Mn)Te quantum wells: a spectroscopic study.

Wiktor Maslana

Uniwersytet Warszawski

Instytut Fizyki Doświadczalnej

Wiktor Maślana

Carrier induced ferromagnetism in (Cd,Mn)Te quantum wells: a spectroscopic study.

PhD Thesis supervised by

prof. Joël Cibert and prof. Jan Gaj

Warszawa - Grenoble – 2007

UNIVERSITE JOSEPH FOURIER-GRENOBLE 1

THESE

pour obtenir le grade de

DOCTEUR DE L'UNIVERSITE JOSEPH FOURIER

Discipline: Physique

Présentée et soutenue publiquement

par

Wiktor Maślana

le 2 juillet 2007

Ferromagnétism induit par les porteurs dans des puits quantiques de (Cd,Mn)Te: etude spectroscopique du desordre.

Composition du jury

Président	Michał NAWROCKI
Rapporteurs:	Marian GRYNBERG Aristide LEMAITRE
Examinateur:	David FERRAND
Directeurs de thèse:	Joël CIBERT Jan GAJ

Université Joseph Fourier-Grenoble 1 - (CNRS - UMR 5588)
Laboratoire de Spectrométrie Physique
Uniwersytet Warszawski - Instytut Fizyki Doświadczalnej - Zakład Fizyki Ciała Stałego

Here I am,
Here I am,
Waiting...

Acknowledgments

This thesis was written under joined supervision of two universities: Warsaw University (Warsaw, Poland) and Université Joseph Fourier-Grenoble 1 (Grenoble, France). The presented work is a result of collaboration between the Solid State Division of Institute of Experimental Physics (Warsaw University) and Laboratoire de Spectrométrie Physique (Université Joseph Fourier).

I am grateful to all the people that helped me in course of my work. Unfortunately, it is not possible to name them all here, but I would like to mention the people of essential importance to this work.

I would like to thank prof. **Marian Grynberg** for opening my eyes to the beauty of physics of semiconductors and the most inspiring lectures in course of my studies.

I am much indebted to my supervisors: prof. dr hab. **Jan Gaj** and prof. **Joël Cibert** for their concern and guidance. It would not be possible to achieve results presented in this work without their patience and support.

I am deeply grateful to dr hab. **Piotr Kossacki** for his willingness to share his vast knowledge and experimental skills. His helping hand, extended during many hours we have spend together in the laboratory was priceless. I wish to thank for the fruitful discussions on physics and other topics that we so often drifted into. I am grateful for his friendship I could always rely on during our unforgettable mountain adventures.

I would like to thank dr **Mikaël Bertolini** and dr **Serge Tatarenko** for the samples we together investigated.

I am much indebted to the people who have enormously helped me during my experiments and taught me how to operate the experimental setups sharing their wisdom and experience. Among the personnel of the *Spectro* dr **David Ferrand**, dr **Hervé Boukari** and **André Wasiela**. At Warsaw University none of experiments would work without gentle care of dr hab. **Andrzej Golnik**.

I wish to thank all the employees and students of the Solid State Division of Institute of Experimental Physics and Laboratoire de Spectrométrie Physique for their kind spirits that contributed to the creative environment of both places. I have had great pleasure working together with them. I would like to thank all the girls from Solid State Division (especially Kasia and Paulina) that brought me the light of hope and warm smiles, even in the darkest hours of despair when all possible (and more) disasters fallen on my experiments.

None of that would possible without love and support of my family. I can never repay for that, so please accept my deepest gratitude.

Dziękuję bardzo! Merci beaucoup! Thank you very much!

Table of Contents

Introduction

Motivation : Spintronique

La découverte de la Magnéto-Résistance Géante (*Baibich et al.*, 1988) à ouvert un nouveau champ à lélectronique basé sur les propriétés du spin des électrons. Ce nouveau champ, la *spintronique*, utilise le spin électronique pour traiter et enregistrer linformation (*Wolf et al.*, 2001). Les avantages attendus pour augmenter les vitesses de traitement de données et pour diminuer la consommation énergétique des futurs dispositifs spintroniques attirent lattention des principaux laboratoires de recherche ainsi que des industriels. La quête de nouveaux matériaux semiconducteurs présentant des propriétés ferromagnétiques représente une partie importante des efforts de recherche dans le domaine de la spintronique. Le bon contrôle obtenu des porteurs de charge dans les matériaux semiconducteurs rend le ferromagnétisme induit par porteurs libres particulièrement intéressant dans loptique dobtenir un contrôle efficace du ferromagnétisme pour le traitement de linformation.

Ferromagnétisme induit par porteurs libres

La réalisation du ferromagnétisme induit par porteurs libres (*Dietl et al.*, 2001; *Haury et al.*, 1997) a attiré lattention sur les études des semiconducteurs dilués magnétiques (*DMS*) avec une forte densité de porteurs. Les études expérimentales se sont essentiellement portées sur (Ga,Mn)As, et ont ainsi permis des avancées rapides dans les domaines du contrôle des défauts dans les couches mince élaborées par épitaxie par jet moléculaire (*EJM*), et de lobtention de hautes températures critiques (T_c). Des composants ont déjà été développés (*Koshihara et al.*, 1997).

Les résultats les plus concluant ont été obtenu pour des structures de type p. Dans les DMS III-V, la même impureté (Mn) porte un moment magnétique et joue le rôle daccepteur (*Ohno*, 1998), ce qui implique de forte limitation à la réalisation de puits quantiques (QWs) et de systèmes bidimensionnels (2D) (*Ohno et al.*, 2000) utilisant des couches minces de DMS III-V (*Boselli et al.*, 2000; *Lee et al.*, 2000).

Les semiconducteurs II-VI représente un système unique pour lequel Mn est une impureté magnétique isoélectrique, ce qui permet de contrôler de manière indépendante la concentration électronique et la concentration dions magnétiques. En particulier, la méthode de modulation de dopage peut alors être utilisée pour introduire un gaz délectrons ou de trous 2D dans un puits quantique contenant un DMS. Bien que le ferromagnétisme ne soit observé dans ces matériaux dans des gammes de température trop basses pour des applications industrielles, ils constituent néanmoins un système modèle pour étudier le ferromagnétisme induit par porteurs libres (*Haury et al.*, 1997).

Dans les études réalisées sur lordre ferromagnétique dans des puits quantique de $Cd_{1-x}Mn_xTe$ (*Haury et al.*, 1997; *Kossacki et al.*, 2002; *Ferrand et al.*, 2001; *Boukari et al.*, 2002), les structures à modulation de dopage ont été élaborées par EJM en utilisant lazote comme impureté accepteur et des barrières de $Cd_{1-y-z}Zn_zMg_yTe$. Un modèle de champ moyen (Zener)

à permis de décrire avec succès les propriétés ferromagnétique des structures dopés à lazote, (*Dietl et al.*, 1997; *Kossacki et al.*, 2000). Bien quefficace, cette méthode de dopage présente de limitations. Un dopage efficace de $Cd_{1-y-z}Zn_zMg_yTe$ nest possible que pour des valeurs de y inférieures à 30% et ceci nest possible quen réduisant la température de croissance de 280°C à 220°C pour éviter une top forte interdiffusion dans lhétérostructure (*Arnoult et al.*, 1998), ce qui affecte grandement la qualité des échantillons (*Grieshaber et al.*, 1994). De plus, la présence dazote empêche pratiquement tout traitement post-croissance sur léchantillon.

Fluctuations

Il est largement reconnu que la compréhension du désordre (extrinsèque (*Hayashi et al.*, 2001; *Potashnik et al.*, 2001; *Edmonds et al.*, 2004) ou intrinsèque) est un des problèmes majeurs pour la matrise du ferromagnétisme induit par porteurs libres dans un semiconducteur. Les fluctuations thermiques ont été introduites dans le modèle de Zener en considérant les excitations élémentaires (*Konig et al.*, 2000). Le désordre de spin provient du caractère aléatoire de la distribution des moments magnétiques localisés. Le dopage électrique des semiconducteurs implique de même une distribution aléatoire des impuretés électriquement active (désordre électrostatique). Les échantillons actuels sont proches de la transition métal-isolant, bien loin de lapproximation des porteurs libres (modèle de Zener), ou fortement localisés (modèle de percolation de polarons magnétiques (*Berciu and Bhatt*, 2001; *Kaminski and Sarma*, 2002)).

Objectifs

Deux objectifs principaux ont été fixés :

- Etendre la plage des paramètres des systèmes ferromagnétiques.
- Examiner le rôle des fluctuations dans la phase ferromagnétique.

Pour atteindre ces objectifs nous avons développé une nouvelle méthode de dopage utilisant les états de surface comme source de trous pour le QW. Les fluctuations de densité de porteurs, dions magnétiques, ainsi que les fluctuations résultantes daimantation locale ont été étudié par micro-photoluminescence.

Organisation de la thèse

Les chapitre 2 et 3 introduisent les propriétés générales des hétéro-structures étudiées et les méthodes expérimentales développées pour cette étude.

Dans le chapitre 4, nous explorons la possibilité dutiliser les états de surface accepteurs comme source de trous pour le puits de CdMnTe. Les propriétés spectroscopiques dun tel gaz 2D sont evaluées.

Dans le chapitre 5, nous appliquons le dopage par étas de surface à létude du ferromagnétisme induit par porteurs libres. Nous étudierons des échantillons contenant jusquà 11% de Mn dans le QW, donc des densités non étudiés jusquà maintenant. Grace à une meilleure compréhension des spectres de luminescence des gaz 2D de forte densité, nous améliorons lapproche expérimentale utilisée.

Dans le chapitre 6, nous étudierons le problème des fluctuations de densité. Nous utiliserons la micro-photoluminescence (PL) pour mesurer localement la densité de porteurs et dions Mn dans un puits de (Cd, Mn)Te contenant un 2DHG résultant du transfert délectrons soit sur les impuretés dazote dans la barrière supérieure, soit sur des défauts surfaciques. Nous étudierons de plus limpacte des fluctuations sur laimantation spontanée dans la phase ferromagnétique.

Le chapitre 7 expose les conclusions finales.

Publications

- *"Control of Ferromagnetism in $Cd_{1-x}Mn_xTe$ Based Quantum Wells"*, M. Bertolini, H. Boukari, D. Ferrand, J. Cibert, S. Tatarenko, B. Gilles, W. Maślana, P. Kossacki, J.A. Gaj and T. Dietl, *Acta Phys. Pol.* **102** 603 **(2002)**.

- *"New structures for carrier-controlled ferromagnetism in $Cd_{1-x}Mn_xTe$ quantum wells"* M. Bertolini, W. Maślana, H. Boukari, B. Gilles, J. Cibert, D. Ferrand, S. Tatarenko, P. Kossacki and J. A. Gaj, *Journal of Crystal Growth* **251** issue 1-4, 342 **(2003)**.

- *"p-type doping of II-VI heterostructures from surface states: application to ferromagnetic $Cd_{1-x}Mn_xTe$ quantum wells"* W. Maślana, P. Kossacki, M. Bertolini, H. Boukari, D. Ferrand, S. Tatarenko, J. Cibert and J. A. Gaj, *Appl. Phys. Lett.* **82**, 1875 **(2003)**.

- *"Spin engineering of carrier-induced magnetic ordering in (Cd,Mn)Te quantum wells"*, P. Kossacki, W. Pacuski, Maślana, J. A. Gaj, M. Bertolini, D. Ferrand, S. Tatarenko and J. Cibert, *Physica E* **21** 943 - 946 **(2004)**

- *"Localization of neutral and charged excitons in (Cd,Mn)Te quantum well: a microphotoluminescence study"* J. A. Gaj, A. Golnik, P. Kossacki, K. Kowalik, Maślana, M. Kutrowski, and T. Wojtowicz, *phys. stat. sol. (c)*, 1- 4 (**2004**) / DOI 10.1002/pssc.200304221

- *"Microphotoluminescence study of p-type (Cd,Mn)Te quantum wells"* W. Maślana, P. Kossacki, P. Pochocka, A. Golnik, J. A. Gaj, D. Ferrand, M. Bertolini, S. Tatarenko, and J. Cibert, *Appl. Phys. Lett.* **89**, 052104 **(2006)**.

- *"Carrier Density Control by Illumination in Surface Doped, p-Type (Cd,Mn)Te Quantum Wells"*, W. Maślana, P. Kossacki, J. A. Gaj, D. Ferrand, M. Bertolini, S. Tatarenko, J. Cibert, M. Kutrowski and T. Wojtowicz, *Acta Phys. Pol.* **110** 255 **(2006)**.

CHAPTER 1

Introduction

Motivation: Spintronics

The discovery of Giant Magneto Resistance (*Baibich et al.*, 1988) initiated a new field in electronics related to spin properties of electrons. This new field, *spintronics*, uses electron spin for recording and processing of information (*Wolf et al.*, 2001). The expected advantages for high operation speed and low energy consumption of future spintronic devices attract attention of leading research laboratories and industrial companies. Quest of new semiconductor materials with ferromagnetic properties represents an important part of research effort related to spintronics. A good control of the carriers in semiconductors makes carrier – induced ferromagnetism particularly interesting in view of the hopes to achieve efficient control of ferromagnetism for information processing.

Carrier – induced ferromagnetism

The realization of carrier-induced ferromagnetism (*Dietl et al.*, 2001; *Haury et al.*, 1997) has boosted the interest in the study of diluted magnetic semiconductors (*DMS*) with a large density of carriers. The experimental work has been mainly focused on (Ga,Mn)As, resulting in a rapid advancement in the control of defects in layers grown by molecular beam epitaxy (*MBE*), and the achievement of relatively high values of the critical temperature T_c. Some devices have already been implemented (*Koshihara et al.*, 1997).

The most conclusive results have been obtained for p-type doped structures. In III-V DMS, the same impurity (Mn) carries the localized spins and acts as an acceptor (*Ohno*, 1998) which puts strong limits on the realization of quantum wells (QWs) and two dimensional (2D) systems (*Ohno et al.*, 2000) using thin layers of III-V DMS (*Boselli et al.*, 2000; *Lee et al.*, 2000).

II-VI semiconductors form a unique system where Mn is an isoelectronic magnetic impurity, so that carrier density can be controlled independently of magnetic ion concentration. In particular, modulation doping can be used to introduce a 2D electron or hole gas in a quantum well containing a diluted magnetic semiconductor. Although ferromagnetism in these materials is observed only in temperature range too low for commercial applications, the II - VI heterostructures constitute a model system to study carrier induced ferromagnetism (*Haury et al.*, 1997).

In previous studies on ferromagnetic ordering in Cd_{1-x} Mn_xTe quantum wells (*Haury et al.*, 1997; *Kossacki et al.*, 2002; *Ferrand et al.*, 2001; *Boukari et al.*, 2002), the modulation-doped structures were grown by molecular beam epitaxy (MBE) using nitrogen acceptors in the $Cd_{1-y-z}Zn_zMg_y$Te barriers. A mean field (Zener) model has been sucessfully aplied to describe the properties of the ferromagnetic phase in N - doped structures, (*Dietl et al.*, 1997; *Kossacki et al.*, 2000) Although efficient, this doping method brings restrictions. Effective doping of

$Cd_{1-y-z}Zn_zMg_yTe$ with nitrogen is only possible for y lower than 30%, it requires lowering the growth temperature from the usual 280 down to 220 °C to avoid a strong interdiffusion of the heterostructure (*Arnoult et al.*, 1998), and thus affects the quality of the samples (*Grieshaber et al.*, 1994). Moreover the presence of nitrogen precludes almost any postgrowth treatment of the sample.

Fluctuations

It is widely recognized that understanding disorder (either extrinsic (*Hayashi et al.*, 2001; *Potashnik et al.*, 2001; *Edmonds et al.*, 2004), or intrinsic) is a crucial issue for mastering carrier-induced ferromagnetism in semiconductors. Thermal fluctuations have been early incorporated in the Zener model by considering elementary excitations (*Konig et al.*, 2000). Spin disorder arises due to the random character of the distribution of localized spins. Electrical doping of semiconductors also involves a random distribution of electrically active impurities (electrostatic disorder). Actual samples are close to the metal-insulator transition, far from the extreme assumptions of free carriers (Zener model), or strongly localized carriers (model of percolating magnetic polarons (*Berciu and Bhatt*, 2001; *Kaminski and Sarma*, 2002)).

Objectives

Two main objectives have been set for this work:

- Extend the range of ferromagnetic system parameters.
- Examine the role of fluctuations in ferromagnetic phase.

To achieve these goals we developed a new doping method using surface states as a source of hole gas for the quantum well. Density fluctuations of carries and magnetic ions, as well as resulting fluctuations of local spontaneous magnetization were studied by microphotoluminescence mapping.

Organization of the thesis

Chapters 2 and 3 introduce the general properties of the studied heterostructures and experimental techniques used in this work.

In chapter 4 the possibility of using surface acceptor states as a sources of hole gas for (Cd,Mn)Te quantum well is explored. The spectroscopic properties of such two dimensional carrier gas are evaluated.

In chapter 5 we apply surface doping in studies of carrier induced ferromagnetism. We study the samples containing up to 11% of Mn in the quantum wells - densities unavailable in previous studies. Thanks to better understanding of photoluminescence spectra in presence of large density of hole gas the experimental approach is revised with respect to previous studies of such system.

In chapter 6 we address the problem of the density fluctuations. We use microphotoluminescence (μPL) to measure locally the carrier density and the Mn spin density in a (Cd,Mn)Te QW containing a 2DHG resulting from the transfer of electrons either to Nitrogen acceptors in

the top barrier, or to electron traps at the surface. We also investigate impact of fluctuations on spontaneous magnetization in the ferromagnetic phase.

Chapter 7 brings final conclusions.

Parts of this thesis have been published in following works

- *"Control of Ferromagnetism in $Cd_{1-x}Mn_xTe$ Based Quantum Wells"*, M. Bertolini, H. Boukari, D. Ferrand, J. Cibert, S. Tatarenko, B. Gilles, W. Maślana, P. Kossacki, J.A. Gaj and T. Dietl, *Acta Phys. Pol.* **102** 603 **(2002)**.

- *"New structures for carrier-controlled ferromagnetism in $Cd_{1-x}Mn_xTe$ quantum wells"* M. Bertolini, W. Maślana, H. Boukari, B. Gilles, J. Cibert, D. Ferrand, S. Tatarenko, P. Kossacki and J. A. Gaj, *Journal of Crystal Growth* **251** issue 1-4, 342 **(2003)**.

- *"p-type doping of II-VI heterostructures from surface states: application to ferromagnetic $Cd_{1-x}Mn_xTe$ quantum wells"* W. Maślana, P. Kossacki, M. Bertolini, H. Boukari, D. Ferrand, S. Tatarenko, J. Cibert and J. A. Gaj, *Appl. Phys. Lett.* **82**, 1875 **(2003)**.

- *"Spin engineering of carrier-induced magnetic ordering in (Cd,Mn)Te quantum wells"*, P. Kossacki, W. Pacuski, Maślana, J. A. Gaj, M. Bertolini, D. Ferrand, S. Tatarenko and J. Cibert, *Physica E* **21** 943 - 946 **(2004)**

- *"Localization of neutral and charged excitons in (Cd,Mn)Te quantum well: a microphotoluminescence study"* J. A. Gaj, A. Golnik, P. Kossacki, K. Kowalik, Maślana, M. Kutrowski, and T. Wojtowicz, *phys. stat. sol. (c)*, 1- 4 (**2004**) / DOI 10.1002/pssc.200304221

- *"Microphotoluminescence study of p-type (Cd,Mn)Te quantum wells"* W. Maślana, P. Kossacki, P. Pochocka, A. Golnik, J. A. Gaj, D. Ferrand, M. Bertolini, S. Tatarenko, and J. Cibert, *Appl. Phys. Lett.* **89**, 052104 **(2006)**.

- *"Carrier Density Control by Illumination in Surface Doped, p-Type (Cd,Mn)Te Quantum Wells"*, W. Maślana, P. Kossacki, J. A. Gaj, D. Ferrand, M. Bertolini, S. Tatarenko, J. Cibert, M. Kutrowski and T. Wojtowicz, *Acta Phys. Pol.* **110** 255 **(2006)**.

CHAPTER 2

Materials and experimental techniques

Contents

2.1 Materials

The studies were carried out on heterostructures made of II-VI semiconductors belonging to the Tellurides family. They were grown by Molecular Beam Epitaxy (*MBE*). We minimized the strain built into the samples by choosing appropriate composition of (Cd,Zn)Te substrate and the parameters of structure. The state of the art mastering of the crystal growth parameters results in the superb optical quality of the samples. Moreover the high (few meV) exciton binding energy and significant exciton oscillator strength enable fine optical experiments. Furthermore, we were able to design the sample structure so that the substrate was transparent in the spectral range corresponding to the energy of optical transitions in the quantum well thus enabling direct absorption measurements of excitonic transitions in the quantum well. In contrary the structures grown on most commonly used GaAs substrates, do not allow direct measurements of transmission. It is possible only after troublesome sample preparation including polishing and etching of the substrates. As the materials used for sample growth were well known we benefited from the good knowledge of their properties. In particular mixed crystals with magnetic Mn ions were carefully studied in the past. Thus we were able to focus on the specific features of the heterostuctures designed and grown for the purpose of this study. The recent reports on the discoveries of room temperature ferromagnetism in (Zn,Cr)Te by *Ando et al.* (2001); *Saito et al.* (2002, 2003*a*,*b*) encouraged our efforts.

2.1.1 Tellurides

We have used MBE grown CdTe, $Cd_{1-x}Mg_xTe$, $Cd_{1-x}Mn_xTe$ and $Cd_{1-y-z}Mg_yZn_zTe$ materials for the construction of heterostructures.

Let us remind some of the main properties of the telluride semiconductor family. The interatomic binding is of a sp^3 type: 2 electrons from s-type orbital (coming from elements of the group II and group VI) and 4 electrons from p-type orbital (coming from from tellurium) form the bonds. The resulting crystal structure is of a zinc-blende type as shown in figure 2.1 on the example of CdTe. The zinc-blende structure is the native also for for ZnTe and (Cd,Zn)Te alloys in the whole range of compositions. For $Cd_{1-x}Mg_xTe$ and $Cd_{1-x}Mn_xTe$ grown by equilibrium techniques there are boundary compositions (x=0.3 and 0.75) below which the zinc-blende structure is favored. All the structures discussed in this work were grown by MBE technique (in non-equilibrium conditions) therefore the crystal structure is determined mostly by the choice of the substrate and the growth parameters. The substrates that we used were 001 oriented $Cd_{0.88}Zn_{0.12}Te$ and $Cd_{0.96}Zn_{0.04}Te$. This ensured that all the samples had zinc-blende stucture. Lattice parameters of the main telluride semiconductors are presented in table 2.1. The lattice parameter of alloy $A_xB_yC_zTe$ (where x, y, z sum to 1 : $x + y + z = 1$) compound can be obtained by using values from the table 2.1 and the Vegard law:

$$a_{xyz} = xa_{ATe} + ya_{BTe} + za_{CTe}$$

2.1.2 Bandgap

CdTe, (Cd,Mn)Te and (Cd,Mg)Te have direct bandgap near Γ point of Brillouin zone. Figure 2.2 presents it schematically for CdTe (and the discussed telluride family). The conduction band has Γ_6 symmetry at $\vec{k} = 0$ and it is twofold spin degenerate. It consists of two $\pm\frac{1}{2}$ spin subbands. The valence band maximum has Γ_8 symmetry. It is four fold degenerate. It consists of two subbands (two fold degenerate) with $J = \frac{3}{2}$ momentum. The degeneracy is lifted for the $\vec{k}$ values higher than 0. At the center of the Brillouin zone the degeneracy can be reduced by reducing symmetry. For example, it can be achieved by application of uniaxial pressure as discussed in section 2.2. The degeneracy can be completely lifted by application of magnetic field. The subbands differ by the value of the momentum $\vec{J}$ projection on the quantization axis: the band with $J_z = \pm\frac{3}{2}$ has higher effective mass along quantization axis and therefore it is called heavy hole subband, the band $J_z = \pm\frac{1}{2}$ is called light hole band due to the smaller effective mass in the same direction. The values of effective masses along [001] direction are $m_{hh} = 0.63m_0$ and $m_{lh} = 0.13m_0$, respectively for heavy and light hole subbands (after *Le-Si-Dang et al.* (1982)). The Γ_7 subband with momentum $J = \frac{1}{2}$ is two fold degenerate. At $k = 0$ it is separated from the maximum of the valence band by the spin-orbit coupling Δ_{SO}. The energy of spin-orbit splitting is so large (930 meV *Kutrowski* (2001)) so that this subband is usually considered as irrelevant in most calculations.

The experimentally determined values of bandgaps for the main representatives of tellurides semiconductor family are gathered in table 2.2. The table also includes formulae helpful for describing properties of alloys that has been used in our samples. Graphical presentation of

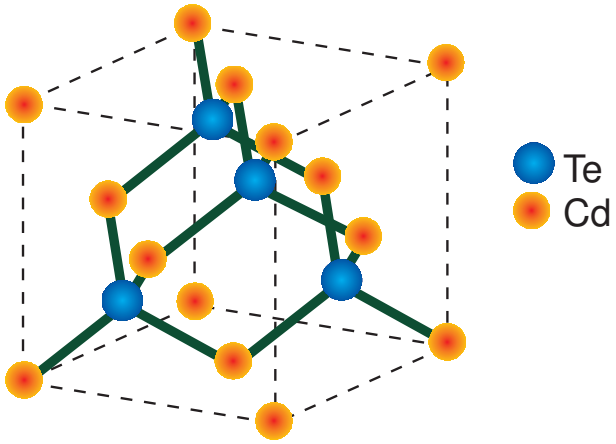

Figure 2.1: CdTe Zinc-Blende structure.

Material	a [Å]	source
CdTe	6.4810	*Landolt-Börnstein* (1982)
ZnTe	6.1037	*Landolt-Börnstein* (1982)
MgTe	6.42	*Hartmann et al.* (1996)
MnTe	6.337	*Janik et al.* (1995)

Table 2.1: Lattice parameters of selected tellurides

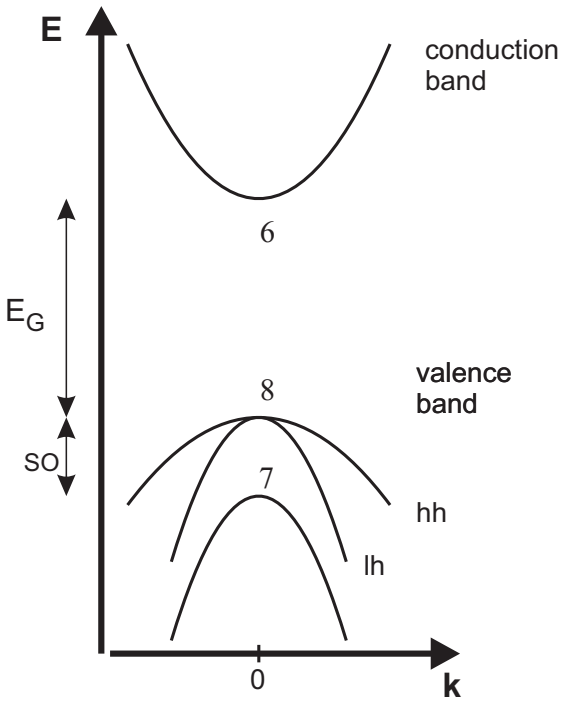

Figure 2.2: CdTe band gap structure.

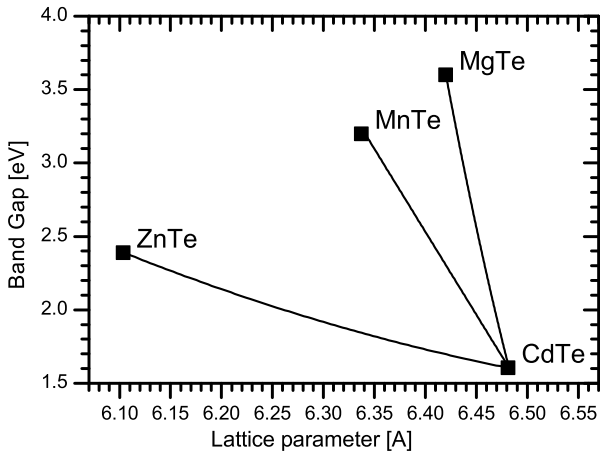

Figure 2.3: Dependence of Tellurides energy band gap on lattice parameter.

Material	E_G [meV]	source
CdTe	1606	*Landolt-Börnstein* (1982)
ZnTe	2391	*Landolt-Börnstein* (1982)
MgTe	3600	*Hartmann et al.* (1996)
MnTe	3198	*Furdyna and Kossut* (1988)
$Cd_{1-x}Zn_xTe$	$1606 + 525x + 260x^2$	*Tyagai et al.* (1974)
$Cd_{1-x}Mg_xTe$	$1606 + 1700x + 300x^2$	*Hartmann et al.* (1996)
$Cd_{1-x}Mn_xTe$	$1606 + 1592x$	*Furdyna* (1988)
$Cd_{1-y-z}Mg_yZn_zTe$	$1606 + 525y + 1750z$	*Arnoult* (1998)

Table 2.2: Bandgaps of tellurides at liquid helium temperature.

dependence energy bandgap on lattice parameters in tellurides family is shown in figure 2.3. Solid lines represent properties of alloys.

2.1.3 (Cd,Mn)Te: a semimagnetic semiconductor

Diluted Magnetic Semiconductuctors (DMS), also called Semimagnetic Semiconductors are the class of semiconductor materials in which part of the ions constructing the crystalline lattice possesses non vanishing magnetic momentum (Mn, Cr and Eu are commonly used). Contrary to Magnetic semiconductors such as MnTe, EuTe, EuS, in DMS material the ions with magnetic momentum do not form a distinguished sub lattice because their percentage in the host material is small. This is the result of the sole concept of DMS (*Furdyna and Kossut*, 1988) in which the magnetic ions are embedded into semiconductor with well known properties. The small addition of magnetic ions is intended to enhance the response of the material to external magnetic field without altering the main features of the host material. One of the most spectacular phenomenon in DMS is enhancement of Zeeman splittings as a result of a strong interaction between the magnetic ions and carriers. Due to the magnitude of enhancement, the phenomena is often called "giant Zeeman effect" (the observed Zeeman splitting in DMS are several orders of magnitude bigger than in ordinary semiconductors at a given external magnetic field (*Gaj et al.*, 1979; *Furdyna and Kossut*, 1988)).

For the construction of samples discussed in this work we used (Cd,Mn)Te. This is one of the best known semimagnetic semiconductor. In CdTe crystal isolated Mn ions have $3d^5$electronic shell configuration. Electrons from tightly bound 3d shell are the source of Mn magnetic properties. In the lowest energetic state all the electronic spins on 3d shell are aligned parallel. Therefore, the effective spin of Mn ion is $5/2$. As the basic excitation (turning the spin of one of the 3d electrons with respect to the remaining four) requires about 2.2 eV of energy, we can assume that all individual Mn ions are in the lowest energy state.

The magnetic system is described by a macroscopic magnetization $\vec{M}$. In the case of (Cd,Mn)Te, the magnetization is given by the mean value of spin $\langle S \rangle$ averaged thermodynamically over all Mn ions. The magnetization depends on the applied field, temperature(T) and Mn fraction in $Cd_{1-x}Mn_xTe$ (x). If we consider a magnetic field applied along the z axis we can write

$$\mathrm{M}(x, B, T) = -g_{Mn}\mu_B N_0 x \langle S_z \rangle \tag{2.1}$$

where: g_{Mn} – Mn Lande factor, equal 2

N_0 – number of crystalline elementary cells per unit volume

μ_B – Bohr magneton

For a system of isolated ions (a case of very diluted, – $x < 1\%$, $Cd_{1-x}Mn_xTe$ compound) the mean value of spin can be calculated. It is expressed by the Brillouin function[1]:

$$\langle S_z \rangle = -SB_S\left(\frac{g\mu_B SB}{k_B T}\right) \tag{2.2}$$

Therefore for isolated Mn ions with S=$^5/_2$ we have:

$$\mathrm{M}(x,B,T) = \frac{5}{2} g_{Mn}\mu_B N_0 x B_{\frac{5}{2}}\left(\frac{\frac{5}{2}g\mu_B B}{k_B T}\right) \tag{2.3}$$

In the crystals with larger Mn content, magnetization is rather complex. This is due to $d-d$ interactions between Mn ions. In case of two close ions it favors antiparallel alignment of spins. Such an antiferromagnetic behavior, combined with occupational disorder, leads to the formation of spin glass phase for compounds rich in Mn.

In the range of liquid helium temperatures, moderate (smaller than 67%) Mn concentration, and magnetic field smaller than 5T, the magnetization can be described by a modified Brillouin function (*Gaj et al.*, 1994, 1979):

$$\mathrm{M}(x,B,T) = \frac{5}{2} g\mu_B N_0 x_{eff}(x)\mathrm{B}_{5/2}\left(\frac{5}{2}\frac{g\mu_B B}{k_B\left(T+T_{AF}(x)\right)}\right) \tag{2.4}$$

In this case the expression: $\frac{5}{2}g\mu_B N_0 x_{eff}(x)$ represents the saturation value of the magnetization under magnetic field. Due to antiferromagnetic interactions between particular ions, the presence of pairs as well as open and closed triangles reduces the saturation value. Therefore the lowest energy configuration is reached when not all Mn spins are aligned parallel to the applied magnetic field. We can consider part of Mn spins to be "frozen" and thus consider $x_{eff}(x)$ as a effective density of "free" Mn spins. The number of Mn pairs and, triangles can be determined statistically, yet it is not possible to include all possible configurations of spins into analytical calculations. However, good results are achieved in Monte Carlo simulations (*Fatah et al.*, 1994). In work (*Gaj et al.*, 1994) authors found that following empirical formula can be used to describe experimental data with good accuracy:

$$x_{eff}(x) = \frac{2}{5}\frac{x}{1100}\left[718.2\exp\left(-\frac{x}{0.02307}\right) + 1988\exp\left(-\frac{x}{0.1615}\right) + 19.66\right] \tag{2.5}$$

The presence of antiferromagnetic interactions makes the whole system more resistant to the applied magnetic field. This behavior is simulated by adjusting the effective temperature of the system by T_{AF}. For the experimental data studied in (*Gaj et al.*, 1994) the antiferromagnetic adjustment to effective temperature was found to depend on actual Mn composition as follows:

$$T_{AF}(x) = \frac{x\,35.37}{1+2.752\,x} \qquad \text{(in K)} \tag{2.6}$$

Figure 2.4 presents the x_{eff} and T_{AF} versus the actual Mn composition as proposed by (*Gaj et al.*, 1994).

[1] $B_J(x) = \frac{2J+1}{2J}\coth\left(\frac{2J+1}{2J}x\right) - \frac{1}{2J}\coth\left(\frac{1}{2J}x\right)$

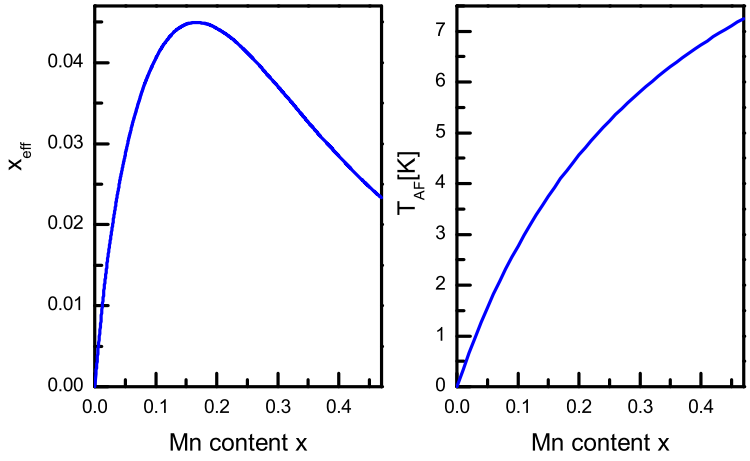

Figure 2.4: Effective spin density x_{eff} and T_{AF} versus Mn compositions as proposed by *Gaj et al.* (1994).

Introduction of Mn ions into the CdTe crystal results in enhancement of influence of magnetic properties with respect to pure CdTe. The enhancement is due to exchange interaction between localized Mn spins and delocalized carriers of valence and conduction bands. This interaction is described by Kondo (*Furdyna and Kossut*, 1988):

$$H_{ex} = -\sum_n J(\vec{r} - \vec{R_n})\hat{\vec{S_n}}\hat{\vec{\sigma}} \tag{2.7}$$

where J – operator acting on orbital part of electron wave function
$\hat{\vec{S_n}}$ – spin localized on n-th ion operator
$\hat{\vec{\sigma}}$ – band electron operator.

Solving such problem requires including into calculations all the Mn ions. It is not feasible in general case due to the random distribution of ions. As a result, the problem lacks translation symmetry of a perfect crystal. Since, in most cases the number of ions is a few orders of magnitude larger than the number of carriers (usually we consider semi insulating materials), we can describe the influence of a magnetic field in a following way: external magnetic field aligns magnetic ions which in turn, through exchange interactions, affect carriers. Additionally the wave function of band electrons is so vast in space (as the electrons are delocalized) that it covers many sites occupied by magnetic ions. This allows us to restore the translational symmetry in the virtual crystal approach by attributing to each cation site a fraction of average spin value accordingly to the overall ratio of sites occupied by Mn. Moreover we can apply the mean field approach and replace all operators of magnetic ions by thermodynamic mean value $\hat{\vec{S_n}}$.

When considering magnetically isotropic crystal placed in external magnetic field oriented along z axis, values of mean spin along x and y axis are zero: $\langle S_x \rangle = \langle S_y \rangle = 0$. Therefore Hamiltonian operator can be written in simplified form (*Furdyna and Kossut*, 1988):

$$H_{ex} = -N_0 I_{sp-d} x s_z \langle S_z \rangle \tag{2.8}$$

where: N_0 – number of crystalline elementary cells per unit volume
I_{sp-d} – exchange integral: s–d or p-d
x – Mn fraction in $Cd_{1-x}Mn_xTe$

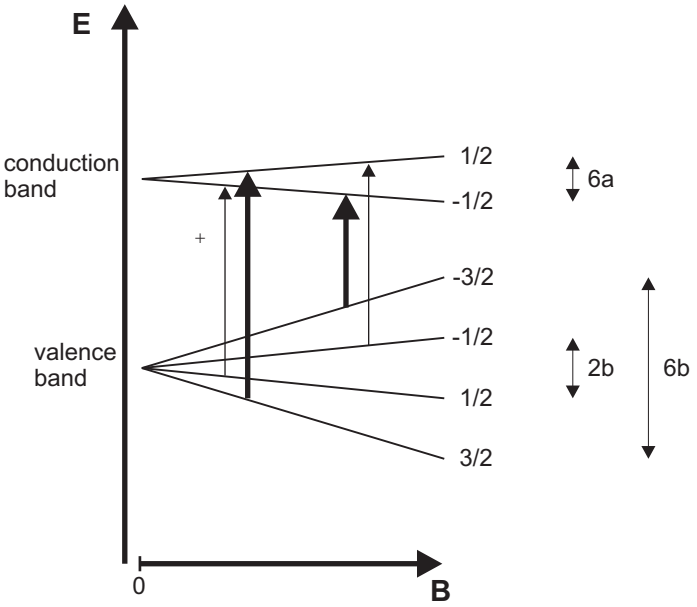

Figure 2.5: Band structure of $Cd_{1-x}Mn_xTe$ in vicinity of $\vec{k}$=0, splitting of the valence and conductivity bands. Arrows indicate optical transitions in Faraday configuration. Thicker arrows indicate stronger transitions (squared matrix elements of stronger transitions are three times larger than in weaker case). Parameters a and b are described in text.

s_z – electron spin along quantization axis z

$\langle S_z \rangle$ – average value of Mn spin along z axis.

Such Hamiltonian describes splitting of electron bands which is proportional to the average spin of Mn ions. It is also proportional to the magnetization. Figure 2.5 schematically presents splitting of band structure in vicinity of Γ point of Brillouin zone. Arrows indicate optical transitions in Faraday configuration.

Parameters a and b describing the values of splitting are defined as:

$\mathrm{a} = -\frac{1}{6} N_0 \alpha x \langle S_z \rangle$

$\mathrm{b} = -\frac{1}{6} N_0 \beta x \langle S_z \rangle$

where α, β are values of corresponding exchange integrals (I_{p-d} and I_{s-d} of equation 2.8).

Values of the parameters determined experimentally by *Gaj et al.* (1979) for (Cd,Mn)Te are:

$N_0\alpha = 0.22$ eV,

$N_0\beta = -0.88$ eV.

The energy difference between the two strong optical transitions is:

$$\Delta E = -N_0(\alpha - \beta)x\langle S_z \rangle \tag{2.9}$$

The mean value of the Mn spin $\langle S_z \rangle$ can be expressed by modified Brillouin function used to describe magnetization 2.1). We obtain formula expressing the experimentally observed splitting of two strong optical transitions for a given value of field, temperature and Mn content *Gaj et al.* (1994).

$$\Delta E(x, B, T) = \frac{5}{2} N_0(\alpha - \beta) x_{eff}(x) \mathrm{B}_{5/2} \left(\frac{5}{2} \frac{g\mu_B B}{k_B \left(T + T_0(x)\right)} \right) \tag{2.10}$$

2.2 Quantum Wells

The quantum well is one of the classic problems of quantum mechanics. The idea of confining a particle within barriers of potential can be realized practically in semiconductors. The most straightforward way to obtain a quantum well it is to embed a thin layer of semiconductor between the barriers of a different material with larger energy bandgap. In such a structure the confining potential is present along the axis perpendicular to the layer plane. Therefore, the movement of quasiparticles trapped in the quantum well is restricted to the two remaining dimensions. Thus a 2D quantum well is formed. Further reduction of particle movement by the confining potential is achieved in quantum wires (1D) and quantum dots (0D). Despite the interesting properties of systems with lower dimensionality, so far, the best control over the crystal parameters is still achieved in 2D (quantum wells). The variety of materials accessible to the novel crystal growth techniques such as Molecular Beam Epitaxy or Metal-Organic Chemical Vapour Deposition (MOCVD) allows for such a number of possible material configuration that a semiconductor crystal can be tailored to meet any needs. The control over the resulting crystal parameters is very efficient so it is often called bandgap engineering. Due to the specifics of the crystal growth in MBE or MOCVD techniques the quantum wells are formed along the growth axis of the crystal.

Although the choice of material is broad, several parameters are essential for the best quality of samples. For instance, as we consider heterostructure consisting of two different materials the actual formation of the well trapping potential depends strongly how the valence and conduction bands energies are placed with respect to each other. The offset between valence bands is usually described by the *valence band discontiniuity parameter* α_V. It is used to compute the depth of trapping potential in valence band of the quantum well V_V for semiconductors with energy bandgaps E_B and E_Q:

$$V_V = \alpha_V(E_B - E_Q)$$

The situation of positive value of α_V is shown in figure 2.6 where an example of bangap alignment is illustrated. In real structures we can stumble upon all possible realizations: $\alpha_V = 0$ when well potential is formed only for the conduction band, and also situations described by negative values of α_V where repulsing potential in valence band is matched to a deep well of potential in the conduction band (the lattice of materials with such a band offsets forms a quantum well superlattice of type II). The value of α_V for the CdTe/MgTe was experimentally determined by *Kuhn-Heinrich et al.* (1993) as 0.3 or 0.4 according to *Kutrowski* (2001). The calculations by *Wei and Zunger* (1998) determine α_V to be 0.33 for this material. The similarity of the alloys used for the samples in this work to the materials described in those works allows to describe our samples with $\alpha_V = 0.33$ with good accuracy. Anyway, the small variations of the α_V parameter do not significantly affect the calculation results in our case. This is due to the fact that confining potential is relatively deep in case of our structures.

In order to achieve best quality of samples the crystal structure and the growth parameters of the barriers and quantum well have to be matched. Growth techniques such as MBE allow to relax the need of exact lattice constant match, nonetheless the closest the match the better

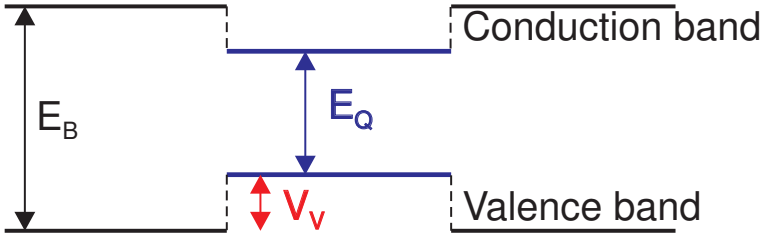

Figure 2.6: Quantum well band structure

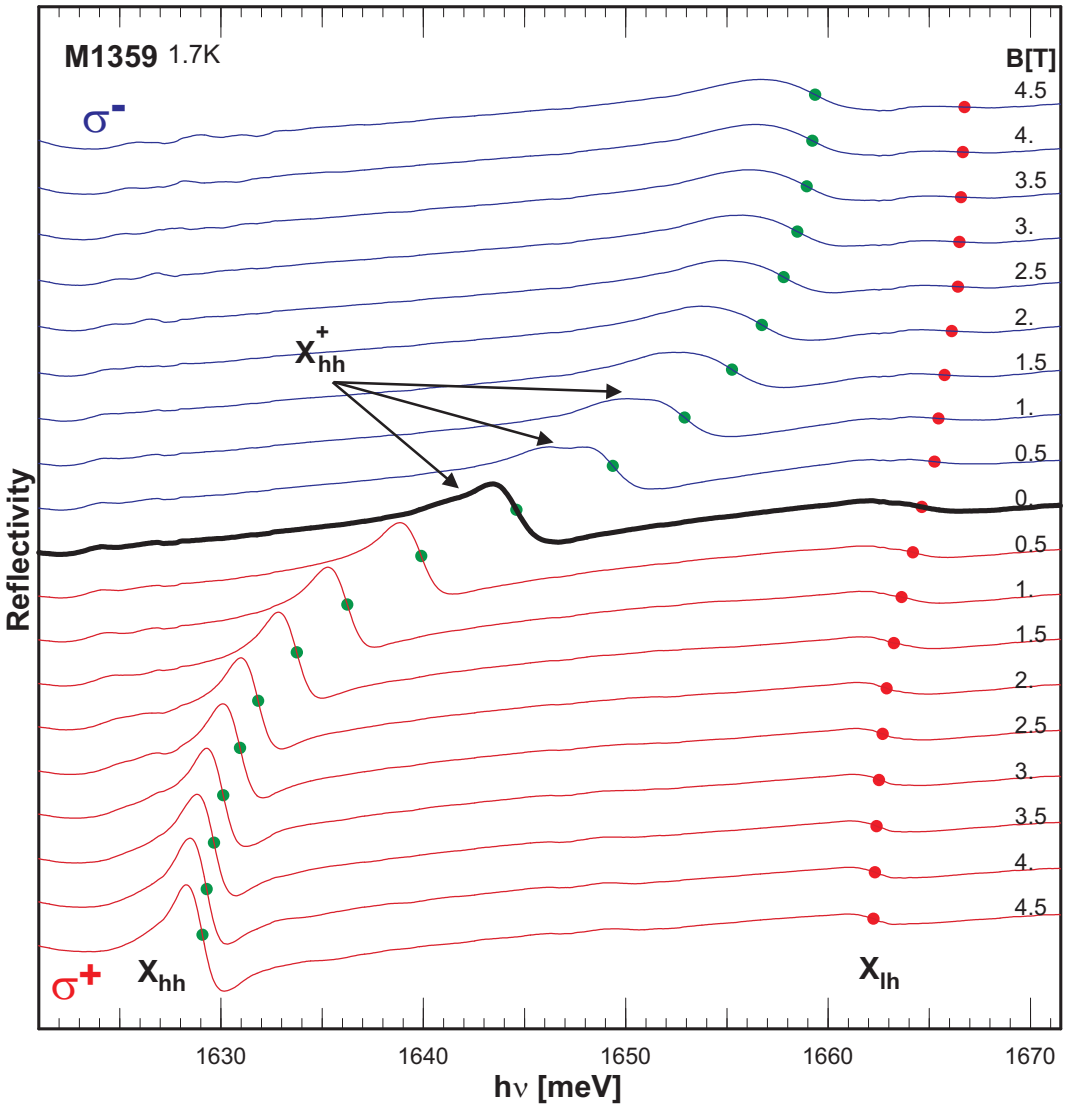

Figure 2.7: Broadband reflectivity spectra displaying the evolution in the magnetic field for sample M1359, at 1.7K. Both heavy and light hole exciton transitions are present, their transition energies are marked. The presence of small density of hole gas in the quantum well is manifested as a trace of charged exciton found in spectra below main excitonic line at small magnetic field in σ^- polarization.

quality of sample is achieved (an example of perfect pair of barrier quantum well material is GaAs and (Al,Ga)As where the lattice constants are almost the same). In case of materials with different of lattice constant the material of the quantum well is subject to tensile or compressive strain. The thickness of the quantum wells is usually chosen to be significantly smaller than the relaxation thickness of quantum well material so the danger of structural defect formation is negligible. However, the presence of strain in quantum well bears important consequences for the band structure of the quantum well (calculations of the influence of strain on the quantum well structure can be found in work by *Fishman* (1995)). The strain embedded in the quantum well can be used to the advantage: In (Cd,Mn)Te/(Cd,Mg)Te quantum wells compressive strain reduces the degeneracy of the Γ point of the valence band by lowering the energy of $\pm 1/2$ spin subband (light holes). In case of samples discussed in this work the value of heavy hole - light hole splitting is about 16 meV (example can be seen in figure 2.7). Besides the strain it contains also a contribution due to different confinement energies of light and heavy holes due the different effective masses. Both effects increase the value of heavy and light hole splitting in case of compressive strains (signs of both components are the same). The strain has been used to tailor the properties of the ground state of quantum well in (*Kossacki et al.*, 2004*b*; *Cibert et al.*, 2004).

The split light and heavy hole bands are anisotropic, their names are related to the masses along the growth axis. For example in typical CdTe/(Cd,Mg)Te quantum wells the in plane mass of heavy hole is much smaller than the longitudinal mass (*Fishman*, 1995). Numerical values depend strongly on quantum well parameters. In particular heavy hole in plane mass can be smaller than in plane light hole mass ($m^*_{hh} = 0.17m_0$ and $m^*_{lh} = 0.33m_0$ values are reported in work by *Le-Si-Dang et al.* (1982)).

2.2.1 Magnetospectroscopy of QW with carriers

Optical spectra of quantum wells (such as reflectivity presented in figure 2.7) are dominated by excitonic features. They are enhanced compared to bulk materials due to the confinement which brings electron and the hole closer together. In typical CdTe/(Cd,Mn)Te quantum wells the exciton binding energy is two times bigger than in bulk CdTe (10 meV) (*Gaj et al.*, 1994).

Excited states of the exciton in a typical quantum well (2s *etc.*) are sufficiently separated from the ground state. In many experiments they are not observed because of their small oscillator strength.

The excitonic features of the spectra are strongly affected by the presence of carriers in quantum wells.

Without magnetic field

For the zero and small magnetic fields in σ^- polarization, in figure 2.7, there is small notch visible on the spectra, for the energies, just below the heavy hole exciton transition. It is attributed to the residual presence of a carrier gas in the quantum well (the presence of a carrier gas in this sample is confirmed by experimental results described in following chapters). Created by light, an electron - hole pair forming an exciton in presence of a carrier gas can bind additional carrier and thus lower the energy of a resulting state. The quasi particle formed in such way is

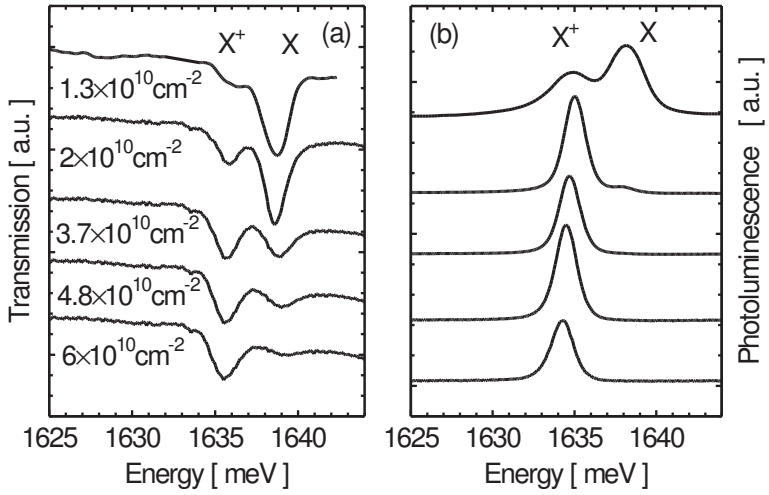

Figure 2.8: Absorption (a) and photoluminescence (b) spectra of an 8 nm wide $Cd_{0.998}Mn_{0.002}Te$ quantum well with $Cd_{0.66}Mg_{0.27}Zn_{0.07}Te$ barriers at indicated concentrations of 2D hole gas (after *Kossacki* (2003)).

electrically charged and is called a *trion* or simply referred to as a charged exciton. Depending on a carrier type bound to the exciton we identify positively charged X^+ and negatively charged X^- trions. The formation of trions was predicted by *Lampert* (1958). The very small binding energy makes the observation of trions very difficult in crystals (only exceptional quality of samples allowed for observations by *Thomas and Rice* (1977) and *Kawabata et al.* (1977)). For structures with lower dimensionality (like quantum wells) the trion binding energy is significantly increased making the observations easier. The use of modualation doped structure allowed for the first observation of charged excitons in quantum well by *Kheng et al.* (1993).

Figure 2.8 shows absorption and photoluminescence spectra of an 8 nm wide quantum well at different carrier density. For the smallest carrier density both transmission and photoluminescence spectra display double line structure. Lower line is due to positively charged exciton upper one due to neutral exciton. With increase of carrier density PL spectra are quickly dominated by the charged exciton line while the luminescence due to neutral state vanishes (it is due to the reduction of trion formation time with increase of carrier density - as a consequence less excitons are able to recombine prior to formation of trions). In the absorption spectra the change of intensity is less dramatic: both lines are present even at higher carrier density, but still the gain of charged exciton line intensity at the expense of neutral one is recognizable. This effect is recognized as *oscillator strength stealing* and was extensively studied by *Kossacki et al.* (1999); *Płochocka et al.* (2004). For the quantum wells with high carrier density it may even lead to the complete vanishing of neutral exciton line (like in figures 4.3 or 4.14, located on pages 43 and 56).

Significant magnetic field

The complexity of absorption spectra evolution with carrier density may lead to the confusion during identification of transitions in the spectra. The solution to this problem is provided by applying magnetic field. As seen in figure 2.7, the giant Zeeman effect allows to distinguish between heavy and light hole excitons. Moreover, the charged exciton state is spin singlet.

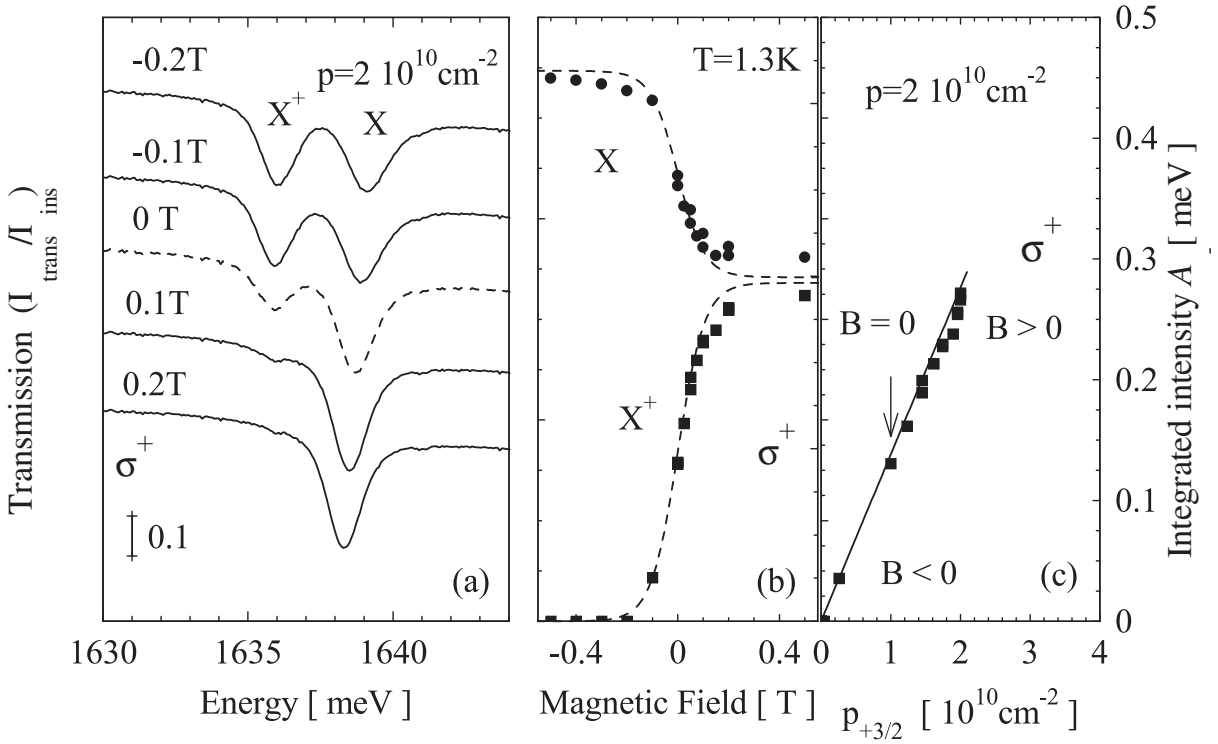

Figure 2.9: Transmission of 8 nm wide $Cd_{0.998}Mn_{0.002}Te$ quantum well with $Cd_{0.66}Mg_{0.27}Zn_{0.07}Te$ barriers in magnetic field, obtained for low hole gas concentration (p=2×10^{10}cm^{-2} at temperature 1.3 K: spectra (a), integrated line intensities as a function of magnetic field (b), and the hole gas concentration in the spin subband promoting the X^+ formation (c). (After *Kossacki* (2003)).

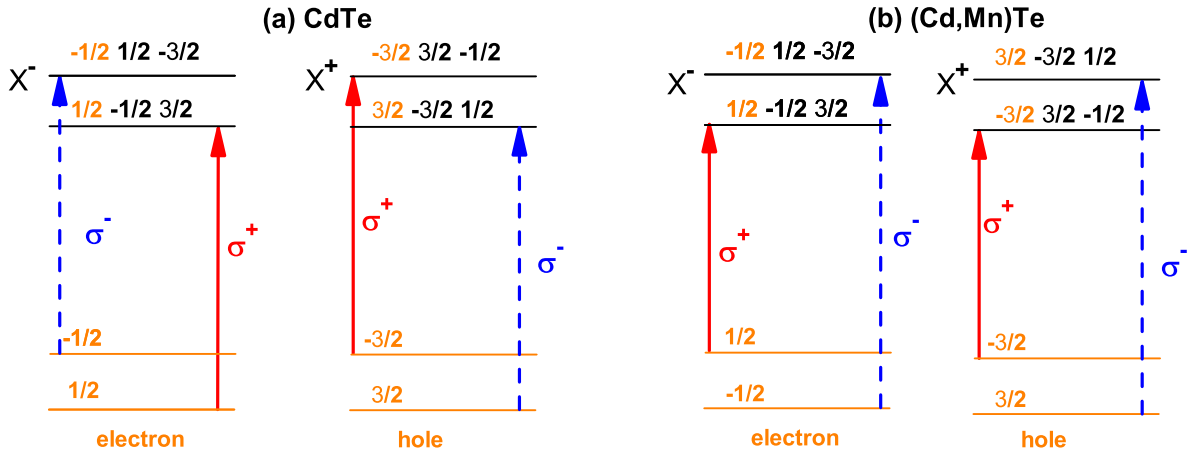

Figure 2.10: Selection rules for formation of charged excitons in absorption experiment under external magnetic field. The presented splinting represent general trend not the actual magnitude, note opposite order of splitting between CdTe and (Cd,Mn)Te. The electrons and holes bound into trions from the population of carrier gas present in the quantum well are highlighted in different color.

Figures 2.9, 4.1 and 4.3 (on pages 16, 40 and 43, respectively) show that the charged exciton line prevails only in σ^- circular polarization. The diminishing of trion line in one of circular polarization is caused by non equal distribution of carrier density between spin subbands split by the magnetic field. Trion absorption is only possible when carriers of the opposite spin to that of photocreated carrier are present. The possibility of trion formation with respect to the circular polarization of absorbed light is determined by the actual splitting of spin subbands. In figure 2.10 a scheme of trion formation is presented for CdTe and (Cd,Mn)Te. Arrows indicate optical transitions between initial state and the trion respectively to the light polarization. Band splitting shown in figure 2.10 indicate only tendency not the actual relative magnitude of splitting in external magnetic field. Note the opposite sign of conduction band splitting between CdTe and (Cd,Mn)Te. In case of CdTe the negatively and positively charged excitons appear in opposite circular polarizations therefore the magnetospectroscopy can be employed to determine the actual sign of the carrier gas in the quantum well. The discussion and optical methods of characterization presented in chapter 4.

2.2.2 Photoluminescence

Moss Burstein shift

One of the fingerprints of presence of the carrier gas in the quantum well is the difference of transition energies between photoluminescence and absorption (like in figure 2.11(b)). It is recognized as a Moss-Burstein shift. [2] The observed difference of transition energies arises from the conservation of momentum: photocreated electron in the valence band can have value of k>0 and therefore there are allowed optical transitions away from the center of Brillouin zone for excitation (*photoluminescence excitation spectra* (PLE), transmission and reflectivity), while photoluminescence occurs after relaxation of the kinetic energy of photocreated electron. It occurs only for electrons from the center of the Brillouin zone (k=0) due to the small amount of momentum that can be carried away by the photon. The schematic presentation of transition scheme can be found in figure 2.11(a). The curvature of the bands in vicinity of Γ point can be described in the effective mass formalism thus Moss-Burstein shift can be expressed:

$$E_{MB} = \frac{\hbar^2}{2}\left(\frac{1}{m_h^*} + \frac{1}{m_e^*}\right)k_F^2 \tag{2.11}$$

For the hole gas Fermi energy (E_F) can be expressed in terms of Fermi wave vector (k_F): $E_F = \frac{\hbar^2 k_F^2}{2m_h^*}$. Therefore Moss-Burstein shift can be expressed in terms of Fermi energy: $E_{MB} = \left(1 + \frac{m_h^*}{m_e^*}\right)E_F$. For (Cd,Mn)Te we can substitute effective in-plane masses for heavy hole and electron values $m_h^* = 0.1m_0$ and $m_e^* = 0.25m_0$ after *Fishman* (1995). Thus $E_{MB} = 3.5E_F$. On the other hand, density of hole gas (p) determines the Fermi energy through the two dimensional density of states (ρ_{2D}): $\mathrm{p} = \rho_{2D}E_F$. The two dimensional density of states, including the two fold spin degeneracy, can be expressed as $\rho_{2D} = \frac{m_h^*}{\pi\hbar^2}$. For $m_h^* = 0.25m_0$ it gives $\rho_{2D} = 1.05 \times 10^{10}\,\mathrm{cm}^{-2}\mathrm{meV}^{-1}$. Therefore it is possible to calculate the hole gas density from

[2] The samples discussed in this work are of p-type therefore discussion of Moss-Burstein effect is presented with respect to the hole gas. Similar conclusions are reached when considering electron gas.

Moss-Burstein shift (expressed in meV):

$$\mathrm{p} = 3.7 \times 10^{10} E_{MB} \tag{2.12}$$

It is important to note, that such interpretation of Moss–Burstein shift is an approximation which neglects excitonic and manybody effects. Moreover it is valid for a fairly large carrier densities.

In semimagnetic materials, at low values of external magnetic field it is possible to obtain spin splitting in valence band larger than Fermi energy due to giant Zeeman effect. Then spin down band is free of holes and an exciton can be formed from photocreated electron and photocreated spindown hole in σ^- polarization (see Figure 2.11(a) lower panel). In the polarization involving opposite spin subband (σ^+), we would expect doubling the value of Moss-Burstein shift with respect to the value at zero magnetic field. Therefore, measurements of Moss-Burstein shift at a field sufficient to lift of degeneracy of hole gas provide better experimental accuracy.

In the experiment (figure 2.11(b) lower panel), a sharp exciton line is observed in σ^- PLE polarization while for $\sigma+$ PLE one can observe a steplike sprectrum. Moreover the shape of PL is significantly altered with respect to the zero field. This is the result of large density of carriers present in the system as carrier-carrier coulomb interactions overcome excitonic effects. In this case for determining Moss-Burstein shift we should take the edge of σ^+ PLE spectra. However, acknowledging the presence of disorder broadening we use the energy in the middle of rising slope of σ^+ PLE. Note also small shift of the experimental spectra in σ^- polarization between PL and PLE spectra. The energy of photoluminescence is lower (in presented case about 0.8 meV) from the maximum of absorption due to the Stokes shift. It results from the disorder present in the structure which broadens the distribution of the density of states. It is also contributes to the difference of energies in σ^+ polarization as well as shift at zero magnetic field therefore it should be noted when determining Moss-Burstein shift.

Evolution of PL spectra with magnetic field

The evolution with magnetic field of the photoluminescence spectra from the quantum well containing hole gas has been thoroughly discussed by *Boukari* (2003) and *Kossacki et al.* (2004*a*). Let us recall issues essential for this works.

An example of luminescence at low carrier density limit - $p < 10^{10}$ cm^{-2} (carrier density was tuned by additional illumination of the sample as discussed in chapter 4.5) is presented in figure 2.12(a). There are compared spectra at different values of magnetic field for both of the circular polarizations. At zero field, the spectrum is dominated by the charged exciton. Neutral exciton line is weaker and placed at high energy shoulder of charged exciton. When magnetic field is increased relative intensities of lines change. In σ^- polarization neutral exciton line vanishes at 0.1T, the intensity of charged exciton line also decreases: disappearing at 0.3T. In σ^+ polarization the intensity of neutral exciton increases with respect to the intensity of charged exciton. The intensities of both lines become comparable at 0.175T. For higher fields the neutral exciton line becomes stronger. *Boukari* (2003) and *Kossacki et al.* (2004*a*) point that the transition from charged to neutral exciton is governed by the value of giant Zeeman splitting. The destabilization of the charged exciton in favor of neutral one is explained as a

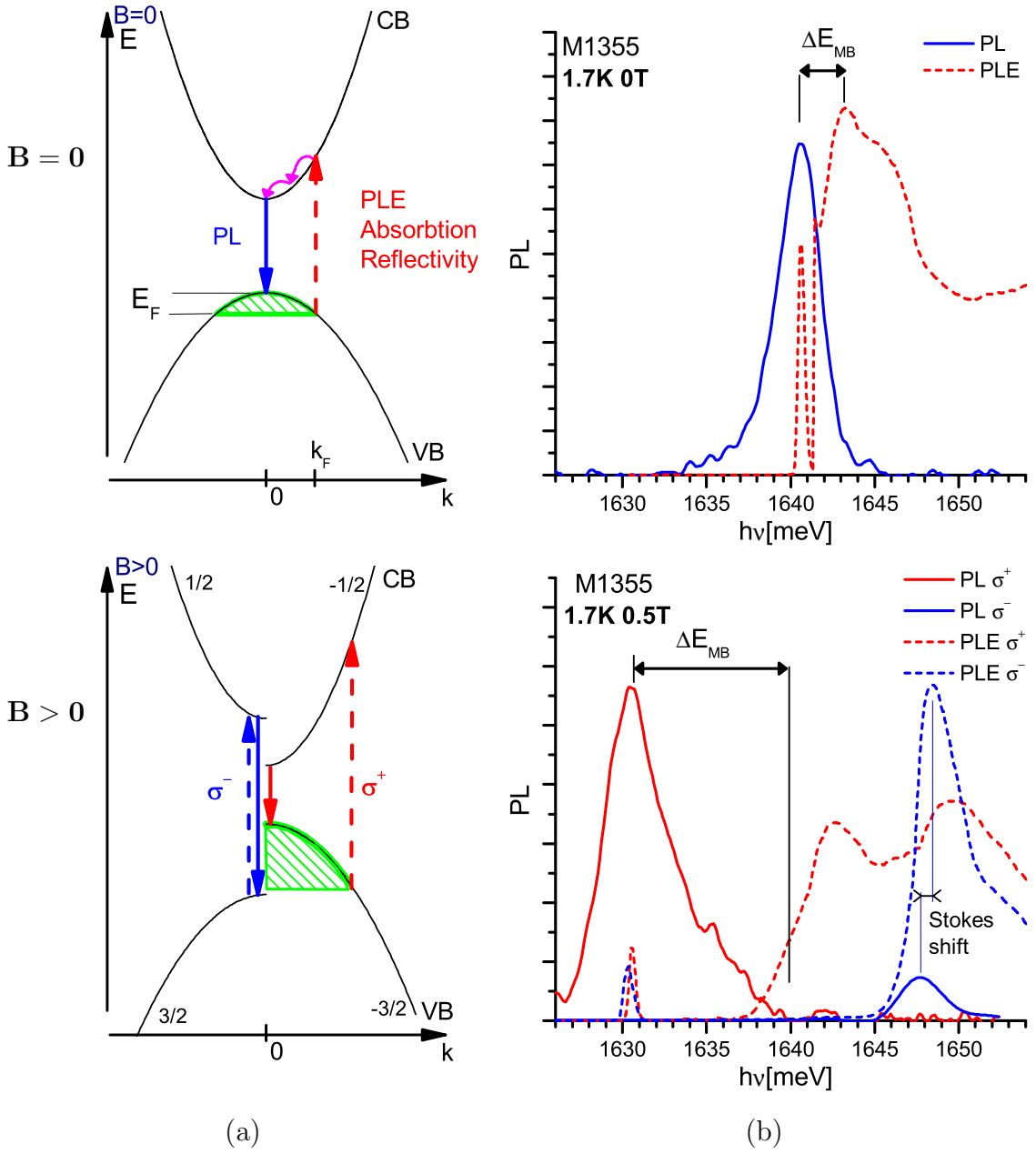

Figure 2.11: Moss-Burstein shift.

(a) Schematic explanation of origin. Two situations are concerned: with and without external magnetic field. Without magnetic field: absorption is possible for electrons with momentum grater than Fermi vector k_F, while emission is possible for the states with $k = 0$. The excess momentum is lost in nonradiative relaxation processes within conduction band. Magnetic field polarizes carrier gas: the population of $-3/2$ band is doubled and $3/2$ band is depleted at sufficiently large magnetic field. Moss-Burstein shift is observable at σ^+ polarization.

(b) Experimental spectra for sample M1355 at 0T and 0.5T magnetic field. Moss-Burstain shift can be determined from σ^+ PLE and PL spectra. At σ^- polarization absorption and emission correspond to the empty well situation, small difference between transition energies is due to the Stokes shift.

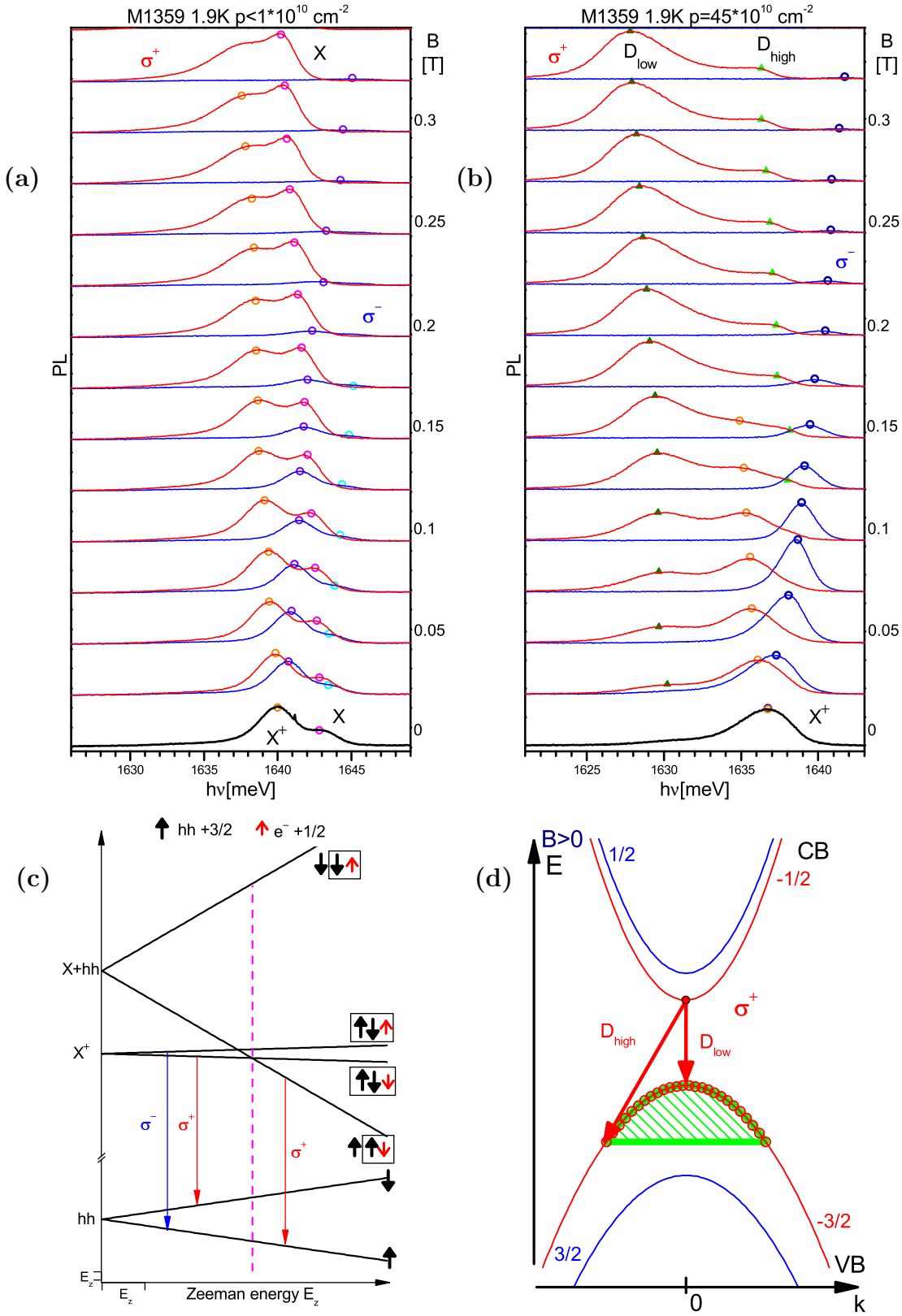

Figure 2.12: Photoluminescence from quantum well containing hole gas. **(a)(b)** Experimental data for sample M1359 with 1.4% (Cd,Mn)Te QW for different values of magnetic fields. The carrier density was tuned by additional illumination. Circular polarization resolved spectra are marked blue for σ^-, red for σ^+. **(c)** Three-carier diagram of optical transitions after (*Kossacki et al.*, 2004*a*). Dashed vertical line indicates level crossing. **(d)** Single particle diagram visualizing D_{high} and D_{low} transitions in band-to-band style.

result of different Zeeman splittings of three-particle system containing two holes and electron. The concerned particles can be either arranged as charged exciton or a system made of hole and exciton. Suggested diagram of transitions is presented in figure 2.12(c). Charged exciton is formed out of two holes with singlet spin arrangement, therefore the Zeeman shift is governed only by the shift of the electron. Bright state of neutral exciton consists of hole and electron of opposite spins, while the remaining hole is free. Thus the arrangement of two holes with parallel spins (emitting in σ^+ polarization) is subject to huge shift in magnetic field as all shifts of individual particles contribute to that of a system. At zero magnetic field charged exciton state has lower energy (it is bound state) but in magnetic field (when Zeeman splitting of heavy hole is equal to the X^+ dissociation energy) neutral exciton level (emitting in σ^+) becomes lower. Thus giant splitting of a hole can destabilize singlet state of charged exciton.

Experimental spectra for high hole density case are shown in figure 2.12(b). The sample is the same as discussed in previous paragraph, the carrier density of 45×10^{10} cm^{-2} was achieved by different illumination condition. [3] At zero magnetic field photoluminescence spectra is dominated by the charged exciton line. Contrary to the low carrier density limit there is no trace of neutral exciton line. As the magnetic field is applied, the charged exciton line in σ^- polarization increases its transition energy. At small magnetic field it appears to increase intensity but the effect is due to the narrowing of the linewidth. For higher magnetic fields the line vanishes (at about 0.25T), similarly to the low carrier density case. This vanishing line was identified as emission from charged exciton state (consisting of two hole spin singlet and electron from $+\frac{1}{2}$ spin subband). In this process electron recombines with hole from $-\frac{3}{2}$ subband (this is the band of the lower energy therefore remaining hole is in the majority band and the final state of transition is ground state).

In the moderate magnetic field range, the charged exciton line in σ^+ polarization broadens and lowers its transition energy. The initial state of this transition consists of (similar as in σ^- polarization) a singlet arrangement of holes but with an electron located in $-\frac{1}{2}$ spin subband. The recombination of electron with the $+\frac{3}{2}$ hole doesn't leave the crystal in the ground state as the remaining hole is located in minority subband: the final state of transition is the excited state. The energy of this state is higher than the ground state by, at most, the value of Zeeman splitting for the hole subbands.

At higher magnetic field, the shape of photoluminescence in σ^+ changes substantially. The line identified as a charged exciton at lower magnetic field vanishes at about 0.15T and the spectra evolves into double line structure. Although the double line is subject to Zeeman shift as implied by content of Mn in the quantum well, the shape of double line structure remains constant even at very high values of magnetic field (up to 3T - not shown here)[4]. The high energy line of the two line spectra in σ^+ is labeled as D_{high}, stronger line in lower energies is labeled D_{low}. The change from charged exciton line to the two lines occurs at magnetic field similar to the value at which X to X^+ crossing was visible for low carrier density.

[3] The influence of illumination on the carrier density is discussed in detail in section 4.5.

[4] In work by *Boukari* (2003) and *Kossacki et al.* (2004*a*) authors performed experiments up to 20T, on similar structure, and report that Landau levels emerge at fields larger than 4T and thus whole spectra transforms again. All measurements presented in this work were performed in magnetic fields way below this limit. Therefore we do not need consider additional complications.

The transition energy of D_{high} at the crossing point is close to the energy of σ^- charged exciton transition. At this field the initial states in σ^+ are degenerate differing from σ^- by the (small) splitting of electron subbands. Thus the D_{high} was identified as a transition in which final state is the ground state of the hole gas. The transition D_{low}, on the other hand leaves the ole gas in excited state. In figure 2.12(d) double line in σ^+ is shown in band-to-band description. The transition D_{low} is a direct one at $k = 0$, and the final state corresponds to the excitation of the hole gas with energy equal to the doubled value of Fermi energy (at zero field). The transition D_{high} is an indirect one involving electron from the bottom of conduction band and a hole at Fermi level. *Boukari* (2003) and *Kossacki et al.* (2004*a*) attribute relaxing of selection rules to the presence of disorder, influence of many body effects as well as emission of phonon with a wave vector k_f . Indeed the relative intensities of the lines vary from sample to sample (an example can be found in figure 4.9). The attribution of indirect type of transition to the D_{high} is supported by enhanced coupling to the LO phonon. This results in phonon replica observed only for the D_{high} at higher values of the field in σ^+ polarization.

2.2.3 Enhancement of susceptibility due to carriers

It has been observed that carrier – carrier interactions lead to an enhancement of the spin susceptibility (*Tanatar and Ceperley*, 1989; *Attaccalite et al.*, 2002; *Boukari et al.*, 2006). It is possible to notice it in our experimental results presented in figure 2.12(a) and (b). There, at low magnetic fields, the positively charged exciton Zeeman splitting is different for different carrier densities at a given magnetic field. Most of the experimental results are focused on two dimensional electron gas (2DEG). The influence of spin interactions on spin susceptibility have been investigated in transport experiments (*Vakili et al.*, 2004; *Kravchenko and Sarachik*, 2004; *Tutuc et al.*, 2002). Experimental results as well as theoretical studies point out that spin susceptibility is indeed enhanced. However, no general description, valid through broad range of carrier density available.

Important role of enhancement of spin susceptibility on carrier induced ferromagnetism in ferromagnetic quantum wells was indicated by *Dietl et al.* (1997) and *Haury et al.* (1997). It was introduced in simplified approach by using A_F parameter (called Fermi liquid parameter) for adjusting the carrier susceptibility According to *Kossacki et al.* (2000) the value of A_F is estimated by $1 + g_3$, where g_3 is a parameter that controls the spin-splitting-induced positive magnetoresistance in disordered systems (*Altshuler and Aronov*, 1985; *Dietl*, 1994). For, example, by taking g_3 determined for bulk n- $Cd_{0.95}Mn_{0.05}Se$ (*Sawicki et al.*, 1986; *Jaroszynski et al.*, 1995; *Smorchkova et al.*, 1997) and superlattices of n-Si/$Si_{0.5}Ge_{0.5}$ (*Brunthaler et al.*, 1996) we obtain A_F equal 2.3 and 2.5, respectively. According to *Kossacki et al.* (2000) the Curie temperature in (Cd,Mn)Te quantum well takes the correct value with $AF = 2.1 \pm 0.5$ used in calculations.

Recent study by *Boukari et al.* (2006) addresses the problem in p-type (Cd,Mn)Te quantum wells - an experimental configuration like the one discussed in this work. The spin susceptibility enhancement is discussed in broad range of hole gas densities. The experimental results are compared to the calculations (made within model derived for electrons yet adopted to the hole gas with success)as presented in figure 2.13.

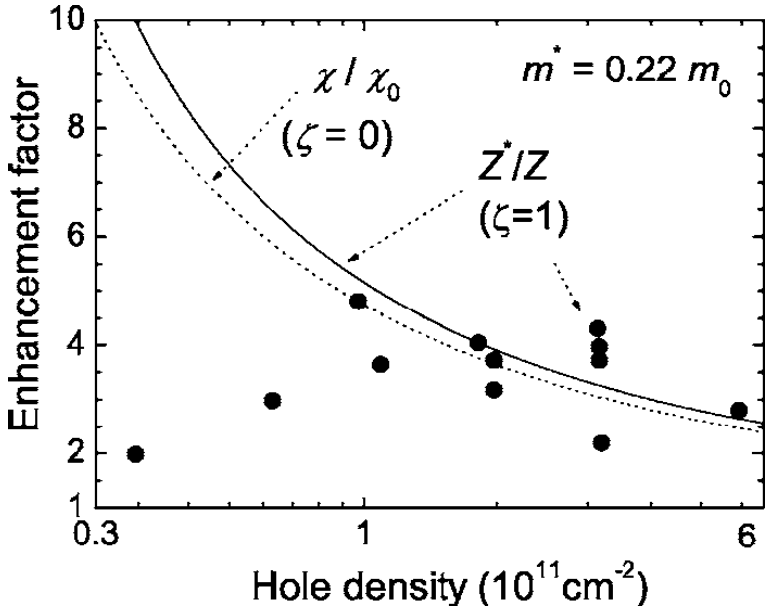

Figure 2.13: Enhancement factor of the spin susceptibility and spin splitting, as a function of the carrier density, using $m^* = 0.22m_0$; the lines give the result of the calculation at complete polarization (solid line) and vanishing polarization (dashed line); symbols are experimental data. After (*Boukari et al.*, 2006).

The experimental (points) and calculated (solid line marked as Z^*/Z) enhancement of Zeeman splitting were obtained at full polarization of carrier gas. However, for carrier induced ferromagnetism more relevant is is enhancement at vanishing carrier gas polarization. The calculations within this regime are presented as dotted line in figure 2.13 and marked as χ/χ_0. The difference between the calculation results for fully polarized and (almost) non polarized gas are of the order of 10% for high carrier densities and increase up to 15% in low carrier density range and the enhancement in fully polarized gas is larger. Reasonably good agrement between calculation and experimental result is achieved for hole densities larger than 10^{11} cm^{-2}. The discrepancy at low carrier densities is combined by large experimental uncertainties of Zeeman splitting determination. In this region a strong effects due to localization and disorder are expected (*Kechrakos et al.*, 2005; *Kossacki et al.*, 2000).

The values of enhancement parameter are higher than previously used, reaching 4 for the 3×10^{11} cm^{-2}. It indicates that enhancement of susceptibility due to exchange and correlation Coulomb interactions were underestimated in carrier induced ferromagnetism studies (*Haury et al.*, 1997; *Dietl et al.*, 1997; *Kossacki et al.*, 2000).

2.3 Characterization

This section describes methods used for the determination of main properties of the samples. The presented techniques base solely on the results of magnetooptical experiments. The techniques discussed in this section concern general properties. More specific experiments (like determination of critical temperature of ferromagnetic transition in quantum wells) are discussed in appropriate, following chapters.

2.3.1 Hole gas density

Moss-Burstein shift

As discussed in previous section it is possible to use the Moss-Burstein shift to determine density of carrier gas present in the quantum well. The measurements of Moss Burstein shift in magnetic field sufficient to completely polarize the carrier gas allow to increase the accuracy of the determined value. The complicated nature of the photoluminescence spectra makes the measurement of the Moss-Burstein shift difficult. The Stokes shift has to be accounted for, and therefore determined from the separate experimental procedure (for example comparison of energies of photoluminescence and absorption energies in σ^- polarization). Additional difficulty is posted by the change of the PL spectra from excitonic type to the double line structure with increase of magnetic fields. Authors of (*Kossacki et al.*, 2004*a*) refer to the several different cases: "excitonic Moss-Burstein shift" observed for the fields smaller than the jump to the double line structure in σ^+ PL. In cases when the double line is visible in PL the Moss-Burstein shift is measured between the D_{low} and the absorption energy in σ^+ polarization. Authors found that although the "excitonic Moss-Burstein shift" is easier to measure the densities obtained from it are smaller by factor 1.5 from the calculated values of the Moss-Burstein shift. However, it still provides an accurate evaluation of relative carrier density. The problem of obtaining absolute values may be solved by the proper calibration. In (*Kossacki et al.*, 2004*a*) the carrier density obtained from transport measurements of Hall effect and the positions of Landau levels observed in absorption in high magnetic fields (ranging from 14T to 21T) are used to verify measurements of the Moss-Burstein shift. After the calibration we can use relation:

$$p = 5.6 \times 10^{10} E_{MB(B=0)} \quad (\text{in meV}) \tag{2.13}$$

for the measurements without magnetic field. The Moss-Burstein shift of the completely polarized hole gas is described by formula:

$$p = 2.8 \times 10^{10} E_{MBpol} \quad (\text{in meV}) \tag{2.14}$$

Splitting D_{high}-D_{low} in PL at σ^+ polarization

The initial and final states of the components of the split doublet in σ^+ polarization suggest that the value of the splitting can be used as a measure hole gas density. Indeed, the splitting D_{high}-D_{low} (for the convenience sake we shall use the name *High Field Splitting (HFS)*) gives the energy of the excited hole gas, which depends on the carrier density. For a completely polarized

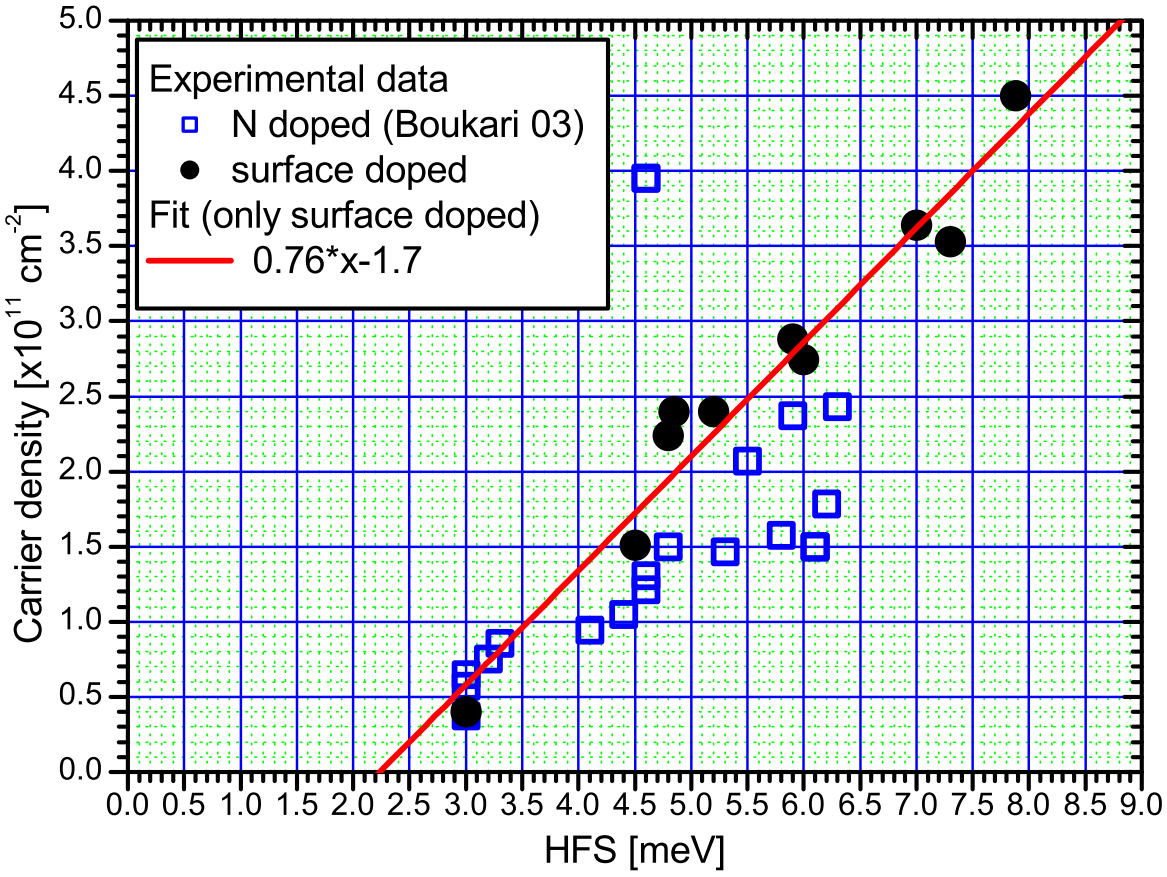

Figure 2.14: Calibration of D_{high}-D_{low} splitting (HFS) by the carrier density obtained from Moss-Burstein shift for surface doped samples with small Mn content. Data for nitrogen doped samples (after *Boukari* (2003) are displayed for comparison.

hole gas we can consider the situation shown in figure 2.12(d) where in D_{low} transition an electron recombines at $k = 0$ with a hole at the top of the $-\frac{3}{2}$ spin subband while in D_{high} transition (indirect) recombines with the hole of a Fermi wave vector k_F. Thus from the differences of the energy of both transitions it is possible to determine the value of k_F and the hole gas density. In order to calculate exact values of carrier density, it is necessary to use the value of the heavy hole mass. It inputs serious uncertainty as there are different values of heavy hole mass in (Cd,Mn)Te reported by different authors. The reported values vary from $0.17m_0$ (*Le-Si-Dang et al.*, 1982) to $0.25m_0$ (*Fishman*, 1995). Despite this difficulty, it is still interesting to use HFS as a measure of carrier density because it is free of error resulting from the presence of Stokes Shift. Another great advantage of using HFS is that carrier density can be deduced from a single PL spectra measured at sufficiently high magnetic field. Moreover it is most accurate at large hole densities where HFS tends to match the fermi energy, as expected for simple band to band transitions. Therefore, following *Boukari* (2003) and *Kossacki et al.* (2004*a*) example we decided to calibrate the values of D_{high}-D_{low} splitting by comparing them with values of hole density obtained from Moss-Burstein shift. The results are presented in figure 2.14. Experimental data for calibration were obtained for samples with a small Mn content described in chapter 4 - examples of experimental spectra can be seen in figure 4.9 (on page 48) .

The D_{high}-D_{low} splitting turned out to be the most valuable tool for the determination of carrier density in samples used to study carrier induced ferromagnetism. The samples contained

more than 5% Mn in the quantum well and large carrier density. The values obtained from Moss Burstein shift were highly inaccurate due to broadening of the lines and the change of spectra type at high carrier density. In extreme cases of PL line so broad that the D_{high} line is not well resolved from the high energy tail of the stronger D_{low} line it is convenient to deduce the position of D_{high} line from the position of its phonon replica which is usually well pronounced.

2.3.2 Mn density

Another important parameter defining properties of our systems is the Mn composition in the quantum well. It is possible to determine it from optical experiments. The giant Zeeman splitting allows us to obtain sensible accuracy without necessity to apply very strong magnetic field (In our case measurements were done in magnetic field up to 5T). The best results are achieved when the splitting is deduced it from the magneto-reflectivity experiment.

For the determination of Mn density, the presence of carriers is an obstacle due to the carrier related effects such as enhancement of magnetic susceptibility, polarization of carrier gas and influence of carrier gas on the line shape. Fortunately, in case of studied samples it is possible to deplete the quantum well using illumination of photon energy above barrier bandgap (Depletion mechanisms are discussed in chapter 4.5). In most cases, sufficient depletion can be achieved, when the reflectivity is measured under strong white light illumination. Examples of experimental spectra used for the determination of Mn density are presented in figures 2.7 and 4.1 (on pages 13 and 40). The positions of excitonic lines are determined from the spectra (like in figure 2.7). In work *Gaj et al.* (1994) modified Brillouin function (as in equation 2.10) was used to describe the splitting of the bulk (Cd,Mn)Te. Apparently it also yields good description of the excitonic Zeeman splitting in (Cd,Mn)Te quantum wells [5].

For our purposes it is more convenient to interpret the variation of excitonic transition energy (E_X) in magnetic field instead of Zeeman splitting because we perform measurements for a fixed alignment of polarizer used for detection of circular polarization. The change of polarization sign is achieved by reversal of magnetic field. It allows us to collect necessary data in a single sweep of magnetic field from negative to positive value. Considering E_X instead of actual Zeeman splitting reduces the possibility of making error of calculating the splitting between data points measured at slightly different values of magnetic field. Therefore the equation 2.10, after substituting constants and material parameters (after *Gaj et al.* (1994)) can be converted into form:

$$E_X = 275\,[\mathrm{meV}]\; x_{eff}\left(6\coth\left[\frac{4.03028\left[\frac{\mathrm{K}}{\mathrm{T}}\right]\;\mathrm{B}}{T+T_{AF}}\right]-\coth\left[\frac{0.671714\left[\frac{\mathrm{K}}{\mathrm{T}}\right]\;\mathrm{B}}{T+T_{AF}}\right]\right)+E_0 \qquad (2.15)$$

where: E_X – exciton transition energy

E_0 – exciton transition energy at zero magnetic field

T – temperature at which reflectivity was measured

The only fitting parameters are effective Mn density x_{eff} and antiferromagnetic temperature T_{AF}. An example of experimental data and fits performed with function 2.15 are presented in figure 2.15

[5] Note, that it assumes that the exciton binding energy does not depend on the magnetic field. This assumption is valid in the relatively small fields considered here

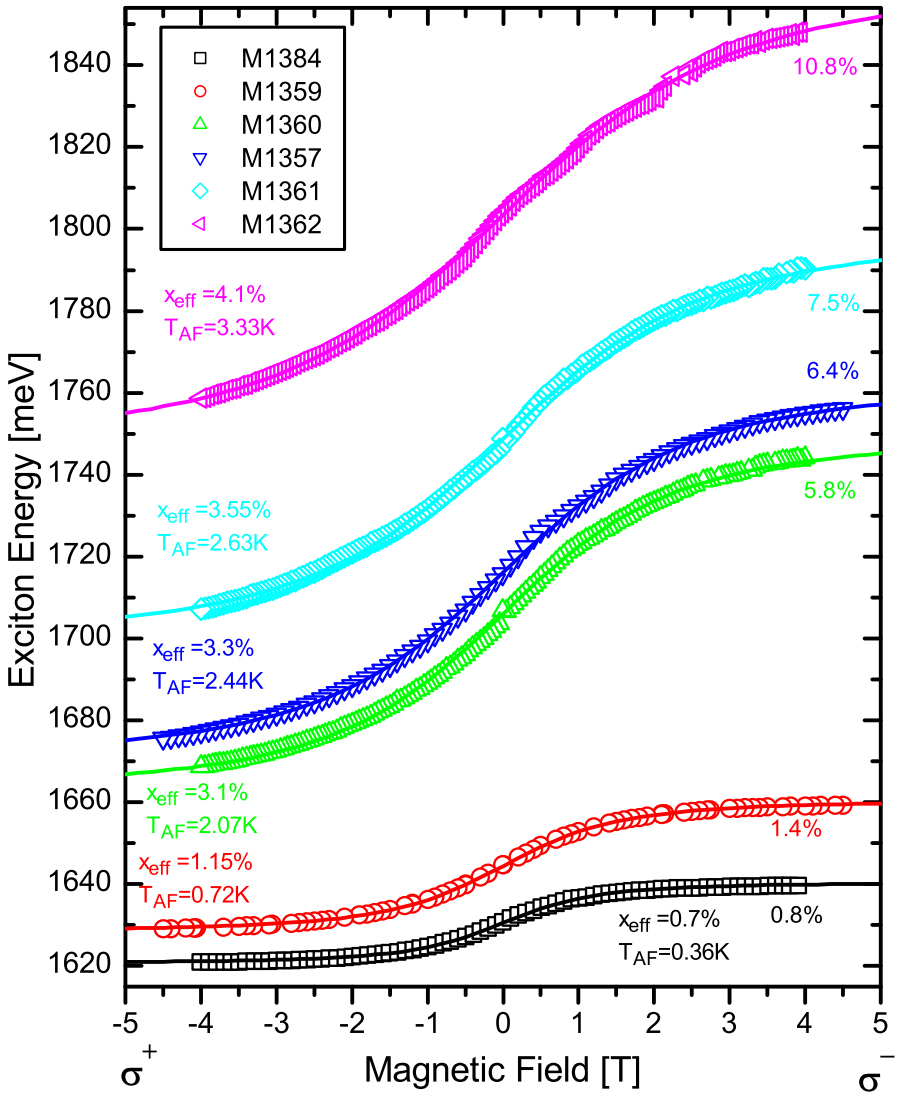

Figure 2.15: Determination of Mn composition from the reflectivity measurements for the surface doped samples with 10 nm wide quantum wells Temperature at which experiments were performed was 1.7K. Points – positions of exciton line in the reflectivity spectra, lines – fits of 2.15 function.

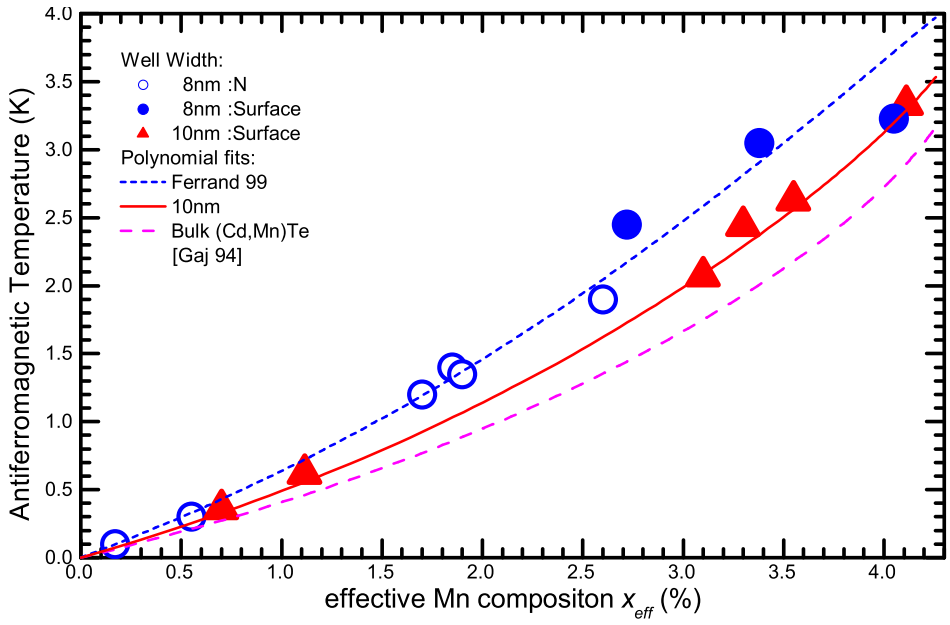

Figure 2.16: Antiferromagnetic temperature in quantum wells of different Widths. Plotted versus effective density of Mn spins - x_{eff}.

Although the proposed function describes well the experimental data it is important to note that the interpretation of obtained parameters might be different from the interpretation used in bulk (Cd,Mn)Te crystals. The main difference is caused by the presence of semimagnetic material only in quantum well region. We probe it through exciton state which has a wave function penetrating into the non magnetic barriers. Therefore the Mn compositions computed from the x_{eff} value (relation 2.5) are not exact. The complicated shape of wave function, combined with possible inhomogeneities of Mn distribution makes the interpretation difficult. Therefore the fitting parameters, should be treated only as an estimate of actual Mn composition of a quantum well material. The estimation is more accurate for smaller (less than 1%) Mn densities. Fortunately, x_{eff} obtained from presented fit is the parameter relevant for most of the calculations within mean field approach. Therefore we shall use x_{eff} rather than calculated Mn density for description of our samples. It is well to keep in mind that there is still some minor systematic error due to the changes of excitonic wave function in presence of carrier gas.

A clear discrepancy is observed when comparing the second fitting parameter – antiferromagnetic temperature T_{AF} to x_{eff}. Such comparison is free from uncertainty of the true Mn content (x) determination. It shows that the formula describing giant Zeeman effect has to be modified in order to accurately describe quantum well excitons. The results for the samples discussed in this work along with data for comparable structures used by *Kossacki* (1998) and *Ferrand* (1999) are collected in figure 2.16. The obtained antiferromagnetic temperatures are higher than the results for bulk (Cd,Mn)Te presented by *Gaj et al.* (1979). The results for quantum wells are placed along two polynomial curves. First one, describing 8 nm wide quantum wells was proposed by *Ferrand* (1999) the points obtained for surface doped quantum well of the same width also follow this curve. Results for 10 nm wide quantum wells are placed between curves describing bulk (Cd,Mn)Te and the one proposed by *Ferrand* (1999); results for 8 nm wide. The dependence of T_{AF} for 10 nm wide quantum wells can also be described by quadratic function. In figure 2.16 there is presented line obtained from fitting experimental data.

As one may expect the results for wider quantum wells are closer to the bulk results. The enhancement of T_{AF} in quantum wells is contrary to expectations based on the reduction of antiferromagnetic interaction of the outer atomic layers of quantum wells (*Ossau and Kuhn-Heidrich*, 1993). Part of the observed differences can be attributed to different penetration of excitonic wave function into non magnetic barriers. In case of typical 80 Å wide quantum well about 7% of the wave function lies outside the well. For a 100 Å wide quantum well this value is reduced to 4%.

Calculations based on the model of interfaces discussed by *Gaj et al.* (1994) confirm the tendency of our experimental results: in narrower quantum wells the T_{AF} is higher. However, to our surprise, the magnitude of T_{AF} enhancement obtained from calculations was an order of magnitude smaller from experimental results. Therefore additional source of differences is necessary to fully explain the observed differences. Works by (*Zehner et al.*, 1996; *Ossau et al.*, 1996) study experimentally the properties of thin (Cd,Mn)Te layers. Their results show that these effects contribute significantly to the T_{AF} variation shown in figure 2.16. The authors explain the results by the effect of excitonic wave function confinement and a k-dependence of the antiferromagnetic coupling.

As a result we may expect that the actual value of Mn composition is slightly smaller than values obtained from x_{eff} and T_{AF} determined by fitting the Zeeman splitting data with modified Brillouin function (In fits the x_{eff} is increased in odred to "make up" for T_{AF} rise).

Despite the discussed problems with interpreting the meaning of x_{eff} and T_{AF} those parameters can still be used to describe with good accuracy the properties of the studied samples within mean field model. Determining exact values would require the use of complicated models of quantum well interface profiles and Mn distribution along the structure as well as including the detailed properties of excitonic states in the structures of lowered dimensionality. The gain of accuracy of interpretation would probably be lost in the number of additional parameters necessary to address all the issues. Thus we decided to use in further reference experimentally determined parametrization by x_{eff} and T_{AF}.

CHAPTER 3

Experimental setups

Contents

Experimental work was carried out at Warsaw University and Laboratoire Spectrométrie Physique in Grenoble. For each of the measurement sessions the experimental setups were individually configured, therefore in this chapter I will present only the schematics of main arrangements.

3.1 Absorption and photoluminescence

Excellent quality of chosen samples allowed us to rely solely on magneto-optical experiments in our study. The experiments were conducted in Faraday configuration where magnetic field is perpendicular to the sample surface. Very often we were interested in comparing data from photoluminescence and absorption (or reflectivity) therefore we used versatile setup configuration shown in figures 3.1 and 3.3. The setup was configured in such way that choosing between both types of experiments required only switching on appropriate light source: laser for photoluminescence or tungsten lamp for absorption and reflectivity experiments. Such configuration assures that the same spot on the sample is studied in both cases.

3.1.1 Transmission and Reflectivity

The choice between transmission or reflectivity depends on the structure of the sample (see chapter 4.1). The actual experimental configurations of light beam used for transmission and reflectivity are presented by dark color in figures 3.1, 3.2 and 3.3. The configurations differ only by small details: in reflectivity experiment a mirror is used to direct the beam toward the sample surface while in transmission the light passes directly through the substrate of the sample. A tungsten lamp was used as a source of light. In order to prevent heating of the sample

infrared cutoff filters were used (not marked in the figures). It was followed by a two lenses and diaphragm which produce parallel beam. Diaphragm is used to improve the homogeneity of power distribution across the beam. It also helps to minimize the size of light spot on the sample. It is achieved at the expense of light power.

3.1.2 Additional Illumination

The strong influence of light on the carrier density in the sample (discussed in 4.5) forced us to use additional spectral filters (marked as SF in figures) in to order to probe the sample in unaltered state. In case of transmission such filters turned out unnecessary because the thick substrate layer of the sample acts as a spectral filter itself. In some cases the sensitivity of the samples to the light of certain energy was used to control carrier density. For this purpose another illumination line was added to standard configuration. It is marked with light color in the figures 3.1, 3.2 and 3.3. The choice of appropriate wavelength was achieved by spectral filters (bandpass or narrow band interference) or a monochromator as shown in figure 3.2. The intensity of additional illumination was tuned by gray filters (neutral optical density). The maximal power of additional illumination was always set in such a way that the photoluminescence due to the additional illumination was negligible. In every experiment with additional illumination it was crucial that the spot of additional illumination on the sample surface was larger than that of a transmission and reflectivity beams or a laser spot used in PL experiment.

3.1.3 Photoluminescence

In photoluminescence experiments various lasers were used for excitation. The 514 nm line of ion argon laser as well as 532 nm green solid state laser were used in studies of photoluminescence from the barriers. Photoluminescence from the quantum well was excited by red lasers: 680 nm laser diode or tunable Al_2O_3:Ti laser. The tunable Al_2O_3:Ti was connected to the computer controlled driver which allowed us to tune the laser from 705 nm to 770 nm. The ability to tune the laser was used to record the photoluminescence excitation spectra.

The power of laser light used in experiments was always kept as small as possible in order to prevent local heating of the sample. Usually we did not exceed 1 mW/cm^2 and still the signal to noise ratio was satisfactory. Furthermore, in most experiments a lens was used (visible in figures 3.1 and 3.3), preventing focalization of the laser on the sample surface. The lens was selected to provide a spot on the sample surface of approximately 2 mm diameter.

3.1.4 Detection

Usually the spectra were recorded by a CCD camera attached to the exit of the monochromator. The high sensitivity of CCD detectors allowed to minimize the power of light employed in experiments. Instant capture of broad spectra allows to collect many spectra in the time of single scan when as a detection device photo multiplier tube (PMT) is used. It allows to substantially speed up the experiments. Despite obvious disadvantage, a photo multiplier tube has been used during the PLE measurements. In this case the detection energy is fixed very close to the excitation energy therefore using narrow spectral window in detection is favorable. This

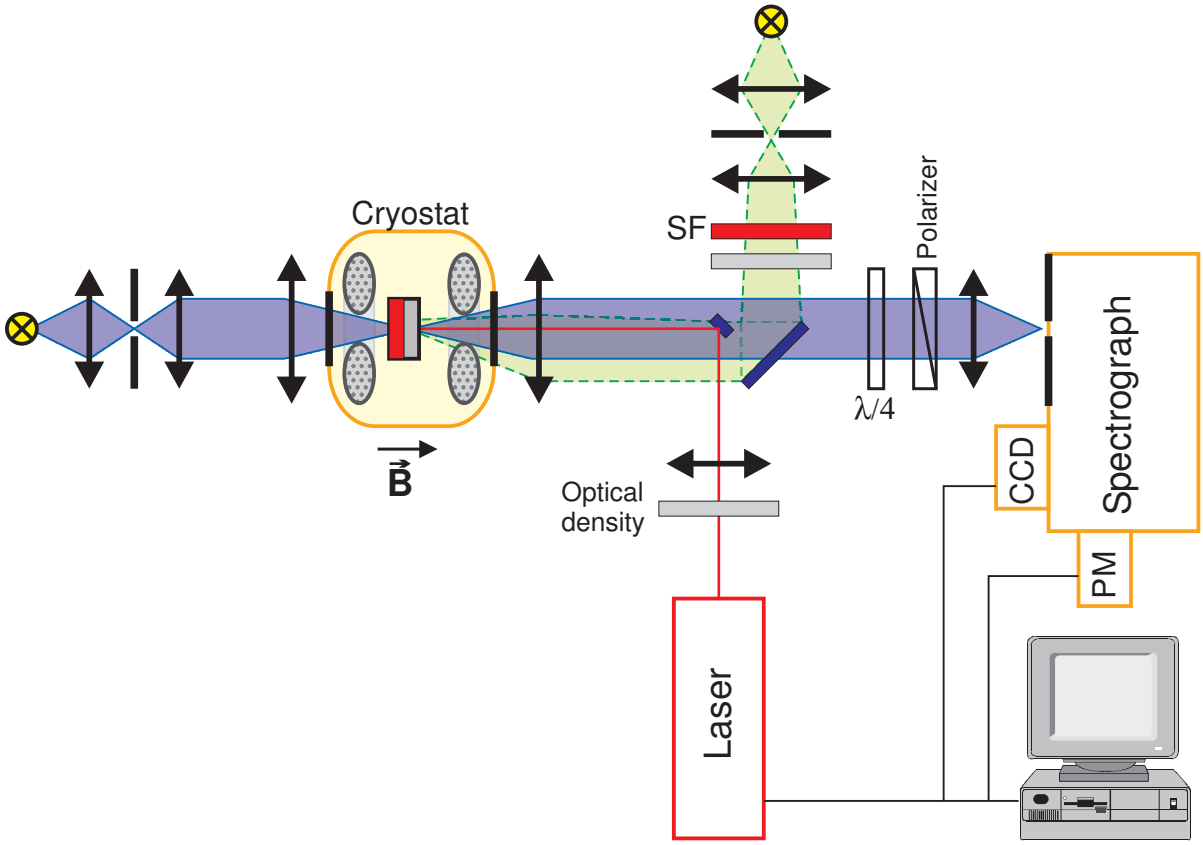

Figure 3.1: Setup for absorption and PL measurements with additional illumination

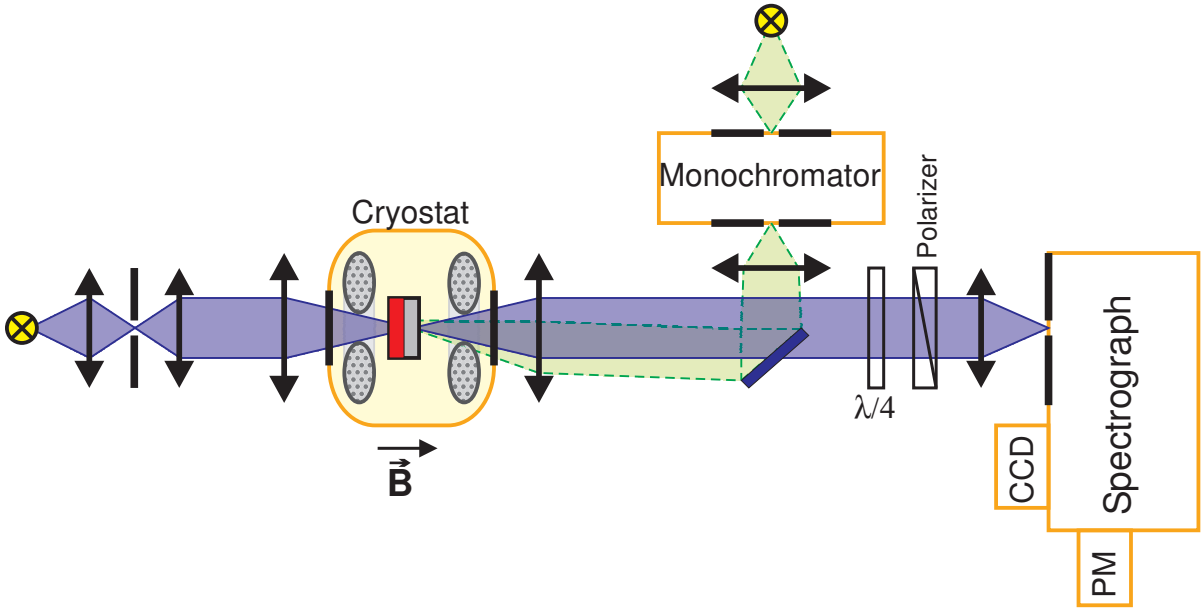

Figure 3.2: Setup for absorption measurements with additional illumination through monochromator.

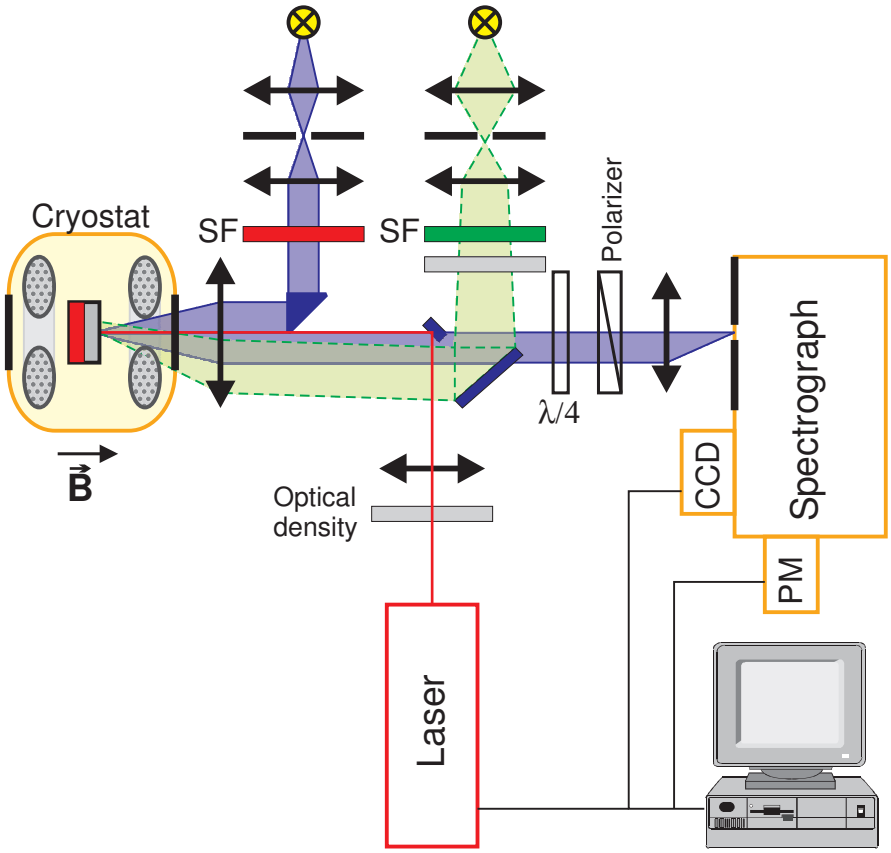

Figure 3.3: Setup for reflectivity measurements with additional illumination.

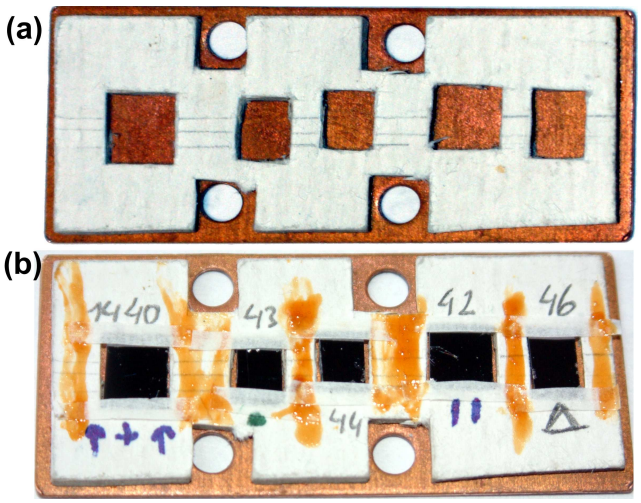

Figure 3.4: Strain free mounting of the samples. **(a)** Cardboard with holes matching sample sizes is glued to the coper plate. **(b)** Samples are placed inside the cardboard and secured with straps of cigarette paper. The coper plate is next screwed to the sample holder. The screws are passing through 4 holes visible in the copper plate.

arrangement minimizes the possibility of damaging the detector. Anyway, in PLE experiments the scanning is achieved by changing the emission wavelength of a laser (tuning the Lyot filter placed inside the Al_2O_3:Ti laser cavity) therefore the broader detection window cannot speedup the experiment.

The magnetic field was applied in Faraday configuration. Therefore the circular polarizations form a proper basis for analyzing optical transitions. The circular polarization resolved detection was achieved by placing broadband $\lambda/4$ retarding plate and linear polarizer (with axis tilted 45° with respect to optical axis of retarding plate)at the entrance slit of monochromator. Usually, in order to compensate the polarizing properties of monochromator another $\lambda/4$ plate (with optical axis parallel to the first plate) was placed after the linear polarizer. The switching between $\sigma^+$and σ^-polarization was usually achieved by reversing the orientation of magnetic field rather than adjusting linear polarizer. It was preferred due to better accuracy and stability.

3.1.5 Temperature

During measurements samples were placed in helium bath. Lowering of the temperature below 4.2 K was possible due to pumping of helium vapor. Most of the measurements were carried out in temperatures below λ point of helium (below 2.17 K). The properties of superfluid helium (such as infinite heat conductivity) result in excellent stability of experiment. The stability of temperature was ensured by use of a manostat stabilizing the pressure of the helium vapor. The very efficient pumping system allowed us to reach temperatures as low as 1.4K.

Some of the experiments required the temperatures up to 30 K. In this case the sample was placed in flow of helium vapor. The pressure was fixed by manostat at 250 mbar. The helium vapor temperature was stabilized by heater with controller coupled to temperature sensor located close to the heater. This allowed us to achieve precise control of the temperature as well as satisfactory stability. The temperature of the sample was additionally monitored by measuring resistance of a carbon resistor located on sample holder in the vicinity of the sample.

3.1.6 Mounting of the samples

The measurements were carried out in temperatures ranging from 1.4K to 30K. Therefore, mounting of the samples was designed in order to minimize the risk of introducing additional strain to the samples. It could be due to the differences in thermal expansion coefficients between the sample holder and the sample. The samples were placed inside the holes (of the dimensions chosen to fit each sample individually) carved inside thick cardboard glued directly to the metal of the sample holder (figure 3.4a). The samples were secured inside the cardboard by thin straps of cigarette paper glued on top of the cardboard (figure 3.4b). The cardboard thickness was always larger than thickness of the sample.

Due to the delicate nature of the samples a special care was taken during heating up of the samples. After each measurement in low temperatures the process of heating up the samples was conducted slowly in helium gas. After removing from cryostat the samples were placed in nitrogen gas in order to prevent the condensation of moisture on the sample and possible degradation of the sample surface.

3.2 Micro photoluminescence

The access to a unique microscope objective allowed us to study the the sample in sub micron scale. The lens was designed by *Jasny et al.* (1996) and has been adopted to measurements on solid state crystals by A. Kudelski during his preparation of PHD thesis (*Kudelski*, 2004).

A schematic drawing of the microscope lens can be seen in figure 3.5. The lens has numerical aperture of 0.722 with a dark spot due to central mirror of 0.329 numerical aperture. The microscope provides a magnification of 100. Observed surface has to be directly in contact with back surface of the lens. The image plane of microscope is located 25 cm before the lens. The body of microscope was made of *suprasil* which provides constant optical properties and small thermal expansion coefficient in broad range of temperatures (ranging from 1 K to 300K). The dimensions of the case holding the lenses was designed to fit used cryostat. Therefore it was possible to immerse the microscope in helium bath with sample securely attached to the back surface of the lens. Such configuration provides excellent mechanical stability of measurements. Moreover the microscope case was made of nonmagnetic material therefore it was possible to apply magnetic field during the experiments.

The configuration of experimental setup is presented in figure 3.6. Similar configuration was used in works by *Golnik et al.* (2004) and *Gaj et al.* (2004). For PL excitation a solid state laser diode of 680 nm wavelength was used. The laser beam was expanded to diameter of about 10 mm. It resulted in 0.5 μm diameter of laser spot focalized on the sample. In order to prevent sample heating special care was given to the power of exciting laser beam. As the focal spot is orders of magnitude smaller than in usual experiments the increased density of power may result in permanent damage of the sample even if the initial power of the laser was relatively small. The experimental setup included video camera used to monitor the quality of laser spot on the sample as well as trace its position.

Large heat capacity of the lens makes precise temperature control difficult. Practically, two temperatures can be well stabilized in the cryostat with microscope lens inside: 4.2K (the temperature of helium bath at normal pressure) and temperatures below 2K. The lowest possible temperature was determined by the actual pressure of helium in vicinity of the sample. The sample temperature was monitored by carbon resistor, unfortunately the configuration of microscope forced large distance of the sensor from the sample. Therefore the temperature determination may be inaccurate, however it is possible to verify if the temperature remains constant during the measurements. It was essential during photoluminescence mapping experiments which extended over several hours each.

Photoluminescence mapping was accomplished using a 10mm thick, plane-parallel, fused-silica plate placed between the microscope and the first lens of the optical system. The plate was rotated around two perpendicular axes by step motors. The correlation between the angle of tilt and the displacement of excitation - detection spot on the surface of the sample is presented in figure 3.7. The typical area of scans was $32 \times 32 \mu\mathrm{m}^2$. It is limited by the geometry of microscope lens. The resolution of scan is determined by size of laser spot and control of the angle deflecting

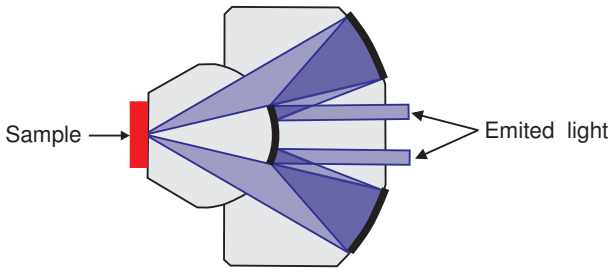

Figure 3.5: Microscope lens.

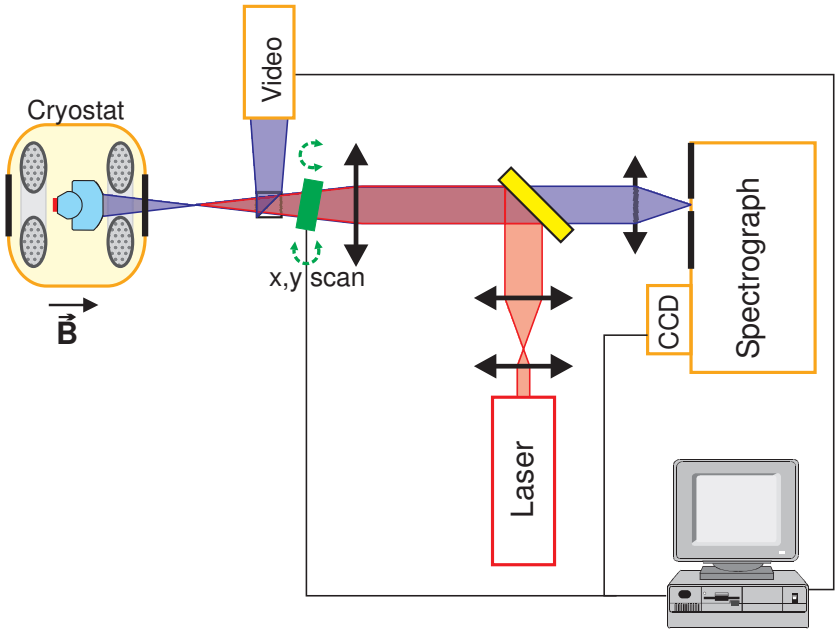

Figure 3.6: Setup for micro photoluminescence mapping measurements.

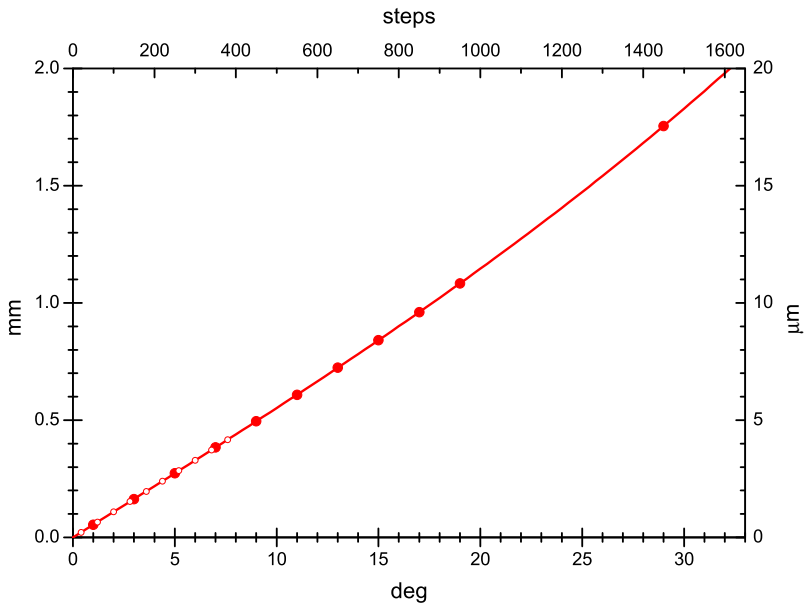

Figure 3.7: Calibration of excitation and detection spot position with respect to the tilt of plane-parallel fused-silica plate. The upper axis indicates the number of steps of the used motors.

plate. In our case precise stepping motors give control superior to the laser spot dimensions making the later key factor of the experimental resolution.

For the significant change of scanned area remounting of the sample on the microscope lens is required. It is complex, as it requires removing the whole lens from the cryostat. Furthermore it is not possible to precisely pick the area of sample accessible for particular experiment. However once the sample is mounted the area does not change during the experiment. In other experiments by *Suffczynski et al.* (2006) the excellent stability of this setup allowed to maintain one particular quantum dot of 100 nm diameter in laser spot during experiments lasting several days.

Photoluminescence spectra were taken by a CCD camera attached to the spectrograph exit. During photoluminescence mapping up to 4096 spectra were recorded at different spots over the sample surface per single map. It was possible only due to large aperture of the used microscope lens which, combined with high sensitivity CCD camera allowed to perform such measurements during sensible amount of time. The superb mechanical stability was also essential during this type of experiments.

CHAPTER 4

Surface doping of quantum wells

Contents

The onset of modulation doping (*Stormer et al.*, 1979; *Dingle et al.*, 1978) advanced studies of quantum structures containing two dimensional carrier gas. The idea of keeping the dopants away from the carrier gas opened the possibility for increase of carrier mobilities by reducing the scattering on the ionized impurities. The impact on the construction of fast semiconductor devices was tremendous. One of the new fields opened were studies of quantum transport phenomena like quantum Hall effect.

The properties of two dimensional carrier gas have been also studied optically (*Skolnick et al.*, 1987*a*,*b*). Optical experiments favor moderate ($10^9 - 10^{11}$ cm^{-2} in II-VI materials) carrier concentrations where the excitonic effects are still strong and the many body effects gain significance. In such conditions first observations of charged excitons were performed (*Kheng et al.*, 1993). The charged excitons are an interesting case of exciton – carrier gas interactions (*Kossacki et al.*, 1999; *Płochocka et al.*, 2004; *Cox et al.*, 2004).

We are interested in studies of carrier induced ferromagnetism in diluted magnetic semiconductors (DMS). The most conclusive results have been obtained so far for p-type doped structures. In III-V DMS, the same impurity (Mn) carries the localized spins and acts as an acceptor (*Ohno*, 1998). This puts strong limits on the realization of quantum wells (QWs) and two dimensional (2D) systems (*Ohno et al.*, 2000) using thin layers of III-V DMS (*Boselli et al.*, 2000; *Lee et al.*, 2000). However recent experimental works by (*Nazmul et al.*, 2002, 2003, 2005) indicate very promising results for GaAs structures δ-doped with Mn. Ingenious combination of

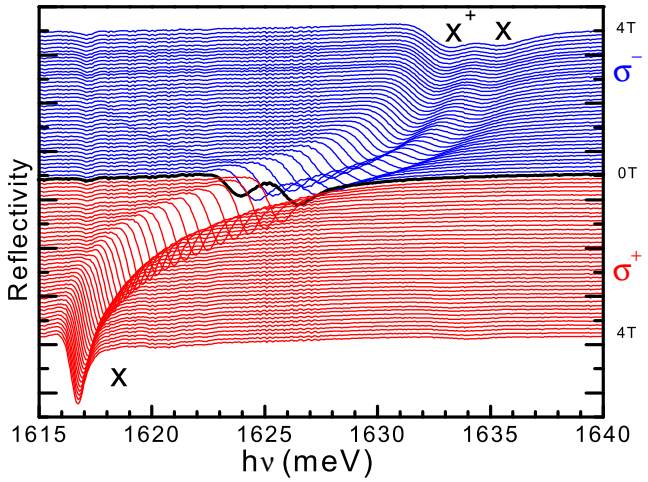

Figure 4.1: Broadband reflectivity spectra displaying the evolution in the magnetic field of charged and neutral excitons transitions In sample M1384, at 1.69K.

heterostructure design and growth conditions allowed to increase the hole gas density in vicinity of Mn layer. The sample structure contained Mn δ-doped GaAs layer and (Al,Ga)As layer doped with Be. The additional p doping with beryllium allowed to increase the Curie temperature of the carrier induced ferromagnetism up to 250K (*Nazmul et al.*, 2005). Similar effects are far easier to obtain in II-VI materials. For example in $Cd_{1-x}Mn_xTe$ the transition metal possessing magnetic moment may be incorporated as a neutral ion. This permits to control independently magnetic moments and carrier doping.

It has been proposed theoretically (*Dietl et al.*, 1997) and shown experimentally (*Haury et al.*, 1997) that the presence of a 2D carrier gas can induce a ferromagnetic ordering due to the strong exchange coupling of Mn spins to charge carriers. In Ref. (*Haury et al.*, 1997), the modulation-doped structures were grown by molecular beam epitaxy (MBE) using nitrogen acceptors in the $Cd_{1-y-z}Zn_zMg_yTe$ barriers. Although efficient, this method brings restrictions. Effective doping of $Cd_{1-y-z}Zn_zMg_yTe$ with nitrogen is only possible for y lower than 30%. It requires lowering the growth temperature from the usual 280 down to 220 °C to avoid a strong interdiffusion of the heterostructure (*Arnoult et al.*, 1998), and thus affects the quality of the samples (*Grieshaber et al.*, 1994). Moreover the presence of nitrogen excludes almost any postgrowth treatment of the sample.

Typically in samples with CdTe or (Cd,Mn)Te modulation doped quantum wells the nitrogen doped layer is placed between the quantum well and the sample surface (or at both sides of the well in case of symmetrical doping). Such placement ensured screening of the surface states which was considered helpful in the studies of quantum wells with hole gas. The investigations of a quantum well close to the surface had begun with the idea of using a single (Cd,Mn)Te quantum well as a probe of magnetization in the metallic layer deposed on top of the semiconductor structure. The magnetization in metallic layer was supposed to be witnessed by the Zeeman splitting of the excitonic transition in the quantum well (*Bourgognon*, 2001; *Bertolini*, 2004). The chosen quantum well material ensured high sensitivity to magnetic field. The experiments have begun with optimization of the semiconductor structure. To our surprise, the spectroscopy

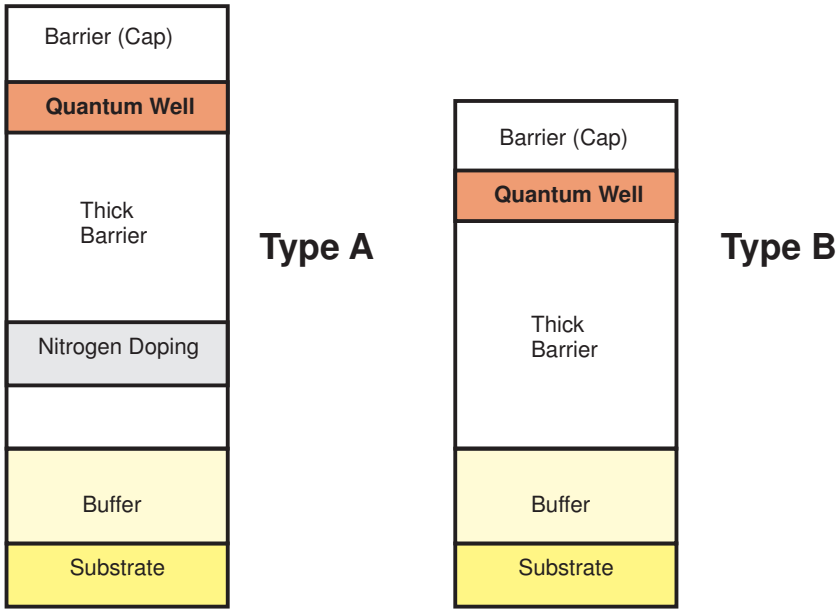

Figure 4.2: Schematic presentation of samples structures.

of intentionally undoped sample[1] displayed the features typical for the samples with carrier gas present in the quantum well [2]. The presence of holes in quantum wells close to the surface might also explain spectra observed in nominally undoped parts of gradually doped samples (*Wojtowicz et al.*, 2000).

Figure 4.1 shows evolution of reflectivity spectra in magnetic field for such a sample. The low energy line is observed in magnetic field only σ^- circular light polarization. We identify it as a positively charged exciton - a whitness of appearance of free holes in the quantum well (*Kossacki et al.*, 1999).

This chapter is as an attempt to understand and exploit the possibility of using the surface states as a source of carriers for the quantum well.

4.1 Structure

All the samples were grown in MBE chamber at CEA-CNRS in Grenoble. During the growth process the samples quality was controlled by the observation of RHEED oscillation. Two types of substrates were used for the growth of samples: $Cd_{0.88}Zn_{0.12}Te$ and $Cd_{0.96}Zn_{0.04}Te$. Both were (001) oriented. The 12% Zn substrate, has wider band gap (approximatively 1673 meV) than the 4% one (approximatively 1610 meV). The structures were designed so that the excitonic transition energy was approximately 1630 meV. Therefore for the samples grown on the 12% zinc substrates it was possible to observe the quantum well transitions in transmission experiments. The shortage of 12% Zn substrates as well as technical problems with Zinc cell in the MBE

[1] The chapter title is a shortening. More accurately it should sound: "Surface states as a source of carriers for the quantum well" since we do not actually introduce any foreign dopant into the structure.

[2] Influence of the vicinity of the surface on the population of carriers was also noted by M. Kutrowski and P. Kossacki during their experiments in 1999 yet the results were unpublished until PHD thesis: (*Kutrowski*, 2001)

machine forced us to work with nontransparent 4% Zn substrates. The structure of the samples followed general schemes presented on figure 4.2.

For comparison purposes the growth parameters were first kept in the range typical for the growth of the nitrogen doped samples, including the substrate temperature 220 °C. Each sample contained a 100 Å wide QW made of $Cd_{1-x}Mn_xTe$ or CdTe. The QW was embedded between $Cd_{0.7}Zn_{0.08}Mg_{0.22}Te$ barriers in case of 12% Zn substrate and $Cd_{0.78}Mg_{0.22}Te$ for the samples grown on the 4% Zn substrate, so that the whole structure could be grown coherently strained to the substrate. The thickness of the top barrier (cap layer) was in the range from 150 Å to 1000 Å. Most of the samples were of the A-type structure of figure 4.2. The nitrogen doped layer placed between the quantum well and the buffer layer was purposed to screen any electrically active defects in the buffer layer from affecting the quantum well. It was located far from the quantum well to avoid any direct transfer. Only the first structures with CdTe quantum well follow the B-type scheme. The detailed sample structures are in appendix A. Actual alloy parameters were verified by the optical experiments. The composition of barriers was checked from the PL transition energy (*Hartmann et al.*, 1996). The Mn content in the QW was checked from fitting a modified Brillouin function (*Gaj et al.*, 1994) to the Zeeman splitting measured in reflectivity as described in chapter 2.3.2.

4.2 Evidence of carrier presence and identification of carrier type

The first evidence of the presence of a carrier gas in a QW close to the surface comes from transmission or reflectivity spectra with applied magnetic field (figures 4.1 and 4.3b). Two narrow absorption lines are observed. The upper line is identified as neutral exciton (X) in the quantum well as witnessed by the giant Zeeman splitting (*Gaj et al.*, 1994). The lower line exhibits properties of a charged exciton (*Kossacki et al.*, 1999):

- transition energy 3meV below neutral exciton
- full circular polarization achieved at low magnetic field
- Zeeman shift at full polarization same as in X

The charged exciton transition, is therefore an indication of the presence of a carrier gas (*Kheng et al.*, 1993; *Haury et al.*, 1996; *Kossacki et al.*, 1999). The photoluminescence spectra in the presence of magnetic field (figure 4.4) also exhibit features typical for the presence of carrier gas in the quantum well. For example, the line intensity decreases rapidly in σ^- circular polarization and a double line appears in σ^+ polarization at higher magnetic fields (*Kossacki et al.*, 2004*a*).

For the purpose of identification of carrier type in the quantum well specially designed samples were grown (M1279 and M1282). The structure remained the same (that of type B in figure 4.2) but contrary to the most of the samples considered here the quantum well was made of pure CdTe without Mn. A CdTe QW grown coherently on a $Cd_{0.88}Zn_{0.12}Te$ substrate is subject to a compressive biaxial strain. The sign of the charge carriers is in this case unambiguously determined from the circular polarization of the charged exciton absorption in Faraday configuration. Due to the negative signs of both the conduction and valence band g

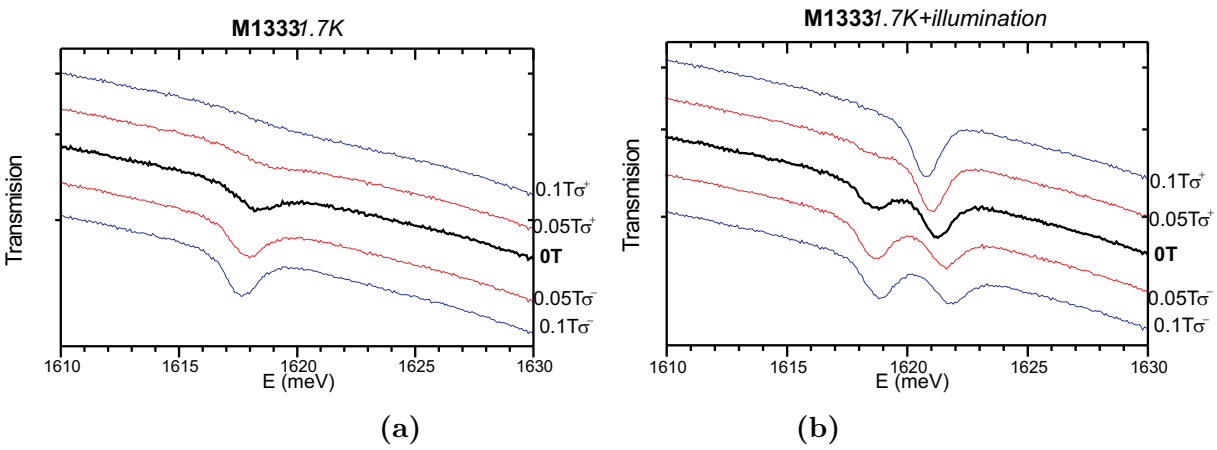

Figure 4.3: Transmission spectra for sample M1333 in magnetic field. (a) The present absorption line results from formation of charged excitons. Large hole concentration ($3.5 \times 10^{-11} cm^{-2}$) is responsible for its evolution toward Fermi edge singularity at 0T. (b) Additional illumination of the sample allows to decrease the carrier concentration in the quantum well. Therefore neutral exciton line becomes visible.

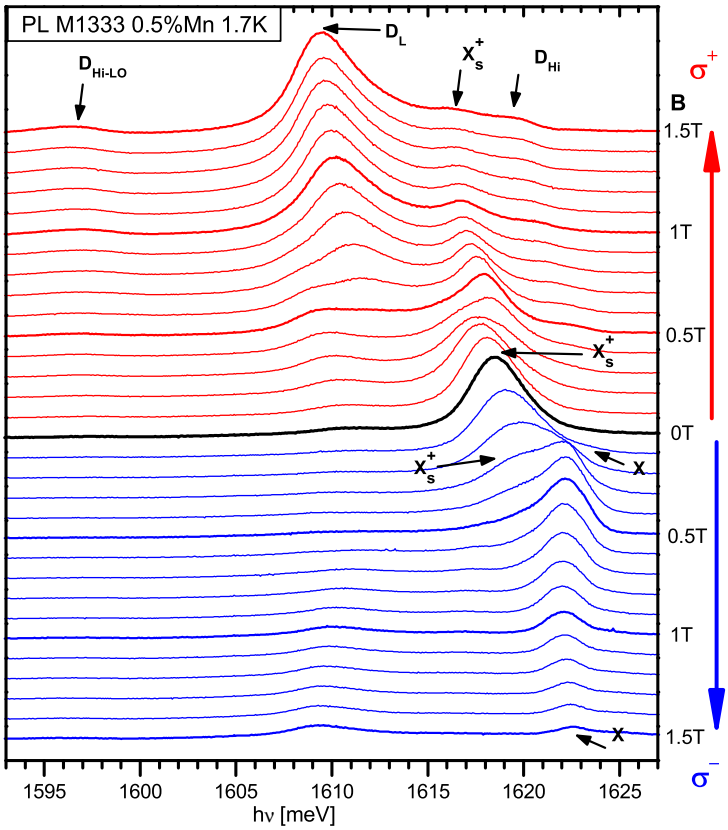

Figure 4.4: Photoluminescence of sample M1333 in the magnetic field at 1.7K. The rapid decrease of intensity in σ^- polarization and the double line in σ^+ polarization at higher magnetic fields are the fingerprints of the presence of carrier gas. The dominant line at zero magnetic field can be identified as positively charged exciton. The concentration as determined from Moss-Burstein shift is $3.5 \times 10^{11}\mathrm{cm}^{-2}$.

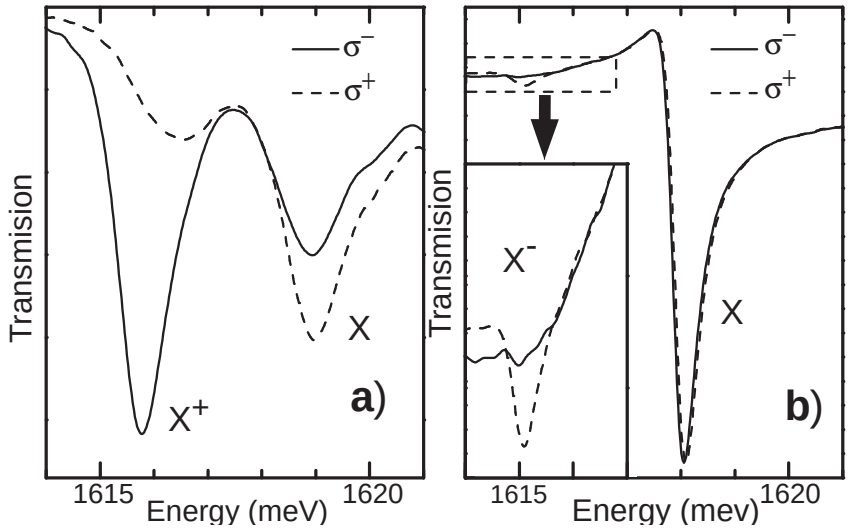

Figure 4.5: Circularly polarized transmission spectra, at 3 T and 1.7 K, for a single CdTe QW with a cap layer thickness of (a) 250 Å (M1279) and (b) 1000 Å(M1283). The inset in (b) presents a close-up of the area of the spectrum attributed to a negatively charged exciton.

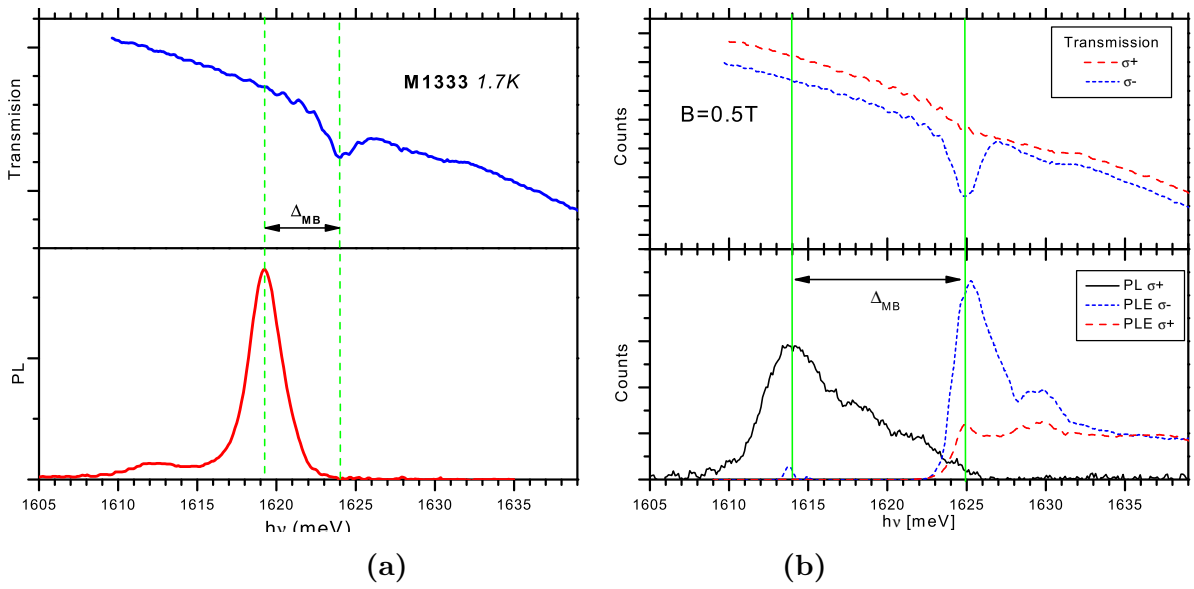

Figure 4.6: Experimental spectra for sample M1333 Moss-Burstain shift can be determined either from PL and transmission spectra at 0T [panel (a)]. In magnetic field transmission spectra in σ^+ polarization or σ^+ PLE spectra and PL in σ^+ can be used.

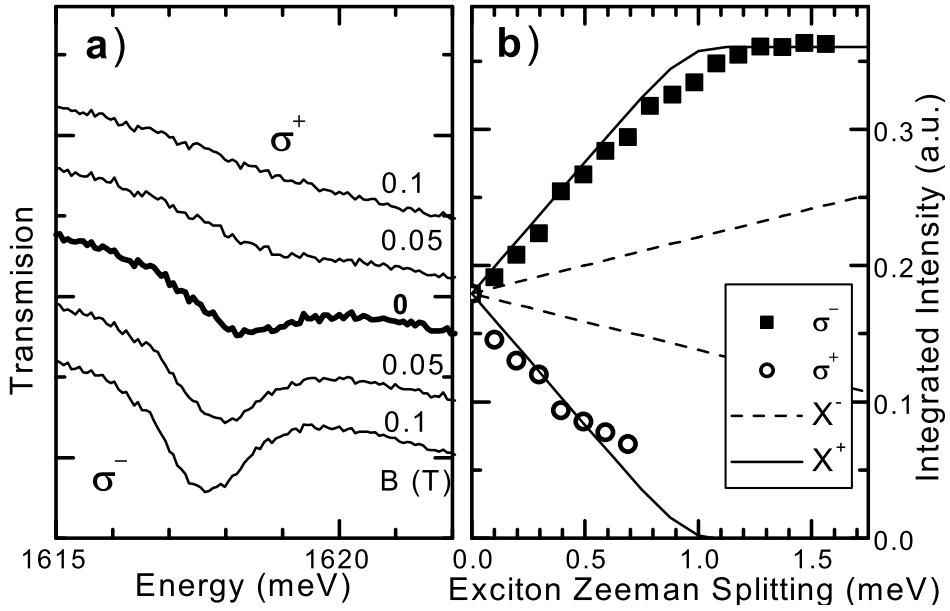

Figure 4.7: **(a)** Transmission spectra, in magnetic field, for a $Cd_{0.995}Mn_{0.005}Te$ QW placed 250 Å below the surface of the sample. Measured hole concentration is 3.5×10^{-11} cm^{-2}. **(b)** Integrated intensity of transmission line versus Zeeman splitting in both circular polarizations (points) and results of calculation for electron (dashed line) and hole gases (solid line). The calculation includes many body contribution (fermi liquid parameter A_f value was assumed 2.1 see chapter 2.2.2).

factors, the positively charged exciton is observed in σ^- polarization (*Haury et al.*, 1996) while the negatively charged exciton is observed in σ^+ polarization (*Kheng et al.*, 1993). In Fig. 4.5 (a), the lower energy line obeys the selection rules for positively charged excitons. This shows that free holes are present in this CdTe QW. Note that no nitrogen acceptors were introduced into this sample. The opposite polarization rule was observed in a CdTe QW identical to the previous one but with a thicker (1000 Å) cap layer [Fig. 4.5 (b)]. The weak intensity of the X^- line indicates a low concentration of electrons. Hence we conclude that we have a weak residual doping, which is n-type and accounts for the low electron density in the deeply buried QW, while the hole gas with a higher density in the QW close to the surface has a different origin.

The presence of a carrier gas was also evidenced in $Cd_{1-x}Mn_xTe$ QWs. In sample with a 250 Å thick cap layer (M1333), the Moss-Burstein shift between the absorption (or reflectivity or PLE) line and the PL line indicates a large density of carriers in the QW (Figure 4.6). As discussed in chapter 2.2.2, in the case of band-to-band transitions, the Moss-Burstein shift is equal to the sum of the kinetic energies of electrons and holes at Fermi wavevector k_F. Therefore it can be used as a tool for measuring the carrier density. The determination of the carrier density from the Moss-Burstein shift requires no assumption on the type (electrons or holes) of the carriers. However, once the density of carriers is known, their sign can be deduced from the value of the magnetic field necessary to fully polarize the carrier gas.

Full polarization is witnessed by the vanishing of the charged exciton absorption in σ^+ polarization (Fig. 4.7). Due to the giant Zeeman effect, characteristic for DMS, complete spin polarization of a hole gas of density 3.5×10^{-11} cm^{-2} in a $Cd_{0.99}Mn_{0.01}Te$ QW is achieved

when applying a magnetic field as low as 0.1 T. In the one-particle approximation[3], this field is expected to be at least five times larger for the same density of electrons (*Gaj et al.*, 1994; *Kossacki et al.*, 1999). This is a simple consequence of two facts: first, the exchange integral in $Cd_{1-x}Mn_xTe$ for heavy holes valence band $N_0\beta = -0.88$ eV (*Gaj et al.*, 1979) is four times bigger than for conduction band $N_0\alpha = -0.22$ eV (*Gaj et al.*, 1979), second, fermi energy for electrons is larger. Therefore the conduction band splitting is responsible for $^1/_5$ of the observed splitting of the excitonic transition, and the remaining $^4/_5$ parts of the excitonic transition splitting are due to the splitting of the valence band.

This qualitative discussion can be backed up by a simple, self consisted calculations, in which constant population of carries is distributed between the two levels (subbands) of different energies. Additionally we add in to consideration thermal factor. In order to compare results of calculations we have to assume that the observed intensity of charged exciton transitions is proportional to the carrier population (*Kossacki et al.*, 1999). The energy difference between the two subbands comes from the Zeeman splitting. For our system we take: in case of conduction band, for electrons we take $^1/_5$ of excitonic zeeman splitting and for the valence band and heavy holes we take $^4/_5$ of excitonic zeeman splitting. The additional difference between electrons and holes is in distance of the Fermi level. Results of the calculations are presented on figure 4.7. It is clearly visible that only calculations for hole gas is capable of describing the experimental data.

Therefore we can conclude that despite native n-type doping of well material we have obtained significant heavy hole concentration without intentional p-type doping.

4.3 Variation of carrier density with cap layer thickness

Previously described experiments allowed to identify the carrier gas present in the quantum well close to the surface as hole gas. This would imply the presence of acceptor states in the vicinity of the sample surface. The energy of acceptor states would be expected in the band gap of the barrier material.

The charge transfer from the surface states to the quantum well can be estimated assuming pining of the Fermi level by the surface states. The effectiveness of transfer depends on the quantum well depth and its distance from the surface. An examples of the possible arrangements are depicted in figure 4.8. Quantum well (a) is close to the surface and the hole gas concentration in the quantum well is high. The quantum well (b) is placed too far from the surface to receive a significant hole concentration. In case (c) the quantum well is deeper (due to the smaller band gap of the well material) than in cases (a) and (b). This allows to obtain a significant hole gas concentration despite a considerable distance from the surface. In case of the wells buried even deeper in the sample it is possible to achieve the crossing of the Fermi level with the conduction band of the well (case not depicted in this figure) and obtain electron gas in the quantum well.

In order to investigate the influence of the cap layer thickness on the QW hole density a set of samples with similar growth conditions, and almost identical structure, was grown. In this

[3]Many body effects can strongly modify the field necessary to obtain full polarization (see 2.2.2).

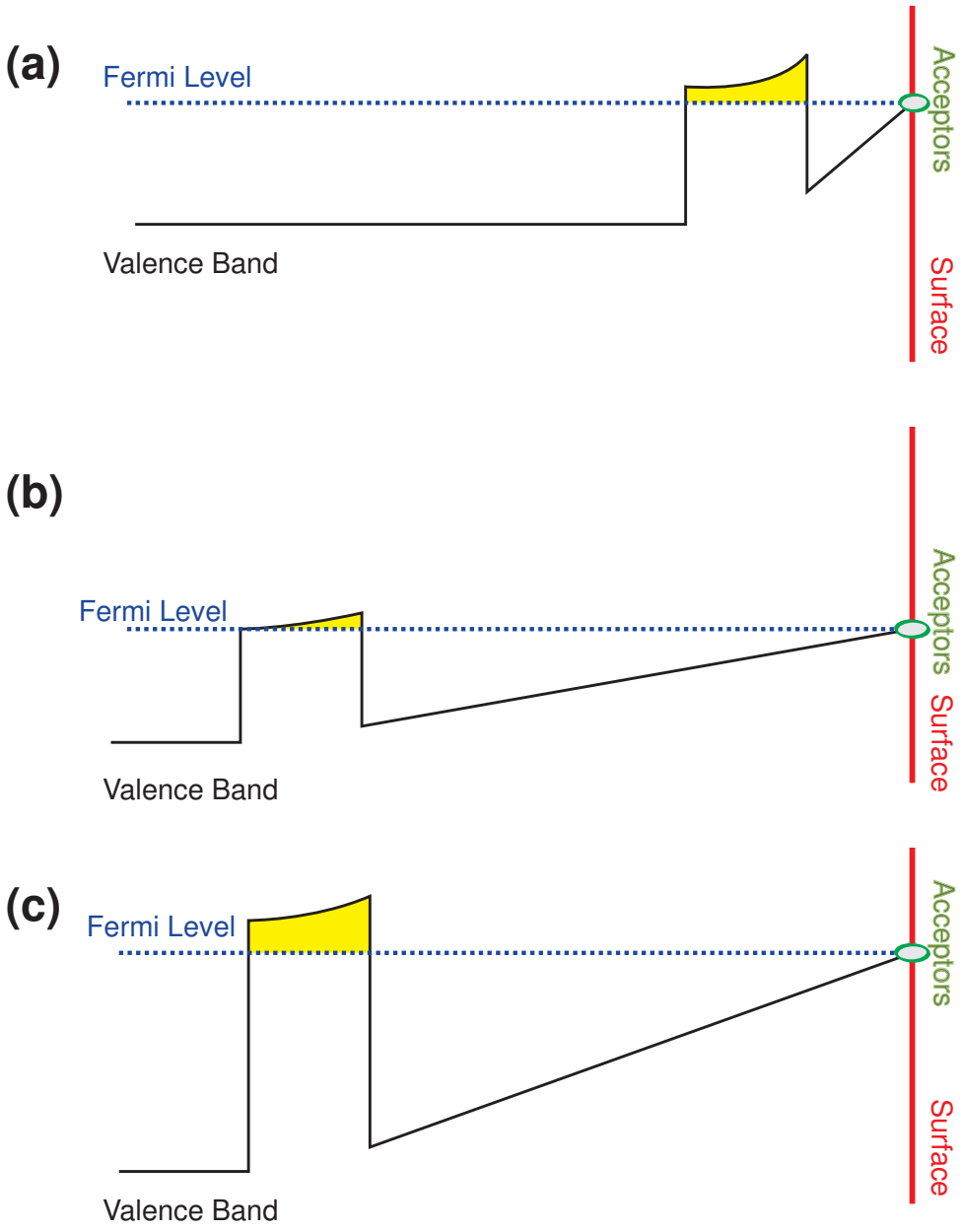

Figure 4.8: Possible realizations of valence band structure with the quantum well close to the surface. We assumed that the Fermi level at the surface is pinned very to the valence band maximum.

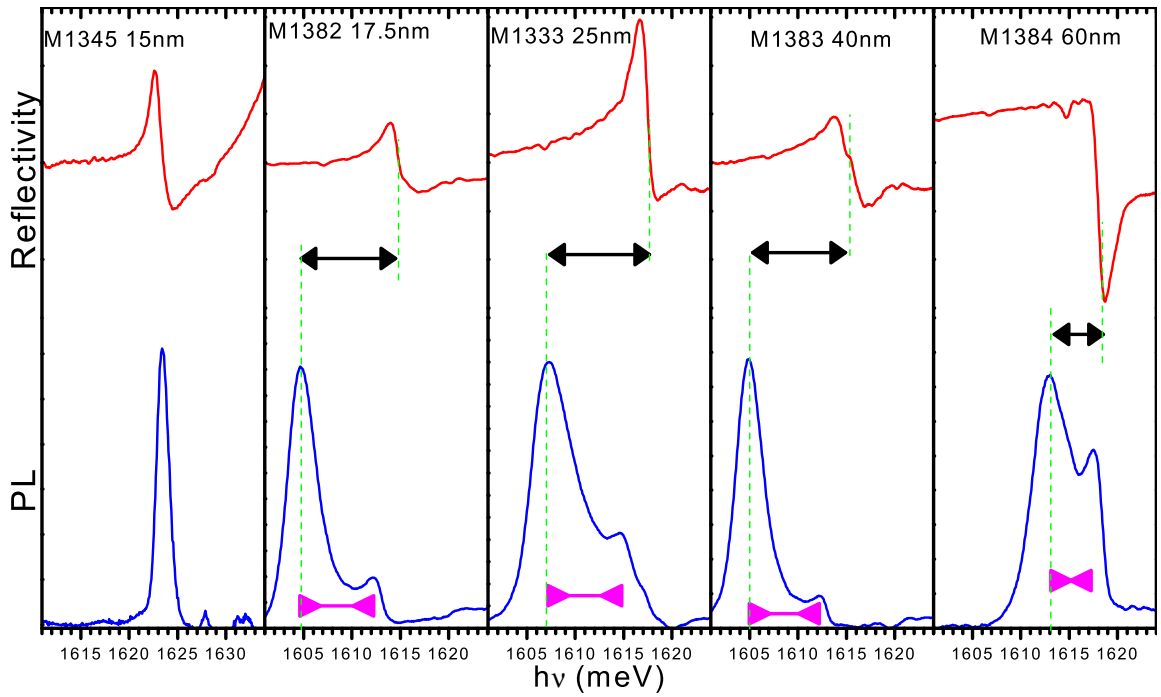

Figure 4.9: Photoluminescence and reflectivity spectra used for determination of hole gas density for different cap layer thicknesses. The spectra were recorded at 1T and 1.7K. Arrows (ordinary) denote Moss-Burstein shift. The arrows ending with reversed triangles indicate the D_{high}-D_{low} splitting, which can be also used for carrier density determination (as discussed in section 2.3.1). It is also possible to trace the changes of reflectivity line shapes.

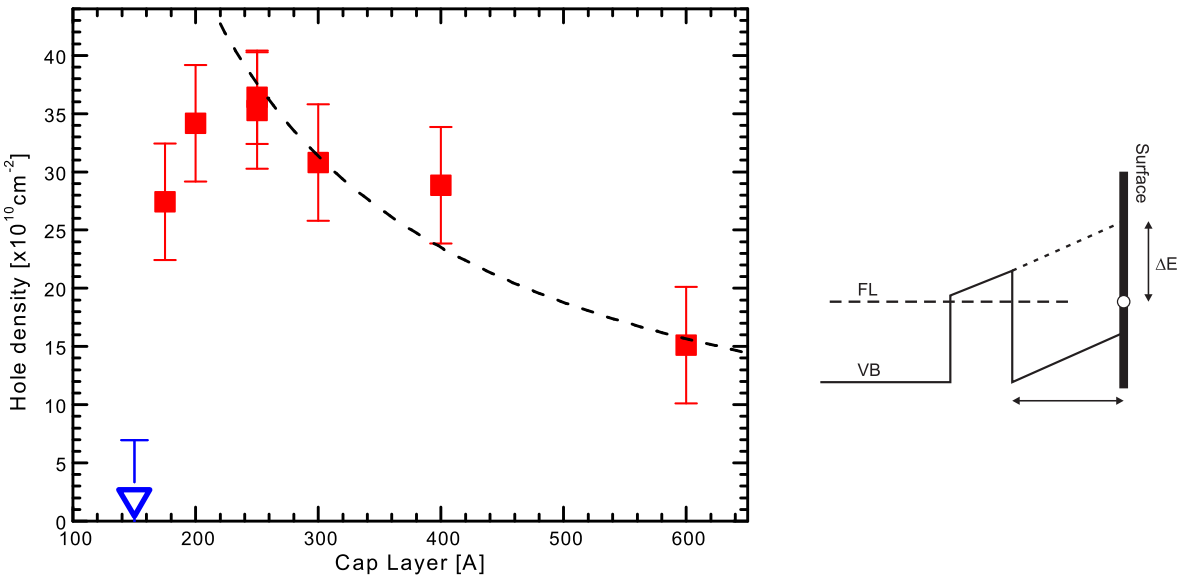

Figure 4.10: Hole density in 100 Å wide $Cd_{0.99}Mn_{0.01}Te$ QWs, determined from the Moss-Burstein shift at 1 T (circles) or from the charged exciton intensity (triangle, two samples). The dashed line is the density expected from surface acceptor states at energy $\Delta E = 170$meV from the QW state (model schematized on the right graph: FL–Fermi level, VB–Valence band, L–distance of the acceptor sheet from the QW.

series of samples, we used a thin layer of nitrogen doped barrier material, 1000 Å below the QW, to screen any spurious effect from the interface with the substrate. The structure followed the type A scheme (figure 4.2).

The hole density was deduced from the Moss-Burstein shift. For a better accuracy, the Moss-Burstein shift was measured at a magnetic field such that the carrier gas was fully polarized: Then the Moss-Burstein shift measured in σ^+ polarization is twice its value at zero field. Figure 4.9 presents a set of experimental spectra used for Moss-Burstein determination. Note the change in the reflectivity line shape with the cap layer thickness. It follows the rules stated by *Zheng et al.* (1988). The carrier density was calculated assuming an effective electron mass $m_e^* = 0.1m_0$, and an in-plane hole mass $m_h^* = 0.25m_0$ (*Fishman*, 1995; *Kossacki et al.*, 1999). The obtained value is then adjusted by the factor 1.5 determined by (*Kossacki et al.*, 2004*a*).

The hole gas density significantly increases when the thickness of the cap layer decreases from 600 to 250 Å (Fig. 4.10). This reinforces the idea that the origin of the hole gas is not linked to a residual doping of the material, but is due to the presence of electron traps (acceptors) on the surface. We can calculate the hole density expected in the QW assuming a high density of acceptor states on the surface, with the energy position of these surface states as the only adjustable parameter.

The hole density is mostly determined by the effect of the electric field between the QW and the surface - see the right panel in figure 4.10. Denoting by ΔE energy difference between the acceptor state and the the level confined in the QW (without electric field), the QW hole density simply writes:

$$p = \varepsilon\varepsilon_0 \frac{\Delta E}{eL}$$

where: ε – dielectric constant of the cap material (10 value was assumed),
ε_0 – the permittivity of vacuum,
e – electron charge,
L – thickness of the cap layer.

A good fit is obtained if we take $\Delta E = 170$ meV (dashed curve in figure. 4.10). A drop of the carrier density is observed on the samples with a very thin cap layer (below 200 Å). It is quite surprising as one would expect monotonous increase of concentration as the distance from the acceptors decreases. The experiments discussed in the following section imply that for the layers thinner than 25 nm the formation of electron traps can be more difficult. The possible interpretation comes from the better understanding of oxidation process. (*Bertolini*, 2004)

4.4 Surface states

Another way we have used to understand the mechanism of doping based on idea of preventing creation of the hole gas in the quantum well.

Since we knew already that doping is related to surface states we have tried to lower their energy, i.e to increase the ΔE. To achieve this we have grown sample (M1355) with 200 Å of usual (Cd,Mg)Te (18% of Mg) cap layer and additional 50 Å of (Cd,Mg)Te very rich in magnesium - 60% (despite the higher Mg content it remains lattice matched to the usual barrier material). The band gap of 60% (Cd,Mg)Te is 2.73 eV in comparison to 1.91 eV for 18%. Assuming that the surface state position is fixed relative to the valence band we expected a strong increase of ΔE and therefore more effectice charge transfer.

Obtained results show that in contradiction to our expectation hole gas concentration in the quantum well is only slightly larger ($3.65 \times 10^{11}\mathrm{cm}^{-2}$) than in sample M1333 with normal cap layer of 250Å thickess ($3.5 \times 10^{11}\mathrm{cm}^{-2}$). Although a bit disappointing, this result has important consequences as it proves that doping from the surface states is effective also for the barriers with high magnesium content.

4.4.1 Surface oxydation

We have no conclusive information on the nature of the surface centers involved in the formation of the acceptor states. The presence of acceptor states at the surface of $Cd_{1-x}Zn_xTe$ has been detected by surface photovoltage spectroscopy (*Yang et al.*, 2002) and attributed to the formation of TeO_2.

In order to control the formation of oxides on the $Cd_{1-y-z}Mg_yZn_zTe$ surface, a 50 Å thick layer of amorphous tellurium was deposited at –20 °C right after the growth. There were two pieces of the substrate in the MBE chamber during the growth process. This way it was possible to obtain two identical samples. A 50 Å layer of amorphous tellurium was grown on both of them. One sample was removed from the MBE chamber. The other one was heated to 240 °C for approximately 5 seconds in order to evaporate tellurium from the surface ant then removed from the MBE chamber. Results of measurements showed that when the tellurium layer prevented oxidation, we observed no significant hole concentration in the quantum well. As for the sample with removed tellurium layer the results were corresponding to the previously obtained for such cap layer thickness (250 Å): hole concentration was $3.5 \times 10^{11} cm^{-2}$. The only difference, with respect to the normal samples, was a broadening of the line.

The characterization was repeated after 2.5 years. Moss-Burstein shift measurements indicated similar hole gas density in both of the samples (above $3 \times 10^{11} cm^{-2}$). A possible explanation lies in instability of the amorphous tellurium layer. It could have been separated during cryogenic measurement cycles or it could have slowly evaporated over the long period of time or simply, it oxidized with time.

An extensive study of the formation of surface electron traps was described by Mikaël. Bertolini in his Ph.D. thesis (*Bertolini*, 2004). The experiments confirmed essential role of oxygen in formation of electron traps on the surface. Samples were exposed to the pure oxygen in

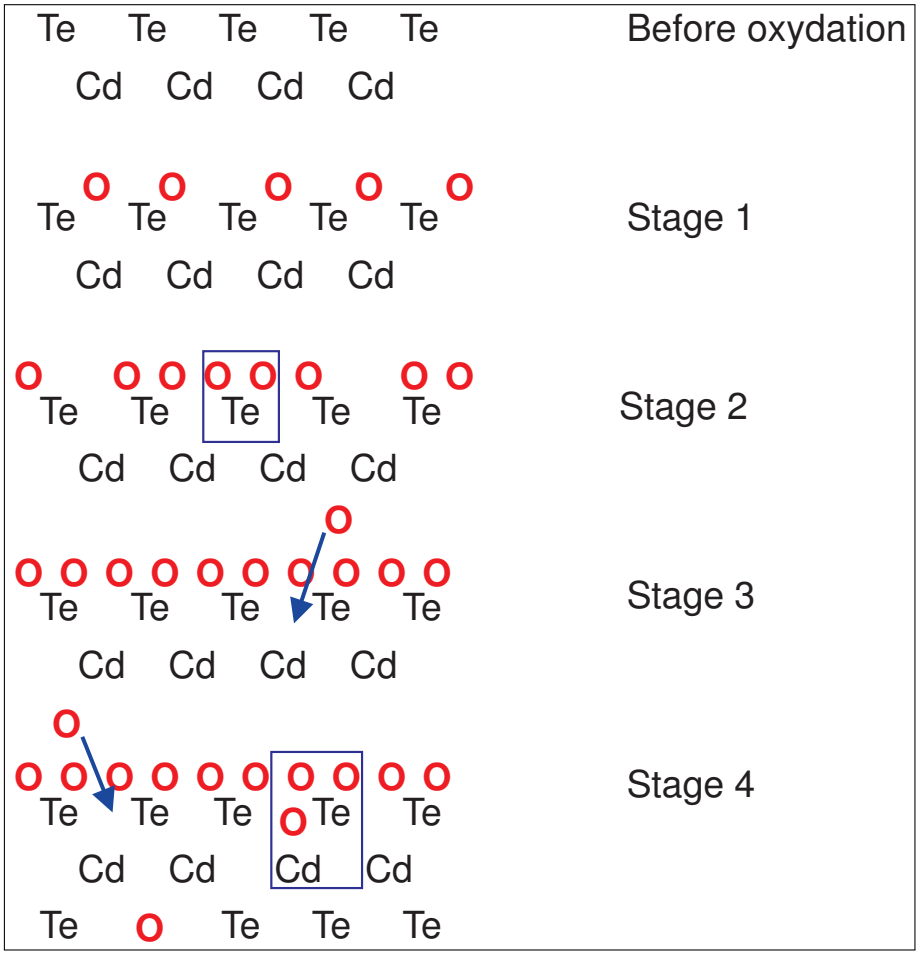

Figure 4.11: Schematic idea of oxidation mechanism for samples with cap layer thicker than 25nm.
Stage 1 Initial phase of oxidation.
Stage 2 the surface is tellurium finished the formation of TeO_2 begins. The quantity of oxygen built into the structure reaches equivalent of 1.5 monolayers.
Stage 3 Saturation with oxygen is so high that it starts to penetrate into the sample.
Stage 4 The $CdTeO_3$ complexes are formed ($CdTeO_3$ is energetically favorable to TeO_2) the system becomes stable and eventually stops absorbing oxygene. The quantity of absorbed oxygen then corresponds to the formation of 2 monolayers of TeO_2 in the vicinity of sample surface.

controlled conditions. The composition of barriers was monitored by the *X-Ray Photoemission Spectroscopy* (XPS) in situ during oxydation. The experiments allowed to estimate the time required for the formation of the oxides: under exposition to oxygen at normal pressure the concentration of TeO_2 reached a saturation after 11 hours. The proposed mechanism of oxidation is presented and explained in figure 4.11 It assigns a crucial role in formation of surface acceptors to $CdTeO_3$ complexes. The experiments were performed both on the ternary (Cd,Mg)Te and quaternary (Cd,Mg,Zn)Te alloys with similar results. This confirms previous spectroscopic observations, where no difference was found between the two alloys in formation of surface traps.

4.4.2 Surface morphology

(a) Cap Layer 150Å **(b)** Cap Layer 250Å

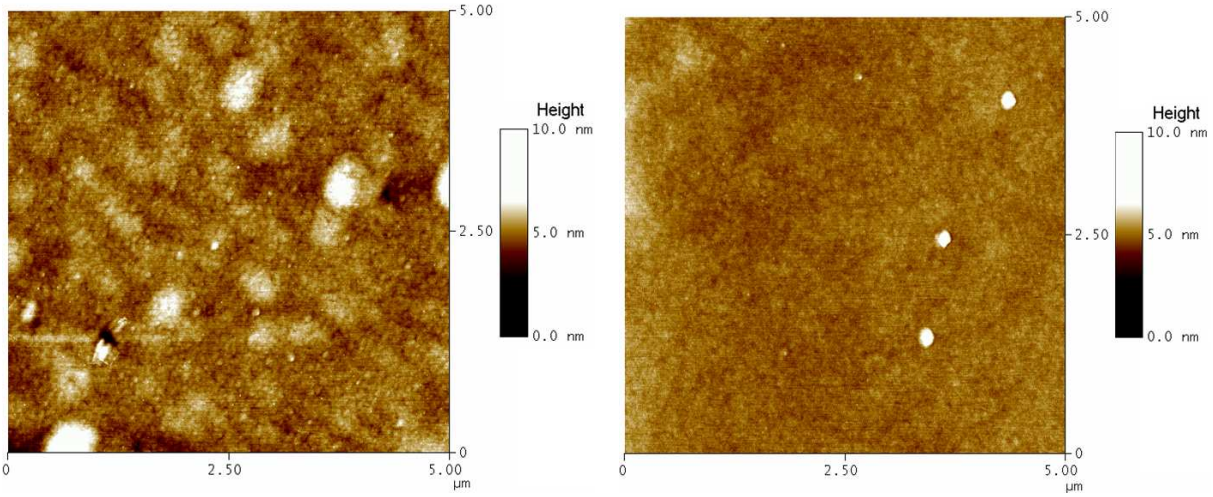

Figure 4.12: AFM images of the surface for the samples with 150 Å and 250 Åcap layers. The scanned area is $5 \times 5\mu\text{m}^2$. The color scales are the same for both pictures.

Understanding of the oxidation process allowed us to interpret the sudden decrease of hole gas density for cap layer thicknesses smaller than 250 Å (as seen in figure 4.10). First hints came from the *Atomic Force Microscopy* (*AFM*) studies of the surface morphology. Maps of the surface obtained by AFM are shown in figure 4.12. The differences in the surface morphology are easy to see: the surface of the sample with 250 Å cap layer is smooth in comparison to the one with 150 Å. As the structures of the samples are identical, differing only in the cap layer thickness. Both samples were grown on the different parts of the same substrate ($Cd_{0.88}Zn_{0.12}Te$) piece. Therefore, the observed differences of the surface morphology are certainly due to the differences in the oxidation processes. The differences in the oxidation process were studied by the *Ultra-violet Photoelectron Spectroscopy* (UPS) measurements of the line attributed to Cd in *4d* electron configuration (*Bertolini*, 2004). During the oxidation of sample with 250 Å cap layer the intensity of this peak increases and the line is broadened which implies that the nearest neighborhood of Cd ions becomes altered. The changes of the crystal structure are probably due to the formation of the $CdTeO_3$. For the sample with 150 Å cap layer the changes to the Cd *4d* line in UPS spectra was negligibly small suggesting that $CdTeO_3$ complexes are scarce.

4.4.3 The effect of the lattice mismatch

A special set of samples has been designed. The samples structures are presented in the table 4.1. The lattice parameters grouped in table 4.2 are essential in the mismatch analysis.

It is convenient to consider lattice mismatch parameter f defined for both interfaces of the quantum well: $f_s = \frac{a_{qw}-a_s}{a_s}$ for substrate/quantum well interface and $f_{qw} = \frac{a_{cap}-a_{qw}}{a_{qw}}$ for quantum well/cap interface, where a_{qw}, a_s and a_{cap} are unstrained bulk lattice parameters of quantum well, substrate and cap material respectively. The lattice mismatch parameter values are collected in Table 4.3.

The photoluminescence and reflectivity experiments confirmed the presence of significant concentration of hole gas in the quantum wells of concerned samples. Concentrations determined from the high field splitting are also presented in the Table 4.3. They are also compared to the previously obtained data in figure 4.13.

For the samples M1535 and M1537 the obtained hole densities are comparable to those obtained for thicker cap layers. The slightly smaller concentration of holes in the sample M1536 may be the consequence of the presence of zinc in the quantum well. The presence of zinc increases the bandgap of the quantum well and thus makes the quantum well less deep affecting the transfer of holes from the surface.

The Mismatch values of samples M1535 and M1537 are identical at substrate/quantum well interface, whereas they differ significantly at quantum well/cap interface. Since the carrier concentrations in both samples are the same, we conclude that main influence of lattice mismatch on carrier density comes from substrate/quantum well interface. In order to determine the detailed mechanism of this influence, further studies are necessary. In particular, any relation between the mismatch and oxidation process should be examined.

	M1345*	**M1535**	**M1536**	**M1537**
Substrate $Cd_{1-x}Zn_xTe$	12%	4%	4%	4%
Buffer 3000Å	see A.3	CdTe	CdTe	CdTe
Barrier 2000Å	$Cd_{1-z-y}Zn_zMg_yTe$ z=8% y=22%	$Cd_{1-y}Mg_yTe$ y=27%	$Cd_{1-y}Mg_yTe$ y=27%	$Cd_{1-y}Mg_yTe$ y=27%
Quantum Well 100Å	$Cd_{1-x}Mn_xTe$ x=1.6%	$Cd_{1-x}Mn_xTe$ x=1.4%	$Cd_{1-z-x}Zn_zMn_xTe$ z=4% x=1.4%	$Cd_{1-x}Mn_xTe$ x=1.4%
Cap Layer 150Å	$Cd_{1-z-y}Zn_zMg_yTe$ z=8% y=22%	$Cd_{1-y}Mg_yTe$ y=27%	$Cd_{1-y}Mg_yTe$ y=27%	$Cd_{1-z-y}Zn_zMg_yTe$ z=4% y=27%

Table 4.1: The structure of the samples designed to investigate the strain effects on the hole concentration. The sample M1345 is described in more detail in appendix A in tableA.3. In this table the main features of M1345 sample are shown for comparison: the barrier and the buffer are of different thicknesses.

Lattice parameter [Å]				
	M1345	**M1535**	**M1536**	**M1537**
Substrate	6.436	6.462	6.462	6.462
Buffer	6.436	6.481	6.481	6.481
Barrier	6.434	6.463	6.463	6.463
Quantum Well	6.481	6.481	6.464	6.481
Cap Layer	6.434	6.463	6.463	6.448

Table 4.2: Unstrained lattice parameters. Values were obtained from formulas described in 2.1.1 basing on the spectroscopic information on the actual composition of the alloys.

	M1345	M1535	M1536	M1537
f_{qw} (10^{-3})	-7.25	-2.48	-0.46	-4.81
f_s (10^{-3})	6.68	2.63	0.62	2.63
Hole density p $(10^{11}\mathrm{cm}^{-2})$	< 0.1	$3.4 \pm .5$	$2.8 \pm .5$	$3.5 \pm .5$

Table 4.3: Obtained results for the samples with engineered strain in the quantum well and the cap layer 150 Å.

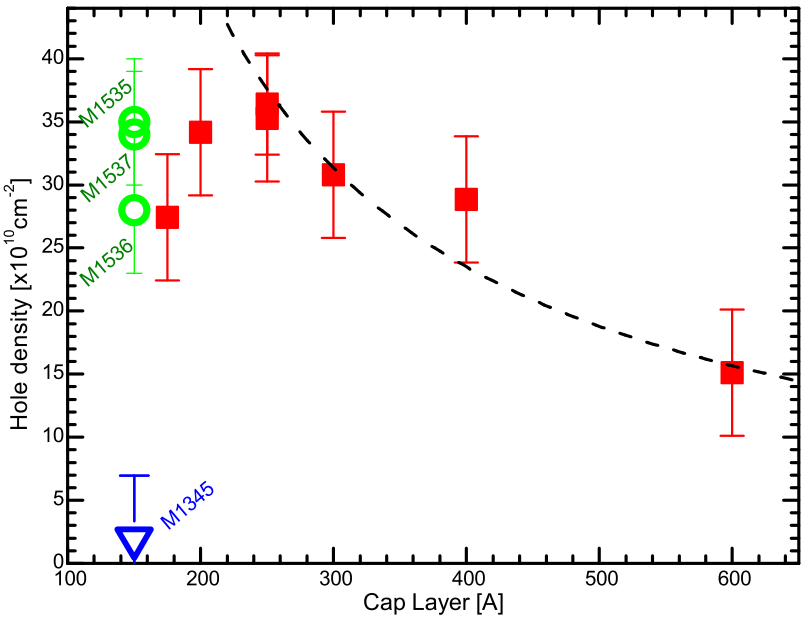

Figure 4.13: Hole density in 100 Å wide $Cd_{0.99}Mn_{0.01}Te$ QWs, determined from the Moss-Burstein shift at 1 T (circles) or from the charged exciton intensity (triangle, two samples), or the PL line splitting at 1T for samples with 150 Åcap layer and the engineered strain marked with circles.

4.5 The influence of light on the carrier density

4.5.1 Known methods of optical carrier density control

Most of the results presented in this work were obtained from optical experiments. Therefore it is important to understand whether the light used as a probe of the properties of the sample may influence significantly its state. Such sensitivity to the light is very often observed in heterostructures. The most pronounced effects of illumination are the changes of the carrier density. Depending on the considered sample structure the light can either increase or decrease the carrier density. Both cases can be exploited to broaden the experimental possibilities of studying the carrier induced effects.

In semimagnetic heterojunctions made of III-V semiconductors studied by *Koshihara et al.* (1997) the light was used to increase the hole gas concentration. In this case photo-created hole density was the necessary condition for the observation of ferromagnetic ordering.

Similar effects are used to study carrier related phenomena in samples containing the double asymmetric quantum well layout (two quantum wells of different widths separated by a thin barrier) (*Paganotto et al.*, 1998; *Klopotowski et al.*, 2004). In this case the photo-generated carriers in the narrower quantum well are tunneling into the wider one. Due to the difference in the masses of holes and electrons affecting the tunneling probability, it was possible to obtain an excess electron concentration (*Siviniant et al.*, 1999). The obtained excess electron density strongly depends on the illumination intensity and energy, the change of one of parameters immediately causes the changes in the hole density.

In the structures containing a single CdTe/(Cd,Zn,Mg)Te modulation n-doped (iodine or aluminium donors) quantum well, blue laser light was found to decrease (*Huard et al.*, 2000*a*,*b*) the electron density inside quantum well. The ability to tune the hole gas density was then applied in studies of negatively charged excitons. On the other hand, in similar structures, illumination with blue light was found to either decrease or increase the electron concentration in the quantum well (*Kutrowski*, 2001). Whether the light increased or decreased the carrier concentration was dependent on the thickness of the doping layer embedded in the structure.

An extensive study was also performed on the p-type (Cd,Mn)Te/(Cd,Mg)Te quantum wells by *Kossacki et al.* (1999). The nitrogen acceptor layer was placed 200 Å from the quantum well and the obtained hole concentration in the quantum well was 2.4×10^{11} cm^{-2} (see figure 4.14). As the structure of the sample studied in that paper closely resembles the structure of surface doped samples we shall recall at the results described therein.

The experimental techniques applied there were identical to those used in the present work. They were based on the transmission and photoluminescence studies. The hole gas density was determined from Moss-Burstein shift measurements. It was found that the blue light of the photon energy larger than the band gap of the barrier material can decrease the hole gas density in the quantum well. For experimental purposes the halogen lamp with appropriate blue filter and controlled power was used. The mechanism responsible for the decrease of carrier population inside quantum well was described as photoneutralization. In this model (see figure 4.15) the absorbed blue light generates in the barriers an electron and the hole. Due to the electric field

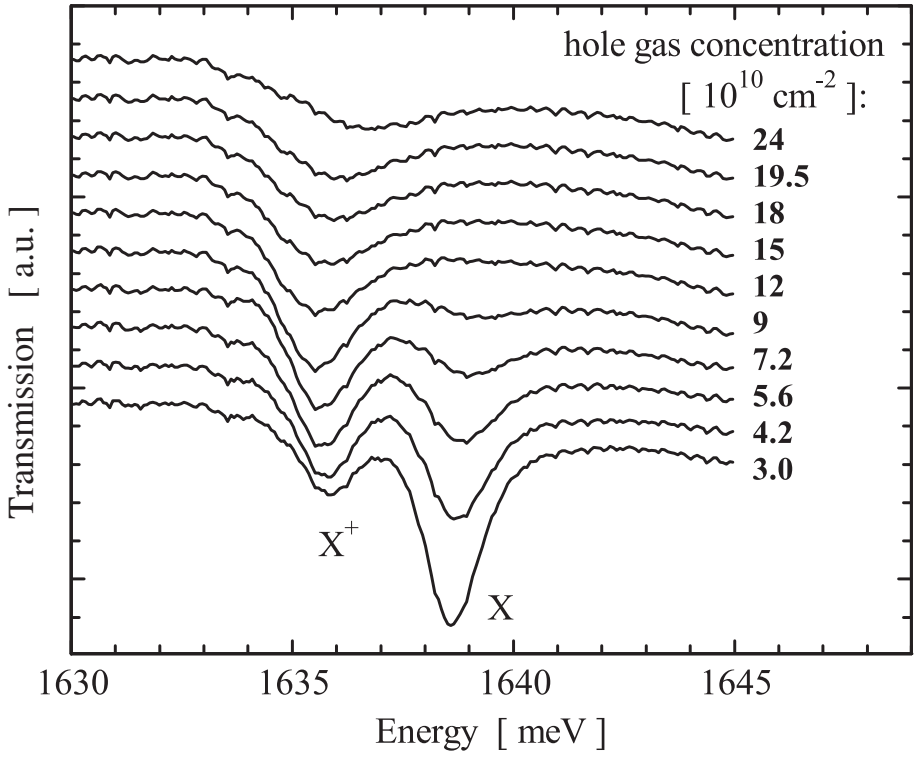

Figure 4.14: Transmission spectra at various hole gas densities. The density values were obtained from Moss-Burstein shift (*Kossacki et al.*, 1999),and suitably calibrated according to (*Kossacki et al.*, 2004*a*).

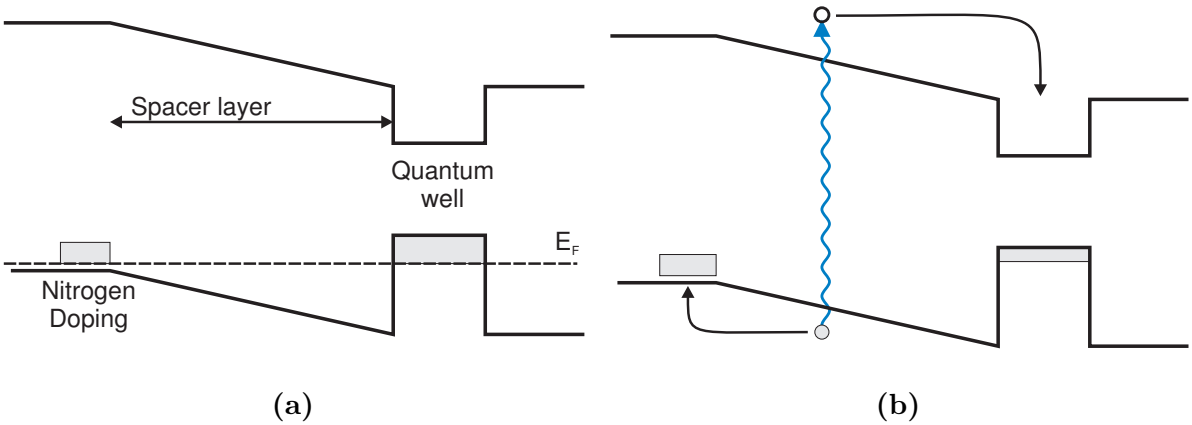

Figure 4.15: The mechanism of photoneutralization of hole gas in the quantum well. **(a)** Equilibrium state (before illumination). **(b)** Steady state under illumination: photo-generated electrons in the conduction band migrate into the quantum well and recombine, holes return to the quantum well via the acceptor sites by a tunnelling proceses.

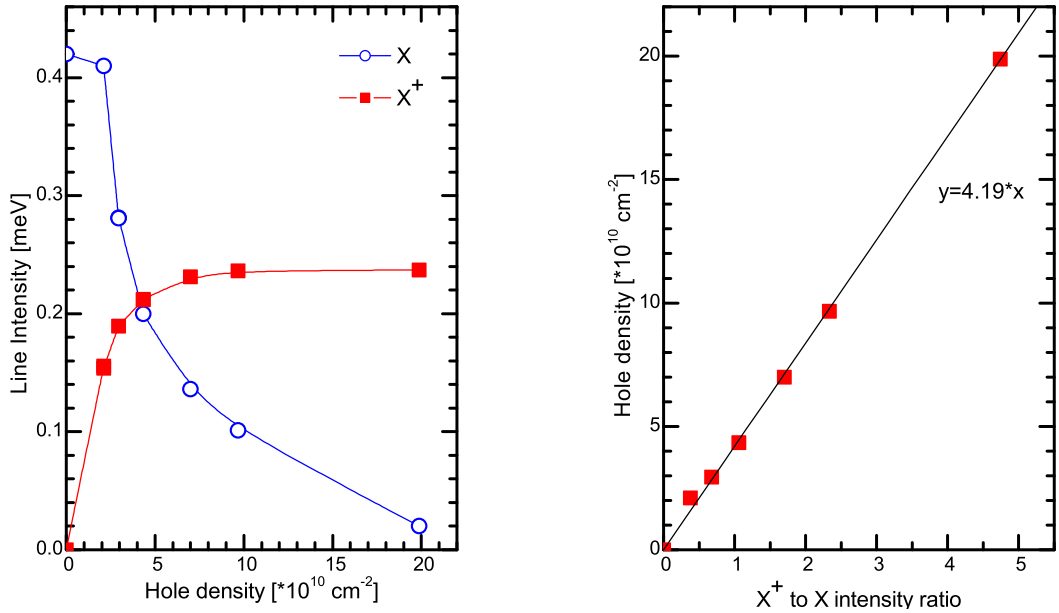

Figure 4.16: **(a)** Neutral and charged exciton integrated absorption line intensities for the spectra presented in figure 4.14 after *Kossacki et al.* (1999). **(b)** Hole gas density as a function of charged to neutral exciton intensity ratio computed for the data presented on panel (a).

present in the spacer layer the electrons quickly migrate into the quantum well. Then the electron recombines with a hole inside the quantum well. The hole photo-generated in the barrier migrates into the doped area. Moreover, the potential shape forms a barrier for holes therefore, the transfer of the hole back to the quantum well is possible as a result of tunneling. Due to the high mass of the hole the probability of tunneling is small and thus the time required for the return of the hole to the quantum well is much longer than the time required by the electron to arrive into quantum well and to recombine there (due to the lack of potential barrier for electrons). Under constant illumination a dynamic equilibrium is achieved with reduced hole density in the quantum well. The resulting hole density depends on the intensity of the illumination and on the ratio of the time required by the electron to diffuse into quantum well and to recombine there to the time necessary for the photo-created hole to reach the quantum well through the acceptor sites and the tunneling (*Kossacki*, 1998; *Haury et al.*, 1997; *Shields et al.*, 1995).

Figure 4.14 presents a set of transmission spectra obtained for different power of blue light illumination (after *Kossacki et al.* (1999)). The changes of absorption intensity are well visible for both charged and neutral excitons. The values of integrated intensities corresponding to the absorption spectra are presented in figure 4.16(a) after *Kossacki et al.* (1999). They follow general tendencies: the intensity od neutral exciton transition decreases while that of the charged one increases with the increase of hole gas density. However the absolute values of line intensities in transmission depend on the structure of the sample, particularly on the thickness of the cap layer, due to the interference effects. Therefore it is better to use the ratio of integrated intensities as a sample independent measure of hole gas density. This approach is shown in figure 4.16(b) where we were able to establish the relation between the intensities of neutral and charged exciton lines determined by *Kossacki et al.* (1999) and the independently determined hole gas density (from Moss-Burstein shift). The dependence can be described by a straight line.

4.5.2 Transmission measurement under illumination

For detailed experiments on the surface doped samples, sample M1333 was chosen. The 10 nm wide quantum well was placed 25 nm below the surface, which gives the maximum hole density. An additional nitrogen doped layer was placed between the quantum well and the substrate, at distance of 100 nm from the quantum well. Such a large distance of the doped layer makes the hole gas transfer from the nitrogen acceptors to the quantum well very small. Its purpose is to screen the quantum well from any possible charge transfer from sources different than the surface states. The Moss-Burstein shift measurements yielded hole gas density of $3 * 10^{11}\mathrm{cm}^{-2}$ in the quantum well.

The experimental setup was configured as in figure 3.1. The arrangement was similar to the one used by *Kossacki et al.* (1999). The light used for transmission measurement was directed from the back side of the sample. The thick $Cd_{0.88}Zn_{0.12}Te$ substrate acts as a high pass spectral filter, absorbing all of the light below 745 nm wavelength preventing heating of the quantum well by the transmitted light. Additionally it prevented absorption by the barrier material (which has a significantly larger band-gap), thus we expected that the transmitted light would not affect the carrier density.

The additional illumination provided by the tungsten lamp was applied on the side of the sample with the heterostructure (see experimental setup in figure 3.1). In an initial attempt we tried to reduce the carrier density by illuminating the sample with the blue light. Although we used the spectral range providing good results on the nitrogen doped samples there were no detectable changes in the transmission spectra. However, the similarity of structure types encouraged further investigations.

In order to check weather the impact of the light on carrier density in the case of surface doping has a different spectral response than in the previously studied case, the experimental setup was modified. The illumination line was modified in order to replace spectral filters by a monochromator (experimental setup presented in figure 3.2). We have used a short unit with a rotating prism. The slits were set to optimize the amount of transmitted light and provided a beam of 3 nm spectral width. For different illumination wavelengths, ranging from the 750 nm to 460 nm, transmission spectra were recorded. The sample temperature was set to 1.7K. The results are presented in figures 4.17 and 4.18. For illumination light at wavelength between 750 nm and 615 nm there seems to be no effect on the transmission spectra. When the illumination wavelength is further decreased below 610 nm a second line appears in the optical density spectra. It has been identified as a neutral exciton transition in further magneto-spectroscopic experiments described in section 4.2. After an initial rise, the neutral exciton intensity reaches a maximum at about 590 nm, and then exhibits a slow decrease. The change of neutral exciton line intensity is accompanied by small changes of charged exciton intensity and a change of charged exciton dissociation energy[4] – typical effects associated with the variation of hole gas density (*Kossacki et al.*, 1999).

Only a part of the studied range of the hole gas density lies in the area where the excitonic transition is pronounced. This is most unfortunate as we would like to analyze changes of hole gas

[4]Charged exciton dissociation energy observed in absorption is different from the true binding energy as determined in *Kossacki et al.* (2004*a*)

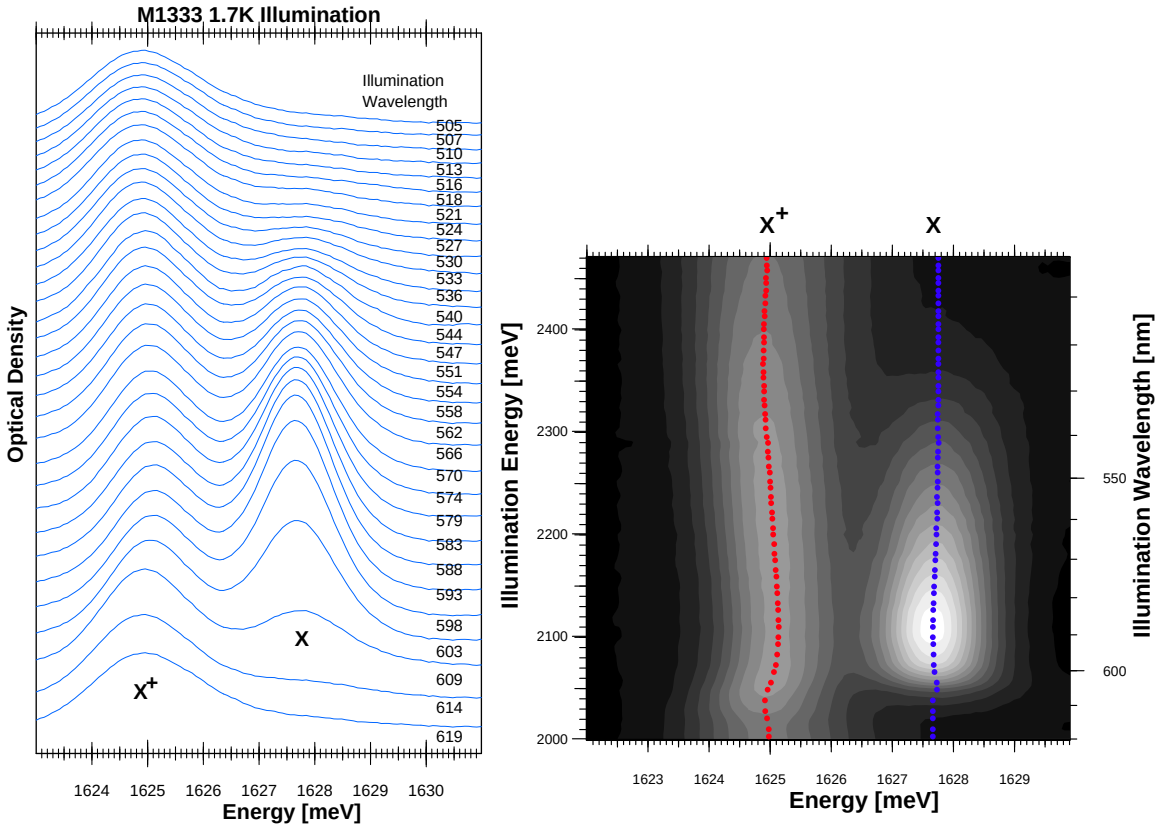

Figure 4.17: The effect of the illumination on the surface doped sample M1333. (a) Optical density spectra. ($-\mathrm{Log}[Transmission]$) (b) Map of optical density intensity with marked line positions obtained from fitting. The illumination range is zoomed in(with respect to left panel) in order to emphasize the changes in optical density.

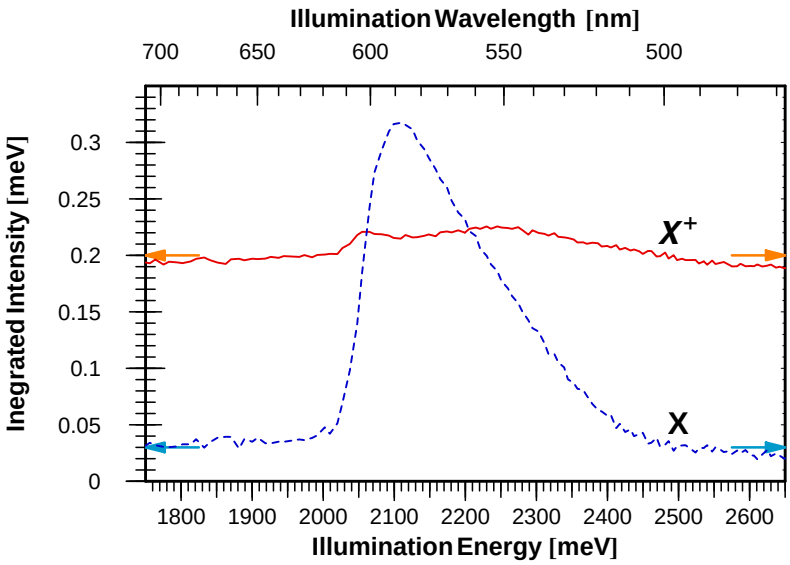

Figure 4.18: Integrated intensities of optical transitions present in the transmission as a function of illumination photon energy. Solid line denotes intensity of charged exciton, dashed one denotes intensity of exciton.

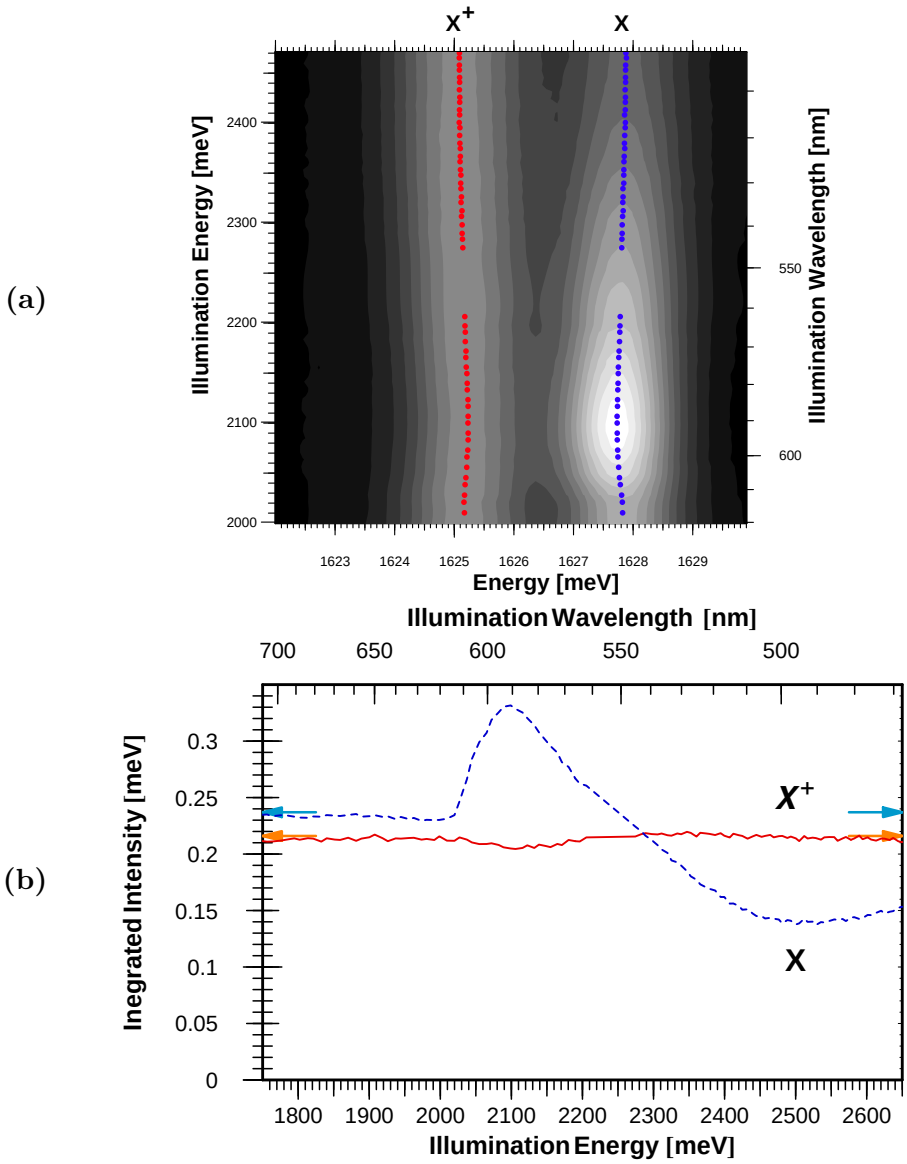

Figure 4.19: The effect of the illumination on the surface doped sample M1333 with additional optical bias (illumination 590nm of moderate power). (a) Map of optical density intensity with marked line positions obtained from fitting. (b)Integrated intensities of optical transitions present in the transmission as a function of illumination photon energy. Solid line denotes intensity of charged exciton, dashed one denotes intensity of exciton.

density through the intensity ratio of both transitions. Therefore for the purpose of increasing the sensitivity of experiment an additional optical bias was applied in order to reduce the initial density of hole gas present in the quantum well. It was achieved by adding to the setup another illumination line (in the configuration shown in figure 3.1). Now there were two of them: one of tunable wavelength with monochromator and the second line with fixed wavelength determined by a narrow bandpass (interference) spectral filter of 590 nm center wavelength. The 590 nm wavelength was chosen due to the maximal efficiency of the quantum well depletion as seen in figure 4.18. The intensity of orange (590 nm) light illumination was tuned ensuring that both excitonic transitions were observed (and pronounced) for the whole range of illumination wavelengths provided by the monochromator. It can be seen in figure 4.19. The initial hole gas density in case of this measurement was reduced to $3.8 * 10^{10}\mathrm{cm}^{-2}$ as determined from the intensities of charged and neutral transitions. The results of the measurements with two illuminations are presented on figure 4.19. Apparently the additional illumination not only enhanced the sensitivity of experiment, but it also allowed us to observe additional processes occurring for illumination with higher photon energies.

The intensities of neutral and charged excitons were converted into the hole gas density accordingly to dependence defined in figure 4.16(b). The results are presented in figure 4.20. Apparently, the strong changes of neutral exciton intensity seen in the experiment with optical bias (as seen in figure 4.19) do not result in high variation of absolute hole gas density when compared to the unbiased case. However, the experimental results obtained without bias for high hole densities exhibit significant noise. This is the result of worse determination of line intensities when neutral exciton transition is weak. In this range of carrier density we are close to the limit of applicability of the relation defined in figure 4.16(b). The lowering of initial carrier density by additional bias improves the accuracy.

In order to compare the biased and unbiased experiments it is more convenient to discuss the changes of hole gas density with respect to their initial values. In the experiment without bias we can consider as an initial value the hole density before any illumination. In biased case we take for the initial value the hole gas density with only bias illumination applied (values marked by arrows in figure 4.20). The values of the hole density variations are presented in figure 4.21.

For the unbiased experiment the most pronounced feature is the drop of hole gas density. It is still visible in experiment with bias although it is less spectacular. The effective reduction of hole gas density starts for the illumination photon energy higher than 2010 meV. This critical energy for depletion is related to the bandgap of barrier material. It can be seen in the inset in figure 4.21 where the PL spectra of barriers is presented with the same energy scale as the main graph. The small shift (about 10 meV with respect to the lower peak of PL from the barrier[5]) of the threshold towards the higher energies is probably the result of Stokes shift between absorption and photoluminescence in the barriers.

In both cases the depletion reaches a maximum at 2100 meV. Apparently in both experiments we have achieved almost the same minimal hole gas density. It was 2.5×10^{10} cm^{-2} with bias and 3×10^{10} cm^{-2} without. This indicates that additional bias power was very close to the power of light passing through the monochromator. Only a small reduction of hole density for

[5]Double line of the barrier photoluminescence is caused by the presence of the nitrogen doped screening layer in the sample.

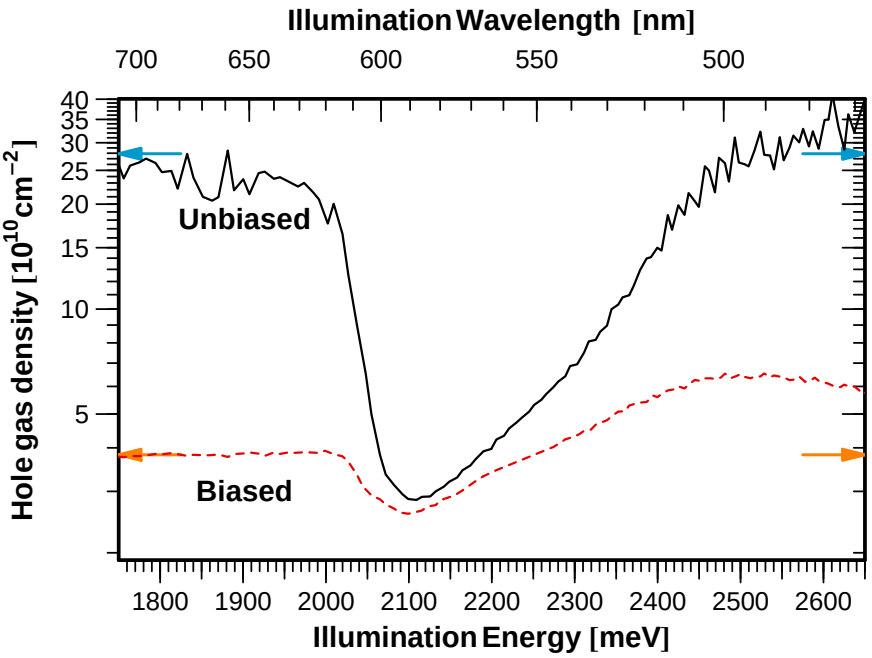

Figure 4.20: Hole gas density determined from ratio of charged to neutral exciton oscillator strength as a function of illumination photon energy. Solid line denotes results for the single illumination experiment, dashed line presents results for the experiment with 590 nm illumination bias. The vertical scale is logarithmic.

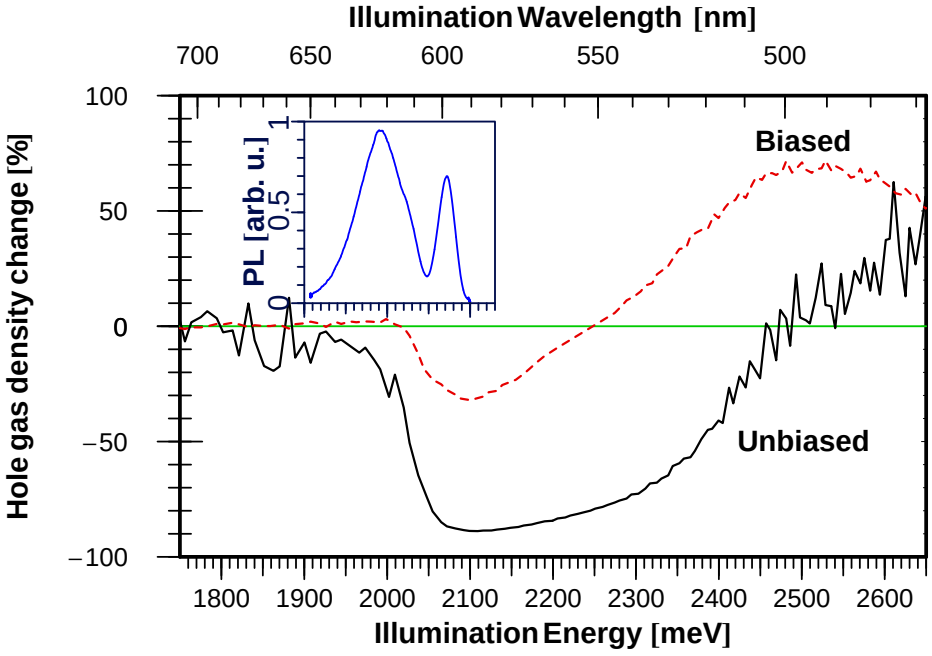

Figure 4.21: Dependence of hole gas density change on the illumination photon energy. Continuous line denotes results for the single illumination experiment, dashed line presents results for the experiment with 590nm illumination bias. The inset presents photoluminescence spectra from the barriers under ion Ar Laser excitation - the photon energy scale is the same as for the main plot.

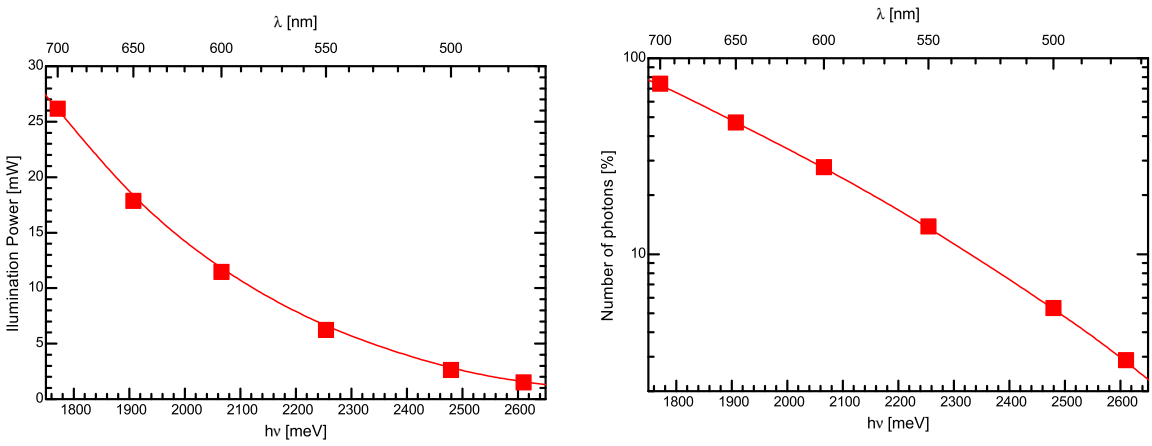

Figure 4.22: **(a)** Measured power of additional illumination versus photon energy. The detector was placed before the cryostat window. **(b)** Computed change of number of photons reaching the surface plotted in semi logarithmic scale.

almost doubled power of light indicates that we approached the maximal efficiency of depletion with illumination. The effect of illumination power (at constant wavelength) was analyzed by *Kossacki et al.* (1999) and similar effects are reported under strong illumination.

After reaching the minimal value the concentration increases for the increasing photon energies. One could expect it as a natural consequence of the decrease of illumination power due to the transmission characteristic of the applied monochromator and the spectral characteristic of the light emitted by the tungsten bulb used in the experiment. The measured spectral dependence of illumination power reaching the sample surface can be seen in figure 4.22.

Even if we know the spectral dependence of illuminating light power it is not possible to accurately adjust the obtained experimental results since for the discussed processes the most important is the actual number of absorbed photons. In this experiment we can only analyze the number of photon reaching the surface of the sample. For detailed analysis we lack information on the decrease of photon penetration length in semiconductor which is associated with increase of the photon energy far above the energy gap of the barrier material. The spatial dependence of the absorbed light is probably crucial due to the fact that the source of the hole gas is placed only on one side of the quantum well.. There are several features in figure 4.21 indicating that such a simple explanation is insufficient.

First for both experimental curves the rise of hole density for high illumination photon energies surpasses the initial hole density. Secondly, the rise of hole gas density is much steeper for the sample with additional bias despite the fact that the changes of illuminating light power are the same for both curves. In my opinion, the effect of power is probably dominating only in the range between 2100 meV and 2250 meV in unbiased experiment because for the 50% decrease of illumination power we have only 10% rise of hole gas density: this is comparable to the results of *Kossacki et al.* (1999) for variation of illumination power at constant wavelength.

Steep slope of hole gas density change for both curves at photon energies higher than 2300 meV is a result of competition between the depletion mechanism and another mechanism leading

to the increase of hole gas density. For high photon energies the increase of hole gas density is favored.

The additional optical bias besides reducing the initial hole gas density in the quantum well also significantly affects the spectral response to the illumination. This might result from the difference of efficiency of the two competing effects which saturate differently. The maximal depletion is achieved at the same illumination wavelength as without bias but the depletion mechanism was neutralized for much smaller photon energies (2250 meV). Further increase of photon energy results in actual increase of hole gas density beyond initial value. The increase reaches maximum of 70% at 2480 meV (at this point in the unbiased experiment the hole gas density is restored to its initial value), note that the illumination power was the only fourth part of the power at 2100 meV illumination (maximum of depletion). The saturation of increase is probably caused by the significant decrease of the illumination power as compared to the initial bias. For the unbiased experiment even such small intensity turns out sufficient to increase the hole density above the initial value, as in this case the depletion mechanism is not aided by additional light.

4.5.3 Carrier control mechanism in surface doped samples

The decrease of the hole gas density is possible only for the illumination with photons of higher energy than the energy band gap of the barrier material. Such behavior is in agreement with the discussion and the model used for the nitrogen doped samples by *Kossacki et al.* (1999). Since the origin of the hole gas is attributed to the acceptor surface states the schematic picture of the photo-neutralization is modified and presented in figure 4.23. The input of the screening layer to this processes is negligible as it is too distant from the quantum well. That has been confirmed by the observations of the time necessary to return to the nominal hole gas density after shutting down the additional illumination depleting the quantum well. For the studied sample (M1333) it was relatively quick, as the change from depleted to nominal concentration occurred in time shorter than 1s. For the samples with thicker cap layers this time is significantly elongated to about 2s at 400 Å cap and about 5s in the case of 600 Å cap layer.

The understanding of the mechanism responsible for increasing of the hole gas density by high energy photons is more difficult. One possibility is a decrease of the electron trapping efficiency by the quantum well for high energy electrons, combined with an enhancement of the hole tunneling probability at high kinetic energies. The high energy electrons penetrate deep in the sample while the holes tunnel into the quantum well. When the photocreated electron penetrates deep into the sample structure, it has to pass over the barrier of nitrogen acceptors in the screening layer, present in the discussed case. The idea of the proposed mechanism is presented in figure 4.24.

The lowering of the threshold energy for this process when optical bias is applied may result from the altered balance between the two competing effects: one increasing hole density and the second depleting it. This may happen because the depletion and decrease mechanisms most likely saturate differently.

One may expect that the absence of the nitrogen doping layer may strengthen the effects enhancing the hole density increase under blue illumination due to the lack of any potential

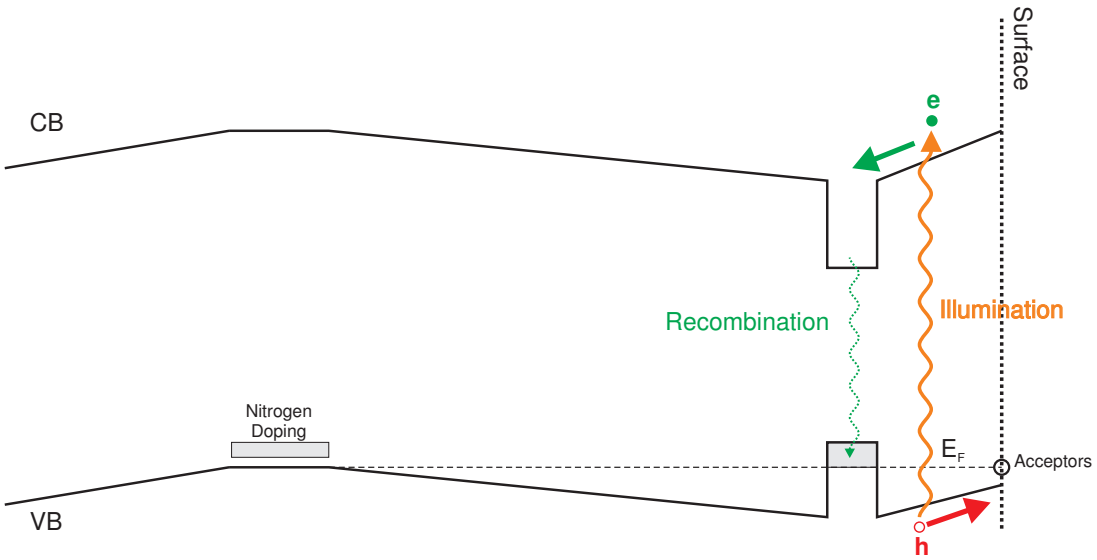

Figure 4.23: The mechanism of photoneutralization of hole gas in the quantum well close to the surface. During illumination photo-generated electrons in the conduction band migrate into the quantum well and recombine, hole returns to the quantum well via the acceptor sites on the surface and the tunnelling process. The distances between the nitrogen doping, quantum well and the surface are in the same proportions as in the M1333 sample.

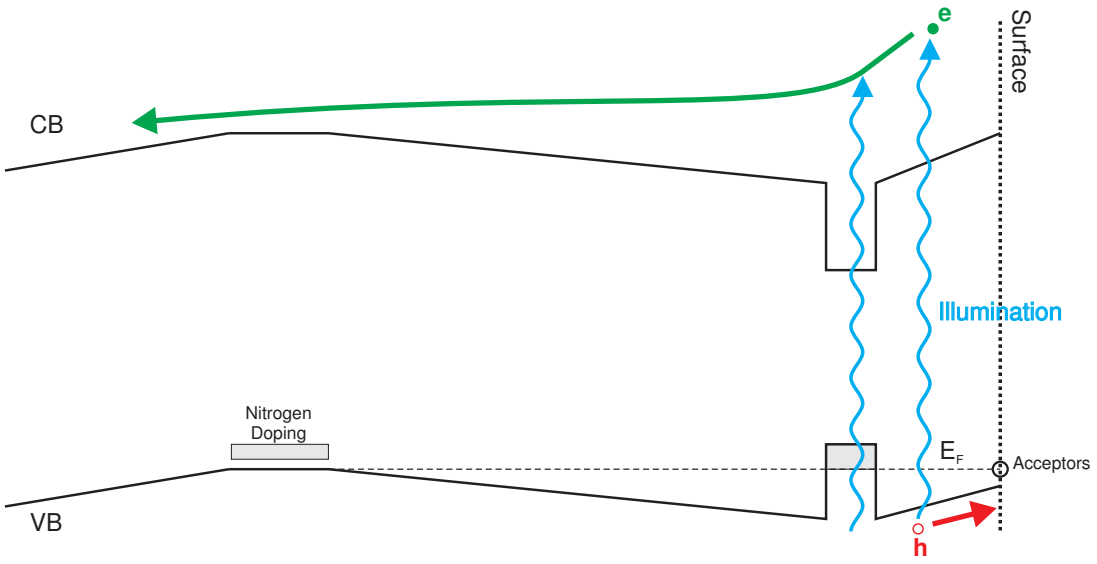

Figure 4.24: The mechanism of increase of hole gas density in the quantum well doped from the surface. The additional photon energy is necessary for photocreated electron in the conduction band to pass over the barrier of nitrogen acceptors and penetrate deep into the sample structure, while the hole gas remains in the vicinity of the quantum well.

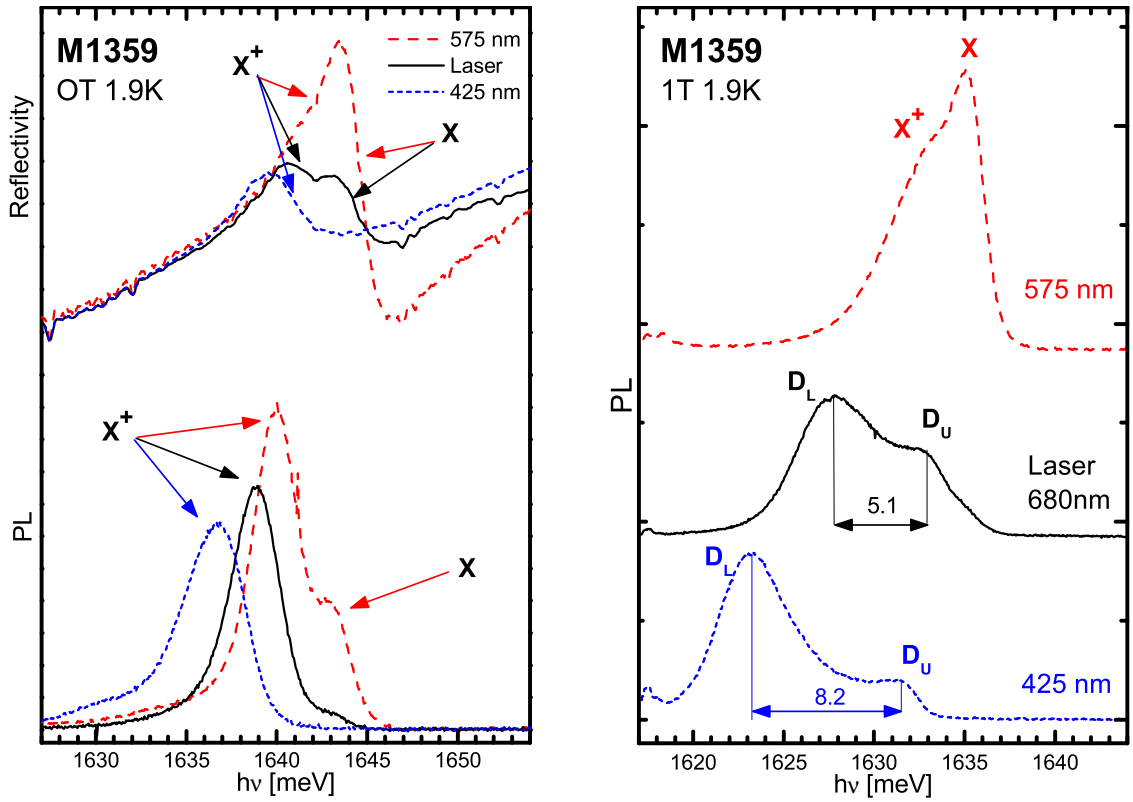

Figure 4.25: PL and reflectivity spectra for sample M1359 at various hole gas densities. The changes of hole gas density were obtained by additional illumination. Without illumination (solid, black line) the density was $24 \times 10^{10}\text{cm}^{-2}$. Orange (575 nm) light (dashed red line) depleted hole gas to density below $1 \times 10^{10}\text{cm}^{-2}$. Blue (425nm) illumination increased hole gas density to $45 \times 10^{10}\text{cm}^{-2}$. **(a)** Measurements at 0T magnetic field. Although the changes of PL line position due to the change of hole density are clear, it is difficult to determine the hole density from the Moss-Burstein shift due to the complicated shape of reflectivity lines. **(b)** PL measurements at 1T. For high hole gas densities the triplet line splitting can be used for determination of hole gas density. The presence of both neutral and charged exciton lines in PL from depleted quantum well confirms low hole gas density.

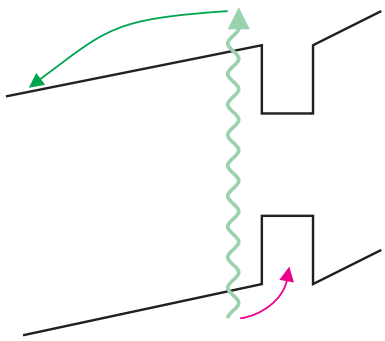

Figure 4.26: The schematics of an enhancement of hole gas density increase mechanism in surface doped samples without nitrogen screening layer.

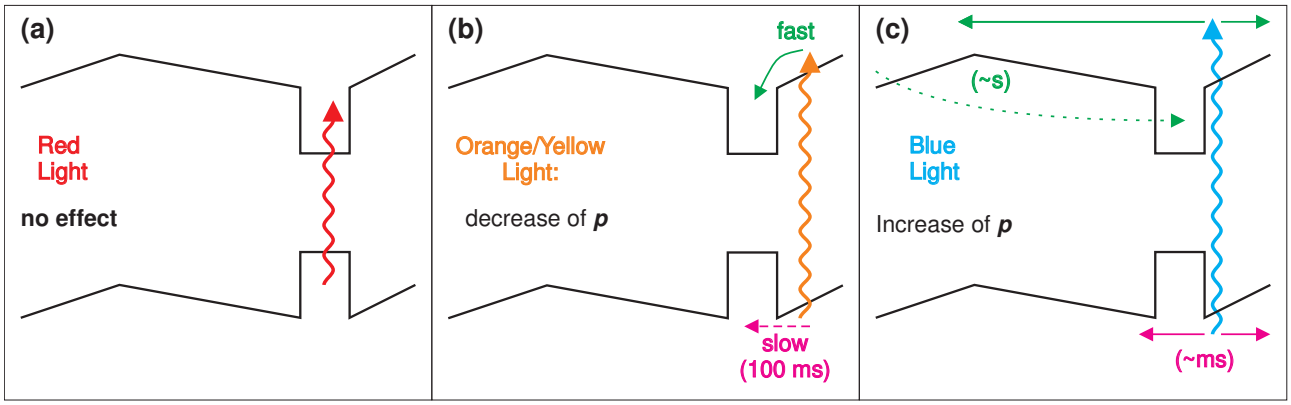

Figure 4.27: The influence of light on hole density. **(a)** red light: no effect, **(b)** decrease of hole density under orange/yellow illumination, **(c)** increase of density under blue illumination.

barrier for electrons preventing migration of electrons deep into the structure. Indeed, we found an experimental confirmation of this enhancement. In figure 4.25 are presented results for the sample M1359. In this case the sample structure is similar to the previously discussed sample M1333: the cap layer has 25 nm thickness but the screening layer was not embedded in the structure. The presented results show that the additional illumination with 425 nm wavelength allowed to almost double the hole gas density reaching 4.5×10^{11} cm^{-2} from the initial 2.4×10^{11} cm^{-2}. Note that also in this case the depletion mechanism was still effective. It allowed to almost empty the quantum well from the carriers with the yellow (575 nm) light illumination. Figure 4.26 presents the idea of band alignment leading to the enhancement of hole density increase mechanism.

To summarize: the influence of the illumination depends on the wavelength of the used light (4.27). Red light has no effect on the carrier density. Orange/yellow illumination depletes the hole gas in the quantum well. Blue illumination increases the hole gas density.

The depletion mechanism for orange/yellow light (figure 4.27(b)) is analogous to the one observed in nitrogen doped samples. It results from the difference of times in which the photo generated carriers reach the quantum well. Electrons quickly migrate into the quantum well while holes have to tunnel through potential barrier (characteristic time for this tunneling is of the order of 100 ms).

Under the blue illumination (figure 4.27(c)) the hole gas density is increased. The photo created electrons have higher energy and penetrate deeper into the sample. The holes return to the quantum well through the same process as under orange/yellow illumination, however electrons this time get trapped for seconds. This creates the increased hole density which can persist even for several seconds after the illumination is turned off (it can be probed with red light without altering). The increase mechanism should also work with the nitrogen doping not only surface doping. Except that the cap layer is thicker with nitrogen doped samples, therefore majority of electrons are created in the cap layer and cannot reach the traps located deeper in the sample.

4.6 Influence of growth temperature

Undoped samples have been shown to exhibit sharper lines when grown at higher temperatures (*Grieshaber et al.*, 1994) due to reduction of interface roughness. Since no additional doping was necessary to obtain the hole gas in the quantum well we were not restrained by the growth condition limits imposed by the nitrogen doping technique (as discussed in the begining of this chapter). This gave us hint to try to improve the optical quality of samples by increasing the temperature of growth.

In fig. 4.28 we compare the widths of PL spectra of samples containing high (more than 4%) Mn percentage in the quantum well. The discussed samples were grown for the purpose of studies on carrier induced ferromagnetism and their properties are discussed in detail in chapter 5. Most of the samples use the surface states as the source of the hole gas for the quantum well and were grown at 280 °C. The exceptions are samples M952, M1364 and M1357, which were grown at 220 °C. In case of samples M952 and M1364 it is the result of using nitrogen δ–doping for providing the hole gas in the quantum well. The lower growth temperature in case of surface doped, M1357 sample was kept for comparison purposes. The samples contained either 80 Å (circles) or 100 Å (squares) wide quantum well. The hole concentrations of the samples in the dark were similar (of about 3×10^{11} cm^{-2}). We present results for the spectra measured in zero magnetic field under illumination in order to deplete the QW from hole gas.

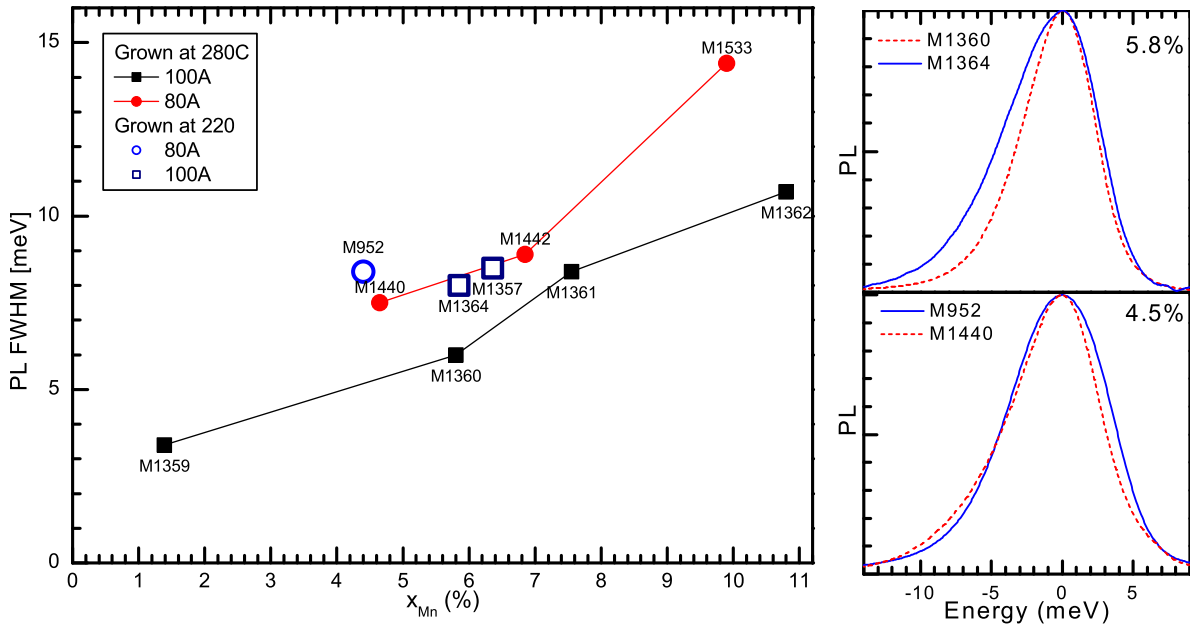

(a) **(b)**

Figure 4.28: (a) PL linewidth comparison of the samples with high Mn content in the quantum well. Full symbols are for samples grown at higher temperature (280°C), empty for the samples grown in condition appropriate for nitrogen doping (220°C) Note that M1357 sample is surface doped - the lower growth temperature was kept for comparison purposes. (b) Experimental spectra. Upper panel: samples with 100 Å QW and Mn content of about 5.8%. Lower panel: Samples with 80 Å QW and Mn content of about 4.5%.

In case of wider quantum well the PL is narrower. This is a natural consequence of the fact that in the wider quantum well the exciton energy is less sensitive to interface roughness (*Weisbuch et al.*, 1981; *Singh et al.*, 1984; *Grieshaber et al.*, 1994).

We would like to stress that sharper lines are observed case in the of samples grown at higher temperature also while the hole gas is present in the quantum wells. This allows to partially compensate the broadening of the lines induced by the increased Mn content in the samples designed for studies on the quantum well ferromagnetism. For example, sample M1442, grown at 280 °C contains much more Mn (by 50%) than sample M952 grown at 220 °C, while the linewidths are are very close for both samples. This would not be possible without surface doping.

4.7 Summary

The main result is that we demonstrated possibility to obtain hole densities exceeding 3.4×10^{11} cm^{-2} in the quantum wells without any doping by impurities introduced into the samples. This was achieved by placing a quantum well 25 nm below the surface of the sample.

This method can be as efficient as modulation doping with nitrogen in supplying a hole gas to the QWs, and can be used to induce a ferromagnetic order in the QW. Efficient doping can be achieved without the technological restrictions arising from incorporating nitrogen impurities into the structures. The Mg in the barriers limits the solubility of nitrogen. Thus the barriers of (Cd,Mn)Te quantum wells that can be effectively doped are limited to below 30% of Mg in the alloy(*Arnoult*, 1998). The nitrogen acceptor level ionization energy in $Cd_{0.7}Mg_{0.3}Te$ is about 60 meV (*Baron et al.*, 1998; *Arnoult*, 1998), which sets a practical limit of Mn concentration in nitrogen doped quantum wells to about 5%. Surface doping is free of those restrains: we have grown $Cd_{1-x}Mn_xTe$ QWs with the x up to 10.9% and significant hole density. This allowed us to broaden the range of experimental conditions in studies of quantum well ferromagnetism discussed in chapter 5.

Furthermore, we show a possibility to use higher temperatures for the growth of the samples and in further post growth processing if required. Due to higher growth temperature we were able to improve sample quality, obtaining narrower spectral lines with respect to the nitrogen doped samples.

The properties of 2D hole gas originating from surface states are very much like those in nitrogen doped samples. For example, in photoluminescence, the transition from singlet exciton line to the split D_{high}-D_{low} triplet occurs at similar values of Zeeman splitting (see figure 2.14). Also the illumination affects the hole gas in similar way, despite the differences in the carrier origin. However, thinner cap layer in surface doping makes the mechanism of increasing hole density more effective. It allows to significantly increase (even double) the hole gas density with the blue light illumination. The uniqueness of surface doped samples lies in fact that both depletion and hole gas density increase mechanisms are efficient. Depending on the applied illumination wavelength it is possible to chose between them. This provides an access to a broad range of hole gas density in the quantum well in the same structure.

The lack of control over the oxidation process brings up an issue of homogeneity. The μ-PL studies discussed in chapter 6 indicate that there are significant differences between nitrogen and surface doping: apparently in the surface doping there exist long range (of order of few μm) fluctuations of carrier density.

CHAPTER 5

Ferromagnetic quantum wells

Contents

The idea of compensation of antiferromagnetic interaction between localized spins by ferromagnetic coupling indicates a way to achieve ferromagnetism in typical semimagnetic semiconductors. The ferromagnetic coupling can be due to the mediation of free carriers (*Pashitskii and Ryabchenko*, 1979). This mediation turned out to be efficient in the DMS materials (*Story et al.*, 1986). It was proven that it is more efficient to employ heavy hole gas instead of electrons due to the larger coupling of the holes to the magnetic ions and the larger density of states in the valence band (*Dietl et al.*, 1997).

The most difficult experimental task is to provide sufficient number of carriers to make it work. One of possible approaches was used by *Story et al.* (1986) where in (Pb,Sn,Mn)Te $10^{20} - 10^{21}$ cm^{-3} density of holes was present due to stochiometric defects. The combination of large hole gas density and Mn density was sufficient to observe the hole mediated ferromagnetism. Another approach is to use III-V materials in which Mn itself acts as an acceptor (*Munekata et al.*, 1989). The main difficulty in this approach is small solubility of Mn ions. This difficulty is partially overcome in non equilibrium growth techniques like MBE which allow to obtain materials that yield high critical temperatures after special thermal processing. Most interesting results have been reported for III–V heterostructures where clever design allowed to increase critical temperatures as high as 250K (*Nazmul et al.*, 2005).

Compared to bulk materials quantum wells possess interesting advantages, for example non vanishing density of states at $k = 0$ (resulting in enhancement of Pauli susceptibility) and the possibility to spatially separate the doping centers from the confined carriers. Therefore,

as the experimental system for our studies we chose δ-doped (Cd,Mn)Te quantum wells. Well established MBE growth techniques allow us to vary independently the hole density and Mn spin density. In such a system ferromagnetic transition has been already studied by (*Haury et al.*, 1997; *Kossacki et al.*, 2002; *Ferrand et al.*, 2001; *Boukari et al.*, 2002). In this work we extend the studies into the region previously unaccessible due to the constrains set by the sample growth conditions, and the applied growth techniques. By using the surface states as a source of hole gas for the quantum well, we were able to study the samples with Mn content exceeding 5%. We also used the sensitivity of hole gas density to the illumination to investigate the ferromagnetic transitions at different conditions for a given density of Mn spins. We were also able to study carrier densities larger than those available previously. We can benefit from the better understanding of photoluminescence of a 2D system containing hole gas (*Kossacki et al.*, 2004*a*).

The study of ferromagnetic ordering in (Cd,Mn)Te quantum wells is experimentally challenging. The typical magnetic susceptibility measurements in SQUID magnetometer were proven to be futile as the amount of magnetic material subject to the ferromagnetic ordering is very small. Even the experiments with specially designed samples allowing for electric control of the ferromagnetic transition and thus increasing the magnetometer's sensitivity to 10^{-9} emu by applying phase sensitive lock-in detection techniques lacked the sensitivity necessary to study the magnetic ordering in quantum wells (*Boukari*, 2003).

Another tool commonly used to probe the magnetic properties of semiconductors are the measurements of magnetotransport (*Chiba et al.*, 2003; *Takamura et al.*, 2002; *Chiba et al.*, 2000). Typically the measurements are performed in Hall configuration. Unfortunately, so far we were unable to obtain proper electrical contacts to the quantum well without destroying doping from surface acceptor states.

However the outstanding optical quality of samples (see 4.6) allows us to study optical transitions involving the states confined in the quantum well. The giant Zeeman splitting in (Cd,Mn)Te enhances the sensitivity of optical studies. Therfore it is possible to detect very subtle effects and small magnetization. In the class of studied material (II-VI quantum wells), it has been the preferred experimental technique (*Haury et al.*, 1997; *Kossacki et al.*, 2000; *Boukari et al.*, 2002).

5.1 State of the art

5.1.1 Mean field approach

The first suggestion of using ion-carrier coupling to achieve ferromagnetism in DMS is due to *Pashitskii and Ryabchenko* (1979) who used a mean field approach. Later on RKKY coupling mechanism has been applied to explain the ferromagnetism in (Pb,Sn,Mn)Te alloys by *Story et al.* (1986) and proposed by *Dietl et al.* (1997) to describe carrier induced ferromagnetism not only in DMS bulk crystals but also quantum wells. It has been shown that RKKY approach is equivalent to the mean field approximation at sufficiently low carrier density.

In the studied case the oscillations of RKKY integral are very slow ($2k_F^{-1} \simeq 13$ nm) (*Dietl et al.*, 1997) compared with mean distance between magnetic ions (of order 1 nm in typical 8 nm wide $Cd_{0.95}Mn_{0.05}Te$). This justifies the use of mean field model for the explanation of our results. It is interesting to note that mean field approach is an approximation. However, when considered interaction has infinite length the approach becomes exact one. In our case, for perfectly delocalized carriers at reasonable carrier densities (long Fermi wavelength) we can approach situation where mean field becomes exact. This explains why mean field calculation yield sensibly accurate description despite its simplicity.

In chapter 2.1.3 the mean field approach was used to describe the influence of magnetic ions on band carriers. Now we would like to include also the problem of carriers affecting alignment of magnetic ions. We start from empirical description of local magnetization of (Cd,Mn)Te, in insulating state, as a function of temperature and magnetic field: (equation 2.4 repeated)

$$M_{(Cd,Mn)Te}(\vec{B},T) = \frac{5}{2} g\mu_B N_0 x_{eff} \mathrm{B}_{5/2}\left(\frac{5}{2}\frac{g\mu_B B}{k_B\left(T+T_{AF}\right)}\right) \tag{5.1}$$

In mean field approximation the influence of carriers can be represented by an effective field B^* acting on Mn ions. After *Dietl et al.* (1997) we can write:

$$B_z^* = \frac{I}{2g\mu_B}\left(n_\downarrow - n_\uparrow\right) \tag{5.2}$$

Where I is appropriate exchange integral denoted α for conduction band and β for valence band (compare equation 2.8). The $n_{\uparrow\downarrow}$ denotes density (3D) of spin up an spin down carriers . Therefore, in presence of carriers the expression for magnetization takes form:

$$M(T,\vec{B}_{ext}) = M_{(Cd,Mn)Te}\left(T,\vec{B}_{ext}+\vec{B}^*\right) \tag{5.3}$$

As shown by *Dietl et al.* (1997) the effective field resulting from hole gas is larger than that due to electrons. In what follows we shall focus on quantum well systems containing two dimensional hole gas and magnetic ions.

One of peculiarities distinguishing the quantum well system is parallel to the growth axis alignment of heavy hole spins induced by the strain and confinement. This produces the Ising-like magnetic system, where the only non vanishing component of $\vec{B^*}$ is B_z^*. The B_z^* is determined by the sheet densities $p_{\pm 3/2}$ of the hole gas in the $+^3/_2$ and $-^3/_2$ spin subbands:

$$B^*(z) = \frac{\beta}{2g\mu_B}\left(p_{+3/2}-p_{-3/2}\right)|\phi(z)|^2 \tag{5.4}$$

Where $|\phi(z)|^2$ is one dimensional envelope of wave function of a hole in the quantum well.

The polarization of the hole gas is a result of a valence band splitting (Δ_{hh}) due to the magnetization.

In analogy to equation 2.9 we obtain: $\Delta_{hh} = N_0\beta\langle S_z\rangle x_{eff}$ or $\Delta_{hh} = \frac{-\beta M}{g\,\mu_B}$. As discussed in chapter 2.2.2 the hole gas density in each heavy hole spin subband in effective mass formalism can be expressed in terms of zero–field Fermi energy $p = \rho_0 E_F$ where density of states is given as $\rho_0 = \frac{m_{||hh}}{2\pi\hbar^2}$. This allows us to calculate the low temperature carrier density in respective spin subbands: $p_{\pm 3/2} = \rho_0(E_F \pm \frac{1}{2}\Delta_{hh})$ in case of incomplete gas polarization ($\Delta_{hh} < 2E_F$). When hole gas becomes completely polarized ($\Delta_{hh} \geq 2E_F$) we can write $p_{-3/2} = 0$ and $p_{+3/2} = \rho_0 2E_F$.

We can calculate hole gas polarization and resulting B^*. For incomplete gas polarization we obtain:

$$B^*(z) = \frac{\beta}{2g\mu_B}\rho_0\Delta_{hh}|\phi(z)|^2 \tag{5.5}$$

For complete hole gas polarization we obtain saturation value of effective magnetic field:

$$\max[B_z^*] = \frac{\beta}{2g\mu_B}p\,|\phi(z)|^2 \tag{5.6}$$

Here we discover the second interesting feature of the ferromagnetic phase in quantum wells: Wave vector independent density of states in a 2D carrier gas ($\rho_{2D}(E_F) = \text{const}$) leads to effective magnetic field independent of carrier density (for incomplete polarization of hole gas). This peculiarity has also significant impact on the transition temperature obtained from the discussed model. Once the hole gas becomes fully polarized, the value of effective magnetic field depends on the total carrier density (equation 5.6).

The transition temperature can be derived from the analysis of magnetic susceptibility:

$$\chi = \left(\frac{\partial M}{\partial B_{ext}}\right)_{B_{ext}\to 0} = \frac{C_C}{T - T_{CW}} \tag{5.7}$$

Instead of full expression for (Cd,Mn)Te magnetization (equation 2.4) applied to the quantum well it is more convenient to analyze only first term of expansion in vicinity of zero field:

$$M = \frac{CB_{ext}}{T + T_{AF} - \Theta} \tag{5.8}$$

With constant C defined as (compare with *Spalek et al.* (1986)):

$$C = \frac{1}{3k_B}N_0S(S+1)(g\,\mu_B)^2x_{eff} \tag{5.9}$$

C can be recognized as Curie constant C_C from equation 5.7.

As opposed to classical Curie-Weiss approach (*Spalek et al.*, 1986) we introduced here the effective concentration of "free" Mn spins (x_{eff}). This form of the Curie-Weiss law is applicable in a temperature range (below $\sim$ 10 K) where part of Mn spins ($x - x_{eff}$) is bound in antiferromagnetic pairs and thus excluded from magnetization. The Curie-Weiss law represents a high temperature expansion . In this case it means that the thermal energy must be higher than Mn Zeeman energy in exchange field. For $B^* \approx 0.2$T it yields T$\gg 0.12$ K.

According to equations 5.7 and 5.8 the Curie-Weiss temperature is:

$$T_{CW} = \Theta - T_{AF} \tag{5.10}$$

The two dimensional case is given by (*Dietl et al.*, 1997; *Kossacki*, 1998):

$$\Theta = \frac{S(S+1)}{6k_B}N_0\beta^2x_{eff}\rho_0A_F\tilde{L}_W^{-1} \tag{5.11}$$

The coefficient A_F (discussed in section 2.2.2) is introduced to account for the susceptibility enhancement due to carrier–carrier interaction.

Including the presence of effective magnetic field due to polarization of carriers in expression for magnetization results in appearance of carrier density at Fermi energy $\rho_d(E_F)$ in the formula

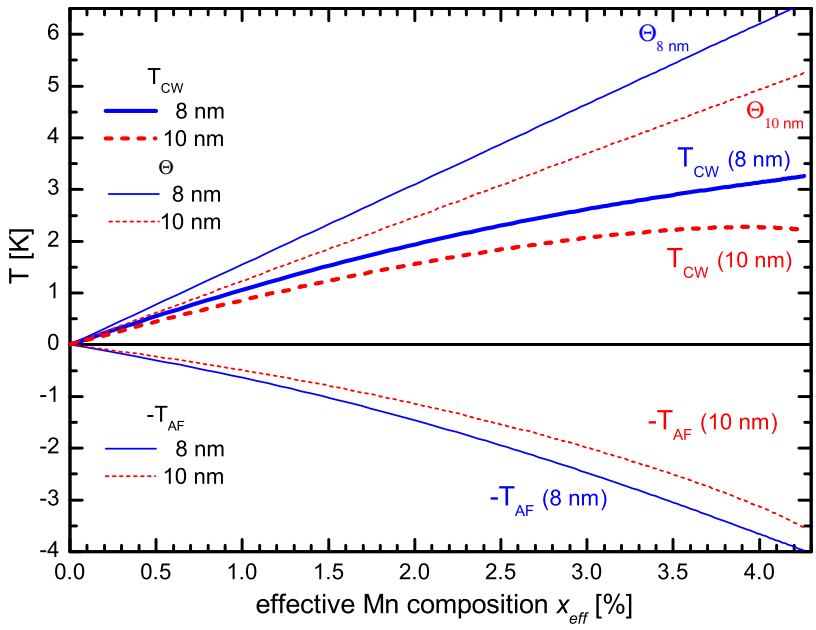

Figure 5.1: Mean field predictions of Curie-Weiss temperatures for two widths of quantum well (8 nm and 10 nm). Calculated Θ temperature and corrections due to T_{AF} are shown. The T_{AF} is plotted basing on the experimental results discussed in chapter 2.3.2.

5.11. In the simplest model (equation 5.5) the density of states in quantum well does not depend on k therefore we can replace $\rho_d(E_F)$ by ρ_0. The resulting Curie-Weiss temperature does not directly depend on the carrier density. The only influence of the carrier density is hidden in the effective width of quantum well $\tilde{L}_W$. It is obtained from integrating one dimensional wave function envelope of a hole over the region of quantum well:

$$\tilde{L}_W^{-1} = \int_{-\frac{L}{2}}^{+\frac{L}{2}} |\phi(z)|^4 \mathrm{d}z \tag{5.12}$$

Depending on the model used for obtaining the shape of the hole wave function it is possible to address various parameters of a system. The basic approach is made within model proposed by *Fishman* (1995) to describe valence band. It can be further enhanced by including electrostatic potential (resulting from the presence of carriers in the quantum well and dopants nearby). The shape of electrostatic potential is obtained from self consistent calculations. Such basic calculations allow to include the effects due to quantum confinement and carrier density. It is also possible to apply more realistic models of quantum wells including for example the effects of interfaces and non homogenous distribution of Mn ions in the quantum well. However, more precise models of band structure would dramatically increase the number of arbitrary parameters and affect clarity of a model. On the other hand even simplest model yielded satisfactory description of experimental data (*Kossacki*, 1998; *Ferrand*, 1999; *Kossacki et al.*, 2002).

In this work two widths of quantum well were used in the design of samples: 8 nm and 10 nm. Assuming realistic carrier density of 3×10^{11} holes per cm^2 in the quantum well $\tilde{L}_W = 6.2$nm and 7.8nm has been obtained by *Haury et al.* (1997) for 8 nm and 10 nm quantum well widths respectively. It was found that $\tilde{L}_W$ is very weakly affected by the electrostatic potential and other details of the quantum well shape.

In figure 5.1 dependence of calculated Θ and experimentally determined T_{AF} and resulting T_{CW} on effective Mn density is plotted for the two widths of quantum wells. Apparently the reduction of T_{AF} due to wider quantum well can be balanced by the influence of $\tilde{L}_W$ on Θ which results in higher Curie-Weiss temperatures for narrower quantum wells. The highest Curie-Weiss temperature is slightly over 3K for 8 nm quantum well with maximum effective Mn spin density (in typical layers it is not possible to achieve more than 4.3% of x_{eff} see chapter 2.1.3).

5.1.2 Experimental results for low Mn content:

New possibilities of p type doping allowed us to venture into previously unavailable experimental conditions of quantum wells made of (Cd,Mn)Te containing more than 5% Mn. Substantial effort in studying carrier induced magnetic ordering has been already carried out on similar structures with smaller Mn density in works published by *Kossacki et al.* (2000, 2002) and *Boukari et al.* (2002). The results presented in those works are reproduced in the structures with surface doping containing comparable density of Mn ions in quantum well. The discussed results were obtained by experimental techniques similar to those used in this work. Therefore in this section I will summarize the achievements prior to my study so the original part of this work can be considered as a further development of experiments, applied to the new samples. The figures in this section are copied from original works thanks to courtesy of authors.

The authors use optical transitions to probe the magnetic state of quantum well. Large values of the spin splitting of effective mass states enable them to observe either spontaneous or field induced magnetization in PL experiments despite the low amount of magnetic material in the quantum well. The PL line corresponding to the transition in the quantum well shows a splitting and a critical shift of its spectral position below a characteristic temperature T_C as seen in figures 5.2(a) and 5.3(a). The observed splitting is attributed to the presence of spontaneous magnetization. It is similar to the splitting in presence of small external magnetic field, which can be seen in circular polarization resolved experiment. *Boukari et al.* (2002) report two ways of crossing the phase boundary transition of considered system: by varying temperature at constant carrier density (as in figures 5.2(a) and 5.3(a)) or isothermally at low temperature by varying the carrier density (figure 5.3(b)). The carrier density changes can be achieved by applying electric field to a specially designed structures (*Boukari et al.*, 2002) or by illumination with blue light as seen in figure 5.3(b) (*Kossacki et al.*, 2002). The effect of light on carrier density was discussed in detail in chapter 4.5 and can be applied also to the structures used in this work.

The critical behavior of line splitting together with divergence of magnetic susceptibility (discussed in chapter 5.3) are not present in undoped or non magnetic quantum wells. The abruptness of changes is contrary to the gradual evolution ascribed to the formation of bound magnetic polarons (*Dietl and Spalek*, 1982; *Mackh et al.*, 1994). This confirms the ferromagnetic type of the ground state.

Mean field model (presented in section 5.1.1) describes well the dependence of the critical temperature on the Mn density as can bee seen in figure 5.4. In order to reproduce the experiment the theory was adjusted by assuming the value of Fermi liquid parameter A_F to be 2.1. On the other hand the experimental data presented in figures 5.2 and 5.4, contrary to the mean field model prediction shows a dependence of the transition temperature on the carrier density.

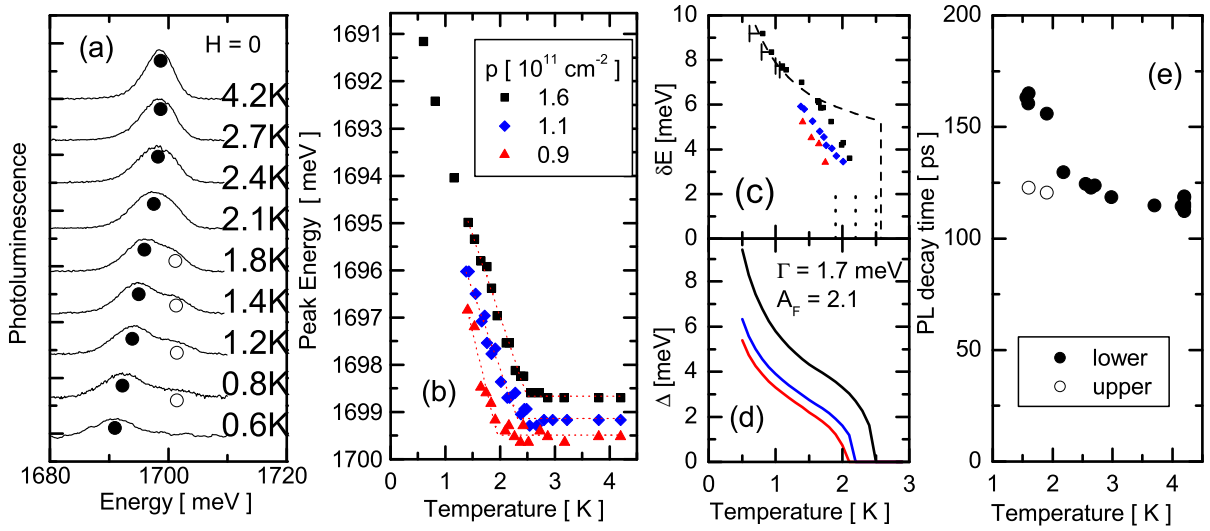

Figure 5.2: PL spectra at selected temperatures (a). Peak positions of the low- and high-energy lines are marked by full and empty points, respectively. Temperature dependence of the low-energy peak positions and the line splitting are shown for selected values of the hole concentrations in (b) and (c), respectively. Dashed and solid lines in (c) and (d) are calculated neglecting and taking disorder into account, respectively. Vertical lines in (c) show critical temperatures T_c corresponding to slope changes of the points in (b). PL decay times for upper (empty points) and lower (full symbols) split lines versus temperature are shown in (e). After *Kossacki et al.* (2000).

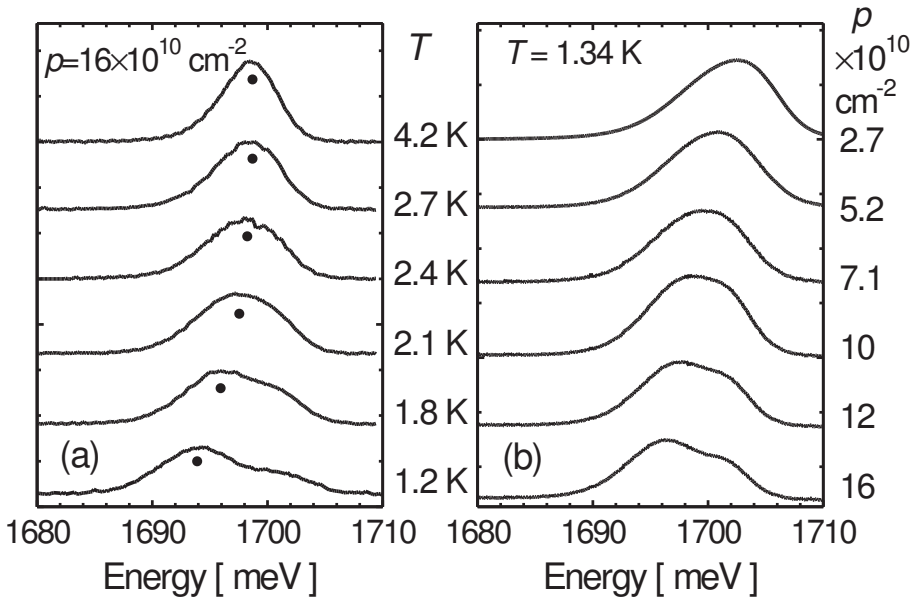

Figure 5.3: PL spectra at various temperatures (a) and hole concentrations (b) in p-type $Cd_{0.96}Mn_{0.04}Te$ quantum well. Peak positions of the low energy line are marked by full circles in (a). After *Kossacki et al.* (2002).

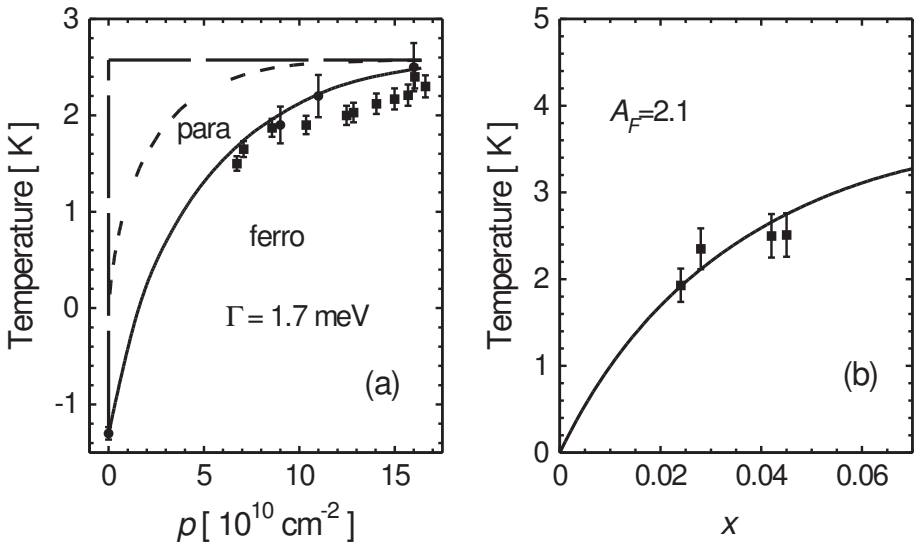

Figure 5.4: Critical temperature T_C of the ferromagnetic transition, as a function of the hole (a) and Mn (b) concentrations in p-type $Cd_{0.96}Mn_{0.04}Te$ quantum well. Solid lines are theoretical taking enhancement of T_C by disorder (a) and hole-hole (b) correlation into account. The dashed line in (a) is theoretical neglecting disorder ($\Gamma = 0$). The step function (dashed line) is calculated for 2D degenerate hole gas neglecting disorder. After *Kossacki et al.* (2002).

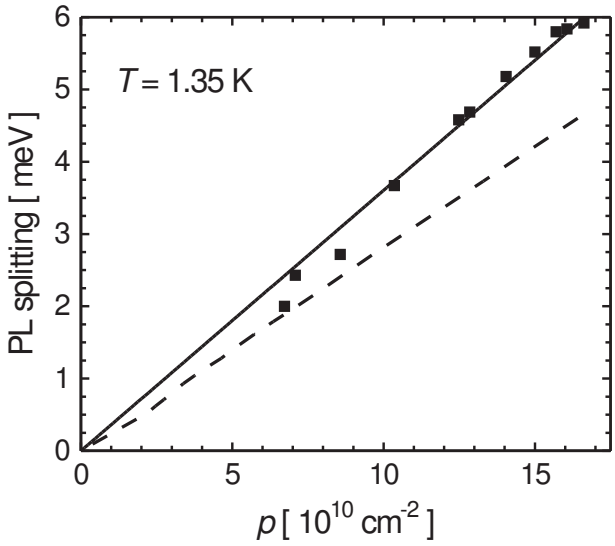

Figure 5.5: Zero-field splitting of the PL line in p-type $Cd_{0.96}Mn_{0.04}Te$ quantum well as a function of the hole concentration. Solid line is drawn through data; dashed line is calculated neglecting effects of hole-hole ineraction on optical spectra. After *Kossacki et al.* (2002).

Furthermore, the measured values of the PL line splitting (δE in figure 5.2 (c)) contradict the mean field predictions: the slow buildup of splitting is seen instead of instantaneous total polarization of hole gas. The authors ascribe the discrepancy to the influence of static disorder on the density of states. The influence has been represented by a Gaussian broadening, with a full width at half maximum ($FWHM$) Γ. It leads to the modification of the expression describing hole polarization used in mean field calculation:

$$p_{\pm} = \frac{m_{hh}}{2\pi\hbar^2} \int_{-\infty}^{+\infty} \frac{\mathrm{d}\varepsilon}{1+\exp\left[\frac{\varepsilon-\varepsilon_F}{k_B T}\right]} \frac{1}{2}\left(1+\mathrm{erf}\left[\frac{\varepsilon \pm \frac{\Delta}{2}}{\Gamma}\right]\right) \tag{5.13}$$

A satisfactory description of the experimental data is achieved for the width of the broadening $\Gamma = 1.7$ meV as seen in figures 5.2 and 5.4. According to figure 5.4 the presence of disorder is responsible for the lowering of the transition temperature in low concentration regime. The authors predict onset of strong hole localization when Fermi energy becomes comparable with broadening width Γ.

For sufficiently low temperatures (about $0.7T_C$) the half metallic situation is reached. Even then Mn spins are far from saturation due to the rather small magnitude of molecular field produced by polarized hole gas. The value of this field is predicted to be of the order of 1000 Oe. In this weak field range of the magnetization of Mn ions and resulting splitting of PL line are expected to be proportional to the exchange field and thus to the hole density. In figure 5.5 values of spontaneous PL splitting are plotted versus carrier density. Although the dependence is linear, the experimental values are about 25% larger from the calculation predictions. The discrepancies in presented comparison originate from the enhancement of valence band Zeeman splitting by carrier-carrier interaction effects (see 2.2.2).

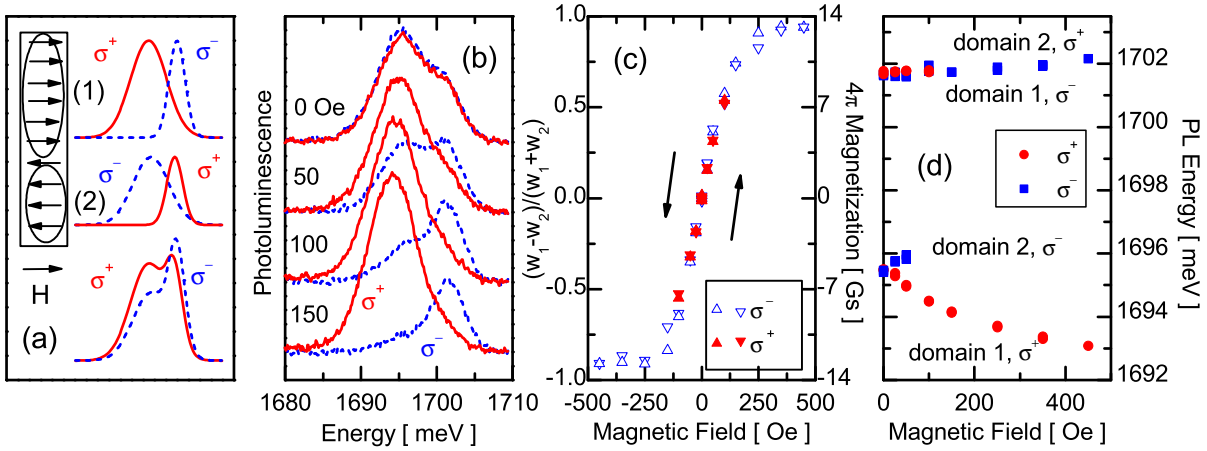

Figure 5.6: Schematic (a) and experimental results on domain structure studied by polarization-resolved luminescence spectroscopy of modulation-doped p-$Cd_{0.957}Mn_{0.043}Te$ at 1.53 K. Peak positions are shown in (d), while (c) presents the difference $\frac{w_1-w_2}{w_1+w_2}$, where $w_i = I_i(H)/I_i(0)$, in the normalized integrated intensities I of the two contributions to the line at each polarization for the field swept up and down. After *Kossacki et al.* (2000).

Microscopic properties of the ordered phase

Substantial experimental attention was also paid to the investigations of microscopic properties of the ordered phase. Contrary to the Zeeman splitting in the external magnetic field, the two split lines are present in both circular polarizations of the photoluminescence from the ordered phase at low temperatures without external magnetic field applied. It was attributed to the presence of magnetic domains with both directions of the magnetization vector in the scope of laser spot used for exciting PL (*Kossacki et al.*, 2000). Neither domain orientation is preferred and thus the resulting PL spectra exhibit no sign of circular polarization.

Careful, circular polarization resolved, studies of PL from the ordered phase in the presence of small external magnetic (up to 450 Gauss) (*Kossacki*, 1998; *Ferrand*, 1999; *Kossacki et al.*, 2002) allowed those authors to identify the σ^+ and σ^- transitions from magnetic domains of both orientations (see figure 5.6) The obtained experimental results supported the explanation of the non polarized zero field spectra character by the presence of magnetic domains. The studies of relative intensities of PL from respectively oriented domains allowed to determine the field sufficient to align the magnetic domains to be of order of 100 Oe. The experimental data point to the presence of a very weak (< 40 Oe) coercive field.

5.2 Samples

For the purpose of studying ferromagnetic phase a special set of samples was grown. The details of the sample growth were in general the same as for the samples used in study of surface doping (described in section 4.1). We used only $Cd_{0.96}Zn_{0.04}Te$ substrates and the sample structure followed type B scheme described in figure 4.2. The detailed structure parameters are given in table A.1 in the appendix. The choice of $Cd_{0.96}Zn_{0.04}Te$ substrates allows to use ternary alloy (Cd,Mg)Te for the barrier material which gives better control over the growth process than in case of quaternary alloy needed for lattice matched barriers to $Cd_{0.88}Zn_{0.12}Te$ substrates. Besides, due to the increase of quantum well bandgap for higher Mn compositions (even 4%), the 12% Zn substrate is not transparent for the energies coresponding to the quantum well transitions.

The samples do not contain any nitrogen doped layer therefore it was possible to increase the temperature of the substrate during growth process to 280°C. The exception is sample M1357 where lower growth temperature was kept for the purpose of comparison with nitrogen doped samples. The temperature close to optimal growth conditions results in very good quality of samples which has been demonstrated in section 4.6.

Some of the experiments were carried out on the sample M952 which represents a legacy of pioneer works by A. Haury and P. Kossacki (*Haury et al.*, 1997; *Kossacki*, 1998). This sample was grown on $Cd_{0.88}Zn_{0.12}Te$ substrate at 240°C. A 8nm wide(Cd,Mn)Te quantum well is embedded between $Cd_{0.67}Mg_{0.25}Zn_{0.08}Te$ barriers. The p type doping was achieved by placing 15nm wide Nitrogen doped layer at a distance of 20 nm from the quantum well (from the side of the surface). Furthermore the quantum well is screened from any spurious charging effects by 25 nm wide nitrogen doped layers placed on both sides of quantum well at a distance of 150 nm.

Sample	x_{Mn} %	x_{eff} %	T_{AF} K	Growth temperature °C	hole density [$\times 10^{10}$cm^{-2}] Native	Maximal
Width 100 Å Surface Doped						
M1357	6.36	3.3	2.44	220	36	39
M1359	1.4	1.15	0.72	280	24	45
M1360	5.8	3.1	2.07	280	36	50
M1361	7.55	3.55	2.63	280	33	44
M1362	10.8	4.11	3.33	280	34	44
Width 80 Å Surface Doped						
M1440	4.65	2.72	2.45	280	47	49
M1442	6.84	3.38	2.63	280	46	48
M1533	9.9	4.05	3.23	280	45	48
Width 100 Å Nitrogen Doped						
M1364	5.85	3.15	2.36	220	50	—
Width 80 Å Nitrogen Doped						
M 952	4.4	2.6	1.9	240	27	—

Table 5.1: Parameters of samples discussed in this chapter.

In addition, a new nitrogen sample was grown for the comparison purpose. The M1364 follows the structural scheme of M952 sample but the quantum well is 10nm wide instead of 8 nm. The new sample has also slightly more Mn ions in the quantum well.

The essential parameters for the studies of carrier induced magnetic ordering such as Mn density and hole gas density were determined accordingly to procedures described in chapter 2.3. The results are presented in table 5.1. The detailed structure parameters of samples are in tables A.1 and A.4 located in Appendix. The samples M1362 and M1533 have the effective spin densities larger than 4%. Such values are very close to the maximal effective spin density in bulk (Cd,Mn)Te ($Max[x_{eff}] = 4.5\%$ for 17% Mn in bulk (Cd,Mn)Te, see section 2.1.3). Therefore, the choice of samples allows us to cover almost whole range of Mn spin densities available in (Cd,Mn)Te quantum wells.

Carrier density was decreased by illumination during reflectivity measurements aiming at Mn density determination. Broadening of lines due to large Mn content in quantum well favors the analysis of PL splitting at magnetic fields as a method of carrier density determination as compared to the Moss–Burstein shift. The unique photosensitivity of surface doped samples (discussed in section 4.5) allows to increase the hole gas density above nominal values by blue light illumination. The maximal carrier densities achieved are for all surface doped samples close to 5×10^{11} per cm^2. The control of carrier density by additional illumination enables us to study the effects related to Mn density in the similar conditions in different samples.

5.3 Magnetic Susceptibility in the paramagnetic phase

In the optical experiments, the magnetization in (Cd,Mn)Te quantum well is expressed as a Zeeman splitting of PL line. Therefore it is possible to determine it from the analysis of circularly polarized PL spectra measured in external magnetic field B. The derivative of PL Zeeman splitting Δ_Z is can be interpreted in terms of an effective g^* factor:

$$g^* = \frac{1}{\mu_B} \lim_{B \to 0} \frac{\partial \Delta_Z}{\partial B} \tag{5.14}$$

g^* is directly related with the magnetic susceptibility χ:

$$g^* = \frac{\alpha - \beta}{\mu_B} \chi \tag{5.15}$$

Therefore the effective g^* factor and the magnetic susceptibility should obey the Curie-Weiss law (Equation 5.7).

In our case, we plot the position of PL line in the magnetic field up to 0.16 T. For the purpose of accuracy, the change of detected PL circular polarization was achieved by the application of a magnetic field in reverse direction, rather than manipulation of a circular polarizer.

Figure 5.7 presents examples of experimental spectra for sample M1360 with 5.8% Mn. The ability to change the hole gas density with the additional illumination provides the means to study the influence of carriers on the magnetic ordering. In the presented figure one can clearly observe the enhancement of Zeeman splitting due to the coupling of carrier gas to the magnetic ions. In order to analyze the divergence of magnetic susceptibility it is necessary to trace the Zeeman splitting in a sufficient range of temperatures. Figure 5.8 presents the collected results of experimentally determined Zeeman splittings versus magnetic field for the sample M1360. The results corresponding to the spectra shown in figure 5.7 are marked as red circles. The determination of effective g^* factor from the PL Zeeman splitting becomes difficult for the measurements at higher temperatures as the susceptibility becomes smaller. The experimental difficulties are especially pronounced in the case of small carrier density. The value of $g*$ can be determined by fitting the line to the values of Zeeman splitting for the range of fields close to zero. As the temperature increases the range of magnetic fields where linear dependence between magnetic field and Zeeman splitting is obeyed expands, allowing for more accurate determination of g^* and thus partially counteracting the difficulty coming from the small magnetization values. In order to further increase the number of experimental points used to determine g^* it is more convenient to analyze the position of PL line instead of Zeeman splitting. Thus g^* is proportional to the doubled value of the slope of PL position, plotted versus magnetic field, in the vicinity of zero field.

Figure 5.9 presents the effective g-factors obtained for the data presented in figure 5.8. For the purpose of analysis of Curie-Weiss law it is more convenient to analyze the inverse g^*. Then the experimental data should follow a linear dependence: the extrapolation to zero determines the Curie-Weiss temperature (T_{CW}), the inverse of the slope represents the Curie constant. The linear fits to the experimental data are presented on the graph as solid lines.

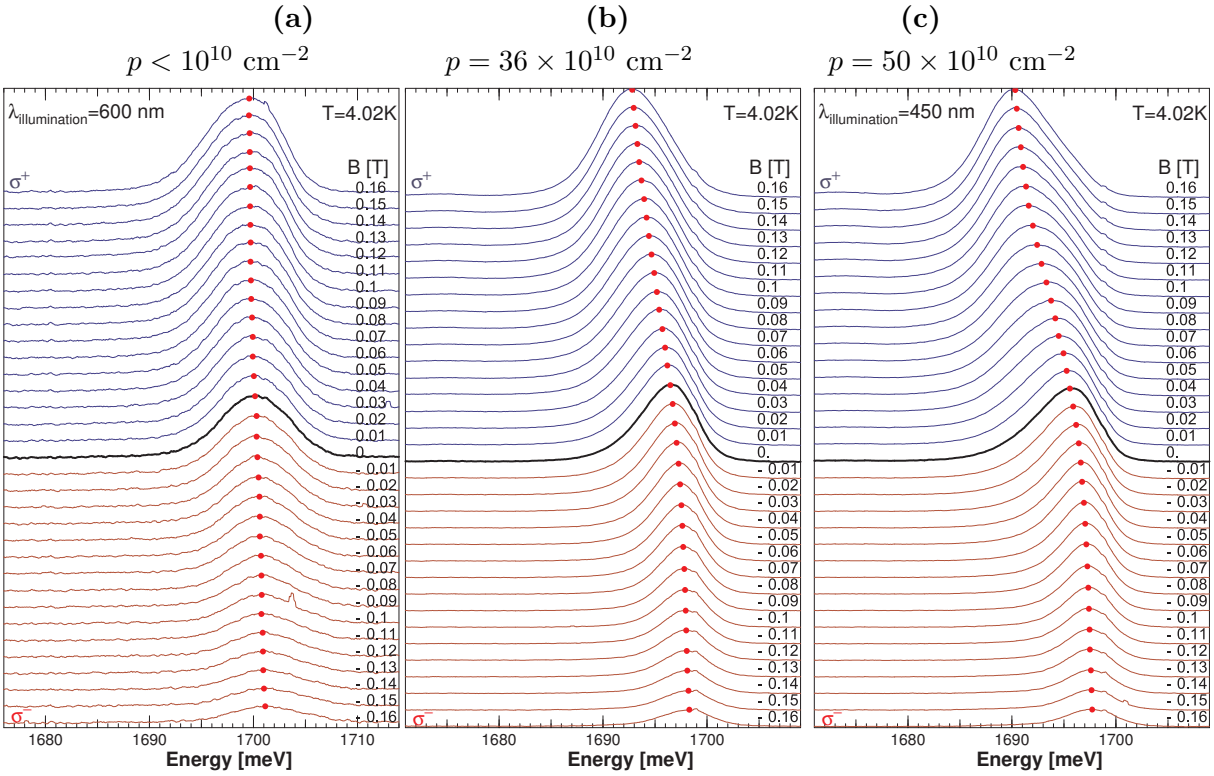

Figure 5.7: Example of experimental PL spectra used for determination of susceptibility. The panels show the results for the sample M1360 with 5.8% Mn in 10 nm quantum well but different carrier concentration. The changes of concentration were obtained by the additional illumination. Panel (a) results for empty quantum well (carrier concentration is less than 10^{10} cm^{-2}), panel (b) native concentration of 36×10^{10} holes per cm^2, panel (c) blue light enhanced concentration of 50×10^{10} holes per cm^2.

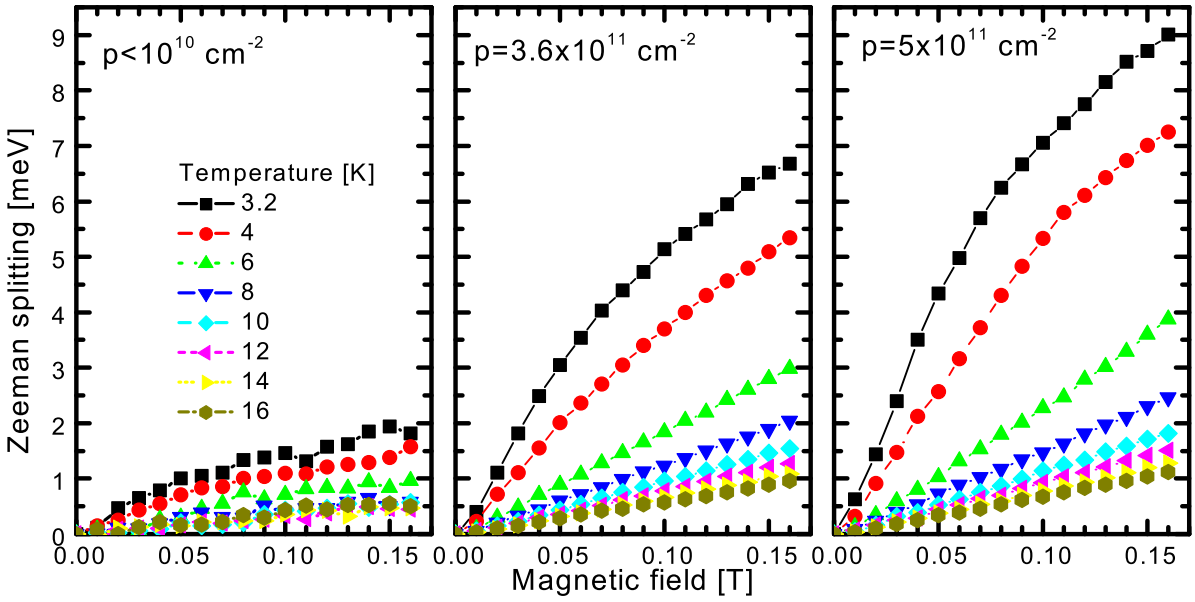

Figure 5.8: Zeeman splittings deduced from the PL spectra for different temperatures. The sample M1360 contains 10 nm QW. The changes of concentration were obtained by the additional illumination.

The dashed line represent a simulation based on equation 2.4 without influence of the carriers (although this equation was derived for temperatures bellow 4.2K other experiments indicated that it provides sensible description for experimental data up to 10K). Sample parameters from Table 5.1 were used. The determined Curie–Weiss temperatures depend on the carrier densities. For the highest hole gas density (5×10^{11}) cm^{-2} the $T_{CW} = 2.5\pm0.1$ K, while for the lower density of 3.6×10^{11} cm^{-2} the $T_{CW} = 2.2\pm0.1$ K. The increase of critical temperature with the hole gas density is noticeable yet close to the experimental resolution. The dependence of Curie–Weiss temperatures on the Mn density will be addressed in the following sections. Noticeable differences are also present in the slopes of the $\frac{1}{g^*}$ and thus the experimentally determined Curie constants for the different carrier densities. The Curie constant is larger (the slope is smaller) for the higher hole gas density. Those general trends are also followed by the other samples: the results are presented in figure 5.10. The dependence of critical temperature as well as of Curie constant on the carrier density is especially pronounced on the results for the samples M1359 and M1364 where significant changes of hole gas density were achieved.

The results obtained for the quantum wells depleted of carriers quite well reproduce the simulation based on the bulk Mn properties (formula 2.4) and the experimentally determined parameters (Table 5.1) for the sample M1360 (Figure 5.9). Although the agrement of the experimental data with the calculation is good, in this case, high experimental errors occur due to the very small values of g^* at higher temperatures. Limitations of the experimental procedure are crucial in this case, as it is most difficult to determine values of splitting that are small compared to the photoluminescence linewidth. It appears that the experimental errors

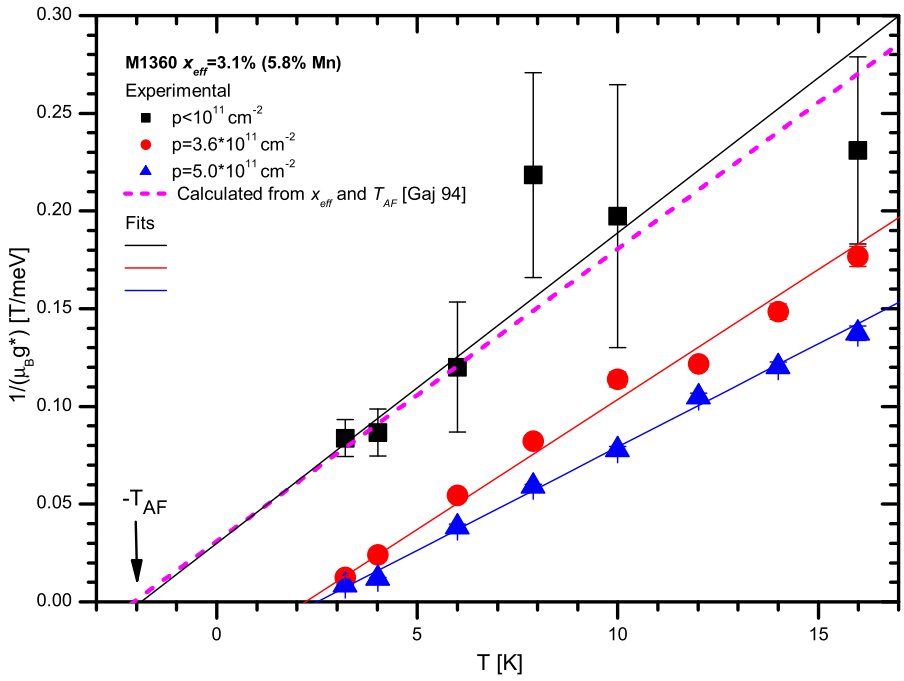

Figure 5.9: Inverse effective g-factor g^* for the sample M1360 as a function of temperature. The different carrier densities were obtained by the additional illumination. The dashed line presents the simulation done by application the experimentally determined parameters of the sample (Table 5.1) to formula describing effective g^* factor for the bulk (Cd,Mn)Te obtained from manipulating the formula 2.4.

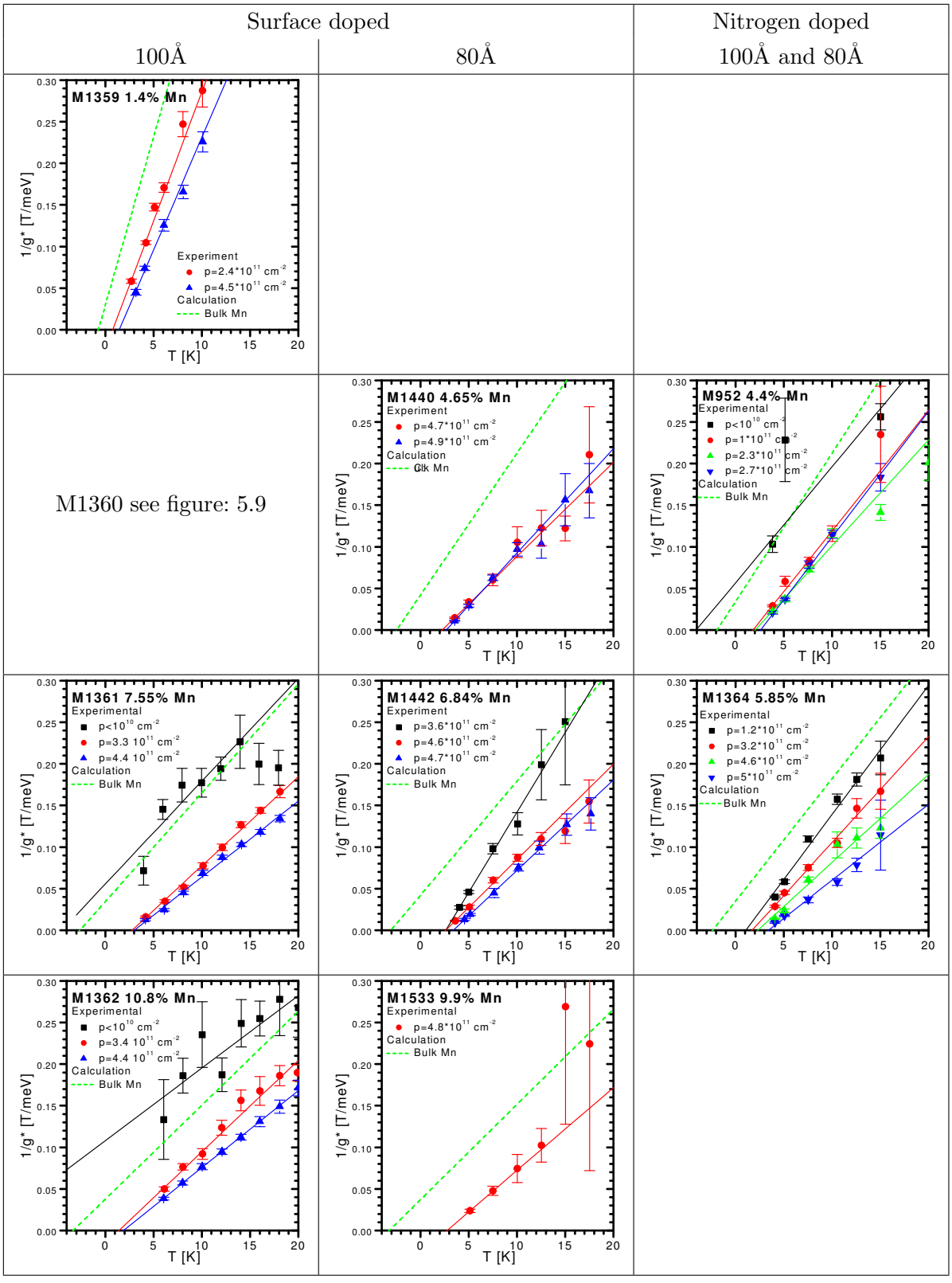

Figure 5.10: Inverse effective g-factor g^* as a function of temperature. The different carrier densities were obtained by the additional illumination. The dashed line presents the simulation done by application the experimentally determined parameters of the sample (Table 5.1) to formula describing effective g^* factor for the bulk (Cd,Mn)Te obtained from the formula 2.4.

increase significantly for the values of $\frac{1}{g^*}$ higher than 0.2 T/meV (Note that the highest value of magnetic field osed in this experiment was 0.16 T.)

Apparently for the sample M1360 in figure 5.9 the splitting in the quantum well depleted of carriers was high enough, for the given photoluminescence linewidth, to allow for the determination of $\frac{1}{g^*}$ with the sensible accuracy in the sufficient range of temperature. In other samples we were either unable to deplete the quantum well to the satisfactory degree or the splittings were too small to allow for reasonable comparison with the calculations. Therefore, in those cases the experimental results fail to achieve accuracy permitting even a coarse comparison to the bulk Mn predictions. The increase of accuracy would require applying bigger magnetic fields during the PL measurements.However, the properties of the experimental setup obliged us to keep the magnetic field small in order to minimize the risk of arising significant remanence field in the magnet.

The values of Curie constant obtained at significant carrier densities are higher than the predictions of calculations based on the bulk (Cd,Mn)Te properties. The results are presented in figure 5.11. On the upper panel (a) the results for the high (approximately 5×10^{11} cm^{-2}) carrier density are compared with the bulk (Cd,Mn)Te parameterized dependence. The experimental points seem to be shifted by a constant value from the model while the points obtained for the depleted quantum well (triangles) coincide with the parameterized dependence within the experimental error. The discrepancy results from the fact that the phenomenological description was performed for the undoped (Cd,Mn)Te crystals, therefore it omits any interactions arising from the presence of the hole gas. The important role of carriers, especially at high concentrations, is depicted in the lower panel (b) of figure 5.11, where the difference between the experimentally determined Curie constants and the bulk simulation is plotted as a function of carrier density. The difference is increasing with the hole gas density reaching over 50% with respect to the predicted value.

The observed enhancement of the Curie–Weiss constant due to the presence of the two dimensional carrier gas is conform with the behavior of typical ferromagnets close to the transition temperature. Such enhancement is usually explained by the presence of magnetic fluctuations. In our case of an exceptionally long–range interaction producing ferromagnetism, it would be natural to expect the fluctuations to be insignificant. The present experimental results suggest that when increasing carrier density, the role of fluctuations also increases. They cannot be neglected for densities above 25×10^{10} cm^{-2} from which $\frac{1}{2k_F} = 8$ nm which is anyhow longer than average distance between Mn ions (1 nm for 5% Mn in 8 nm quantum well). However, direct determination of carrier density fluctuations by microphotoluminescence (see Chapter 6) does not confirm this suggestion. The difference may originate from insufficient spatial resolution of μ-PL measurement (of the order of 1μm). Further studies are required to clarify this point.

It is interesting to note that similar effect on the susceptibility in (Cd,Mn)Te quantum well were reported by *Kechrakos et al.* (2005). However in the discussed work, the effect was achieved by switching on and off antiferromagnetic interaction between Mn ions in Monte Carlo simulations performed for the system very similar to ours. Within corresponding temperature range, the antiferromagnetic interactions reduced the susceptibility almost threefold with respect to the paramagnetic case.

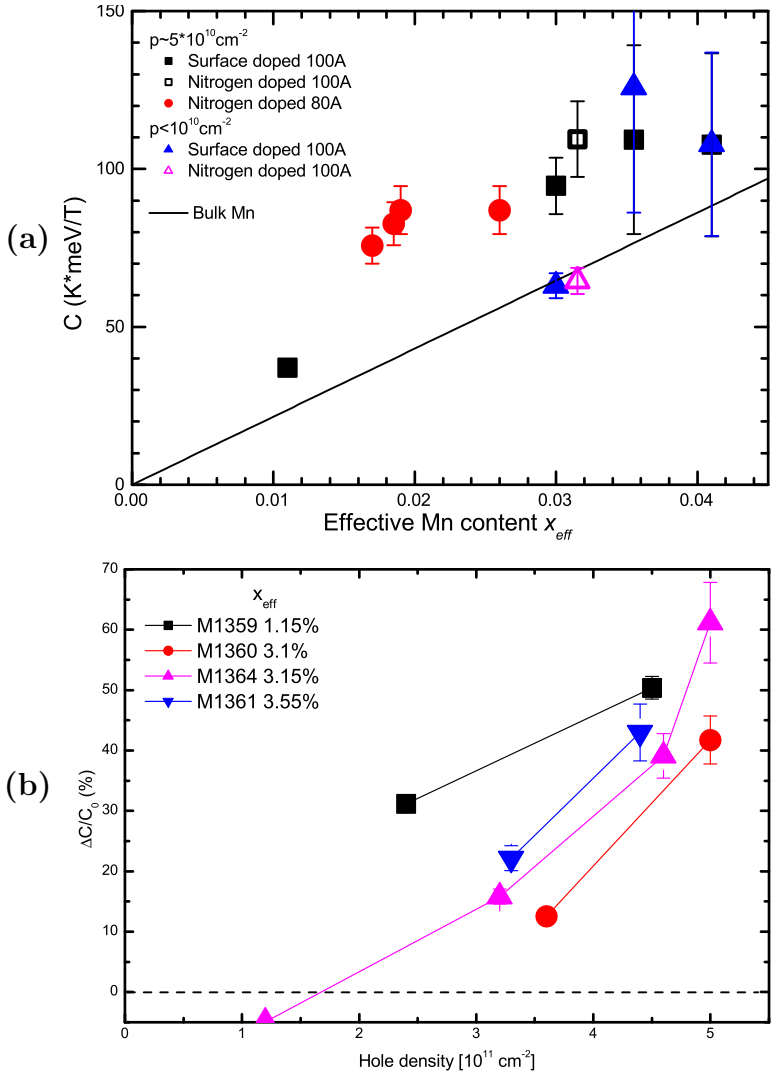

Figure 5.11: Curie constants derived from the experimental data. **(a)** points represent values obtained for the high (approximately 5×10^{11} cm^{-2}) carrier density, the solid line is the calculation for the bulk (Cd,Mn)Te. **(b)** Difference between the experimental value from the bulk(Cd,Mn)Te calculation (normalized by the simulation value) as a function of hole gas density.

5.3.1 Mn density dependence

Surface doped samples allow us to study the dependence of Curie-Weiss temperature on Mn density in the quantum well in a range previously unavailable. The used choice of samples raised the limit of our study up to $x_{eff} = 4.1\%$ from 2.6% in previous studies on nitrogen doped samples. Therefore we were able to cover most of the range of effective Mn compositions possible in rectangular (Cd,Mn)Te quantum wells determined by antiferromagnetic coupling of Mn ions.

The results are presented in figure 5.12. For better consistency we compare the results obtained at maximal carrier density possible in each sample. According to table 5.1 those carrier densities reach values close to 50×10^{10} cm^{-2} when additional illumination is used. The differences are minor compared to the overall density therefore we can consider the carrier density to be constant from the point of this experiment. For the completeness, results obtained by *Ferrand* (1999) on nitrogen doped samples (up to $x_{eff} = 2.6$) with substantially lower carrier density are also presented in figure 5.12 as blue circles.

The monotonic rise of Curie-Weiss temperature with increase of effective Mn density predicted by mean field theory is visible as well for the experimental results. The exception from this tendency are two samples with quantum wells richest in Mn where Curie–Weiss temperatures are significantly lower than for smaller compositions. Such behavior is indicated as well by mean field calculations for quantum wells 10 nm wide where saturation of Curie-Weiss temperature results from competition between ferromagnetic and antiferromagnetic interactions. Despite the substantial drop, experimental results stay within experimental error from calculations (except of the 8 nm quantum wells with $x_{eff} = 4\%$. The only surprise is similarity of results between quantum wells of 10 nm and 8 nm width

We can conclude that simple mean field model yields good description of experimental data providing similar carrier densities are concerned. The influence of manybody effects is compensated by adjustment of A_F parameter and its value depends on actual carrier density.

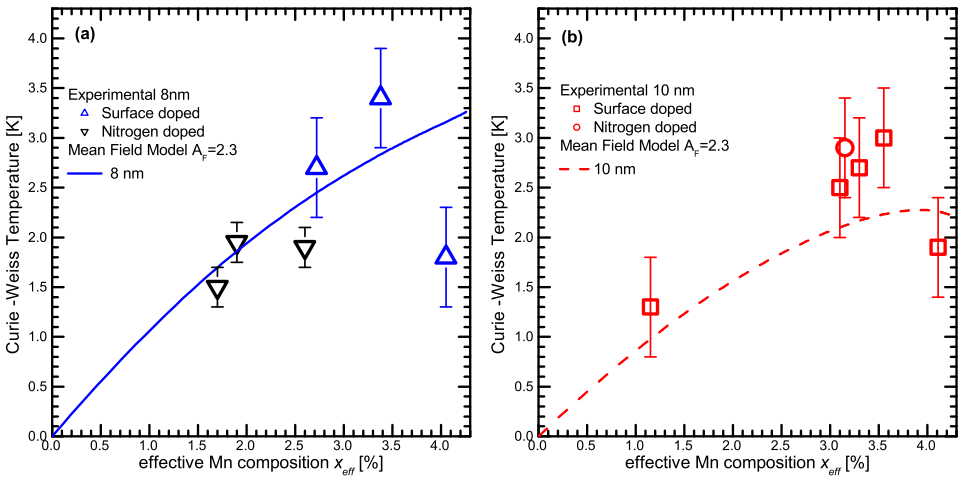

Figure 5.12: Experimentally determined Curie–Weiss temperatures for 8 nm and 10 nm quantum wells: panels (a) and (b), respectively. The carrier density was approximately 5×10^{11} cm^{-2} for all new results. Lines represent mean field model predictions for 8 nm and 10 nm quantum wells. Black down triangles mark previous results for the nitrogen doped samples with smaller carrier density.

5.4 Photoluminescence studies of magnetic ordering

Below the transition temperature, spontaneous ordering of Mn results in a local magnetization. According to the mean field model (*Dietl et al.*, 1997) the polarization of hole gas is expected to be instantaneous (in an extremely narrow range of temperatures). Therefore the effective magnetic field should also rapidly achieve its maximal value. The value of this field obtained within mean field approach is described by formula: 5.6. For carrier density of 5×10^{11} we obtain values of 180 mT for 8 nm wide quantum wells and 140 mT for 10 nm wide quantum well. Such fields should result in noticeable splitting of photoluminescence Therefore analysis of the spontaneous splitting of photoluminescence can be used in studies of magnetization of the ordered phase and the transition temperature.

Let us consider the changes in photoluminescence spectra with temperature. Experimental data can be seen in figure 5.13 (figures 5.2 and 5.3 present previous results). Indeed, below a certain temperature the PL line features a splitting despite no external magnetic field applied. The origin of this splitting has been attributed to the onset of local magnetization. As the temperature becomes lower the splitting becomes larger, allowing to distinguish between the two lines present in the PL spectra. The splitting is best visible for the lowest temperatures. Although the source of the splitting is magnetization the photoluminescence spectra is not polarized (nor linear or circular polarization analysis yielded any differences). The lack of polarization is due to the domain structure of the ordered phase: in the area probed by photoluminescence there are magnetic domains of both orientations. The efforts to determine the actual size of those domains did not yield final answers: the resolution of microphotoluminescence experiments of 0.5 μm was either insufficient or the time of domain wall shifting is too short for this kind of experiment. Despite the difficulties with magnetic domains the experiments in external magnetic field discussed in 5.1 still confirm the identification of PL lines.

The change of PL spectra can be used to determine the temperature at which the transition to the ordered magnetic phase occurs. In figure 5.13 the points indicate the supposed positions of the two lines. As the splitting becomes smaller the guess on the position of the upper line is more difficult (for example at 2.2K), yet the change of the PL spectra with respect to the 4.2K line shape is still unquestionable.

Instead of guessing, it would be more sensible to obtain the line positions from fitting the spectra with lines described by a model. Unfortunately, most commonly used, simple line shapes described by Gaussian and Lorentzian functions do not give satisfactory description of luminescence from the quantum well containing carrier gas. The complexity of the theoretical models describing photoluminescence line shape in presence of large density of 2D carrier gas (*Cox et al.*, 2004; *Ramon et al.*, 2003) allows to treat only a single, well resolved line. Moreover, in the most interesting range of temperatures close to the transition the lines contributing to photoluminescence are not well resolved which makes the fitting more difficult. The obtained results would not be very convincing unless we could use a model providing a perfect description of photoluminescence with only minimal number of free parameters used in fits. Unfortunately no such model is available.

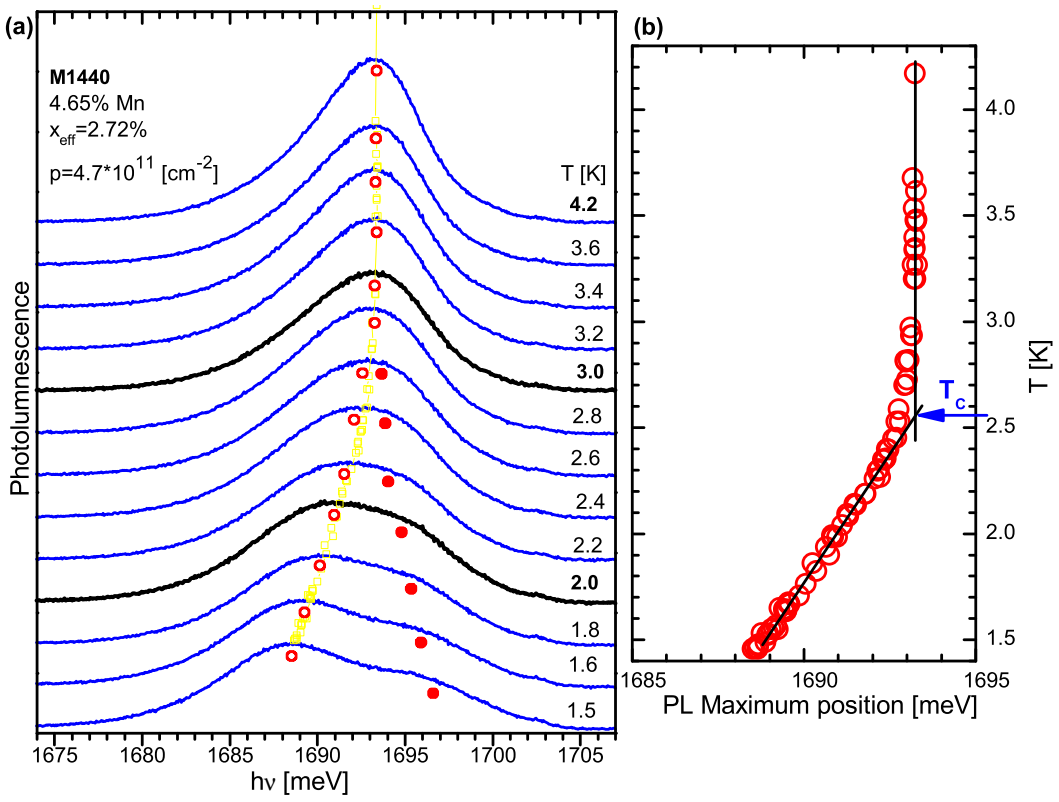

Figure 5.13: Photoluminescence spectra at selected temperatures for sample M1440. Carrier density is $p = 4.7 \times 10^{11}\text{cm}^{-2}$. Right panel presents variation of photoluminescence maxima position with temperature. Lines are drawn in order to aid determination of critical temperature. Critical temperature is indicated by an arrow.

In order to avoid guessing of the position of lines contributing to the PL shape (as it is difficult and doubtful especially at the higher temperatures close to the transition) an experimental procedure has been established, helping to determine the transition temperature (*Kossacki*, 1998; *Kossacki et al.*, 2000). Instead of looking for the first fingerprints of spontaneous magnetization in the PL shape itself, it is more convenient to trace the variation of the position of maximum of PL intensity with temperature. The intensity of upper PL component is smaller than the lower one, so the maximum of total intensity is expected to follow the lower line position. As shown in figure 5.13(b) the maximum of PL plotted versus the temperature for the temperatures below 2.5K shifts rapidly towards lower energies. The position of the kink is determined by crossing point of lines drawn manually along the experimental data. The crossing is additionally marked with an arrow. It is used to determine the critical temperature T_C. For the purpose of estimation of experimental error of T_C obtained by this procedure I have assumed it to be equal to the distance between the critical temperature and the temperature at which the experimental curve leaves the linear dependence, bending towards the lower energies, on the side of higher temperatures.

The described procedure of critical temperature determination has been established for the samples with moderate amount of Mn in the 8 nm wide quantum well. Relatively large value of magnetic field due to spontaneous magnetization combined with narrow photoluminescence lines allowed to obtain consistent results. However application of this method to the samples

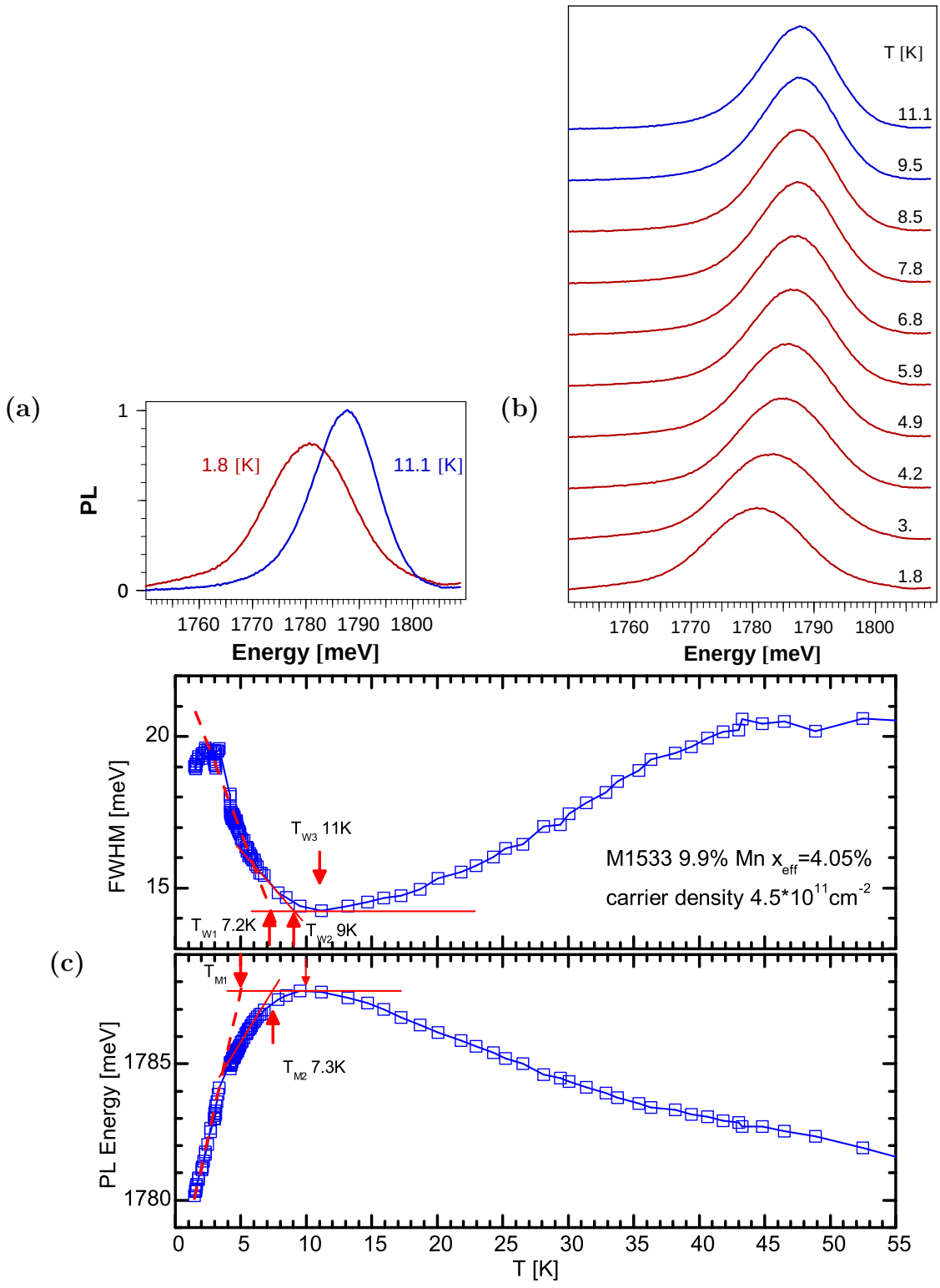

Figure 5.14: Sample M1533: Photoluminescence at selected temperatures. Carrier density is $p = 4.5 \times 10^{11}\mathrm{cm}^{-2}$. **(a)** Comparison of photoluminescence spectrum for temperature just above transition (blue) and spectrum at low temperature in ordered phase (red). **(b)**Photoluminescence spectra at selected temperatures. Blue color was chosen for spectra above transition temperature. Red color corresponds to spectra at ordered phase. **(c)** Analysis of variation with temperature of PL line width (FWHM) – upper panel and PL maxima positions. Labeled arrows indicate positions of characteristic points discussed in text.

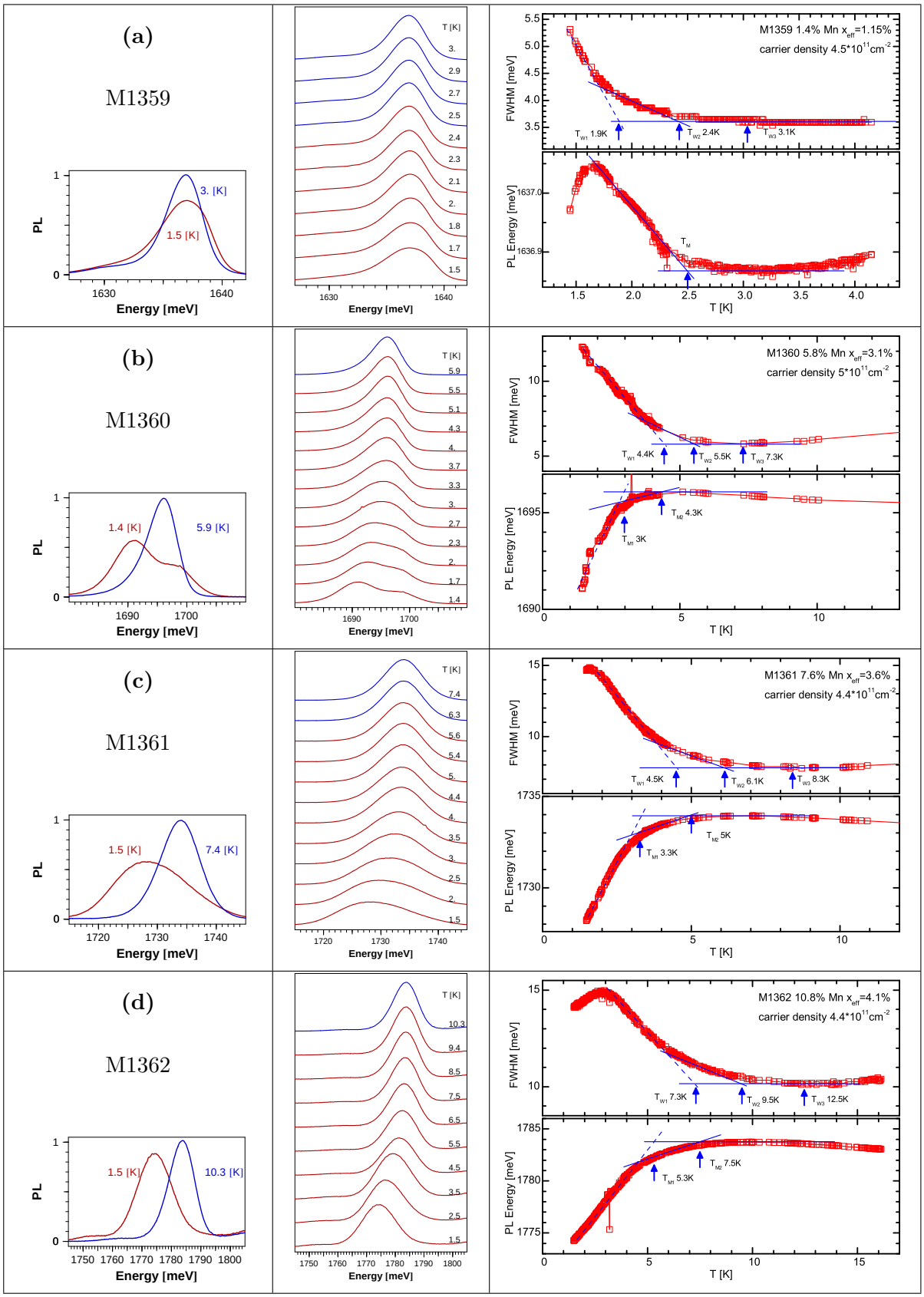

Figure 5.15: for series of samples containing 10nm wide quantum well with different Mn contents. For detailed plot descriptions refer to caption of figure 5.14.

with quantum wells containing more manganese indicated weak points of this method of critical temperature determination. Introduction of more Mn ions into the quantum well makes the spectral lines broader. At the same time, it raises the critical temperature forcing us to broaden the range of investigated temperatures. In case of sample M1533 the PL was studied from 1.5K up to 60K. The results are presented in figure 5.14(c). The experimental spectra presented in panels (a) and (b) of figure 5.14 illustrate the changes of PL line shape at selected temperatures[1]. The broader range of temperature allows us to analyze better the transition. At higher temperatures (in the range of 11 K to 55 K) it is possible to observe the usual changes of PL present in all semiconductor quantum wells: thermal broadening of PL and shift of luminescence line due to temperature induced bandgap changes. However, (when looking from the high to low temperatures) at certain temperature those natural processes are gradually overcome and, due to spontaneous magnetization, the line begins to broaden and PL maximum again shifts to lower energies. Although, for the reasons discussed later, it is not possible to identify the upper line present at low temperatures in the spectra the similarity to the case presented in figure 5.13 allows us to attribute this evolution to the spontaneous splitting.

The increased (about 9.9%) Mn content in the analyzed case results in less abrupt changes of PL maxima position with temperature. The tendency to broaden the temperature changes of PL maximum position with increasing Mn content can be well seen in figure 5.15 where results for a set of samples are shown.

The critical temperature determined according to the previously used procedure (using the PL peak positions from the lowest range of temperatures to draw the line indicating transition temperature) is marked as T_{M1}. The obtained temperature of 5 K is far from the bending point of the curve (around 10K) where the usual effects are starting to be countered by magnetic ordering induced ones. When the similar procedure is applied to the part of the results closer to the bending point a temperature $T_{M2} = 7.3$ K is obtained.

Similar analysis applied to the changes of the PL linewidth returns slightly higher temperatures: from the low temperature part we obtain $T_{W1} = 7.2$ K. When data closer to the bending point (11 K) are used we obtain $T_{W2} = 9$ K. The results for other samples shown in figure 5.15 also allow to notice the difference between temperatures obtained from PL maxima and PL width analysis. The discrepancy increases with increasing Mn content. In all cases the analysis of PL width returns higher values. In order to chose the best method of determination the temperature of transition to the ordered magnetic phase we have to perform careful analysis of PL spectra.

[1]The temperatures at which the presented spectra were recorded are indicated on graph. The highest presented temperature was chosen to present the spectra of smallest width. Then the evolution of the spectra with lowering of the temperature is illustrated.

5.4.1 Simulation

We lack the theoretical model providing satisfactory description of PL line shapes. Instead, we can use experimental spectra from polarization resolved experiments in external magnetic field. Thus by adding σ^+ and σ^- spectra at a given field we can obtain simulation of the non polarized spectra from ordered magnetic phase. Figure 5.16 presents such simulation for sample M1360 at natural carrier density. The simulation is based on experimental data discussed in previous section (5.3) where polarization resolved measurements were carried out (The spectra used in this simulation are also displayed in figure 5.7. It is more convenient to consider the actual Zeeman splitting than magnetic field as it provides more general information.

The comparison of spectra from experiment (figure 5.16(a)) with simulation 5.16(b)) allows us to consider the simulation as a sensible approximation of real spectra. The spectra at temperatures down to 2.3 K are well reproduced by simulation with splitting up to 5 meV. For lower temperatures the simulation is not able to reproduce the intensity of the upper line (despite the manual increase of upper line intensity in simulation by factor 1.25, constant through all simulation). This discrepancy is probably due to changes in spin relaxation induced by the ferromagnetic transition. The actual set of experimental spectra used for simulation construction was chosen because the temperature of this measurement was close to the temperature where PL line has smallest width. Despite the difficulties with intensity, the positions of lines in simulation sensibly reproduce experimental spectra.

The analysis of simulation width and maxima position helps to chose most accurate way to determine the transition temperature from PL spectra. The noticeable changes of PL width occur when the splitting is larger than 1 meV (14% of initial linewidth) while the maximum shifts only when splitting is larger than 3 meV (43% of initial linewidth). The consequences of this observation are serious as it questions accuracy of results discussed in previous works.

The value of the exchange field induced by fully polarized carriers is expected to depend only on carrier density. On the other hand, the splitting at a given field, heavily depends on the temperature. It can be seen on experimental data in figure 5.8 where for maximum carrier density at 0.16T the splitting decreases from 9 meV (at 3K) to 1.5 meV at 12K. Therefore it may happen that transition would remain undetected until the drop of the temperature provided significant increase of splitting. Figure 5.17 presents simulation of the sensitivity of both ways of determining critical temperatures calculated for the parameters of studied samples. The calculations were done with modified Brillouin function (equation 2.15). This analysis proves that the linewidth provides more sensitivity than PL maxima position especially for the samples containing smaller carrier densities. The results presented in figure 5.17 indicate that the previous results were dangerously close to the limit of sensitivity, however it is important to note that the calculations did not include boost of susceptibility due to the carriers nor the sensitivity limits were adjusted to acknowledge the linewidth differences between each sample. Those two factors might save the validity of previous analysis leaving only systematical error responsible for underestimation of critical temperatures.

Keeping in mind small values of splitting expected at higher temperatures we turn to relay solely on analysis of linewidth vs temperature experimental curve. However we have to consider that the changes of width are strongly affected by inhomogeneities and disorder present in the

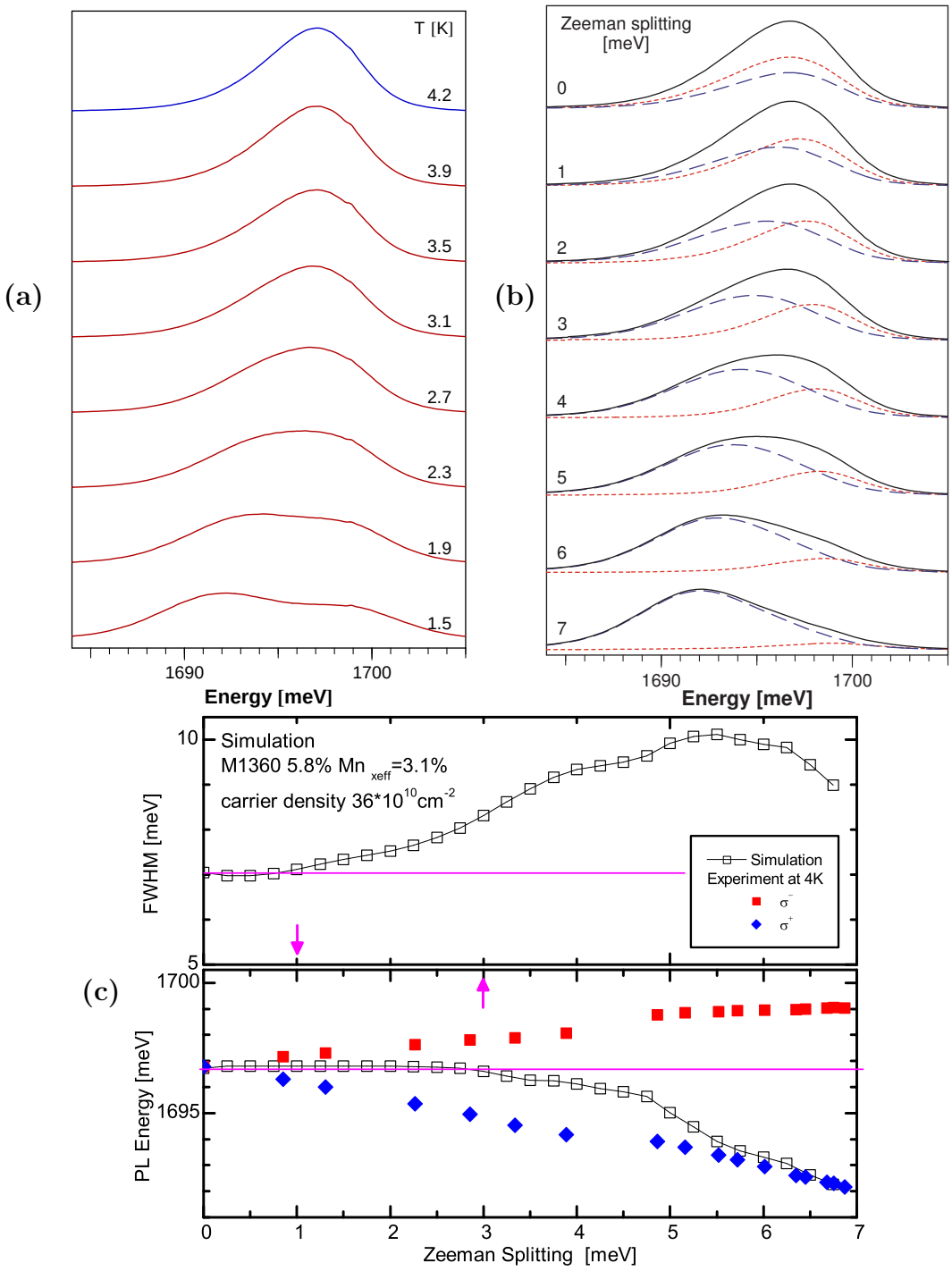

Figure 5.16: Simulation of PL at selected Zeeman splittings. Experimental spectra in magnetic field are from measurements on sample M1360 at 4K (presented also in figure 5.7. The carrier density is $p = 3 \times 10^{11}\mathrm{cm}^{-2}$. **(a)** Photoluminescence spectra at selected temperatures at corresponding carrier density. **(b)** Simulation of photoluminescence spectra for different Zeeman splittings. Experimental spectra used for constructing simulation are plotted with dashed lines. The amplitude of σ^+ component was lowered by factor 0.9 in order to better reproduce low temperature data. **(c)** Analysis of variation with splitting of PL simulation line width (FWHM) upper panel and PL maxima positions (empty symbols). Full square symbols in lower panel indicate actual positions of PL maxima of experimental spectra used in simulation. Horizontal lines indicate initial values.

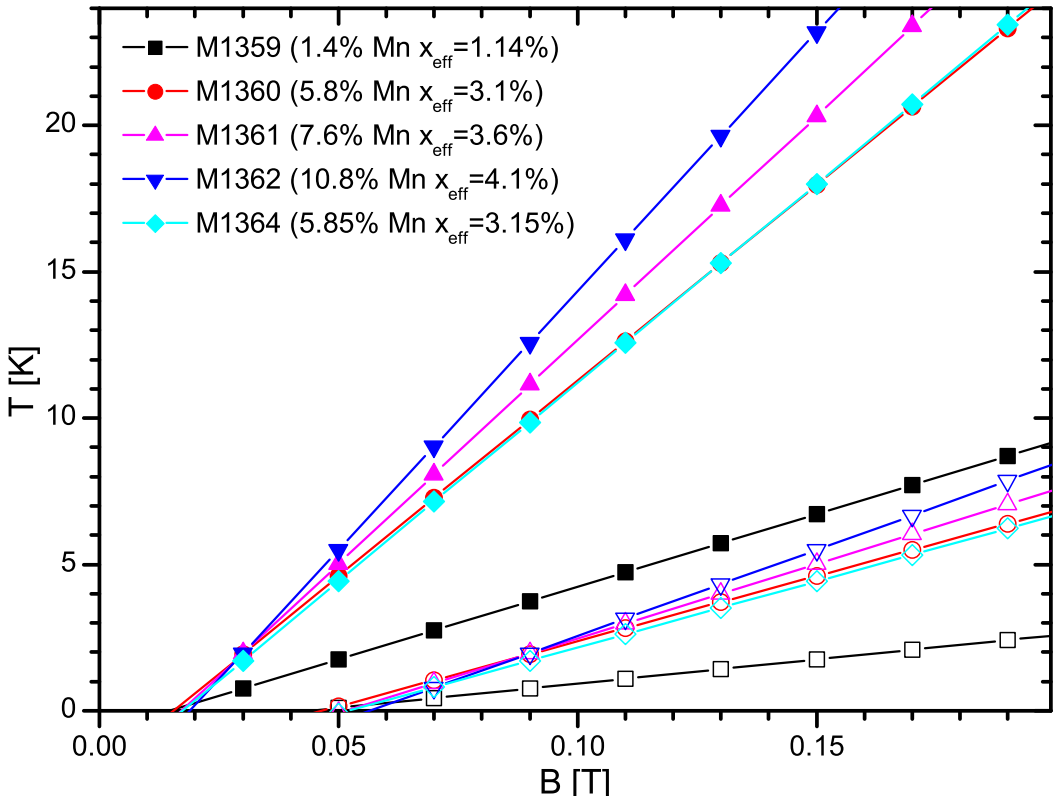

Figure 5.17: Detection limits of critical temperature. The zeeman splitting of 1 meV was assumed for analysis of linewidth (full symbols) and 3 meV for PL maxima analysis (empty symbols). The lines show temperatures (for a given field) below which the splitting is greater than the limits of sensitivity deduced from simulation.

sample. Therefore, to consider as a transition temperature the point at which the dependence bends would mean favoring minority areas where local fluctuations result in quicker response. In order to avoid that we have decided to consider this point only as an upper limit of experimental error of determined temperature. As the transition temperature we chose T_{W2} defined as a crossing point of horizontal line adjacent to the lowest linewidth with straight line drawn across experimental points at vicinity of minima, on the side of smaller energies (see figure 5.14). It is still important to check the behavior of PL maximum as the kink observed in low temperatures is a fingerprint of spontaneous splitting in ferromagnetic phase therefore, it can assure that the changes of width are due to spontaneous magnetization as well.

5.4.2 Photoluminescence shape at low temperatures in ordered phase

The better understanding of the evolution of photoluminescence spectra allows us to address several issues related to experimental results presented in figure 5.15. The first column is useful for comparison of spectra just above transition temperature (when they have the smallest width) with those taken at low temperature (about 1.5K) when the value of the splitting is large. Only in case of sample M1360 with moderate carrier density the two components of the line split due to spontaneous magnetization are clearly distinguishable. For sample M1361 the upper component is still present in the spectra but the lines are so broad that a clean separation is not possible. This situation corresponds to the spectra obtained in simulation for 6 meV splitting. However in this case the splitting is probably much larger which is the reason for the decrease of the upper line intensity.

The spectra from both extremes of the studied Mn density range display single lines at low temperature. In case of sample M1359 with low Mn content the splitting is too small for the separate lines to appear, similarly to simulation results for 1 meV splitting. However in this case the lines are narrow which, due to higher intensity of the upper component (compare figure 2.12b), results in unusual shift of the PL maximum to the higher energies with lowering of temperature seen in the figure 5.15 in right panel.

The high Mn density for the sample M1362 also leads to the observations of single line in the spectrum at low temperature. When the temperature is lowered below 3 K a narrowing of the line accompanied by a decrease of the transition energy indicates an attenuation of the upper component. We can expect (see chapter 2.2.2) that under this conditions the line visible in photoluminescence has changed its character and is, in fact, D_{low} component of the split triplet state. This is because for the carrier density of 44×10^{10} cm^{-2} the value of triplet splitting is 8 meV close to the Zeeman splitting at 3 K. The upper component D_{high} is present in the spectra but due to the width of the line it is not well resolved. The presence of D_{high} is witnessed by an LO phonon replica seen in the low energy tail of PL. The width of PL line makes the changes of PL spectra less spectacular than for sample M1360 despite much larger splitting. The results for sample M1533 presented in figure 5.14 document similar case of PL evolution.

The high values of splitting for samples with smaller Mn content may also result in transition from the trion luminescence to the signal related to the triplet state and PL spectra composed of D_{high} and D_{low} lines. Especially close to the critical value of Zeeman splitting for this transition the spectra become more complicated as instead of excitonic transitions from two split lines

additional two lines are starting to emerge (see figure 2.12), moreover we still have to consider domains of opposite spin orientation at one time. This is most unfortunate as it makes the interpretation of PL splitting most difficult even in the cases where the split components of PL are well resolved. Therefore special caution must be kept when such PL spectra are analyzed.

5.4.3 Carrier density dependence of T_C

The decrease of sensitivity of T_C determination for smaller magnetic fields puts in question the result displaying the dependence of critical temperature on the carrier density (figure 5.4). It may happen that lowering of critical temperature observed for smaller hole densities is due to decreased sensitivity of the experimental technique. In other words: maybe the critical temperature doesn't depend so much on the hole density (as the basic mean field approach would indicate) but it is just easier to detect the transition for the higher hole density (due to the larger field induced). Furthermore this issue becomes more important for the samples with higher Mn content because PL lines become broader and in natural consequence it is more difficult to detect small splitting.

Figure 5.18 helps to clarify those issues. Experimental results displayed in panel (b) show that the differences between the thermal linewidth dependence for different carrier densities are less spectacular than in case of PL maxima. Nonetheless the obtained transition temperatures vary with carrier density. The transition temperatures obtained in both ways are displayed in panel (a) for comparison. The results from more sensitive technique are shifted about 2K into higher values but also display a weak dependence on carrier density. In this case the obtained temperatures are well within computed area of sensitivity (except the point at the smallest

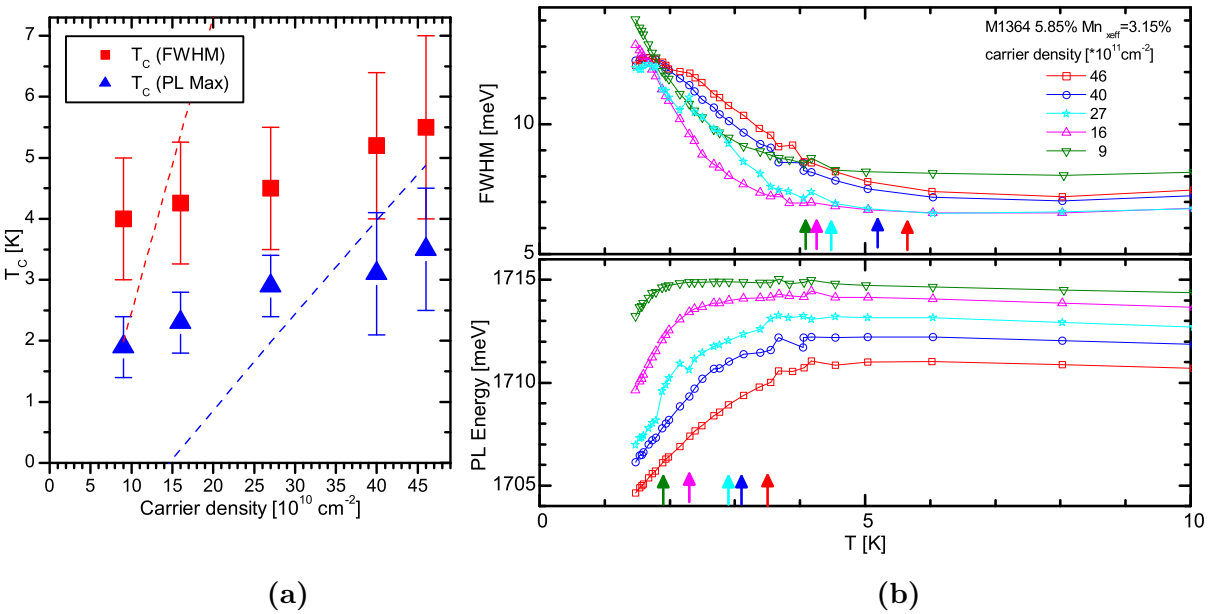

Figure 5.18: Sample M1364, (6.85% Mn $x_{eff} = 3.15\%$): Dependence of transition temperature on carrier density. **(a)** Comparison of temperatures T_C obtained from analysis of width (squares) and previously used technique for analysis of PL maxima (triangles). Lines indicate the calculated sensitivity thresholds. **(b)** Widths (upper panel) an positions of PL maxima (lower panel) at different temperatures for selected carrier densities. Arrows denote determined critical temperatures.

carrier density but in this case the difference should be compensated by sensitivity enhancement due to carriers). However for PL maxima analysis the lowest points are dangerously on the edge of sensitivity.

5.4.4 Mn density dependence of T_C

It is interesting to compare the critical temperatures obtained at maximal carrier density for different samples. In each sample it was increased to approximately 50×10^{10} cm^{-2}. The experimental results from previous section (5.4.3) indicate a weak dependence of T_C on carrier density for large densities, therefore the results presented in figure 5.19 are consistent. Contrary to Curie-Weiss temperatures it is not possible to directly relate our values to the previously published results due to difference in data analysis (5.4.1). However broad range of Mn density in the studied choice of samples covers almost all the cases that are accessible to chosen experimental approach.

The monotonic rise of Curie-Weiss temperature with increase of effective Mn density predicted by mean field theory is visible for the experimental results. In order, to achieve satisfactory description of the experimental data by the mean field model (discussed in 5.1.1), the value of Fermi liquid parameter A_F had to be increased to 4. This value of A_F is almost twice larger than the one used in previous works or for description of Curie-Weiss temperatures. However, now it is in agreement with results of *Boukari et al.* (2006). Surprisingly, the differences between results for quantum wells of 10 nm and 8 nm width are not significant, in contrast with the mean field calculations.

Additionally, two samples with quantum wells richest in Mn have significantly higher transition temperatures than those with smaller compositions.

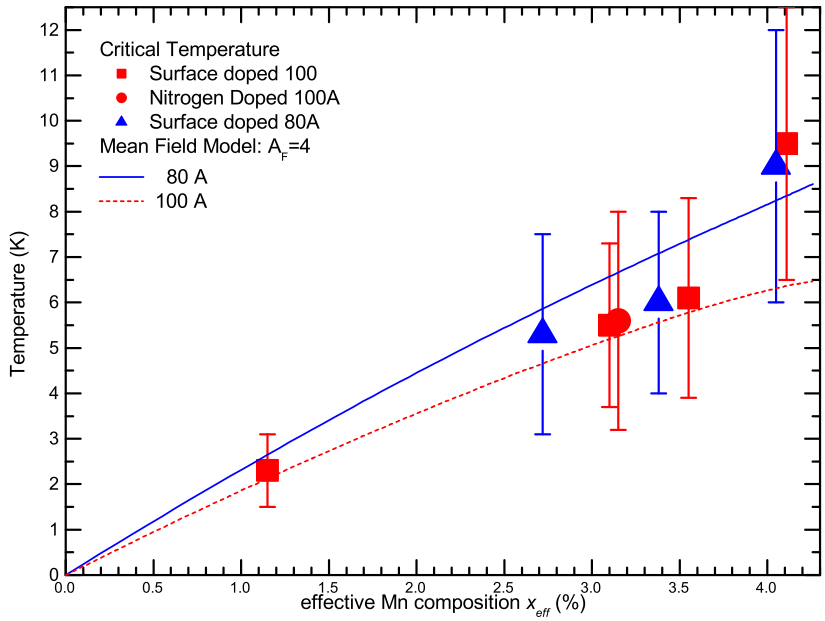

Figure 5.19: Experimentally determined critical temperatures temperatures. The carrier density was approximately 5×10^{11} cm^{-2} for all results. Lines represent mean field model predictions for 8 nm and 10 nm quantum wells.

5.5 Summary

In the present studies of carrier induced ferromagnetism in p - type quantum wells both types of doping were used: nitrogen acceptors embedded in the barrier and acceptor states formed on the surface of the sample. The origin of the hole gas seems to have no influence on the macroscopic properties of the ordered phase. The properties of spontaneous magnetic ordering were examined in two ways. Studies of susceptibility of paramagnetic phase allowed us to determine Curie-Weiss temperature (T_{CW}). Critical temperature (T_C) values were determined from spontaneous splitting of low temperature photoluminescence. However, the lack of satisfactory description of photoluminescence line shape did not allow us to analyze in detail the development of spontaneous splitting with temperature. The same reason kept us from performing a detailed study of the relation between the Mn density and the spontaneous splitting.

The practical application of surface doping allowed us to extend the studied range of Mn densities in quantum well material up to 10.8%. We observed thus the highest ever reported transition temperature for this type of magnetic system $T_C = 9.5 \pm 3$K (for $x_{eff} = 4.1\%$ and $p = 5 \times 10^{11}$ cm^{-2}).

Experimental results for samples with higher Mn content forced us to revise the techniques of data analysis. The analysis of PL line width instead of maximum position provides more sensitivity. It is essential for samples on the extremes of the studied Mn composition range, with either small (below 2%) or high (above 6% Mn) density of Mn spins. New approach resulted in higher estimated values of critical temperatures.

Analysis of the data with more sensitive method confirmed previously observed (*Kossacki et al.*, 2000, 2002) weak influence of carrier density on critical temperature. Our study shows that this also applies to the Curie - Weiss temperatures. It can be attributed to the variation of carrier spins susceptibility enhancement with the hole gas density as discussed in A recent work by *Boukari et al.* (2006). Adjusting the value of A_F enhancement parameter accordingly to carrier density provides the way of describe the experimental data within the mean field approach used previously. However the precise A_F - carrier density relation has yet to be established.

The comparison of Curie–Weiss and critical temperatures is presented in figure 5.20. The difference between Curie-Weiss and transition temperatures, was present in older results, however it was small and the discrepancies were within experimental accuracy. The values obtained from a PL width analysis make the difference more pronounced. It is bigger than experimental errors which are considerable due to cautious approach to the applied analysis technique. As a mater of fact, the critical temperatures are almost twice larger than the Curie–Weiss ones.

Mean field model well describes the Curie–Weiss temperatures for the parameter $A_F = 2.3$ used to describe the influence of the many body effects on susceptibility of hole gas. The value of this parameter had to de slightly increased with respect to older results where $A_F = 2.1$ yielded good description of data. It is due to higher carrier density in studied samples.

In order to apply the mean field calculation to the critical temperatures the A_F parameter has to be increased to 4. Such value is agreement with the experimental and theoretical results presented by *Boukari et al.* (2006) for the carrier density present in the studied samples.

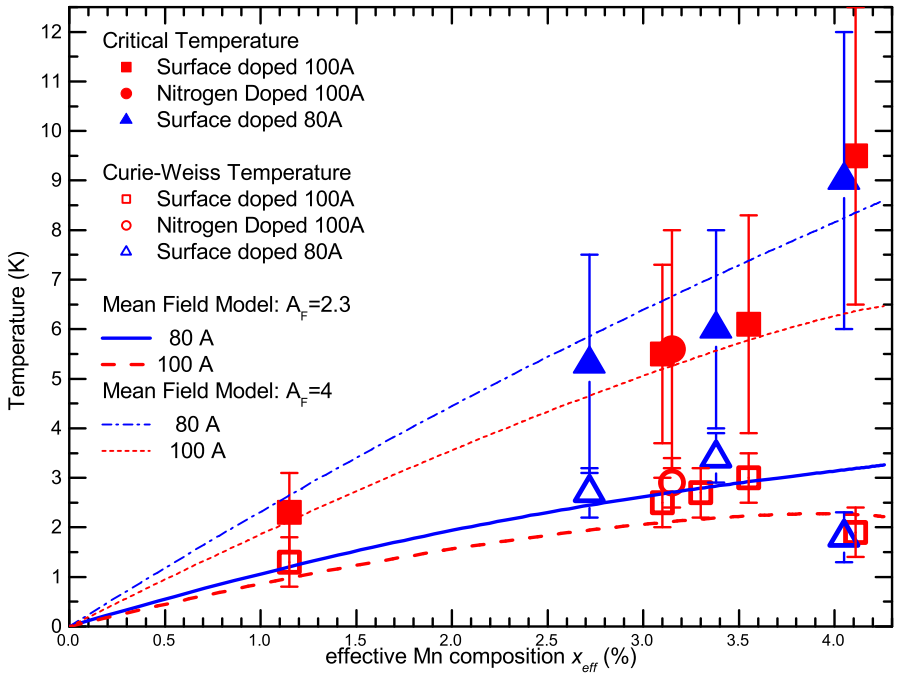

Figure 5.20: Critical (full symbols) and Curie-Weiss (empty symbols) temperatures.

The significant differences between critical and Curie – Weiss temperatures are bigger than experimental errors.

Part of the difference can be attributed to the formation antiferromagnetic bound Mn spin complexes. We have run simulation of susceptibility of bulk (Cd,Mn)Te into which we included only presence of single Mn spins and formation of Mn spin pairs (antiferromagnetically bound). Such approach is valid below 5% of Mn because for higher Mn content more complex arrangement of spins gain importance and should be also included. The proportions between components were set for each Mn composition assuming a random distribution of Mn ions. In our simulation we modeled susceptibility of single spin with Brillouin function. The susceptibility of pairs was determined from appropriate statistical sum. The comparison with calculations in which the presence of pairs was turned of allowed us to estimate the influence of spin complexes on Curie-Weiss temperature determined in our experiment.

For Mn composition of 3% (real) we obtained 1 K difference while for 5% composition the difference increased to 1.2 K. Although the calculated differences are too small to explain the experimental results they indicate the source of discrepancy between T_C and T_{CW}. The differences are due to the fact that experimental techniques used for determination of T_C and T_{CW} are most sensitive to different spin subsystems. The susceptibility measurements are performed at higher temperatures therefore are strongly affected by Mn spins bound in complexes which break with increase of the temperature. The photoluminescence measurements without magnetic fields are performed at low temperatures therefore all of the complexes are frozen so only “free” spins are responsible for the changes of luminescence. Those spins can be easily arranged by carrier mediated interactions therefore the observed critical temperatures are higher than Curie-Weiss temperatures.

The observed differences between critical and Curie - Weiss temperatures exceed the predicted influence of spin complexes. However, a recent theoretical work by *Kechrakos et al.* (2005) significant reports also a suppression of susceptibility due to the presence of antiferromagnetic interaction is reported.

On the other hand, a part of enhancement of T_C values determined in low temperature PL experiments may be due to increased susceptibility of Mn ion system at higher values of $\vec{k}$ vector with respect to the usually considered value of susceptibility at $\vec{k} = 0$. High carrier density makes those wave vectors available to holes present in the quantum well. However, we do not expect very strong effect in the range of accessible values of $\vec{k}$ (between 0 and k_f). It is important to note that this effect does not apply in external magnetic field[2]. Therefore, while it is irrelevant in higher temperature susceptibility measurements it enlarges the critical temperature. Therefore it can contribute to the observed difference between T_C and T_{CW}.

Contrary to mean field predictions, which so far provided satisfactory description of experimental data, there are no significant differences in T_C nor T_{CW} when 8 and 10 nm wide quantum wells are compared. Therefore, we can assume that the gain due to more compact wave functions in narrower quantum well was balanced by stronger antiferromagnetic coupling.

Two samples with highest ($x_{eff} > 4\%$) Mn composition values and therefore highest critical temperatures are worth special attention. Both of them feature significant boost of T_C along with the drop of T_{CW} with respect to the tendency set by the rest of the samples. The drop of the Curie - Weiss temperature might result from the fact that the susceptibility measurements were performed at temperatures too close to the transition temperature (which turned out to be much higher than expected during the time of measurements) and therefore might not be valid. On the contrary, the jump of critical temperature cannot be explained by the inappropriate experimental analysis. However, although the x_{eff} values of the two samples (4.11% and 4.05%) are similar to the next ones (starting from 3.55%), the difference in estimated Mn density is much larger. This fact may contribute to the explanation of the observed peculiar magnetic properties of the two samples.

[2]Homogenous external field probes susceptibility only at $k = 0$.

CHAPTER 6

Microphotoluminescence study of disorder

Contents

The setup presented in section 3.2 gave us opportunity to optically probe the sample properties in the μm range. The most significant gain lies in the ability to probe at a time only very small (0.5 micrometer in the diameter) areas of the sample. Moreover by tilting the quartz plate we can move the excitation and detection spot over the sample. Systematic measurements at adjacent spots were performed by scanning the sample surface, thus entire maps of photoluminescence were gathered. Application of this experimental technique to the studies of quantum wells with hole gas and magnetic ions allows us to study the micrometer sized distribution of fluctuations in the sample properties. It allows us to trace the effect of the disorder on the properties of the ordered magnetic phase. Although the spatial resolution is poorer than those achieved in the magnetic force microscopy (MFM) and similar scanning experimental techniques, the advantage of micro photoluminescence studies lies in the ability to probe magnetic and electronic properties together under experimental conditions as close as possible to those of usual magnetooptical experiments. Therefore we are able to gain the insight into the ways by which disorder is introduced into our samples. Unfortunately even in microphotoluminescence experiment with resolution better than 0.5 μm the photoluminescence is averaged over different domains as was shown in previous work by *Kossacki et al.* (2002).

The magnetic ordering is a result of interaction between the carrier gas and Mn ions. The experimental setup allows us to investigate not only spontaneous splitting but also crucial parameters affecting magnetization like local variation of Mn ion density or carrier density.

The application of the micro photoluminescence spectra measured as a function of the temperature for the determination of the critical temperature should result in the observation of the sharper kink on the plots used for the determination of the transition temperature. This would be the result of the suppression of the broadening due do the disorder. Unfortunately the construction of the microscope makes such experiment difficult to perform as large mass of microscope remains in the thermal contact with the sample causing the difficulty in the precise determination of the actual temperature of the sample.

6.1 Experimental approach

The configuration of experimental setup restricts experiment to photoluminescence measurements. It can be collected at various points on the sample therefore through systematic sweep of excitation and detection location over the sample maps of local properties can be recorded. The size of laser spot limits the resolution to 0.5μm. Such map can be constructed from many spectra (the largest map, in our experiment contained 4096 individual spectra). The usual spatial distance, between experimental points in our experiment was 0.5μm; however, in certain cases it was doubled in order to investigate larger area of sample. Surely, the more spectra, the better information we obtain due to increased scan area or spatial resolution. However, time of experiment is also an issue. Moreover special care should be taken concerning the light power used.

Excitation power

The excitation power is essential in the microphotoluminescence experiment. Since the laser beam was introduced in a way ensuring the size of the excitation area to be smaller than 0.5 μm one could expect very high density of power of light on the surface of the sample. It can result in drastic increase of the temperature, in extreme cases leading to damage of the sample and the microscopic lens. On the other hand, small excitation power forces long integration time during the measurements thus drastically increasing the time of the experiment. Longer integration time of each spectra forces the reduction of number of experimental points and therefore spatial resolution is lost or smaller area of sample can be investigated.

For best illustration of this issue spectra for the ferromagnetic sample collected at one spot of the sample are presented in figure 6.1. The measurements were performed at the temperature bellow the T_c thus we were able to use the spontaneous Zeeman splitting as a very sensitive probe of the temperature. The changes of the PL spectra shape with the increasing power are clearly visible on graph 6.1(b), while graph 6.1(a) indicates intensity of the collected PL as well. The most precise information can be read from the graph 6.1(c) where the positions of the two lines attributing to PL spectra are plotted. We attribute those changes in spectra to the heating of the sample by laser.

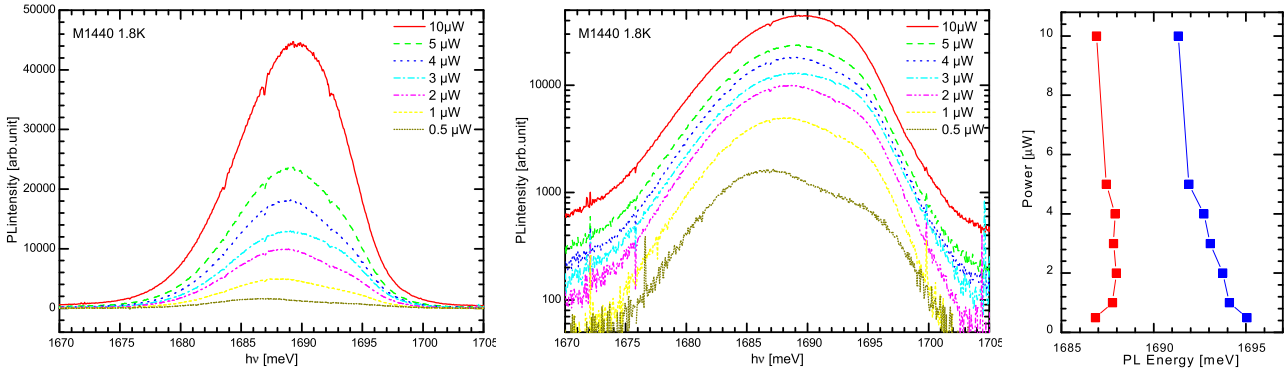

(a) (b) (c)

Figure 6.1: Power dependence of microphotoluminescence. The spectra were recorded at 1.8K at one spot. (a) linear scale, (b) log scale, (c) line positions obtained from fitting.

The optimal excitation power for the experiment is 2 μW providing sensible intensity of a recorded signal thus shortening the acquisition time and allowing to capture more experimental points. Such power calibration was always performed prior to each series of mapping measurements.

6.1.1 Zero field

Interpretation of changes of photoluminescence spectra recorded without magnetic field is difficult because it is influenced by many factors. Alloy fluctuations of quantum well and barrier material would result in the bandgap changes, which would affect optical transition energies. The optical transition energies are also affected by the carrier density and well width fluctuations.

In case of samples with moderate Mn content at low temperatures we can expect characteristic double line spectra. As discussed before, in chapter 5.4, the splitting (in this chapter we will refer to it as *ZFS*, in shortening) is due to spontaneous magnetization, the value of the splitting being proportional to the magnetization value. Providing, the components in the spectra at low temperature are resolved it is possible to determine the local variations of spontaneous magnetization. We achieve it by fitting Gaussian lines to the experimental spectra. Because the shape of lines is not exactly Gaussian, we cannot discuss absolute values of spontaneous magnetization. However, the systematic error due to approximation of line shape should be similar from point to point of one sample. Therefore, we can gain access to local variation of spontaneous magnetization. Thus we can obtain information on one of the key parameters describing the ferromagnetic phase.

Some care must be taken since the destabilization of the X^+ can occur due to the giant Zeeman effect induced by the spontaneous magnetization. This situation is easily recognized, by the observation of a temperature-independent zero-field splitting. In the present study, the spontaneous magnetization was always smaller than the value needed to destabilize the X^+. Note also that at incomplete spin polarization, carrier-carrier interactions lead to additional shifts of the PL line (*Kossacki et al.*, 1999, 2004*a*). For the present values of the spin splitting, there is no doubt that the hole gas is fully polarized, so that carrier-carrier interactions do not change with field and temperature.

6.1.2 Magnetic field

The experimental setup allows to apply magnetic field in Faraday configuration. It allows us to exploit characteristic properties of DMS quantum wells and investigate the two essential parameters of our magnetic system: carrier density and Mn spin density.

Figure 6.2 presents results of microphotoluminescence measurements performed at one point of the sample. The presented sample had sufficient Mn density to observe spontaneous splitting at zero field.

Typically the hole gas concentration is deduced from the Moss-Burstein shift. However, we cannot measure reflectivity (due to the construction of the microscope) nor PLE (because time necessary for such measurements makes them useless in mapping). An alternative way of carrier density determination has been discussed in section 2.3.1. In case of sample shown in figure 6.2 the spectrum evolves toward the line made of the D_{high} and D_{low} components for fields higher than 0.25T. The analysis of the D_{high}–D_{low} splitting – HFS is very convenient as all the necessary data can be obtained from a single spectrum. This makes it a perfect choice for carrier density determination in a mapping experiment.

The Mn concentration is usually obtained from the fits to the Zeeman splitting measured in relatively high field (up to few Teslas). As discussed in section 2.3.2 it is usually determined from the reflectivity measurements, preferably under illumination reducing the hole gas concentration. Such experimental conditions are applied in order to avoid the complications in interpreting the data from the low fields where the effects due to the carriers can mask entirely the excitonic Zeeman splitting (*Kossacki et al.*, 1999). We are limited to the PL experiments, and to make things more difficult, we cannot apply additional illumination to deplete the carriers. Therefore we have to cope with such difficulties. The effects related to increasing polarization of carrier gas can be clearly seen in figure 6.2 at low fields. However, at fields above 0.3T (in the presented case) the situation becomes stable and we can observe the triplet splitting. Moreover, Both PL lines follow the modified Brillouin function.

The difference between the position of line at two relatively high values of the external field is proportional to x_{eff}. For our purposes we decided to analyze the shift of the low energy component D_{low} due to its higher intensity. In order to improve accuracy we chose to analyze the shift of the D_{low} position between 1T and 3T (it provides that the effect of the hole gas is negligibly small). It shall be referred to as "Zeeman shift" – *ZS* in shortening. The figure 6.3 illustrates the idea of this experiment.

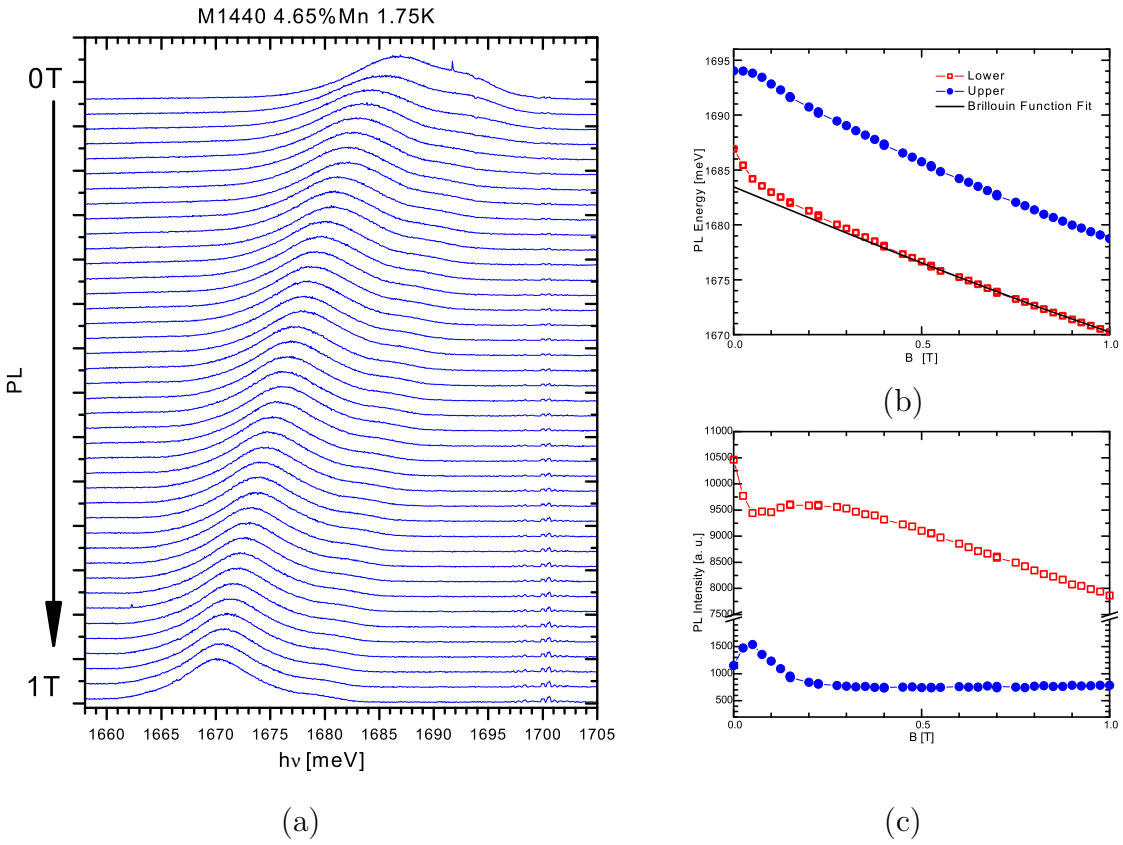

Figure 6.2: Dependence of microphotoluminescence on the external magnetic field. The spectra were recorded at 1.8K at one spot. (a) PL spectra, (b) Line positions obtained from a fit of two gaussian lines, (c) Line intensities obtained from the fitting.

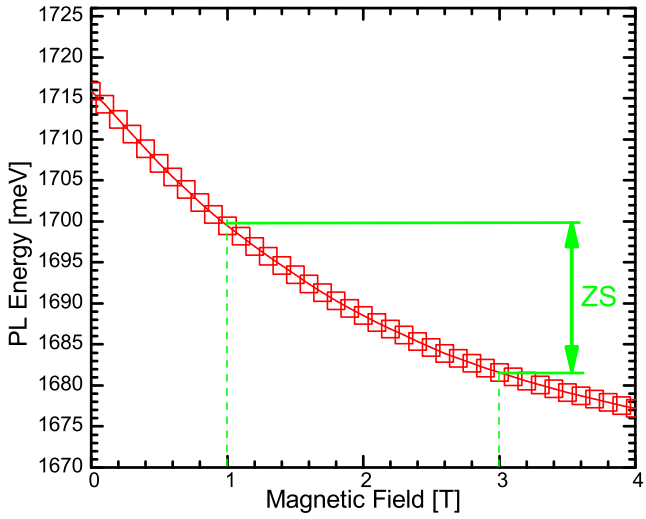

Figure 6.3: The idea of "Zeeman Shift" determination.

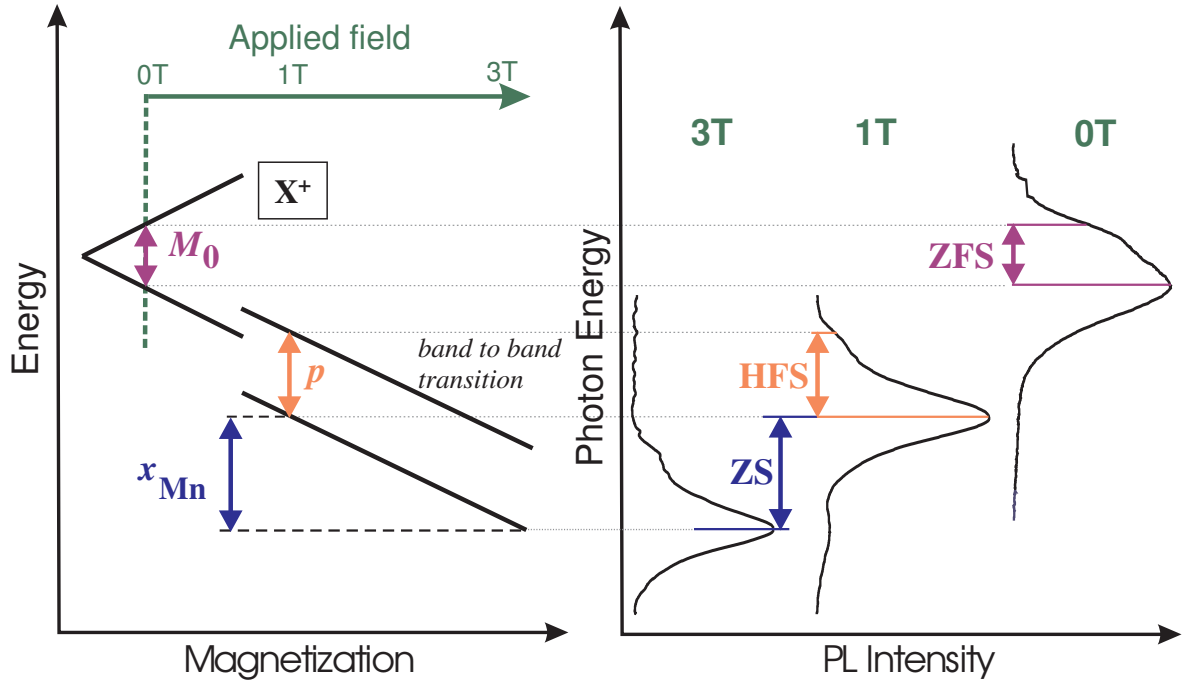

Figure 6.4: The idea of determination of basic parameters **(a)**. The set of spectra **(b)**, demonstrating the experiment, were recorded at the center of investigated area at 1.8K and different magnetic fields. Spontaneous magnetization M_0 is determined from zero-field splitting (ZFS), hole density p is determined from D_{high}-D_{low} splitting (HFS), effective Mn density variation from Zeeman Shift (ZS).

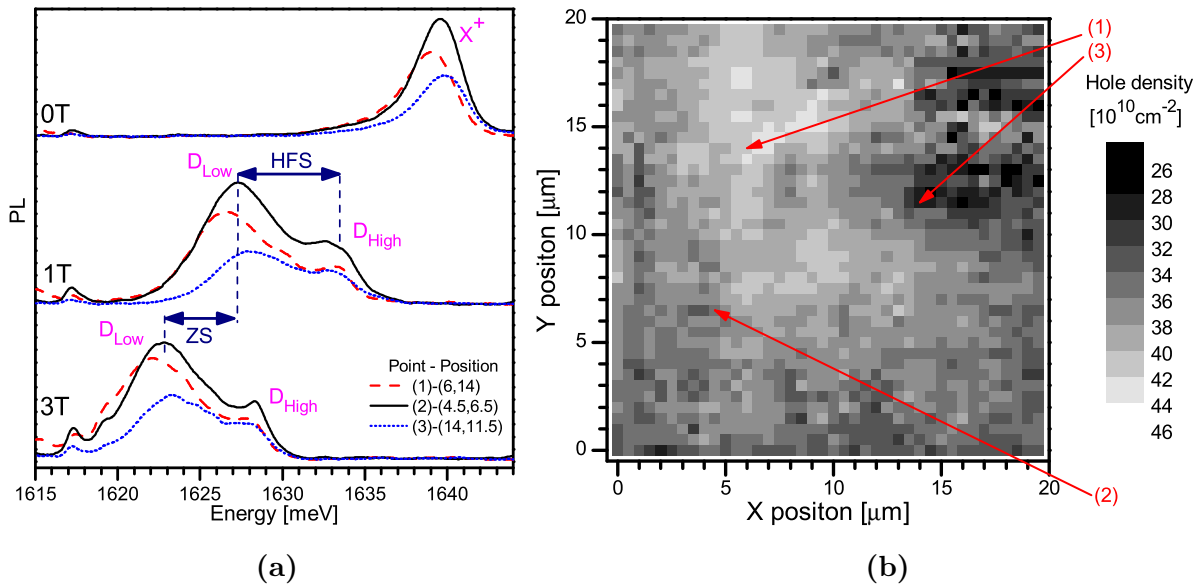

Figure 6.5: **(a)**Micro-PL spectra measured on sample S2 at different spots. **(b)** Micro-PL map of the carrier density obtained from the splitting between the two components of the σ^+ PL line at $B = 1$ T, Arrows indicate location of spectra in panel (a).

6.1.3 Processing of the spectra

As mentioned before the micro-PL experiment gave us an insight into spatial variation of following three quantities:

- Local magnetization manifested as spontaneous Zeeman splitting of PL line without external field applied (*ZFS*).
- Carrier density witnessed by the splitting of PL line at high external magnetic fields (*HFS*).
- Effective concentration of Mn (x_{eff}) measured by local value of shift of line positions induced by the Zeeman splitting in external magnetic fields (*ZS*).

Necessary data can be obtained from three maps of micro-PL recorded at low temperature: one recorded without magnetic field applied, one at 1T, and one recorded at 3T. The idea of experiment is presented in figure 6.4, where the spectra collected at one point of the sample are shown. The shapes of the spectra may vary from point to point on the sample as shown in figure 6.5.

For each studied point on the sample we collect three spectra (like those in figure 6.4(b)). From each spectra we determine line positions.

In case of ferromagnetic samples line positions are obtained by fitting the experimental spectra with Gaussian lines. Three gaussian lines were used in order to take into account the LO phonon replica of D_{high} component. Example fits are shown in figure 6.11. Due to high carrier densities in the studied sample, even without magnetic field, some evidence of the phonon replica can be noticed. In such case, using an additional (third) line helps to improve the accuracy of the fit. A similar procedure was applied to the data at high magnetic field. However, when magnetic field is sufficient, PL line due to phonon replica of D_{high} component can be directly identified. The energy of the considered LO phonon is well known (22meV). Therefore the two lines reproducing the high energy line and its replica were fitted with only one parameter for the transition energy while the distance between them was constant. Such procedure allows to improve the accuracy of the determination of transition energy of D_{high} component. In fact, since due to the large width of main PL line and small (compared to linewidth) splitting between the D_{high} and D_{low} components the phonon replica was often better resolved than the D_{high} component itself.

In case of samples with smaller Mn density the lines were sufficiently resolved, so the line positions could be determined without fitting. For those samples, the zero field data are difficult to interpret and we shall not discuss them.

The temperature was kept constant during the series of measurements for each sample.

In case of studies of the ordered phase the choice of the experiment temperature is critical. If it is set too high, the splitting of the PL lines in the ordered phase would be small and difficult to determine. However, when it is set too low there is a risk of approaching the point where the crossing of singlet and triplet states occurs at the field of spontaneous magnetization. In this case the analysis of zero field splitting may lead to false conclusions. It can be verified with the help of phonon replica. In an ideal case it would be absent at zero field. In our case it is always present, but relatively small intensity at zero field (as compared to higher field data) indicates that the fundamental state is still a singlet trion.

6.2 Statistical analysis

After capturing and processing the spectra we obtain a matrix of data where each number corresponds to a value of physical quantity (like HFS) at specific point of the sample. We can convert the values, as described in section 2.3, into parameters such as carrier density or x_{eff} (In case of x_{eff} it is essential to know the exact value of the temperature, which in microphotoluminescence experiments is difficult to determine). It is possible to plot such matrices of data and 2D maps are obtained. An example can bee seen in figure: 6.5(b), where fluctuations of carrier density can be seen. However, to get a quantitative description we need to apply some statistic analysis. For each set of map data we calculate mean value as well as standard deviation. Homogeneity of distribution can be most easily verified by regarding the histogram plot of the data.

6.2.1 Height-height correlation

The characteristic length of the fluctuations of z can be determined by plotting the height-height correlation function:

$$f_z(R) = \frac{\langle z(\vec{r})z(\vec{r}+\vec{R})\rangle - \langle z\rangle^2}{\langle z^2\rangle - \langle z\rangle^2} \tag{6.1}$$

The averaging runs over $\vec{r}$ vector as well as over the direction of $\vec{R}$. If z is distributed randomly (no correlation from point to point), then f_z decreases from 1 to 0 over a distance which is related to the spatial resolution of the experiment (spot size, diffusion of the excitons, ...). Then $f_z(R) = 1/2$ for R =FWHM/$\sqrt{2}$. Any correlation of z over a larger distance can be detected on the correlation function and its characteristic length determined as the distance for which $f_z(R) = 1/2$. Some of the properties of height–height correlation function are presented in appendix B. We placed there calculated correlations for simulated sets of data constructed from objects of known dimensions.

6.2.2 Correlations

In order to decide what is the nature and the origin of fluctuations we used the Pearson correlation coefficient. It was used to quantitatively analyze the correlations between the parameters deduced from the experimental spectra. It is defined by the following formula:

$$R = \frac{\langle xy\rangle}{\sqrt{\langle x^2\rangle\langle y^2\rangle}} \tag{6.2}$$

where $\langle x^2\rangle$ is the centered second moment of x, etc.

The values of this coefficient fall within the range from -1 to 1. The 0 value represents totally uncorrelated data, while value +1 corresponds to the perfect linear correlation of the X, and Y values. The negative values indicate the anti-correlation of the data: arrangement where the increase of one is followed by the decrease of the other value, assuming -1 for the perfect linear case. The statistically meaningful value of the coefficient depends on the number of data

compared. For the typical set of data containing 1024 points value larger than 8% is considered meaningful with the significance level 0.01 (i.e., 99% confidence), while for sample of 256 points the same significance level is obtained at the coefficient value of 16%.

6.3 Samples

A set of samples was selected for the studies. Their parameters are collected in table 6.1.

In addition to the surface doped samples discussed in previous chapters, we also investigated two nitrogen doped samples: one with a low Mn density and the other one with sufficient Mn density to observe ferromagnetic transition. Both had similar structures and p-doping was achieved by embedding a nitrogen-rich layer in the topmost barrier, 20 nm from the QW. In case of samples S1, S2, S3 and S4, the QW was covered by a 25 nm top barrier, thin enough to observe hole gas generation by surface acceptor states. The growth temperature of sample S1 was kept the same as for nitrogen doped samples for comparison purposes.

Sample	L_{QW} [nm]	x_{Mn} [%]	p [10^{11}cm^{-2}]	Doping	T_{growth} [°C]	Name
N1	8	0.2	3	N	220	M1305
N2	10	5.8	4.5	N	220	M1364
S1	10	0.5	3.5	surface	220	M1333
S2	10	1.4	3.5	surface	280	M1359
S3	10	5.8	3.6	surface	280	M1360
S4	8	4.6	4.7	surface	280	M1440

Table 6.1: Parameters of the studied samples

The focus of this experiment is on studying the properties of the ordered phase therefore we selected samples N2, S3 and S4 with well defined ferromagnetic transition. Due to moderate Mn content we can expect well resolved components in the low temperature spectra. Along with surface doped samples we chose also a nitrogen doped one to examine the influence of doping type. Additionally we also included in this study samples N1, S1 and S2 with small Mn content (where no ferromagnetic phase is observed). By doing so, we planned to verify the influence of average Mn content on the observed fluctuations.

The selected samples provide the following:

- thermal fluctuations are negligible in the ordered phase,
- electrostatic disorder is smaller than in thick layers, thanks to remote doping,
- magnetic disorder due to the random distribution of Mn atoms is preserved,
- we can deduce spin density, carrier density and eventually, the local magnetization , from micro-PL data.

6.4 Results

In this section we collect results of micro-photoluminescence mapping experiments. The plots are gathered in tables. Results for one sample are gathered in a row. First column contains name of the sample. Second column presents density plot of values derived from experiment. Each square corresponds to the point on the surface of the sample, about 0.5 μm in diameter (determined by the laser spot size). The axes are labeled in such a way, that coordinates of the center of each plotted square correspond to the coordinates of the experimental point. The chosen unit for X an Y axes is 1 μm (it is not marked on the plots in order to conserve space). Third column of the table presents contour plots of the data presented in column two. On such plots it is easier to regard the sizes and magnitudes of fluctuations. Fourth column contains histograms of the data. The topmost histogram label contains basic parameters of distribution: mean value and standard deviation.

The measured high field splitting was converted into carrier density as discussed in section 2.3. The values are presented in figures 6.7 and 6.8. The carrier density unit is 10^{10} cm^{-2}.

The Zeeman shift is presented in meV in figure 6.9. For sample N1 due to small Mn density we were not able to determine the Zeeman shift with sensible accuracy. Similar case is sample S1. However in this case, at 1.5 T field (at which measurements were performed) there is still visible weak transition in σ^- polarization. This enables us to judge the Mn density variation from σ^-–D_{low} splitting. Identification of lines in micro PL spectra for this sample is presented in figure 6.6. For further reference reader can refer to spectra shown in figures 2.12 and 4.4 (on pages 20 and 43, respectively).

Finally, the spontaneous splitting at zero magnetic field (in meV) is presented in figure 6.10. The example of experimental spectra for ferromagnetic samples is presented in figure 6.11.

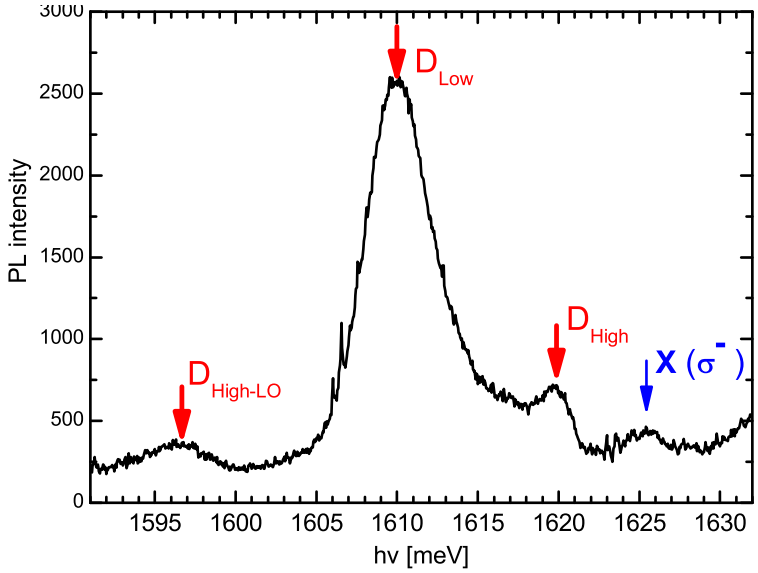

Figure 6.6: Line identification in micro-PL spectra of sample S1

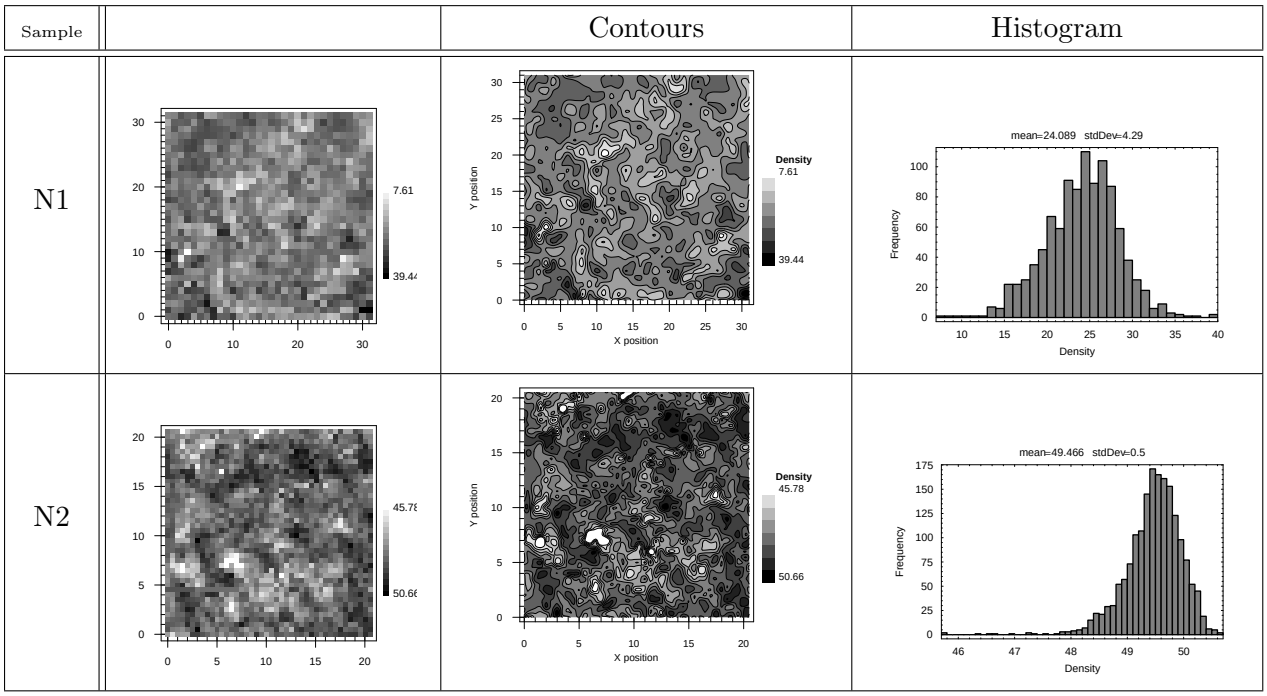

Figure 6.7: Carrier density fluctuations in nitrogen doped samples. The unit for X an Y axes is 1 μm. The carrier density unit is 10^{10} cm^{-2}.

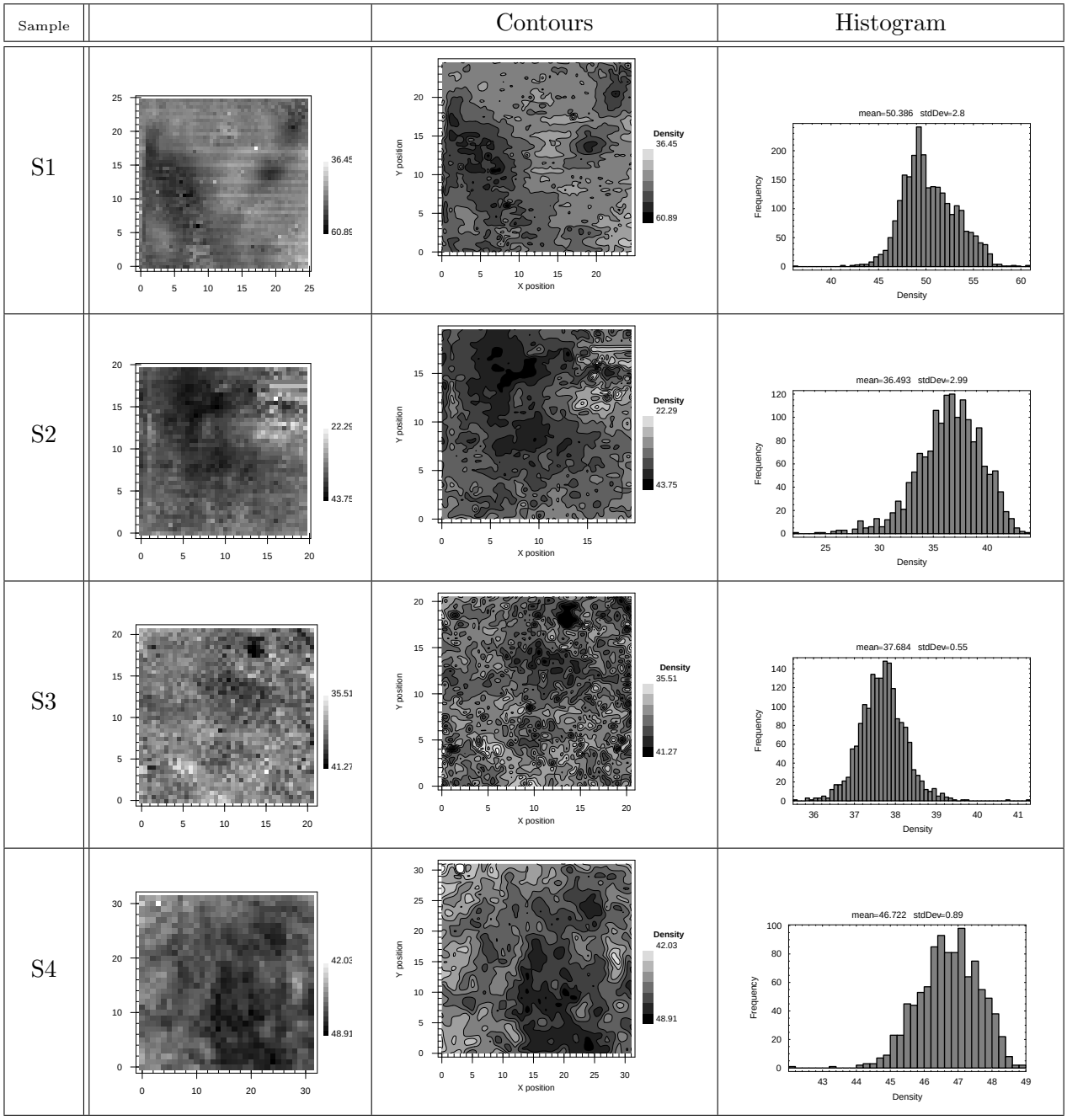

Figure 6.8: Carrier density fluctuations in surface doped samples. he unit for X an Y axes is 1 μm. The carrier density unit is 10^{10} cm^{-2}.

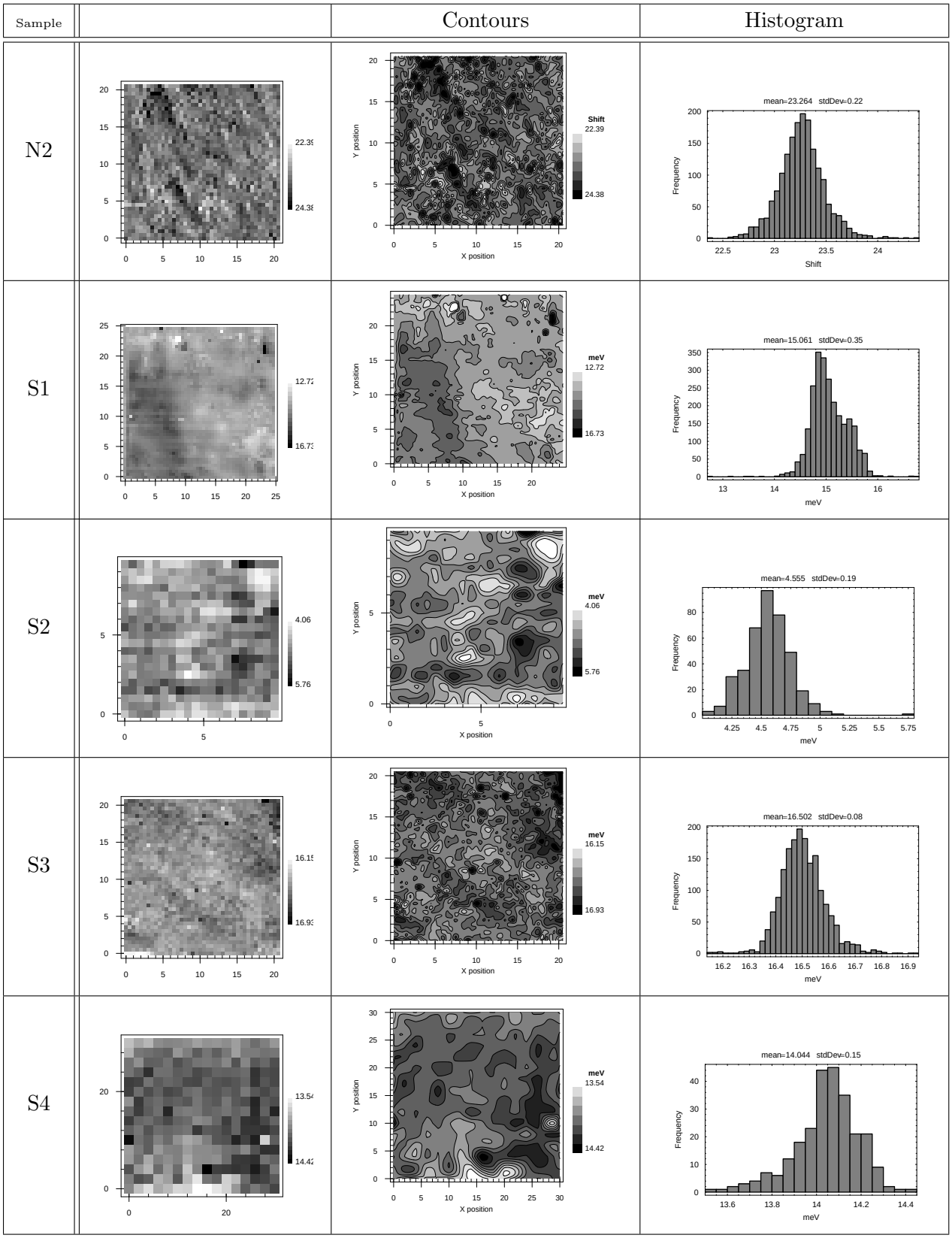

Figure 6.9: Zeeman shift depicting Mn density fluctuations (The unit for X an Y axes is 1 μm).

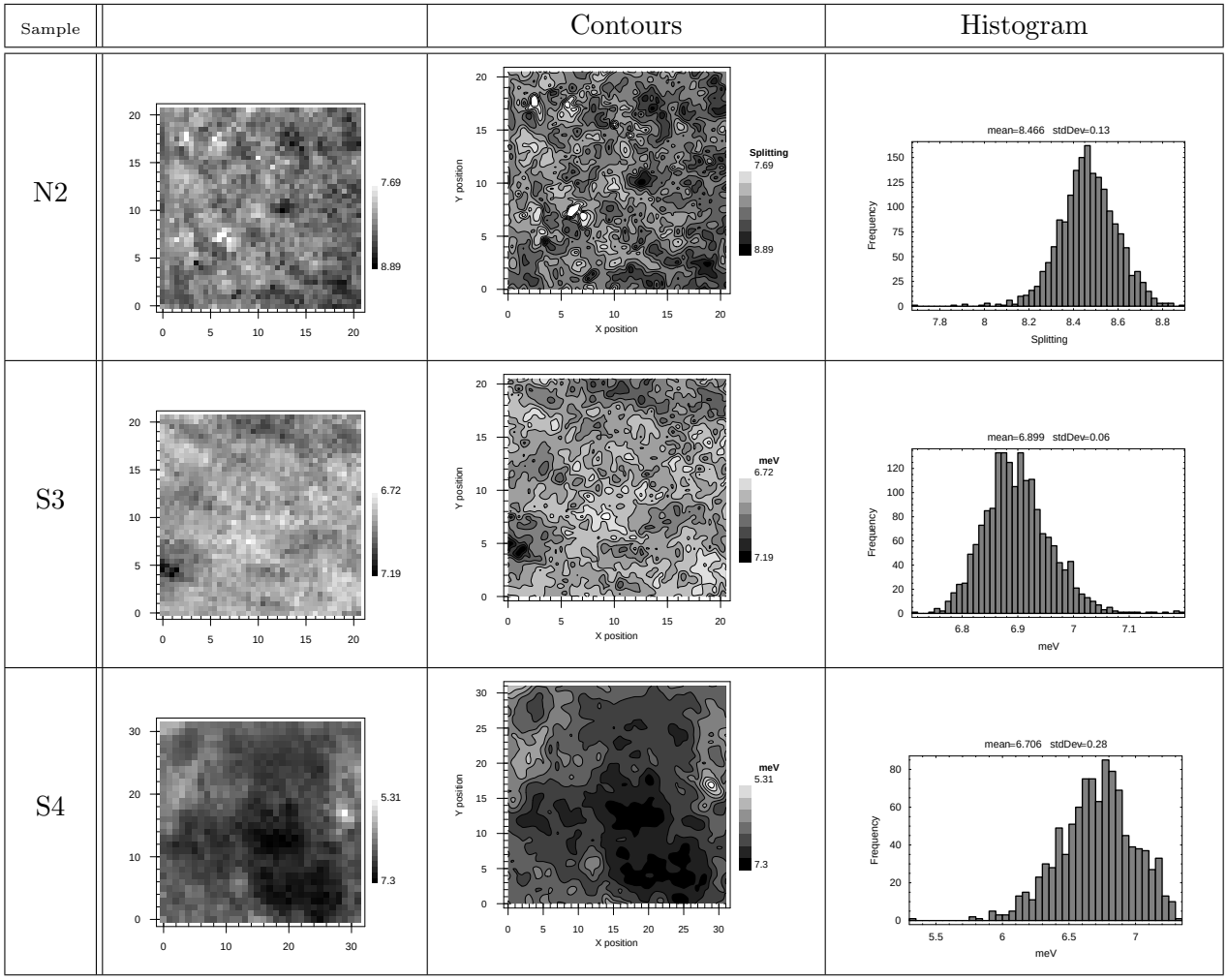

Figure 6.10: Zero field splitting depicting spontaneous magnetization fluctuations. (The unit for X an Y axes is 1 μm)

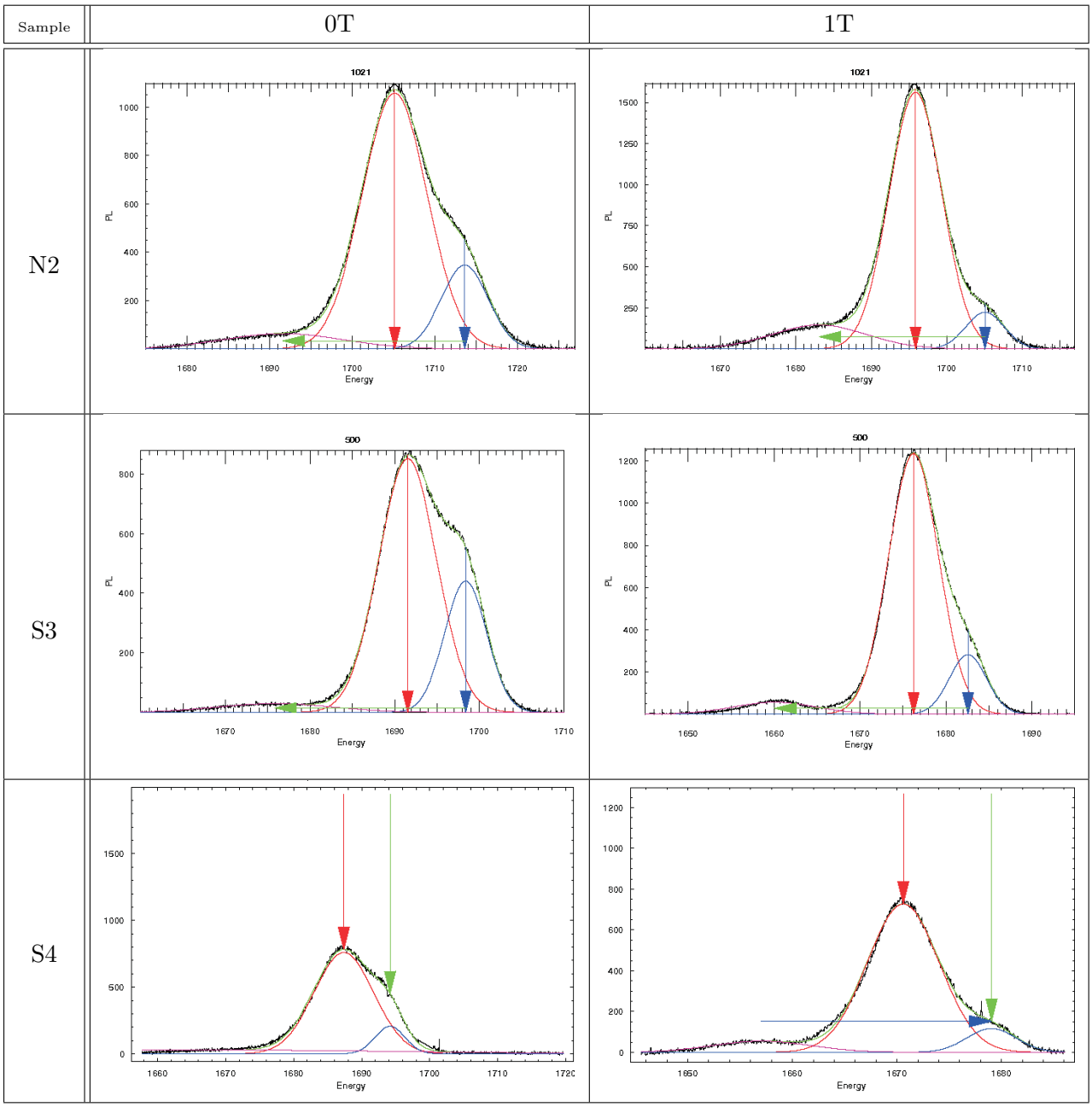

Figure 6.11: Examples of fits to the experimental spectra of μPL for ferromagnetic samples. The fitting was performed with gaussian lines. Arrows denote the determined positions of the lines. Three lines were used. Additional line was necessary to reproduce the the phonon replica of upper line. Horizontal arrow denotes the energy of LO phonon in CdTe (22meV). (a) Determination of Zeeman splitting due to the spontaneous magnetization. (b) Determination of HFS at 1T.

6.5 Discussion

All the maps presented in section 6.4 exhibit significant, irregular, spatial fluctuations. However the distributions of experimental values are generally symmetric around the mean value as can be seen on histograms presented along with the maps. The distribution shape is usually similar to the normal distribution.

In order to directly compare the shapes (relative widths) of distributions of different quantities it is convenient to consider normalized distributions. The normalization is achieved by dividing the distributions by their mean values. The mean value, and standard deviations determined for each of the measured maps are collected in table 6.2. The histograms of normalized distributions are presented in figure 6.12. The horizontal scale of each graph presented in figure 6.12 is set from 0.85 to 1.15 (which shows distribution in range of $\pm 15\%$ with respect to the mean value). The range is constant even if in some cases it ill fits the presented data (like in case of carrier density of N1 sample where it is too narrow or sample S3 where better presentation of data requires smaller range).[1]

When figure 6.12 is regarded it is not possible to notice any pattern allowing to distinguish between nitrogen and surface doped samples. In both cases the distributions can be relatively broad indicating large amplitude of disorder like in hole density in samples N1 and S2. It is possible to notice that, in most samples, the relative amplitude of Mn density fluctuations (ZS) is smaller than the amplitude of hole density variation. The exception is sample S1 where due to small Mn content the results of Mn density fluctuations are difficult to determine.

Sample	Carrier Density $[\times 10^{10}\ \mathrm{cm}^{-2}]$		Zeeman Shift [meV]		Spontaneous Splitting [meV]	
	$\langle p \rangle$	Δ_p	$\langle ZS \rangle$	Δ_{ZS}	$\langle ZFS \rangle$	Δ_{ZFS}
N1	24.1	4.3				
N2	49.6	0.5	23.3	0.33	8.5	0.1
S1	46.8	1.2	6.7	0.3		
S2	36.5	3	4.5	0.2		
S3	37.7	0.5	16.5	0.08	6.9	0.06
S4	46.7	0.9	14.04	0.14	6.7	0.3

Table 6.2: Mean values and standard deviation of measured micro PL maps.

[1] This approach is contrary to the one used while plotting histograms in section 6.4. There, the range of histogram is set to display all of the experimental points. It helps to identify artifacts and "bad" data points resulting from poor fits.

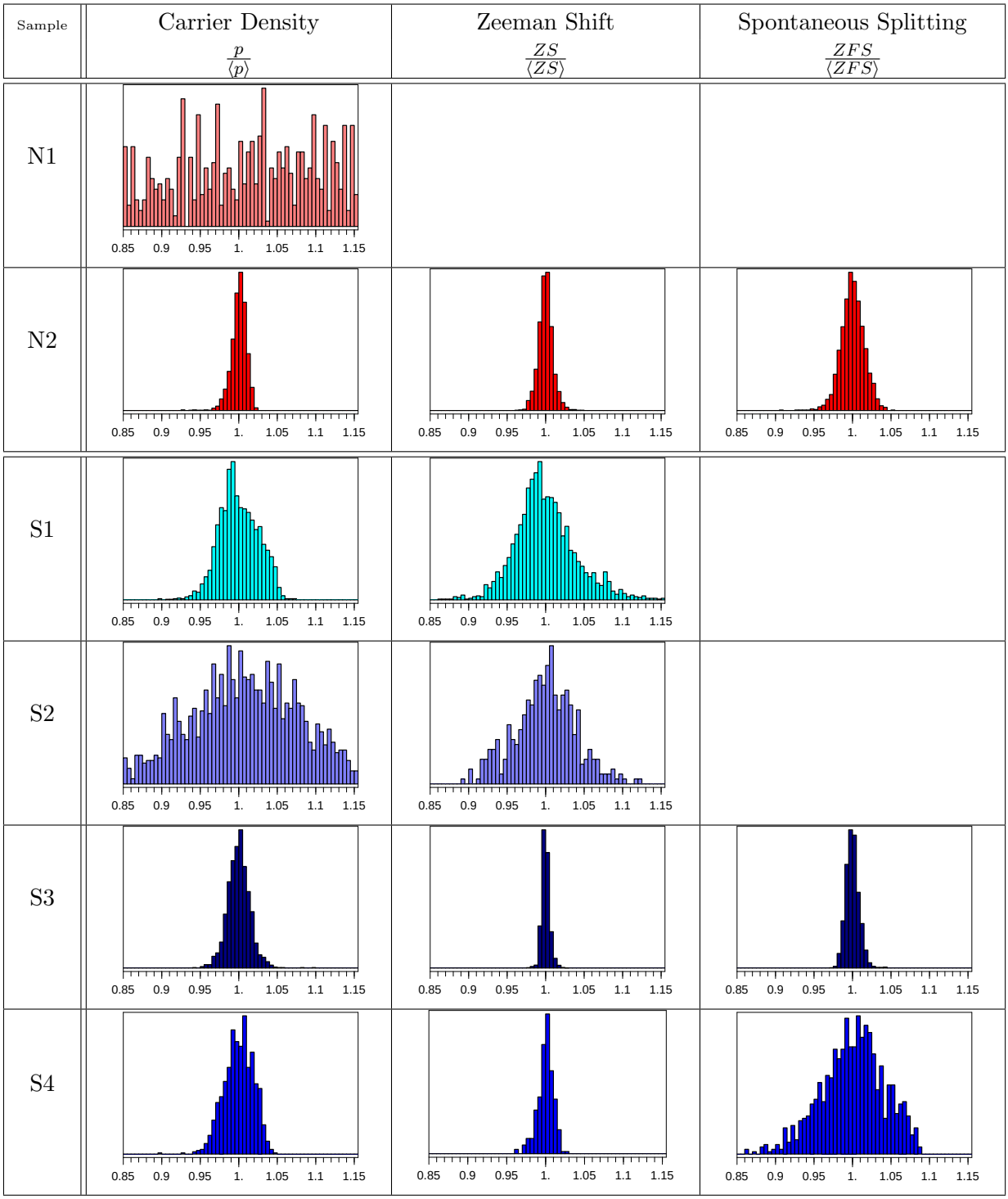

Figure 6.12: Normalized Histograms $\left(\frac{X}{\langle X \rangle}\right)$ of measured micro PL maps plotted in uniform range ±15%.

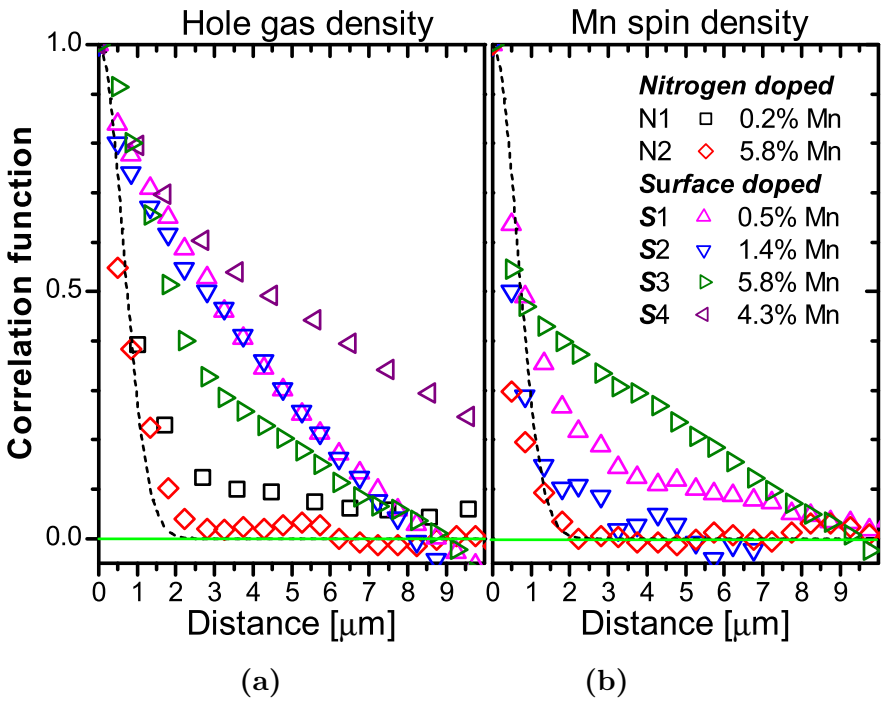

Figure 6.13: Correlation function of the hole gas density (a) and spin density (b). Squares present results for Nitrogen doped samples, triangles for the surface doped samples. The dotted line represents the correlation function calculated for a random distribution, taking into account the spatial resolution of the experiment.

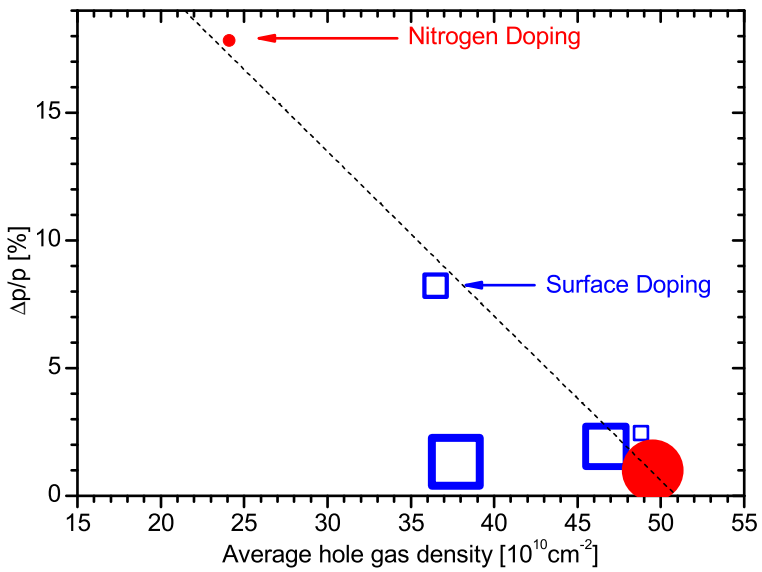

Figure 6.14: Variation of carrier density standard deviation. Squares correspond to the nitrogen doped samples, circles to surface doped ones. Size of symbols is proportional to the Mn density.

6.5.1 Carrier density and Mn density

Typical height-height correlation functions for the hole density and Mn content are shown in figure 6.13 (a) and (b) respectively.

The largest characteristic size of fluctuations was observed for carrier density in surface doped samples. Their size is estimated to be about 3 μm. It is much larger than the experimental resolution and significantly smaller than the limit given by the scanning range. The characteristic length of carrier density fluctuations as well as that of Mn spin density fluctuations were definitely smaller for Nitrogen doped samples (below 1 μm). Sample S3 does not follow this rule. Its exceptional quality makes the fluctuation amplitude very small. Therefore some background effects (such as illumination inhomogeneity due to the microscope objective properties) may dominate in the height-height correlation. However, real large size fluctuations (of small amplitude) cannot be excluded, originating, for example from inhomogeneous strain-dependent surface oxidation. Also in case of carrier density in sample S4 we observe some longer scale fluctuations of smaller amplitude. It is manifested as a change of slope of correlation function. However the steeper slope up to 4 μm distance indicates that shorter range fluctuations (the same as observed in the rest of surfase doped samples) dominate (have larger amplitude). To clarify those issues, it would be interesting to measure the microphotoluminescence maps of larger area (which is unfortunately not possible in present setup), preferably combined with scans of sample surface properties by AFM.

There are no correlations between the Mn and carrier density fluctuations. For all samples the values of Pearson Correlation coefficient were close to zero, well bellow significance level.

We did not observe any significant difference between the size of carrier fluctuations for surface doped samples grown on substrates of different lattice constant (Zn content 4% or 12%) or grown at different temperatures. Also the higher Mn content in the QW of sample N2 and S4 does not seem to influence the size of fluctuations of the carrier density.

The amplitude (standard deviation) of the carrier density fluctuations varied from 1% to above 10% depending on the sample (Figure 6.14). It tends to decrease with increasing carrier density, which might be a result of screening. It is independent of the origin of carrier gas. The size of carrier density fluctuations was smaller for nitrogen doped samples (6.13(a)). It might suggest even larger amplitude of fluctuations in the case of Nitrogen doped ones because the measured fluctuations are averaged by the experimental resolution. The decrease might be described by line (dashed line in figure 6.14) , except for the sample S3 where the variation of carrier density is exceptionally low due to outstanding quality of the sample.

In principle the fluctuations of the carrier density might result from electrostatic fluctuations, or fluctuations of the QW parameters such as strain and QW width. Fluctuations of the QW width should have rather similar effects on the carriers and on the excitons. Their effect is small in the case of samples grown at 280°C, where pseudo-smooth interfaces are formed (i.e., the characteristic scale is smaller than the exciton coherence length) (*Grieshaber et al.*, 1994). This is the case of sample S2, which exhibits large-scale fluctuations. Strain fluctuations are also minimized by a careful design of the sample structure, so that the whole layer is coherently strained to the substrate (sample S1). Moreover those mechanisms should be very similar in surface and N-doped samples. Thus, the main intrinsic source of fluctuations of carrier density are

probably the fluctuations of electrostatic potential. They might originate from the distribution of ionized acceptors. One generally considers (*Efros et al.*, 1993; *Yayon et al.*, 2001) that the typical spatial scale of these fluctuations (caused by a random distribution of acceptors) is determined by two parameters: the distance from the QW to the doping layer (in our case, with doping from surface states, this is the thickness of the cap layer, 25 nm), and the inverse of the Fermi wavevector (about 12 nm for $p = 3 \times 10^{11}\mathrm{cm}^{-2}$). The observed scale of fluctuations is larger, which suggests an extrinsic origin. This might be either a long range non-random distribution of acceptor centers on the oxidized surface of the sample, or fluctuations of the cap layer thickness.

6.5.2 Ordered phase

The samples N2, S3 and S4 contained sufficient amount of Mn ions in quantum well to enable observations of spontaneous splitting at low temperatures. The particular samples chosen for this study exhibit well resolved lines at low temperatures in the ordered phase. It can be seen in figure 6.11. Note that in this experiment it was not possible to tune the carrier density with additional illumination, therefore we deal with nominal carrier densities. The maps of spontaneous splitting are presented in figure 6.10.

Special care was taken to assure that the components of the spectra at zero magnetic field were due to the split charged exciton lines, not the triplet D_{high}-D_{low} transitions. However in order to achieve well resolved lines and stability of the setup during experiment, we chose temperatures providing maximal values of the spontaneous splitting. Apparently, this led us close to the splitting at which the line changes its character. It is witnessed by the presence in the spectra of a week line due to the LO-phonon replica of upper line (see figure 6.11 samples S3 and N2). However, when magnetic field is applied, (see sample spectra in the last column in figure 6.11) the evident increase of phonon replica line intensity is accompanied by decrease of upper component intensity. Such changes indicate that, at zero field, the upper component of PL line is mostly due to the charged exciton while the luminescence due to the D_{high} transition is weak and should not affect the results significantly. Positions of each component line were determined from fit with gaussian lines. Because the applied model of the line does not describe the exact shape of luminescence lines, the absolute value of local magnetization is uncertain. Due to small variation of PL line shape, for a given PL map, we can expect that the systematic error in fits resulting from inadequate line shape modelling is constant. Therefore we can analyze the variation of local magnetization with reasonable precision.

The gathered mean values of zero and high field splitting for the considered samples are presented in table 6.3. Cautious consideration of data from fits is necessary. Despite the obvious changes in spectra for sample S3 when magnetic field was applied (seen in figure 6.11), the obtained mean value of spontaneous splitting (ZFS) is larger than D_{high}-D_{low} splitting in magnetic field in this case. This is, most likely, due to inadequate line model used in fitting resulting in systematic error at zero field splitting determination. We can still consider this result valid if we are discussing variation of local magnetization. The rest of the samples is well within the safety margin and ZFS is noticeably smaller than HFS.

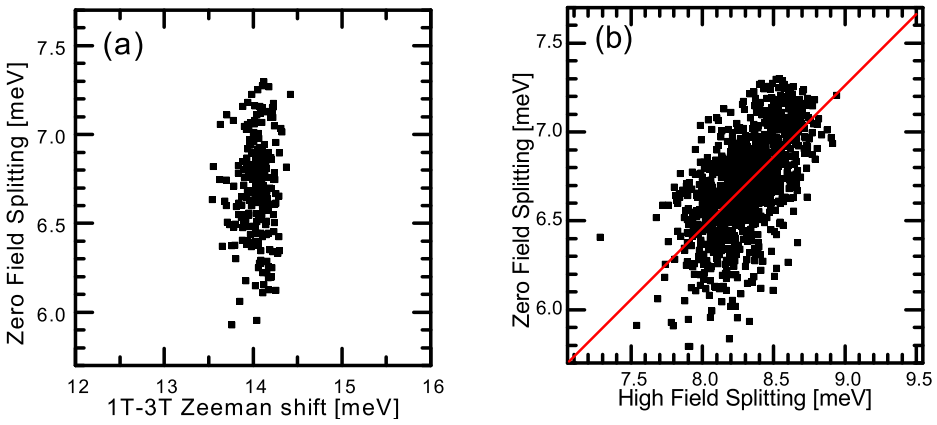

Figure 6.15: Correlation plots. (a) magnetization (ZFS) as a function of x_{eff} (1T-3T Zeeman shift) (b) magnetization (ZFS) as a function of hole has concentration (HFS). The scale ranges cover the ±15% variation around the mean values. Solid line on the plot (b) represents the linear dependence of the magnetization on the hole gas density in the agrement with the macroscopic data

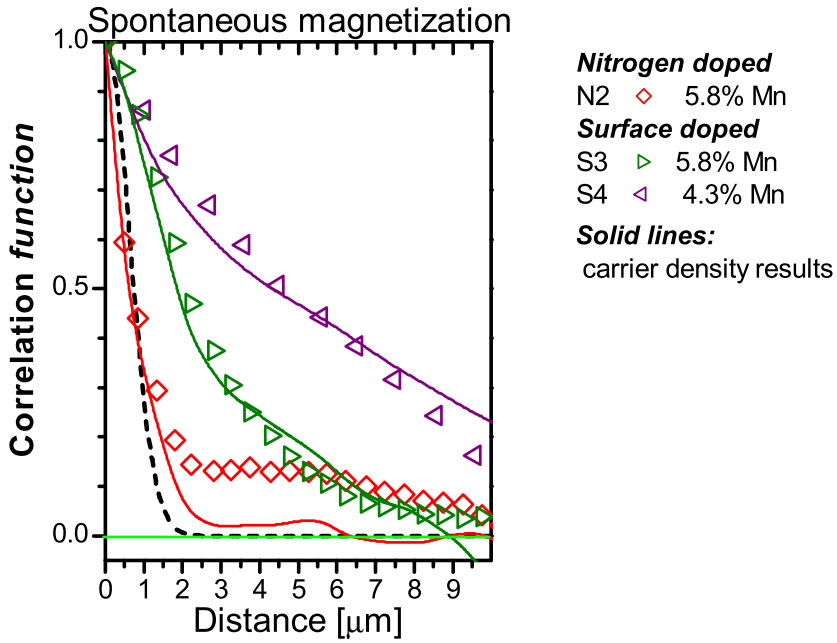

Figure 6.16: Points: height-height correlation function of spontaneous magnetization (splitting). Squares present results for Nitrogen doped samples, triangles for the surface doped samples. The dotted line represents the correlation function calculated for a random distribution, taking into account the spatial resolution of the experiment. Solid lines present correlation functions of carrier density for the selected samples.

For the analysis of the origin of fluctuations it is most interesting to analyze the dependencies between those quantities. The spontaneous magnetization within the mean field model is proportional to the product of hole gas density and the effective Mn concentration:

$$\langle M_0 \rangle \propto p \cdot x_{eff}. \tag{6.3}$$

Since we were able to determine all those three quantities independently it is possible to analyze the dependencies between them. It can be done on the correlation plots, where for each point on the sample data from one experiment are treated as x values, while the y values comes from a second quantity for the same point on the sample. The correlations are quantitatively analyzed with the correlation coefficient.

Figure 6.15 presents example correlations plots. Correlations between the spontaneous magnetization (ZFS) and x_{eff} (1T-3T Zeeman shift) on panel (a) and the hole gas concentration (High field Splitting) are presented on the panel (b) for sample N2. There are no significant correlations visible between the magnetization and x_{eff}, also the correlation coefficient value of 7% is well below the significance level of 16% (for the considered 256 cases). The surprisingly narrow distribution of effective spin density may be responsible for the difficulty in finding any correlations since the changes induced in magnetization by such small variation of spin density are close to the limit of the resolution of this experiment.

On the contrary, the values of the magnetization and the hole density are correlated. The Correlation coefficient value of 58% is well above the threshold of 8% for the statistical significance (the 0.08 value ensures a significance level of 0.01 i.e., 99% confidence) on the 1024 points. For the reduced data sample to 256 points we obtain 62% correlation coefficient. The solid line on the plot displays the linear dependence of the magnetization on the hole gas density in the agrement with the macroscopic data.

This result is repeated in all samples (where ferromagnetic transition is observed): there are no significant correlations between the spontaneous magnetization and Mn density fluctuations, while spontaneous magnetization and carrier density fluctuations are correlated. This demonstrates that the main mechanism responsible for the fluctuations of spontaneous magnetization is the presence of fluctuations of the hole density. However, it is necessary to note that the value of correlation coefficient (last column in table 6.3) decreases with decreasing magnitude of carrier density fluctuations. It is probably due to the approaching the limit of experimental resolution.

Sample	$\langle ZFS \rangle$ [meV]	ΔZFS [meV]	$\langle HFS \rangle$ [meV]	$\Delta\langle HFS \rangle$ [meV]	R %
N2	8.5	0.1	9.2	0.2	40
S3	6.9	0.06	6.6	0.1	42
S4	6.7	0.3	8.3	0.2	60

Table 6.3: Mean values and standard deviations of zero and high field splitting, as well as Pearson correlation coefficient of the ZFS and HFS distributions.

The height-height correlation functions computed for spontaneous magnetization is presented in figure 6.16 as points. The solid lines represent results for carrier density (also shown in figure 6.13(b)). There is undeniable similarity between those functions for each sample. It confirms close relations between those quantities. Moreover, both have the same characteristic length of fluctuations. This indicates that the size of spontaneous magnetization fluctuation is inherited from carrier density fluctuations. However, the drastic change of slope around 0.2 value of correlation function may suggest some longer range ordering of very small amplitude.

6.6 Summary

Microphotoluminescence mapping experiments were performed on a modulation doped (Cd,Mn)Te quantum wells. The carriers were supplied either by nitrogen acceptors or by the surface traps. The broad range of Mn compositions was studied: from 0.5% up to 5.8%. It should be interesting to consider cases when a larger disorder is expected. However, the broadening of the lines complicates the data analysis in such cases. The components of the PL line split due to the spontaneous magnetization are not resolved well enough to permit sensible accuracy of fits. Similar difficulties arise in determination of carrier density.

The spatial resolution of experiment 0.5μm was sufficient to observe the fluctuations of local spontaneous magnetization, hole gas density and the local effective density of Mn spins. All those quantities were determined by independent measurements. The effect of Mn spin density fluctuation on the local magnetization and hole gas density was too small to be detected. The fluctuation of carrier density was found to have the dominant effect on the local magnetization.

The fluctuations of effective density of Mn spins have shorter range than experimental resolution. The characteristic length of of carrier density fluctuations depends on the origin of the carrier gas. It is just on the edge of experimental resolution for nitrogen doping, while for surface doped samples it is of the order of 3 μm. It is also inherited by the fluctuations of spontaneous magnetization. There were no visible correlations between the Mn composition and the magnitude or size of carrier density fluctuations. However, the average hole density strongly affects its magnitude reducing the fluctuations at higher densities due to the screening.

We observe a correlation between the fluctuation of spontaneous magnetization and the fluctuation of carrier density. However, locally, the mean field model still holds, since the local magnetization follows the expected dependence on carrier density.

CHAPTER 7

Conclusions

This work is devoted to spectroscopic studies of carrier induced ferromagnetism in (Cd,Mn)Te quantum wells. Substantial effort was taken to broaden the range of key parameters (Mn spin density and carrier density) in the studied samples. It was possible, due to a new method of modulation doping which we have developed.

The application of surface acceptor states in modulation doping of quantum wells brings several advantages over traditional p-type doping of (Cd,Mg)Te barriers with nitrogen. The sample growth process is significantly simplified. Moreover, the complicated ECR nitrogen plasma cell used is not required during sample fabrication. It opens a way to produce samples of desired hole gas density in typical MBE systems without costly hardware upgrades. In surface doping, there are no foreign acceptors introduced into the crystal, which reduces the problem of dopant interdiffusion to minimum. It also improves thermal stability of the samples which allows to use higher temperatures during sample growth and eventual post-growth processing. The higher growth temperature significantly improves the quality of the optical spectra.

The hole gas densities obtained by surface doping are similar to those obtained by nitrogen doping, reaching up to 3.6×10^{11} cm^{-2} (as determined by optical spectroscopy). Furthermore, the hole gas density in the quantum well can be controlled by illumination. The response of surface-doped samples to the light is very special, as it allows to either increase or decrease the carrier density by choosing illumination wavelength. The high efficiency of carrier increase and reduction mechanisms allowed us to tune the hole density from below 1×10^{10} cm^{-2} up to 5×10^{11} cm^{-2} in a sample with native density of 3.6×10^{11} cm^{-2}. It was achieved without any detectable heating of the system. We obtained thus hole densities unavailable in samples doped with nitrogen.

We found that surface doping is efficient in a broader range of (Cd,Mg)Te barrier compositions than nitrogen doping. This allowed us to obtain high hole gas density in samples with increased Mn content in the quantum well. We have raised the upper limit up to 10.8% of Mn in the quantum well. Therefore we were able to study samples with effective Mn spin density of 4.11% which is very close to theoretical limit for bulk (Cd,Mn)Te (4.5%).

The examination of optical properties of quantum wells with hole gas originating from surface states have shown that they exhibit the same characteristic features as reported for other p-type doped quantum wells (*Kossacki et al.*, 2004*a*; *Boukari et al.*, 2006). This confirms intrinsic nature of the observed spectra. The recently discussed by *Kossacki et al.* (2004*a*) transition from singlet trion state to the split triplet D_{high}-D_{low} (induced by magnetic field) can also be observed in surface doped samples. It turned out to be a very convenient tool for probing of the hole gas density.

However, despite exceptional quality of macroscopic optical spectra, the measurements of local carrier density (determined using spectroscopic features of PL measured with spatial resolution of 0.5 μm) indicated fluctuations with characteristic size of 3 μm for surface doped samples. Fluctuations of that size were not observed for nitrogen doped samples. Regardless of the differences in sizes the magnitude of hole density fluctuations is comparable in both types of samples. Such two sizes of fluctuation in a otherwise very similar systems present an interesting opportunity in studies of influence of disorder on magnetic properties.

The new doping technique allowed us to increase maximal Mn density available in p-type quantum wells. We were able to study the carrier induced ferromagnetism in samples where the effective composition x_{eff} approaches the theoretical limit for bulk (Cd,Mn)Te (4.5%). We were able to observe the highest ferromagnetic transition temperature for this system: $T_C = 9.5 \pm 3$ K at $x_{eff} = 4.11\%$. The access to the full range of effective Mn density and possibility to control the hole gas density allowed us to study magnetic ordering in a wide range of experimental conditions.

We have revised the interpretation of experimental photoluminescence spectra which enabled us to establish a more sensitive technique of the critical temperature determination. This enhanced sensitivity, along with results for samples containing higher, than studied before, Mn composition revealed large differences between critical and Curie-Weiss temperatures. Most of the difference is due to the fact that experimental techniques used for determination of T_C and T_{CW} are most sensitive to different spin subsystems. The susceptibility measurements are performed at higher temperatures therefore are strongly affected by Mn spins bound in complexes which break with increase of the temperature. The photoluminescence measurements without magnetic fields are performed at low temperatures therefore all of the complexes are frozen so only "free" spins are responsible for the changes of luminescence. Those spins can be easily arranged by carrier mediated interactions therefore the observed critical temperatures are higher than Curie-Weiss temperatures.

The possibility to tune the carrier density in experiments highlighted the importance of many body interactions in the hole gas. For example, it turned out that the Curie constant in determined from susceptibility experiments is strongly affected by actual carrier density in the quantum well. Accurate description of this phenomenon requires a detailed knowledge of the susceptibility changes in the hole gas with the density. This complicated matter requires further experimental studies combined with development of suitable theoretical description.

The importance of hole gas properties was confirmed by measurements of local spontaneous magnetization in micro-photoluminescence experiments. We found that spontaneous magnetization is not uniform and the fluctuations are strongly related to carrier density (it even inherits the correlation length of carrier density fluctuation - 3μm). However, we were not able to observe any significant fluctuations of Mn spin distribution within our experimental resolution.

Our experimental results in both local and macroscopic approach were always consistent within mean field model predictions. This shows the robustness of the mean field model down to the micrometer range.

Perspectives

Further theoretical work is required in order to fully address the differences between critical and Curie-Weiss temperatures, or the effect of carrier density on Curie constant.

Up to now, the (Cd,Mn)Te quantum wells have been studied mainly through optical spectroscopy. However, promising applications in spintronics require transport, and this has still to be developed on II-VIs.

The results presented in this work have already found its continuation. The samples developed for this study, thanks to their excellent quality and tunability of carrier gas density were used in studies of magnetization dynamics by *Goryca et al.* (2006). Some of them were also helpful in studies of ferromagnetic domain relaxation dynamics by *Kossacki et al.* (2006). However, the magnetic domains are still to be observed, as they appear to be beyond our present experimental resolution.

APPENDIX A

Samples Parameters

A.1 Samples used for studies of surface doping

	M1353	**M1354**	**M1355**	**M1356a/b**	**M1357**
Substrate $Cd_{1-x}Zn_xTe$	4%	4%	4%	4%	4%
Buffer CdTe	1090Å	1090Å	1090Å	1090Å	1090Å
Spacer $Cd_{1-x}Mg_xTe$	2000Å x=22%	2000Å x=22%	2000Å x=17.5%	2000Å x=32%	2000Å x=32%
Screening Layer $Cd_{1-x}Mg_xTe$:N	500Å x=22%	500Å x=22%	500Å x=17.5%	500Å x=32%	500Å x=32%
Barrier $Cd_{1-x}Mg_xTe$	1000Å x=22%	1000Å x=22%	1000Å x=17.5%	1000Å x=32%	1000Å x=32%
Quantum Well $Cd_{1-x}Mn_xTe$	100Å x=1%	100Å x=1%	100Å x=1%	100Å x=1.6%	100Å x=4.6%
Cap Layer $Cd_{1-x}Mg_xTe$	200Å x=22%	300Å x=22%	200Å x=17.5% 50Å $Cd_{0.4}Mg_{0.6}Te$	250Å x=32% 50Å amorphous Te	250Å x=32%

Table A.1: The structure of the samples grown on 4% zinc substrate. Growth temperature was 220 °C.

Sample	Cap Layer $\AA$	Moss-Burstein shift meV	Hole Gas density $\times 10^{10}\ cm^{-2}$
M1332	150	0	< 1
M1345	150	0	< 1
M1382	175	9.8	27 ± 4
M1353	200	12.2	34 ± 4
M1333	250	12.6	35 ± 4
M1355	250	13	36 ± 4
M1354	300	10.9	31 ± 4
M1383	400	10.3	29 ± 4
M1384	600	5.9	15 ± 4

Table A.2: Results of measurements. Moss-Burnstein shift was measured at 0.5T.

	M1332	**M1333**	**M1345**	**M1382**	**M1383**	**M1384**
Substrate $Cd_{1-x}Zn_xTe$	12%	12%	12%	12%	12%	12%
Buffer	$Cd_{0.88}Zn_{0.12}Te$ 1370 Å $10 \times \begin{cases} Cd_{0.88}Zn_{0.12}Te & 1 \text{ ML} \\ MgTe & 6 \text{ ML} \end{cases}$ $Cd_{0.88}Zn_{0.12}Te$ 1370 Å					
Spacer $Cd_{1-x-y}Zn_xMg_yTe$	2000Å x=8% y=22%	2000Å x=8% y=22%	2000Å x=8% y=22%	2000Å x=8% y=27%	2000Å x=8% y=27%	2000Å x=8% y=27%
Screening Layer $Cd_{1-x-y}Zn_xMg_yTe$:N	250Å x=8% y=22%	250Å x=8% y=22%	250Å x=8% y=22%	250Å x=8% y=27%	250Å x=8% y=27%	250Å x=8% y=27%
Barrier $Cd_{1-x-y}Zn_xMg_yTe$	1000Å x=8% y=22%	1000Å x=8% y=22%	1000Å x=8% y=22%	1000Å x=8% y=27%	1000Å x=8% y=27%	1000Å x=8% y=27%
Quantum Well $Cd_{1-x}Mn_xTe$	100Å x=0.5%	100Å x=0.5%	100Å x=1.6%	100Å x=0.6%	100Å x=0.7%	100Å x=0.7%
Cap Layer $Cd_{1-x-y}Zn_xMg_yTe$	150Å x=8% y=22%	250Å x=8% y=22%	150Å x=8% y=22%	175Å x=8% y=27%	400Å x=8% y=27%	600Å x=8% y=27%

Table A.3: The structure of the samples grown on 12% zinc substrate. Growth temperature was 220 °C.

A.2 Samples used for studies of carrier induced ferromagnetism

	M1359	**M1360**	**M1361**	**M1362**	**M1440**	**M1442**	**M1533**
Substrate $Cd_{1-x}Zn_xTe$	4%	4%	4%	4%	4%	4%	4%
Buffer CdTe	1090Å	1090Å	1090Å	1090Å	1090Å	1090Å	1090Å
Barrier $Cd_{1-x}Mg_xTe$	2000Å x=25%	2000Å x=27%	2000Å x=26%	2000Å x=26%	2000Å x=30%	2000Å x=30%	2000Å x=30%
Quantum Well $Cd_{1-x}Mn_xTe$	100Å x=1.4%	100Å x=5.8%	100Å x=7.55%	100Å x=10.8%	80Å x=4.6%	80Å x=6.84%	80Å x=9.9%
Cap Layer 250Å $Cd_{1-x}Mg_xTe$	x=25%	x=27%	x=26%	x=26%	x=30%	x=30%	x=30%

Table A.4: The structure of the samples grown on 4% zinc substrate. Growth temperature was 280 °C.

Sample	x_{Mn} %	x_{eff} %	T_{AF} K	Growth temperature °C	hole density [$\times 10^{10}$cm^{-2}] Native	Maximal
Width 100 Å Surface Doped						
M1384	0.8	0.7	0.36	220	15	—
M1357	6.36	3.3	2.44	220	36	39
M1359	1.4	1.15	0.72	280	24	45
M1360	5.8	3.1	2.07	280	36	50
M1361	7.55	3.55	2.63	280	33	44
M1362	10.8	4.11	3.33	280	34	44
Width 80 Å Surface Doped						
M1440	4.65	2.72	2.45	280	47	49
M1442	6.84	3.38	2.63	280	46	48
M1533	9.9	4.05	3.23	280	45	48
Width 100 Å Nitrogen Doped						
M1364	5.85	3.15	2.36	220	50	—
Width 80 Å Nitrogen Doped						
M 952	4.4	2.6	1.9	220	27	—

Table A.5: Parameters of samples discussed in chapter 5 (repeated).

A.3 Samples studied in micro-photoluminescence

M1305

Layer	Material	Composition	Thickness [Å]
Substrate	$Cd_{1-x}Zn_xTe$	$x = 12\%$	—
Buffer	CdTe		1000
	$Cd_{1-x-y}Zn_xMg_yTe$	$x = 8\%$ $y = 27\%$	2000
Screen	$Cd_{1-x-y}Zn_xMg_yTe$:N	$x = 8\%$ $y = 27\%$	250
Barrier	$Cd_{1-x-y}Zn_xMg_yTe$	$x = 8\%$ $y = 27\%$	1000
QW	$Cd_{1-x}Mn_xTe$	$x = 0.4\%$	80
Barrier	$Cd_{1-x-y}Zn_xMg_yTe$	$x = 8\%$ $y = 27\%$	20
δ-doping	$Cd_{1-x-y}Zn_xMg_yTe$:N	$x = 8\%$ $y = 27\%$	150
Cap	$Cd_{1-x-y}Zn_xMg_yTe$	$x = 8\%$ $y = 27\%$	650

Table A.6: Structure of the nitrogen doped sample M1305 (N1) studied in chapter 6.

M1364

Layer	Material	Composition	Thickness [Å]
Substrate	$Cd_{1-x}Zn_xTe$	$x = 4\%$	—
Buffer	CdTe		700
	$Cd_{1-x}Mg_xTe$	$x = 10\%$	500
Screen	$Cd_{1-x}Mg_xTe$:N	$x = 10\%$	400
Spacer	$Cd_{1-x}Mg_xTe$	$x = 10\%$	900
Barrier	$Cd_{1-x}Mg_xTe$	$x = 25\%$	100
QW	$Cd_{1-x}Mn_xTe$	$x = 5.8\%$	100
Barrier	$Cd_{1-x}Mg_xTe$	$x = 25\%$	20
δ-doping	$Cd_{1-x}Mg_xTe$:N	$x = 25\%$	50

Table A.7: Structure of the nitrogen doped sample M1364 (N2) studied in chapter 6.

Sample	L_{QW} [nm]	x_{Mn} [%]	p [10^{11}cm^{-2}]	Doping	T_{growth} [°C]	Name
N1	8	0.2	3	N	220	M1305
N2	10	5.8	4.5	N	220	M1364
S1	10	0.5	3.5	surface	220	M1333
S2	10	1.4	3.5	surface	280	M1359
S3	10	5.8	3.6	surface	280	M1360
S4	8	4.6	4.7	surface	280	M1440

Table A.8: Parameters of the studied samples (repeated)

APPENDIX B

Height-Height correlation function

For the analysis of spatial correlations in micro photoluminescence maps we use height-height correlation function. It was already presented in chapter 6.2.1. Here focus on the main properties of this correlation function which are illustrated on the example artificial surfaces constructed from the objects of known dimensions.

Let us start from the formula used for computing height - Height correlation function:

$$H(R) = 1 - 0.5\frac{\sum_r \frac{1}{N_r}\left(F(\vec{R}+\vec{r}) - F(\vec{r})\right)^2}{\frac{1}{N}\sum_r \left(F(\vec{r}) - \langle F(\vec{r})\rangle\right)^2} \tag{B.1}$$

It is in fact equation 6.1 written in a form more closer to the actual implementation in computer code. $F(r)$ represents the distribution of which the correlation is computed. The averaging goes over all possible distances r. It is necessary to note that the real data are not continuous two dimensional density but are gathered in a matrix where each point corresponds to a spot on the surface. The points form an evenly spaced 2 dimensional lattice. In such lattice there are is only discrete set distances between the nodes. For example in matrix of 32 by 32 points we have 431 unique distances between points. Therefore, in order to speed up the calculations and reduce the noise, we introduced the additional averaging in which the considered distances are collected into the ranges from n to $n+1$ lattice constants. Each range is represented by its mean value. The effects of this averaging procedure are presented in table B.1, in last column where correlation function is computed for different cases the red curve presents correlations without averaging, the blue one the averaged value.

The table B.1 presents sets of artificial surfaces (presented as maps in column 3) constructed of objects of known properties and positions. In column 4 there are presented cross-sections along $y = x$ diagonal with marked (where applicable) characteristic dimensions. Those dimensions are also marked on correlation function plots presented in last column. In case of randomly distributed points table B.1(a) there are no correlations and the value of correlation function is zero through out the whole range of densities. In the rest of cases the value correlation function drops from one as the distance decreases. At the distance corresponding to the characteristic dimensions of object used for constructing the surface correlation function has local minima (note that for Gaussian distribution it is not the FWHM). The rest of the characteristic distances in the surface can be also identified as a special features of the correlation function plots. However, here the interpretation is more difficult and can be precise only if the exact type of objects constructing the surface is known. It becomes even more difficult as the number of objects constructing the surface increases (table B.1 (d) and (e)). Therefore, the presented height-height

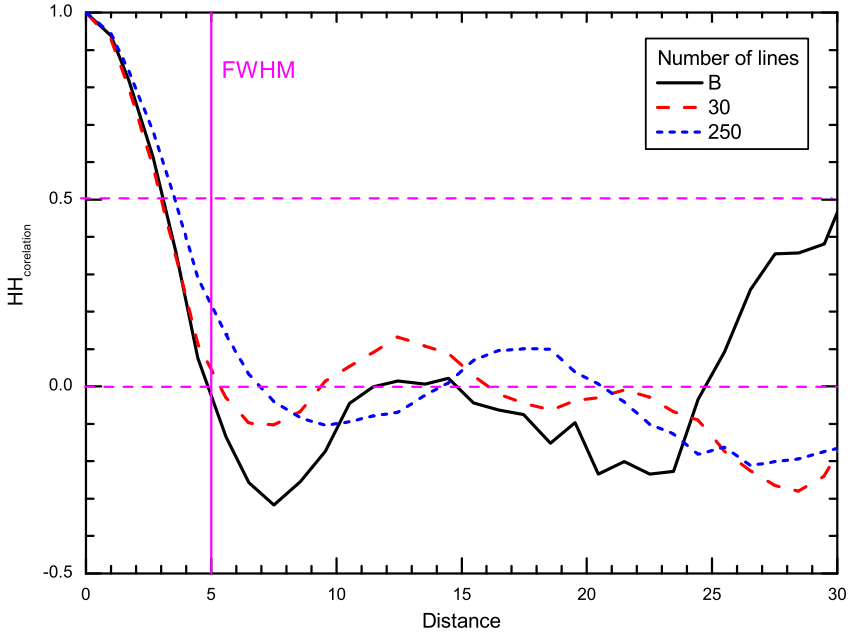

Figure B.1: Height-Height correlation function for Gaussian lines. Different number of lines of the same width, randomly distributed (Table B.1 rows *c* to *e*). The FWHM is marked as vertical line.

correlation function gives the most precise information on the shortest characteristic length which is the characteristic dimension of the objects constructing the surface.

We expect that the spatial fluctuations of real quantities are of the Gaussian dome type. Let us investigate closer the properties of surfaces constructed of such lines. The last three cases (*c*,*d*, and *e*) presented in table illustrate what happens with height - height correlation function when number of lines is increased. The correlation functions are plotted together in figure B.1. The additional lines make the correlation random for longer distances. However, the close rance correlations, even when there are 250 lines still resemble the 2 Gaussian dome model case. The presence of many lines shifts the first minima and zero value crossing point, which in the model case were directly connected with characteristic dimension of the used shape. On the contrary, at $\frac{1}{2}$ value of correlation function the distance is almost the same for all the cases. Therefore, it is more convenient to use this value as a reference point at which characteristic lengths are determined.

In figure B.2(a) the correlation function are plotted for surfaces made of two Gaussian lines (of the same width). Each curve was obtained for the surface with different width of lines. The positions of characteristic values are plotted in B.3(a). Both, zero crossing point and $\frac{1}{2}$ value are proportional to the FWHM of Gaussian lines. In figure B.3(b) Gaussian FWHM is plotted versus the distance at which the correlation function is equal to $\frac{1}{2}$. The parameters of the line drawn through the points may be helpful in computing width of fluctuation sizes for real experiments (assuming that they resemble the Gaussian distribution) where the $\frac{1}{2}$ correlation value is used in analysis.

	Case	Map	$y = x$ crosssection	HH correlation
a	Random	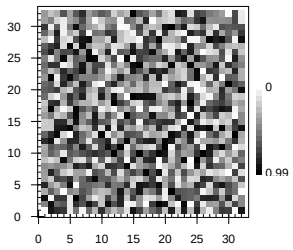	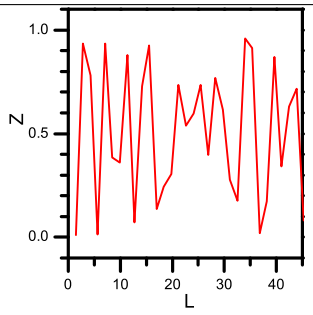	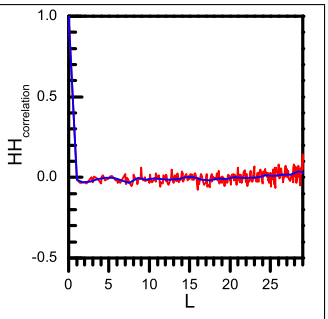
b	2×Circle $D_C = 22.75$ $2r = 10$	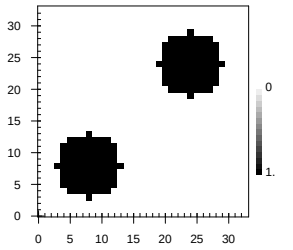	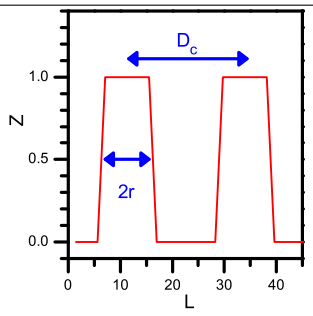	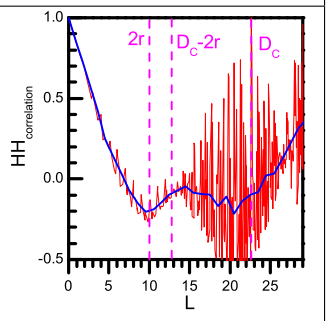
c	2×Gaussian $D_C = 22.75$ $FWHM = 5$	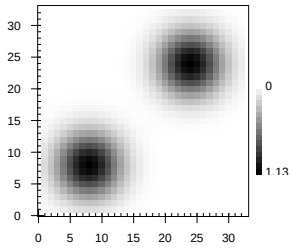	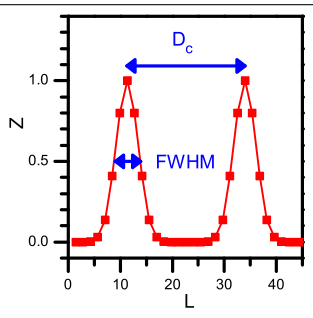	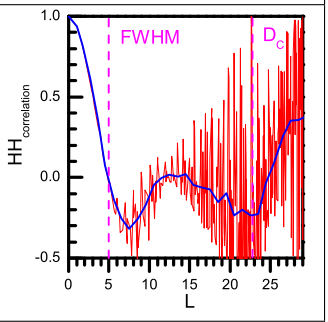
d	30×Gaussian random $FWHM = 5$	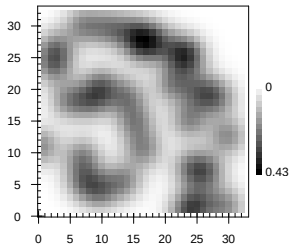	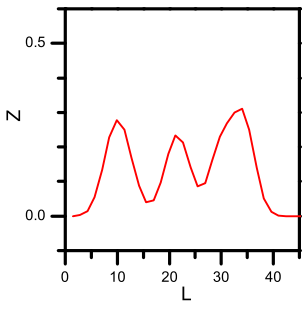	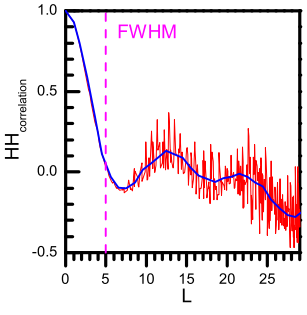
e	250×Gaussian random $FWHM = 5$	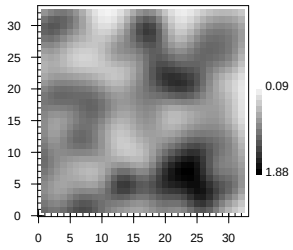	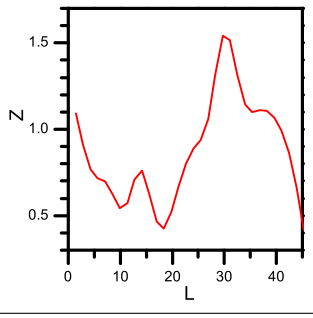	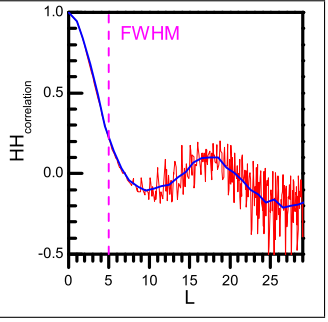

Table B.1: Artificial surface descriptions, map, $y = x$ diagonal cross-section, correlation function plots: red curves stand for direct calculation and blue one are averaged.

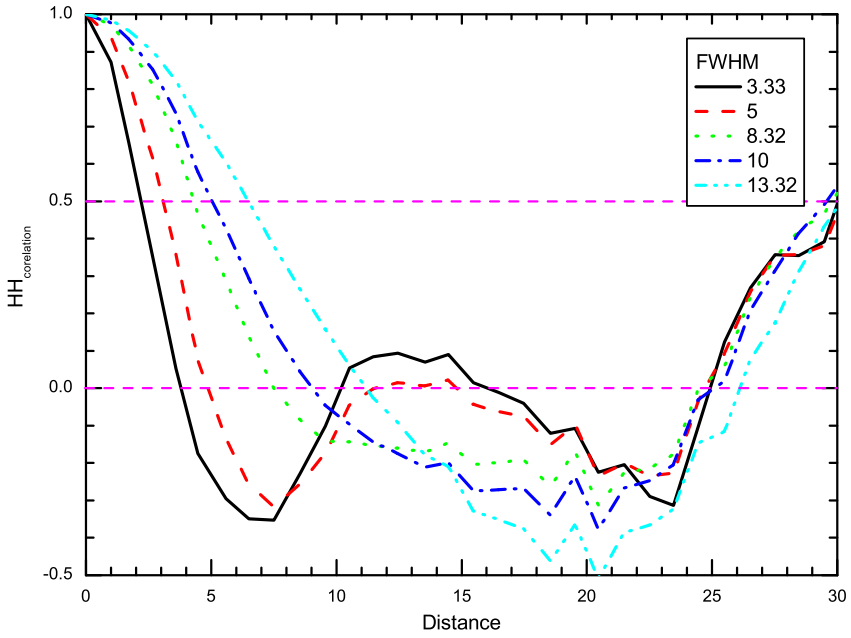

Figure B.2: Height-Height correlation function for Gaussian lines. Each curve represents correlation for a surface made of two gaussian lines of the same widths. Line widths are different for each case.

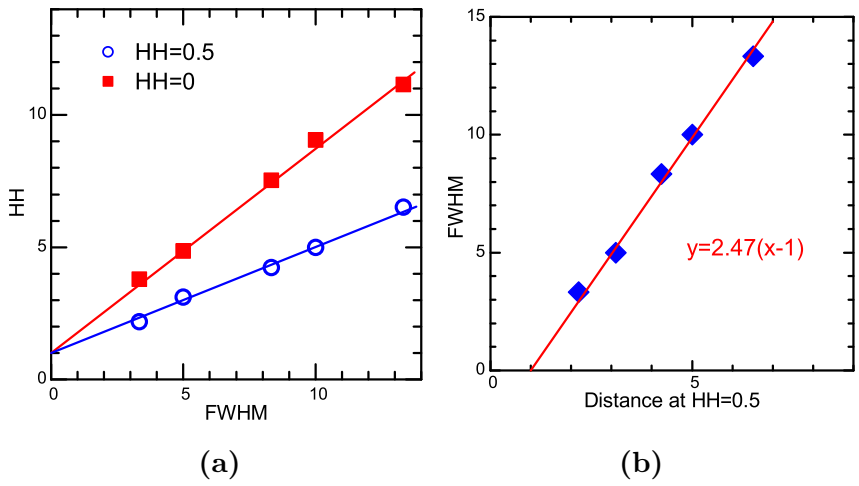

Figure B.3: Height-Height correlation function distances at characteristic values for Gaussian lines of different widths plotted in figure B.2. **(a)** distances at which height - height correlation assumes 0 and $1/2$ values for different widths of lines. **(b)** Dependence of Gaussian line FWHM on the distance at which height - height correlation assumes $1/2$ value.

Bibliography

Altshuler, B. L. and A. G. Aronov (**1985**), *Electron-Electron Interaction in Disordered Systems* (North Holland, Amsterdam).

Ando, K., H. Saito, Z. Jin, T. Fukumura, M. Kawasaki, Y. Matsumoto and H. Koinuma (**2001**), *Applied Physics Letters*, **78**(18), pages 2700.
URL http://link.aip.org/link/?APL/78/2700/1

Arnoult, A. (**1998**), *Dopage par modulation d'hétérostructures de semiconducteurs II-VI semimagnétiques en épitaxie par jets moléculaires*, Ph.D. thesis, Universite Joseph Fourier-Grenoble 1, Grenoble.
URL http://tel.ccsd.cnrs.fr/tel-00002701/en/

Arnoult, A., S. Tatarenko, D. Ferrand, J. Cibert, A. Haury, A. Wasiela and Y. Merle d'Aubigné (**1998**), *J. Cryst. Growth*, **184/185**, page 445.
URL http://dx.doi.org/10.1016/S0022-0248(98)80093-6

Attaccalite, C., S. Moroni, P. Gori-Giorgi and G. B. Bachelet (**2002**), *Physical Review Letters*, **88**(25), 256601.
URL http://link.aps.org/abstract/PRL/v88/e256601

Baibich, M. N., J. M. Broto, A. Fert, F. N. V. Dau, F. Petroff, P. Etienne, G. Creuzet, A. Friederich and J. Chazelas (**1988**), *Physical Review Letters*, **61**(21), pages 2472.
URL http://link.aps.org/abstract/PRL/v61/p2472

Baron, T., K. Saminadayar and N. Magnea (**1998**), *Journal of Applied Physics*, **83**(3), pages 1354.
URL http://link.aip.org/link/?JAP/83/1354/1

Berciu, M. and R. N. Bhatt (**2001**), *Physical Review Letters*, **87**(10), 107203.
URL http://link.aps.org/abstract/PRL/v87/e107203

Bertolini, M. (**2004**), *Contrôle du ferromagnétisme dans des puits quantiques de CdMnTe réalisés en Epitaxie par Jets Moléculaires.*, Ph.D. thesis, Universite Joseph Fourier-Grenoble 1, Grenoble.
URL http://tel.ccsd.cnrs.fr/tel-00008370

Boselli, M. A., A. Ghazali and I. C. da Cuhna Lima (**2000**), *Phys. Rev. B*, **62**, page 8895.
URL http://link.aps.org/abstract/PRB/v62/p8895

Boukari, H. (**2003**), *Puits quantiques de (Cd,Mn)Te et contrôle de la densité d'un gaz de trous 2D : spectroscopie et propriétés magnétiques*, Ph.D. thesis, Universite Joseph Fourier-Grenoble 1, Grenoble.
URL http://tel.ccsd.cnrs.fr/tel-00005381/en/

Boukari, H., P. Kossacki, M. Bertolini, D. Ferrand, J. Cibert, S. Tatarenko, A. Wasiela, J. A. Gaj and T. Dietl (**2002**), *Phys Rev Lett*, **88**(20), page 207204.
URL http://link.aps.org/abstract/PRL/v88/e207204

Boukari, H., F. Perez, D. Ferrand, P. Kossacki, B. Jusserand and J. Cibert (**2006**), *Physical Review B*, **73**(11), 115320.
URL http://link.aps.org/abstract/PRB/v73/e115320

Bourgognon, C. (**2001**), *Epitaxie et caractrisations structurales et magntiques de structures hybrides mtaux ferromagntiques sur semiconducteurs II-VI*, Ph.D. thesis, Universite Joseph Fourier-Grenoble 1, Grenoble.
URL http://www.lsp.ujf-grenoble.fr/vie_scientifique/theses/datas/ChristopheBourgognon.pdf

Brunthaler, G., T. Dietl, M. Sawicki, G. Stoger, J. Jaroszynski, A. Prinz, F. Schaffler and G. Bauer (**1996**), *Semiconductor Science and Technology.*, **11**, page 1624.
URL http://www.iop.org/EJ/abstract/0268-1242/11/11S/030

Chiba, D., N. Akiba, F. Matsukura, Y. Ohno and H. Ohno (**2000**), *Applied Physics Letters*, **77**(12), pages 1873.
URL http://link.aip.org/link/?APL/77/1873/1

Chiba, D., K. Takamura, F. Matsukura and H. Ohno (**2003**), *Applied Physics Letters*, **82**(18), pages 3020.
URL http://link.aip.org/link/?APL/82/3020/1

Cibert, J., H. Boukari, M. Bertolini, W. Pacuski, D. Ferrand, S. Tatarenko, P. Kossacki and J. Gaj (**2004**), *phys. stat. sol. (b)*, **241**, pages 692 .
URL http://dx.doi.org/10.1002/pssb.200304246

Cox, R. T., R. B. Miller, K. Saminadayar and T. Baron (**2004**), *Physical Review B*, **69**(23), page 235303.
URL http://link.aps.org/abstract/PRB/v69/e235303

Dietl, T. (**1994**), *Diluted Magnetic Semiconductors*, chapter 17, page 1251, number 3b in Hadbook on Semiconductors (North Holland, Amsterdam), (edited by T. S. Moss).

Dietl, T., A. Haury and Y. M. d'Aubigne (**1997**), *Physical Review B*, **55**(6), pages R3347.
URL http://link.aps.org/abstract/PRB/v55/pR3347

Dietl, T., H. Ohno and F. Matsukura (**2001**), *Physical Review B*, **63**(19), page 195205.
URL http://link.aps.org/abstract/PRB/v63/e195205

Dietl, T. and J. Spalek (**1982**), *Physical Review Letters*, **48**(5), pages 355.
URL http://link.aps.org/abstract/PRL/v48/p355

Dingle, R., H. L. Stormer, A. C. Gossard and W. Wiegmann (**1978**), *Applied Physics Letters*, **33**(7), pages 665.
URL http://link.aip.org/link/?APL/33/665/1

Edmonds, K. W., P. Boguslawski, K. Y. Wang, R. P. Campion, S. N. Novikov, N. R. S. Farley, B. L. Gallagher, C. T. Foxon, M. Sawicki, T. Dietl, M. B. Nardelli and J. Bernholc (**2004**), *Physical Review Letters*, **92**(3), 037201.
URL http://link.aps.org/abstract/PRL/v92/e037201

Efros, A. L., F. G. Pikus and V. G. Burnett (**1993**), *Physical Review B*, **47**(4), pages 2233.
URL http://link.aps.org/abstract/PRB/v47/p2233

Fatah, J. M., T. Piorek, P. Harrison, T. Stirner and W. E. Hagston (**1994**), *Phys. Rev. B*, **49**(15), pages 10341.
URL http://prola.aps.org/abstract/PRB/v49/i15/p10341_1

Ferrand, D. (**1999**), *Interactions dechange ferromagnetiques induites par un gaz de trous dans des hetereostructures 2D et des couches 3D de semiconducteurs II-VI*, Ph.D. thesis, Universite Joseph Fourier-Grenoble 1, Grenoble.

Ferrand, D., J. Cibert, A. Wasiela, C. Bourgognon, S. Tatarenko, G. Fishman, T. Andrearczyk, J. Jaroszyński, S. Kolesnik, T. Dietl, B. Barbara and D. Dufeu (**2001**), *Physical Review B*, **63**(8), 085201.
URL http://link.aps.org/abstract/PRB/v63/e085201

Fishman, G. (**1995**), *Phys. Rev. B*, **52**, page 11132.
URL http://link.aps.org/abstract/PRB/v52/p11132

Furdyna, J. K. (**1988**), *Journal of Applied Physics*, **64**(4), pages R29.
URL http://link.aip.org/link/?JAP/64/R29/1

Furdyna, J. K. and J. Kossut (**1988**), *Diluted magnetic semiconductors*, volume 25 of *Semiconductors and Semimetals* (Academic Press, New York).

Gaj, J. A., A. Golnik, P. Kossacki, K. Kowalik, W. Maślana, M. Kutrowski and T. Wojtowicz (**2004**), *phys. stat. sol. (c)*, **1**, pages 831.
URL http://dx.doi.org/10.1002/pssc.200304221

Gaj, J. A., W. Grieshaber, C. Bodin-Deshayes, J. Cibert, G. Feuillet, Y. Merle d'Aubigne and A. Wasiela (**1994**), *Physical Review B*, **50**(8), pages 5512.
URL http://link.aps.org/abstract/PRB/v50/p5512

Gaj, J. A., R. Planel and G. Fishman (**1979**), *Solid State Commun.*, **29**, page 435.
URL http://dx.doi.org/10.1016/0038-1098(79)91211-0

Golnik, A., P. Kossackin, K. Kowalik, W. Maślana, J. A. Gaj, M. Kutrowski and T. Wojtowicz (**2004**), *Solid State Communications*, **131**(5), pages 283.
URL http://dx.doi.org/10.1016/j.ssc.2004.05.034

Goryca, M., D. Ferrand, P. Kossacki, M. Nawrocki, W. Pacuski, W. Maślana, S. Tatarenko and J. C. 3 (**2006**), *physica status solidi (b)*, **243**, pages 882.
URL http://dx.doi.org/10.1002/pssb.200564605

Grieshaber, W., C. Bodin, J. Cibert, J. Gaj, Y. M. d'Aubigne, A. Wasiela and G. Feuillet (**1994**), *Applied Physics Letters*, **65**(10), pages 1287.
URL http://link.aip.org/link/?APL/65/1287/1

Hartmann, J. M., J. Cibert, F. Kany, H. Mariette, M. Charleux, P. Alleyson, R. Langer and G. Feuillet (**1996**), *J. Appl. Phys.*, **80**, page 6257.
URL http://dx.doi.org/10.1063/1.363714

Haury, A., A. Arnoult, V. A. Chitta, J. Cibert, Y. Merle dAubigné, S. Tatarenko and A. Wasiela (**1996**), 9th Int. Conf. Superlattices, Microstructures and Microdevices, liege.

Haury, A., A. Wasiela, A. Arnoult, J. Cibert, S. Tatarenko, T. Dietl and Y. M. d'Aubigne (**1997**), *Physical Review Letters*, **79**(3), pages 511.
URL http://link.aps.org/abstract/PRL/v79/p511

Hayashi, T., Y. Hashimoto, S. Katsumoto and Y. Iye (**2001**), *Applied Physics Letters*, **78**(12), pages 1691.
URL http://link.aip.org/link/?APL/78/1691/1

Huard, V., R. T. Cox, K. Saminadayar, A. Arnoult and S. Tatarenko (**2000***a*), *Physical Review Letters*, **84**(1), pages 187.
URL http://link.aps.org/abstract/PRL/v84/p187

Huard, V., R. T. Cox, K. Saminadayar, C. Bourgognon, A. Arnoult, J. Cibert and S. Tatarenko (**2000***b*), *Physica E*, **6**(1), pages 161.
URL http://dx.doi.org/10.1016/S1386-9477(99)00074-0

Janik, E., E. Dynowska, J. Bąk-Misiuk, M. Kutrowski, T. Wojtowicz, G. Karczewski, A. Zakrzewski and J. Kossut (**1995**), *Thin Solid Films*, **267**, page 74.
URL http://dx.doi.org/10.1016/0040-6090(95)06632-2

Jaroszynski, J., J. Wrobel, M. Sawicki, E. Kaminska, T. Skoskiewicz, G. Karczewski, T. Wojtowicz, A. Piotrowska, J. Kossut and T. Dietl (**1995**), *Physical Review Letters*, **75**(17), pages 3170.
URL http://link.aps.org/abstract/PRL/v75/p3170

Jasny, J., J. Sepiol, T. Irngartinger, M. Traber, A. Renn and U. P. Wild (**1996**), *Review of Scientific Instruments*, **67**(4), pages 1425.
URL http://link.aip.org/link/?RSI/67/1425/1

Kaminski, A. and S. D. Sarma (**2002**), *Physical Review Letters*, **88**(24), 247202.
URL http://link.aps.org/abstract/PRL/v88/e247202

Kawabata, T., K. Muro and S. Narita (**1977**), *Solid. State. Commun.*, **23**, page 267.
URL http://dx.doi.org/10.1016/0038-1098(77)90456-2

Kechrakos, D., N. Papanikolaou, K. N. Trohidou and T. Dietl (**2005**), *Physical Review Letters*, **94**(12), 127201.
URL http://link.aps.org/abstract/PRL/v94/e127201

Kheng, K., R. T. Cox, M. Y. d' Aubigne, F. Bassani, K. Saminadayar and S. Tatarenko (**1993**), *Physical Review Letters*, **71**(11), pages 1752.
URL http://link.aps.org/abstract/PRL/v71/p1752

Klopotowski, L., M. Nawrocki, J. Garniere, B. Devaud and E. Janik (**2004**), *Semiconductor Science and Technology*, **19**, page 380.
URL http://dx.doi.org/10.1088/0268-1242/19/4/125

Konig, J., H.-H. Lin and A. H. MacDonald (**2000**), *Physical Review Letters*, **84**(24), pages 5628.
URL http://link.aps.org/abstract/PRL/v84/p5628

Koshihara, S., A. Oiwa, M. Hirasawa, S. Katsumoto, Y. Iye, C. Urano, H. Takagi and H. Munekata (**1997**), *Physical Review Letters*, **78**(24), pages 4617.
URL http://link.aps.org/abstract/PRL/v78/p4617

Kossacki, P. (**1998**), *Magnetism and excitons in $Cd_{1-x}Mn_xTe$ quantum wells*, Ph.D. thesis, Warsaw University Physics Department, Hoża 69 00-681 Warszawa Poland.

Kossacki, P. (**2003**), *J. Phys.: Condens. Matter*, **15**, pages R471.
URL http://dx.doi.org/10.1088/0953-8984/15/13/201

Kossacki, P., H. Boukari, M. Bertolini, D. Ferrand, J. Cibert, S. Tatarenko, J. A. Gaj, B. Deveaud, V. Ciulin and M. Potemski (**2004***a*), *Physical Review B*, **70**(19), page 195337.
URL http://link.aps.org/abstract/PRB/v70/e195337

Kossacki, P., J. Cibert, D. Ferrand, Y. Merle d'Aubigne, A. Arnoult, A. Wasiela, S. Tatarenko and J. A. Gaj (**1999**), *Physical Review B*, **60**(23), pages 16018.
URL http://link.aps.org/abstract/PRB/v60/p16018

Kossacki, P., D. Ferrand, A. Arnoult, J. Cibert, S. Tatarenko, A. Wasiela, Y. Merle d'Aubigné, J. Staehli, J. D. Ganiere, W. Bardyszewski, K. Swiatek, M. Sawicki, J. Wrobel and T. Dietl (**2000**), *Physica E*, **6**, page 709.
URL http://dx.doi.org/10.1016/S1386-9477(99)00178-2

Kossacki, P., D. Ferrand, M. Goryca, M. Nawrocki, W. Pacuski, W. Maślana, S. Tatarenko and J. Cibert (**2006**), *Physica E*, **32**(1-2), pages 454.
URL http://dx.doi.org/10.1016/j.physe.2005.12.087

Kossacki, P., A. Kudelski, J. Gaj, J. Cibert, S. Tatarenko, D. Ferrand, A. W. B. Deveaud and T. Dietl (**2002**), *Physica E*, **12**(1-4), pages 344 .
URL http://dx.doi.org/10.1016/S1386-9477(01)00273-9

Kossacki, P., W. Pacuski, W. Maślana, J. A. Gaj, M. Bertolini, D. Ferrand, S. Tatarenko and J. Cibert (**2004***b*), *Physica E*, **21**, pages 943.
URL http://dx.doi.org/10.1016/j.physe.2003.11.154

Kravchenko, S. V. and M. P. Sarachik (**2004**), *Reports on Progress in Physics*, **67**, pages 1.
URL http://stacks.iop.org/0034-4885/67/1

Kudelski, A. (**2004**), *In Plane Optical Anisotropy of Semiconductor Heterostructires*, Ph.D. thesis, Warsaw University Physics Department, Hoża 69 00-681 Warszawa Poland.

Kuhn-Heinrich, B., W. Ossau, H. Heinke, F. Fischer, T. Litz, A. Waag and G. Landwehr (**1993**), *Applied Physics Letters*, **63**(21), pages 2932.
URL http://link.aip.org/link/?APL/63/2932/1

Kutrowski, M. (**2001**), *Magnetooptyczne własności profilowanych studni kwantowych opartych na związkach $Cd_{1-x}Mn_xTe$ i $Cd_{1-y}Mg_yTe$.*, Ph.D. thesis, Institute of Physics Polish Academy of Science, Al. Lotnikòw 32/46 PL-02-668 Warszawa, Polska.

Lampert, M. A. (**1958**), *Phys. Rev. Lett.*, **450**, page 1.
URL http://link.aps.org/abstract/PRL/v1/p450

Landolt-Börnstein (**1982**), *Numerical data and functional relationships in science and technology*, volume 17b (Springer Verlag, Berlin).

Le-Si-Dang, G. Neu and R. Romestain (**1982**), *Solid-State-Communications*, **44**(8), page 1187.
URL 10.1016/j.jmmm.2005.10.018

Lee, B., T. Jungwirth and A. H. MacDonald (**2000**), *Physical Review B*, **61**(23), pages 15606.
URL http://link.aps.org/abstract/PRB/v61/p15606

Mackh, G., W. Ossau, D. R. Yakovlev, A. Waag, G. Landwehr, R. Hellmann and E. O. Gobel (**1994**), *Physical Review B*, **49**(15), pages 10248.
URL http://link.aps.org/abstract/PRB/v49/p10248

Munekata, H., H. Ohno, S. von Molnar, A. Segmuller, L. L. Chang and L. Esaki (**1989**), *Physical Review Letters*, **63**(17), pages 1849.
URL http://link.aps.org/abstract/PRL/v63/p1849

Nazmul, A. M., T. Amemiya, Y. Shuto, S. Sugahara and M. Tanaka (**2005**), *Physical Review Letters*, **95**(1), 017201.
URL http://link.aps.org/abstract/PRL/v95/e017201

Nazmul, A. M., S. Sugahara and M. Tanaka (**2002**), *Applied Physics Letters*, **80**(17), pages 3120.
URL http://link.aip.org/link/?APL/80/3120/1

Nazmul, A. M., S. Sugahara and M. Tanaka (**2003**), *Physical Review B*, **67**(24), 241308.
URL http://link.aps.org/abstract/PRB/v67/e241308

Ohno, H. (**1998**), *Science*, **281**, page 951.
URL http://www.sciencemag.org/cgi/content/abstract/281/5379/951

Ohno, H., D. Chiba, F. Matsukura, T. Omyla, E. Abe, T. Dietl, Y. Ohno and K. Ohtani (**2000**), *Nature*, **408**, page 944.
URL http://dx.doi.org/10.1038/35050040

Ossau, W. and B. Kuhn-Heidrich (**1993**), *Physica B*, **184**, page 422.
URL http://dx.doi.org/10.1016/0921-4526(93)90392-J

Ossau, W., B. Kuhn-Heindrich, Waag and G. Landwehr (**1996**), *Journal of Crystal Growth*, **159**, pages 1046.
URL http://dx.doi.org/10.1016/0022-0248(95)00873-X

Paganotto, N., J. Siviniant, D. Coquilant, D. Scalbert, J. Lascaray and A. V. Kavokin (**1998**), *Phys. Rev. B*, **58**, page 4082.
URL http://link.aps.org/abstract/PRB/v58/p4082

Pashitskii, E. A. and S. Ryabchenko (**1979**), *Sov. Phys. Solid State*, **21**, page 545.

Płochocka, P., P. Kossacki, W. Maślana, J. Cibert, S. Tatarenko, C. Radzewicz and J. A. Gaj (**2004**), *Physical Review Letters*, **92**(17), page 177402.
URL http://link.aps.org/abstract/PRL/v92/e177402

Potashnik, S. J., K. C. Ku, S. H. Chun, J. J. Berry, N. Samarth and P. Schiffer (**2001**), *Applied Physics Letters*, **79**(10), pages 1495.
URL http://link.aip.org/link/?APL/79/1495/1

Ramon, G., A. Mann and E. Cohen (**2003**), *Physical Review B*, **67**(4), 045323.
URL http://link.aps.org/abstract/PRB/v67/e045323

Saito, H., V. Zayets, S. Yamagata and K. Ando (**2002**), *Physical Review B*, **66**(8), 081201.
URL http://link.aps.org/abstract/PRB/v66/e081201

Saito, H., V. Zayets, S. Yamagata and K. Ando (**2003***a*), *Physical Review Letters*, **90**(20), 207202.
URL http://link.aps.org/abstract/PRL/v90/e207202

Saito, H., V. Zayets, S. Yamagata and K. Ando (**2003***b*), *Journal of Applied Physics*, **93**(10), pages 6796.
URL http://link.aip.org/link/?JAP/93/6796/1

Sawicki, M., T. Dietl, J. Kossut, J. Igalson, T. Wojtowicz and W. Plesiewicz (**1986**), *Physical Review Letters*, **56**(5), pages 508.
URL http://link.aps.org/abstract/PRL/v56/p508

Shields, A., J. Osborne, M. Simmons, M. Pepper and D. Ritchie (**1995**), *Physical Review B*, **52**(8), pages R5523.
URL http://link.aps.org/abstract/PRB/v52/pR5523

Singh, J., K. K. Bajaj and S. Chaudhuri (**1984**), *Applied Physics Letters*, **44**(8), pages 805.
URL http://link.aip.org/link/?APL/44/805/1

Siviniant, J., D. Scalbert, A. V. Kavokin, D. Coquilat and J. Lascaray (**1999**), *Phys. Rev. B*, **59**, page 1602.
URL http://link.aps.org/abstract/PRB/v59/p1602

Skolnick, M. S., K. J. Nash, M. K. Saker, S. J. Bass, P. A. Claxton and J. S. Roberts (**1987***a*), *Applied Physics Letters*, **50**(26), pages 1885.
URL http://link.aip.org/link/?APL/50/1885/1

Skolnick, M. S., J. M. Rorison, K. J. Nash, D. J. Mowbray, P. R. Tapster, S. J. Bass and A. D. Pitt (**1987***b*), *Physical Review Letters*, **58**(20), pages 2130.
URL http://link.aps.org/abstract/PRL/v58/p2130

Smorchkova, I. P., N. Samarth, J. M. Kikkawa and D. D. Awschalom (**1997**), *Physical Review Letters*, **78**(18), pages 3571.
URL http://link.aps.org/abstract/PRL/v78/p3571

Spalek, J., A. Lewicki, Z. Tarnawski, J. K. Furdyna, R. R. Galazka and Z. Obuszko (**1986**), *Physical Review B*, **33**(5), pages 3407.
URL http://link.aps.org/abstract/PRB/v33/p3407

Stormer, H. L., R. Dingle, A. C. Gossard, W. Wiegmann and M. D. Sturge (**1979**), *Journal of Vacuum Science and Technology*, **16**(5), pages 1517.
URL http://link.aip.org/link/?JVS/16/1517/1

Story, T., R. R. Gazka, R. B. Frankel and P. A. Wolff (**1986**), *Physical Reviev Letters*, **56**(7), page 777.
URL http://link.aps.org/abstract/PRL/v56/p777

Suffczynski, J., T. Kazimierczuk, M. Goryca, B. Piechal, A. Trajnerowicz, K. Kowalik, P. Kossacki, A. Golnik, K. P. Korona, M. Nawrocki, J. A. Gaj and G. Karczewski (**2006**), *Physical Review B*, **74**(8), 085319.
URL http://link.aps.org/abstract/PRB/v74/e085319

Takamura, K., F. Matsukura, D. Chiba and H. Ohno (**2002**), *Applied Physics Letters*, **81**(14), pages 2590.
URL http://link.aip.org/link/?APL/81/2590/1

Tanatar, B. and D. M. Ceperley (**1989**), *Physical Review B*, **39**(8), pages 5005.
URL http://link.aps.org/abstract/PRB/v39/p5005

Thomas, G. A. and T. M. Rice (**1977**), *Solid. State. Commun.*, **23**, page 359.
URL http://dx.doi.org/10.1016/0038-1098(77)90232-0

Tutuc, E., S. Melinte and M. Shayegan (**2002**), *Physical Review Letters*, **88**(3), 036805.
URL http://link.aps.org/abstract/PRL/v88/e036805

Tyagai, V., O. Snitko, V. Bondarenko, N. Vitrikhovskii, V. Popov and A. Krasiko (**1974**), *Sov. Phys. Solid State*, **16**(5), page 885.

Vakili, K., Y. P. Shkolnikov, E. Tutuc, E. P. D. Poortere and M. Shayegan (**2004**), *Physical Review Letters*, **92**(22), 226401.
URL http://link.aps.org/abstract/PRL/v92/e226401

Wei, S.-H. and A. Zunger (**1998**), *Applied Physics Letters*, **72**(16), pages 2011.
URL http://link.aip.org/link/?APL/72/2011/1

Weisbuch, C., R. Dingle, P. M. Petroff, A. C. Gossard and W. Wiegmann (**1981**), *Applied Physics Letters*, **38**(11), pages 840.
URL http://link.aip.org/link/?APL/38/840/1

Wojtowicz, T., M. Kutrowski, G. Karczewski, J. Kossut, B. König, A. Keller, D. R. Yakovlev, A. Waag, J. Geurts, W. Ossau, G. Landwerh, I. A. Merkulov, F. J. Teran and M. Potemski (**2000**), *J. Cryst. Growth*, **214-215**, page 378.
URL http://dx.doi.org/10.1016/S0022-0248(00)00113-5

Wolf, S. A., D. D. Awschalom, R. A. Buhrman, J. M. Daughton, S. von Molnar, M. L. Roukes, A. Y. Chtchelkanova and D. M. Treger (**2001**), *Science*, **294**(5546), pages 1488.
URL http://www.sciencemag.org/cgi/content/abstract/294/5546/1488

Yang, J., Y. Zidon and Y. Shapira (**2002**), *J. Appl. Phys.*, **91**, page 703.
URL http://dx.doi.org/10.1063/1.1425071

Yayon, Y., M. Rappaport, V. Umansky and I. Bar-Joseph (**2001**), *Physical Review B*, **64**(8), 081308.
URL http://link.aps.org/abstract/PRB/v64/e081308

Zehner, U., B. Kuhn-Heindrich, W. Ossau, A. Waag, G. Lanwehr, H. H. Cheng and R. J. Nicholas (**1996**), *Acta Phsica Polonica*, **90**, page 989.

Zheng, X. L., D. Heiman, B. Lax and F. A. Chambers (**1988**), *Appl. Phys. Lett*, **52**, page 287.
URL http://dx.doi.org/10.1063/1.99496

List of Figures

Abstract

By employing surface acceptor states a novel technique of modulation doping of (Cd,Mn)Te quantum wells was developed. Its key properties were examined and optimized in order to obtain highest hole gas density. Efficient doping can be achieved without the technological restrictions arising from incorporating nitrogen impurities into the structures. It allowed us to extend the studied range of Mn densities in quantum well material up to 10.8%. Thus in studies of carrier induced magnetic ordering it was possible to cover almost all the range of effective Mn spin density available in (Cd,Mn)Te by reaching $x_{eff} = 4.1\%$. We observed thus the highest ever reported transition temperature for this type of magnetic system $T_C = 9.5 \pm 3$K (for $x_{eff} = 4.1\%$ and $p = 5 \times 10^{11}$ cm^{-2}).

The carrier density and the spin density were measured locally. Both densities were independently derived from microphotoluminescence maps recorded under a magnetic field. The studied samples contained (Cd,Mn)Te quantum wells with two types of doping used: nitrogen and surface acceptor states. We found that the correlation length of the carrier density fluctuations is larger (3 μm) for surface doping than for nitrogen doping (1 μm) with no effect of the disorder introduced by the Mn ions. The spin density fluctuates on a smaller scale. In samples with sufficient Mn density the fluctuations of local spontaneous magnetization were measured. It was found that those fluctuations are strongly correlated with fluctuations of carrier density and inherit the correlation length of carrier density fluctuations.

Keywords: Spintronics, II-VI Semiconductors, Ferromagnetism, Doping, Disorder.

Résumé

En utilisant les états de surface accepteurs, nous avons développé une nouvelle méthode de dopage de puits quantique de CdMnTe. Les caractéristiques de cette méthode sont étudiées et optimisée dans le but d'obtenir des fortes densités de trous. Un dopage efficace est obtenu sans restrictions technologiques liées à l'incorporation de l'azote dans la structure. Cette méthode nous a permis d'étendre la gamme de densités de Mn incorporé dans le puits quantique à 10.8%. Il nous a donc été possible dans les études sur le magnétisme induit par porteurs libres de couvrir pratiquement toute la gamme de spin de Mn effectif dans (Cd,Mn)Te en atteignant $x_{eff} = 4.1\%$. Nous reportons alors la température de transition la plus élevé pour ce type de système magnétique de $T_C = 9.5 \pm 3$K (pour $x_{eff} = 4.1\%$ et $p = 5 \times 10^{11}$ cm^{-2}).

Les densités de porteurs et de spins localisés ont été mesurées localement. Chacune de ces densités ont été déterminées de manière indépendante par des mesures de micro-photoluminescence sous champ magnétique intense. Les échantillons étudiés contiennent des puits quantiques de (Cd,Mn)Te avec deux différents types de dopants : l'azote et des états de surface accepteur. Nous déterminons une longueur de corrélation des fluctuations de densités de porteurs supérieure dans le cas du dopage par la surface (3 μm) que pour le dopage a l'azote (1 μm) sans aucun effet de désordre introduit par les ions Mn. La densité de spin fluctue sur une longueur plus faible. Pour des échantillons contenant une densité d'ions Mn importante, nous avons mesuré les fluctuations locales de l'aimantation spontanée. Nous montrons que ces fluctuations sont fortement corrélées avec les fluctuations de la densité de porteurs et présentent la même longueur caractéristique que les fluctuations de la densité de porteurs.

Mots clefs: Electronique de spin, Semiconducteurs II-VI, Ferromagnétisme, Dopage, Desordre.